Influence of Structure and Topology on the Deformation Behavior and Fracture of Oxide Glasses

Einfluss von Struktur und Topologie auf das Verformungsverhalten und den Bruch von Oxidgläsern

Der Technischen Fakultät
der Friedrich-Alexander-Universität Erlangen-Nürnberg

zur
Erlangung des Doktorgrades Dr.-Ing.

vorgelegt von

Achraf Atila
aus Casablanca, Marokko

Als Dissertation genehmigt
von der Technischen Fakultät
der Friedrich-Alexander-Universität Erlangen-Nürnberg

Tag der mündlichen Prüfung: 22.02.2023

Gutachter/in: Prof. Dr.-Ing. Erik Bitzek
Prof. Dr. Dominique de Ligny

Achraf Atila – Influence of Topology and Network Connectivity on the Deformation Behavior and Fracture of Oxide Glasses

ABSTRACT Oxide glasses are ubiquitous in daily life. They have proven useful as bioactive materials, optical fibers, flexible substrates and displays, solar modules, and many other applications. This enormous number of current applications is due to the sheer number of possible compositions made by the possibility of combining different elements from the periodic table. Nevertheless, their usage is limited by their brittleness and low resistance to damage due to the lack of large and clear deformation (shearing) mechanisms to dissipate stress. Computer simulations, including atomistic simulations, serve as an important tool to understand and reveal the deformation mechanisms at atomic and nanometric scales, thus guiding the development and design of glasses with superior properties.

The objective of this thesis are to understand the role of structure, modifiers, and processing on oxide glasses' deformation and fracture behavior. Large-scale atomistic simulations were performed to reveal these deformation mechanisms at the atomic scale in binary metaphosphate glasses modified with different modifiers, silica, and sodium silicate glasses with varying sodium content. The effect of modifier type on deformation-induced structural anisotropy and deformation behavior was studied in metaphosphate glasses. On the other hand, the effect of the modifier content and topology on the deformation behavior and fracture was investigated in sodium silicate glasses.

In the metaphosphate glasses, the presence of modifiers with high field strength leads to higher mechanical properties when compared to glass compositions with low field strength modifiers. The origin of the structural transient and persistent anisotropy observed in all metaphosphate glasses was shown to be the same, which was discussed at different structural levels. At the short-range structure, it originates from the alignment of P–O bonds. The next structural level involving neighboring tetrahedra is captured by the orientation of the P–P bonds. These short-range alignments of the P–O and P–P bonds lead to the changes in the medium-range order as captured by the orientation of the chain along the tensile axis and orthogonal to the loading axis. The tensile Young's moduli of the anisotropic glasses obtained by either pre-tension or pre-compression measured along the pre-deformation axis is lower than the pristine glass due to a stretching of the structure as indicated by the remaining plastic strain. The tensile Young's moduli of the pre-deformed metaphosphate glasses by pre-tension showed a higher Young's modulus than the glasses pre-deformed in compression when measured in the same direction as the pre-deformation one.

On the other hand, understanding the mechanical behavior of silicate glasses with different compositions and pre-loading modes is highly relevant to many technological applications. Therefore, silicate glasses with different compositions and subjected to different type of deformations at room temperature were studied. The atomic-scale mechanisms of the deformation of these glasses showed that during compression and shear at higher strains, a significant number of atoms that switched bonds was found, which was not the case in tension due to the fracture of the samples. These atoms that have a change in their bonding topology are localized within shear bands in the shear deformation and are homogeneously distributed in samples deformed in compression. The tensile mechanical behavior of the pre-deformed glasses showed that the pre-deformation decreased the material strength, and an increasing ductility was observed in the case of pre-compression. This originates from a homogeneous persistent change in the bonding with pre-compression, which was not the case on pre-tension and pre-shear. The tensile deformation mechanism of pre-deformed glasses was found to be due to the appearance and coalescence of cavities during the deformation. The presence of these cavities is affected by both composition and pre-deformation, which was also discussed for the first time at the atomic scale. The results presented in this thesis highlight the importance of the local events in controlling the macroscopic glass properties. Thus, providing insights at the atomic scale needed for further development of oxide glasses.

Achraf Atila – Einfluss von Topologie und Netzwerkkonnektivität auf das Verformungsverhalten und den Bruch von Oxidgläsern

ZUSAMMENFASSUNG Oxidgläser sind in unserem täglichen Leben allgegenwärtig. Sie haben sich als bioaktive Materialien, optische Fasern, flexible Substrate und Displays, Solarmodule und viele andere Anwendungen bewährt. Diese enorme Zahl an aktuellen Anwendungen ist auf die schiere Anzahl an möglichen Zusammensetzungen zurückzuführen, die sich aus der Möglichkeit ergeben, verschiedene Elemente aus dem Periodensystem zu kombinieren. Ihre Verwendung wird jedoch durch ihre Sprödigkeit und geringe Widerstandsfähigkeit gegen Beschädigungen eingeschränkt, da es keine großen und eindeutigen Verformungsmechanismen (Scherung) zum Abbau von Spannungen gibt. Computersimulationen, einschließlich atomistischer Simulationen, sind ein wichtiges Instrument, um die Verformungsmechanismen auf atomarer und nanometrischer Ebene zu verstehen und aufzudecken und so die Entwicklung und den Entwurf von Gläsern mit besseren Eigenschaften zu unterstützen.

Ziel dieser Doktorarbeit ist es, die Rolle der Struktur, der Modifikatoren und der Verarbeitung auf das Verformungs- und Bruchverhalten von Oxidgläsern zu untersuchen. Es wurden großmaßstäbliche atomistische Simulationen durchgeführt, um diese Verformungsmechanismen auf atomarer Ebene in binären Metaphosphatgläsern, die mit verschiedenen Modifikatoren modifiziert wurden, sowie in Siliziumdioxid und Natriumsilikatgläsern mit unterschiedlichem Natriumgehalt aufzudecken. In Metaphosphatgläsern wurde die Auswirkung der Art des Modifikators auf die verformungsinduzierte strukturelle Anisotropie und das Verformungsverhalten untersucht. Bei Natriumsilikatgläsern hingegen wurde der Einfluss des Modifikatorgehalts und der Topologie auf das Verformungsverhalten und den Bruch untersucht.

In den Metaphosphatgläsern führt das Vorhandensein von Modifikatoren mit hoher Feldstärke zu höheren mechanischen Eigenschaften im Vergleich zu Glaszusammensetzungen mit Modifikatoren mit niedriger Feldstärke. Es wurde gezeigt, dass der Ursprung der in allen Metaphosphatgläsern beobachteten strukturellen transienten und anhaltenden Anisotropie derselbe ist, was auf verschiedenen strukturellen Ebenen diskutiert wurde. Auf der Ebene der Kurzstreckenstruktur ist sie auf die Ausrichtung der P–O-Bindungen zurückzuführen. Die nächste Strukturebene, an der benachbarte Tetraeder beteiligt sind, wird durch die Ausrichtung der P-P-Bindungen bestimmt. Diese kurzreichweitigen Ausrichtungen der P–O- und P–P-Bindungen führen zu Veränderungen in der mittelfristigen Ordnung, die durch die Ausrichtung der Kette entlang der Zugachse und orthogonal zur Belastungsachse erfasst wird. Die Zug-E-Moduln der anisotropen Gläser, die durch Vorspannung oder Vorkompression entlang der Vorverformungsachse gemessen wurden, sind aufgrund der Streckung der Struktur, die durch die verbleibende plastische Dehnung angezeigt wird, niedriger als die des ursprünglichen Glases. Die Zug-E-Moduln der durch Vorspannung vorverformten Metaphosphatgläser wiesen einen höheren Elastizitätsmodul auf als die durch Druck vorverformten Gläser, wenn sie in der gleichen Richtung wie die Vorverformung gemessen wurden.

Andererseits ist das Verständnis des mechanischen Verhaltens von Silikatgläsern mit unterschiedlichen Zusammensetzungen und Vorspannungen für viele technische Anwendungen von großer Bedeutung. Daher wurden Silikatgläser mit unterschiedlichen Zusammensetzungen untersucht, die bei Raumtemperatur verschiedenen Arten von Verformungen ausgesetzt waren. Die Mechanismen der Verformung dieser Gläser auf atomarer Ebene zeigten, dass während der Kompression und der Scherung bei höheren Dehnungen eine signifikante Anzahl von Atomen gefunden wurde, die ihre Bindungen wechselten, was bei der Spannung aufgrund des Bruchs der Proben nicht der Fall war. Diese Atome, die eine Änderung ihrer Bindungstopologie aufweisen, sind bei der Scherverformung innerhalb von Scherbändern lokalisiert und in den unter Druck verformten Proben homogen verteilt. Das mechanische Zugverhalten der vorverformten Gläser zeigte, dass die Vorverformung die Festigkeit des Materials verringerte, während bei der Vorkompression eine zunehmende Duktilität beobachtet wurde. Dies ist auf eine gleichmäßige, anhaltende Veränderung der Bindung bei

Vorkompression zurückzuführen, was bei Vorspannung und Vorscherung nicht der Fall war. Es wurde festgestellt, dass der Mechanismus der Zugverformung von vorverformten Gläsern auf das Auftreten und Zusammenwachsen von Hohlräumen während der Verformung zurückzuführen ist. Das Vorhandensein dieser Hohlräume wird sowohl von der Zusammensetzung als auch von der Vorverformung beeinflusst, was zum ersten Mal auch auf atomarer Ebene diskutiert wurde. Die in dieser Arbeit vorgestellten Ergebnisse unterstreichen die Bedeutung lokaler Ereignisse für die Kontrolle der makroskopischen Glaseigenschaften. Sie liefern somit Erkenntnisse auf atomarer Ebene, die für die weitere Entwicklung von Oxidgläsern erforderlich sind.

Contents

1 Introduction

The history of glassy materials manufacturing dates back to 3500 BC or more, but the use of glass predates recorded history. Today, glass plays an essential role in modern human civilization. Thus, they are one of the most widely used materials by mankind, in a way that we can call our age by "the glass age". Their use in many applications in everyday life has profoundly changed society and contributed to technological advancement. Despite their apparent fragility, which is perceived as their greatest weakness, this disadvantage has been accepted by trying to take advantage of the optical properties and universal processing capability of glasses.

Glasses have found their way into many applications with low levels of tensile stress, starting with simple applications (windows and bottles) to manufacturing complex technologies (screens for smartphones and monitors, or storage of industrial and nuclear waste). Most of the existing glass products are based on silica and phosphate. Silica-based glasses are used for many applications, such as screens for mobile devices, and phosphate-based glasses are often used as optical fibers and solid electrolytes for batteries.

The melt-quenched glasses are generally regarded as isotropic materials. However, it was reported that glasses showed anisotropic properties when processed accordingly, e.g., by fiber drawing [1] or mechanical deformation at room temperature [2] where the structure of the glass is stretched in one preferred direction [3]. Understanding how the structural anisotropy is related to the glass properties is of great importance in designing high birefringence optical fibers and getting insight into the plastic flow and/ or structural relaxation of the glass. Understanding the processes and mechanisms that lead to the anisotropy in oxide glasses is crucial to advancing the development of oxide glasses for many applications. Moreover, the mechanical behavior of the glass is another critical set of properties that hinders the usage of glasses in many applications. Understanding the structural anisotropy and the deformation behavior of oxide glasses is of fundamental importance for designing glass compositions with tailored mechanical properties.

The fact that glasses are non-crystalline materials with an amorphous structure having no long-range order makes analyzing the mechanisms that lead to anisotropy or fracture non-trivial. Most of the important phenomena that happen in the glasses are due to changes at the short- and medium-range orders, which their understanding require insights from the atomic scale. Shifting from mean-field approximations in studying the structure–properties relationship to other approaches that include the role of local and temporal fluctuations and medium-range structure is required to design and further develop oxide glasses [4].

In this thesis, the role of composition, topology, and structure on the anisotropy and deformation behavior of oxide glasses was studied using molecular dynamics simulations. Binary metaphosphate glasses modified with different modifiers and sodium silicate glasses with varying sodium content were simulated. The effect of modifier type on the structural anisotropy and deformation behavior of the metaphosphate glasses was investigated. On the other hand, the effect of the modifier content and pre-deformation on the deformation behavior and fracture, which is largely unknown, was investigated in silica

and sodium silicate glasses. The presence of modifiers with different field strengths was correlated with changes in the mechanical properties. The origin of the structural transient and persistent anisotropy observed in all glasses was found using different analysis tools at different structural levels. Furthermore, the mechanical behavior of the anisotropic glasses was also evaluated. On the other hand, understanding the mechanical behavior of silicate glasses with different compositions and pre-loading modes is highly relevant to many technological applications. We used molecular dynamics simulations to study silicate glasses with different compositions and subjected them to different loading at room temperature. We explained the atomic-scale mechanisms of the deformation of these glasses. Statistical and local analysis tools were used to understand and explain the deformation behavior of the pristine silica and binary sodium silicate glasses and the pre-deformed glasses. We highlighted the important role of the glass structure and topology on the deformation behavior of these glasses. The following scientific questions are addressed in this thesis: (I) Origins of the anisotropy in metaphosphate glasses. In particular, what are the origins of the anisotropy in metaphosphate glasses? What are the structural bases of anisotropy in metaphosphate glasses? What are the differences between transient and persistent anisotropy in metaphosphate glasses? How does the type of the modifiers influence the structure and the structural anisotropy? What is the influence of persistent anisotropy on the deformation behavior of the metaphosphate glasses? (II) The deformation behavior and fracture of silicate glasses. How do the composition and pre-deformation influence initial flaws in silica and sodium silicate glasses? How does pre-deformation change the structure? How does composition influence the deformation mechanism? How does the deformation mechanism depend on pre-deformation?

This thesis is organized as follows. In chapter 2, the fundamentals of glass formation and glass systems studied here are presented. Then, the literature of studies investigating the anisotropy in glasses in general and oxide glasses, in particular, is reviewed. In addition, an overview of the mechanics of glasses is given at the end of this chapter. In chapter 3, the methods of simulations, statistical mechanics, simulation setups, and analysis methods are introduced. The main part of this thesis is divided into two parts based on different glasses studied. The first part deals with the simulation results and discusses the origins of the anisotropy in metaphosphate glasses and its implications on their mechanical properties. In the second part, the results of the simulations on the deformation behavior and fracture of silicate glasses are presented and discussed.

2 Background and literature review

The history of manufacturing of glassy materials dates back to 3500 BC or more, but the use of glasses predates recorded history. Nowadays, glasses play an essential role in modern human civilization. Glasses are one of the most used materials by humankind, so we often hear that we are living in "the glass age" [5], and recently the United Nations general assembly designated 2022 as the "International Year of Glass" [6]. Furthermore, glasses are attractive due to many unique properties, such as universal processability, sustainability, strength, low-cost material, and being environmentally friendly. As a result, glasses have found their place in many applications, from simple applications (windows and bottles) to manufacturing complex technologies (screens for smartphones and monitors or storing industrial and nuclear waste).

2.1 Importance of glasses

Glasses are ubiquitous in our daily lives and find their way into many technological applications [7–10]. Although we have been using glasses for millennials [7, 11, 12] we are not sure when and where glass manufacturing began. Glass products became an integral part of our lives. Glass is commonly known as a transparent and brittle material. Its transparency made noticing its presence difficult, and one must be very careful when handling it due to its brittleness. The glasses mentioned above are based on silica with the addition of some metal oxides such as Na_2O and CaO to form the soda-lime glass, the most used glass by humankind. Technically speaking, glass can be found everywhere in one way or another. It is a practical and environmentally friendly material because most types of glass are reusable. Glass can be easily recycled to be used, after being melted down, to make new products. Glass applications can be divided into several categories. Materials suitable for different applications can be everywhere, from electronics to electrical, household, and industrial products. Optical fibers used in communications are a recent example of the usefulness of glass [8–10, 13–16]. Despite its multiple applications, glass is a less-known material, mainly because of its disordered character; they are difficult to describe. Simulations at the atomic scale have helped to decipher the atomic genome of glasses and better understand the relationship between the structure, composition, and properties of glasses [17–37].

This chapter introduces the glasses and their rules of formations, anisotropy in glasses, and theories of deformation mechanisms of oxide glasses. Section 2.1 briefly presents the importance of glasses. Section 2.2 presents the glasses and the glassy state, summarising the glass formation from a thermodynamic, kinetic, and structural point of view. The glass families and their structural characteristics with a focus on silicate and phosphate glasses are presented in section 2.3. In section 2.4, the anisotropy in glasses, especially in silicate and phosphate glasses, is reviewed from both experiments and simulations. Finally, the glasses' mechanical properties and deformation behavior are presented in section 2.5. At the end of this chapter, we present the scientific questions addressed in this thesis, hope-

fully, answered in the following chapters.

2.2 Glass and glassy state

Glass transition

The glass transition, or vitrification, refers to the slowing down of kinetic processes, such as diffusion, viscous flow, and molecular reorientation [38]. It is a phenomenon describing the transformation of a supercooled melt to glass during the cooling process. It is a universal phenomenon in organic, inorganic, metallic, polymeric, colloidal, and biomolecular materials[39–44]. To better understand the phenomenon that characterizes the formation of glass, i.e., the glass transition, we will draw the diagram of molar volume or enthalpy as a function of temperature (V(T) or H(T)) as in figure 2.1.

When an equilibrated liquid at a temperature above its melting temperature (T_m) is cooled slowly, the volume gradually decreases with decreasing temperature; at T_m, the crystallization is thermodynamically favorable [38]. The T_m can be defined as the temperature at which the solid and the liquid have the same Gibbs free energy [38]. If the system crystallizes, we see a sudden decrease in volume (blue line in the figure 2.1), this discontinuity in the volume corresponds to discontinuity in the first derivative of the Gibbs free energy with respect to the pressure as $V = (\frac{\partial G}{\partial P})_T$, indicating a first-order transition [38]. The volume then decreases during cooling (blue line in the figure 2.1). If the cooling rate is high, the crystallization does not occur, and the liquid goes to another state called supercooled liquid [38], indicated by the green line in Figure 2.1. Under these conditions, there is no discontinuity in the V-T (respectively H-T) diagram. However, the atoms become less and less mobile during cooling due to increased viscosity with decreasing temperature [38]. At a low enough temperature, the atoms can no longer rearrange themselves to reach the characteristic volume at this temperature, i.e., the system cannot adapt its volume to

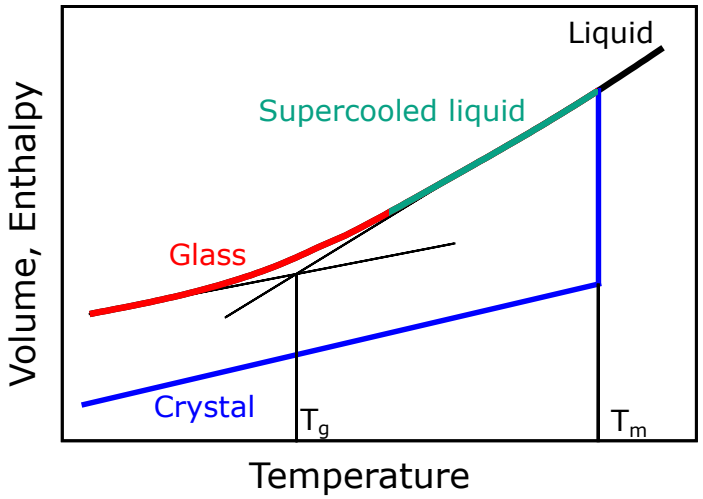

Figure. 2.1: V-T diagram showing the formation of a glass from a liquid.

the temperature. The system's volume gradually decreases its slope from the liquid state to become approximately parallel to that of the crystal, and we have the glassy state. The temperature at which the change in slope occurs is called the fictive temperature (T_f), and the glass transition temperature T_g is defined as the temperature at which the viscosity of the supercooled liquid is equal to 10^{12} Pa.s [38]. Moreover, this slope break depends on the cooling rate and pressure since slow cooling results in a lower T_g, and higher applied pressure during the cooling leads to higher T_g values. This means that the system's state at low temperature depends on the thermal or pressure history of the supercooled liquid.

Definition of a glass

Our daily experience with glass influences our impressions of its nature. The classical view of a transparent solid that breaks easily is only suitable for some glasses, especially soda-lime glass, the basic constituent of windows glasses. In contrast, compared to oxide glasses, chalcogenides and metallic glasses are opaque in the visible spectrum and resistant to brittle failure.

Historically speaking, the American Society for Testing Materials defines glass as an inorganic material initially molten and then cooled to a solid without crystallization. This definition is too restrictive, as many organic glasses are known [45]. According to Gupta, who distinguished between glasses and amorphous solid. Glass is a solid having the structure of a liquid and is continuously transformed into a liquid by being heated [46]. From a thermodynamic point of view, glass can be described as an out-of-equilibrium material with higher internal energy than crystal. The return to the state of equilibrium (crystallization) cannot occur, even after long periods, because of the viscosity, which is high enough to freeze the atoms. The currently adopted definition of glass is as quoted from a paper by E. D. Zanotto and J. C. Mauro ***glass is a nonequilibrium, noncrystalline condensed state of matter that exhibits a glass transition. The structure of glasses is similar to that of their parent supercooled liquids (SCL), and they spontaneously relax toward the SCL state. Their ultimate fate is to solidify, i.e., crystallize"*** [38]. Glasses have a structure similar to that of the supercooled liquid, and they behave mechanically like solids, exhibiting elasticity and rigidity.

Formation rules of oxide glasses

In the early years of the twentieth century, scientists started to develop theories for glass formation and describe the structure of oxide glasses. Tammann was the first one who was interested in how glasses are made and regarded glasses as deeply supercooled liquids or frozen in liquid [47]. Those observations were following interpretations based on data from X-ray diffraction [48] and presented a good start for further development. Afterward, Goldschmidt derived rules for oxide glass formation empirically. Following his rules, an ionic ratio of cation and anion ranging between 0.2 and 0.4 constitute good glass former [49]. This rule was confirmed by the formation of BeF_2 glass [50].

Zachariasen in his paper **"The atomic arrangement in glass"**, inspired research in the field of glass. In this paper, Zachariasen found that the properties of glasses are very close

to those of the corresponding crystals; hence the interactions between the atoms are of the same nature [51]. Zachariasen paid particular attention to oxide glasses, whose vitrification is mainly favored because of the high viscosity of the liquid; it results in excess of internal energy compared to the crystal, so he assumed that the glasses are formed of a random network of atoms. This implies that the entropy of the glasses is higher than that of the corresponding crystals. Furthermore, he noticed that the ionic crystals that easily give rise to glass have a very open structure, where the cation is small and carries a high charge. It is commonly surrounded by oxygen, forming a polyhedron that shares its tops with neighboring polyhedra.

Zachariasen formulates four topological rules that an oxide must obey to form a glassy network :

1. Cation coordination is low 3 or 4 (see Fig. 2.2(a)).
2. The polyhedra are connected by the vertices (see Fig. 2.2(b)).
3. At least three vertices of a polyhedron are shared with neighbors (see Fig. 2.2(b)).
4. An oxygen atom cannot be bound to more than two cations (see Fig. 2.2(c)).

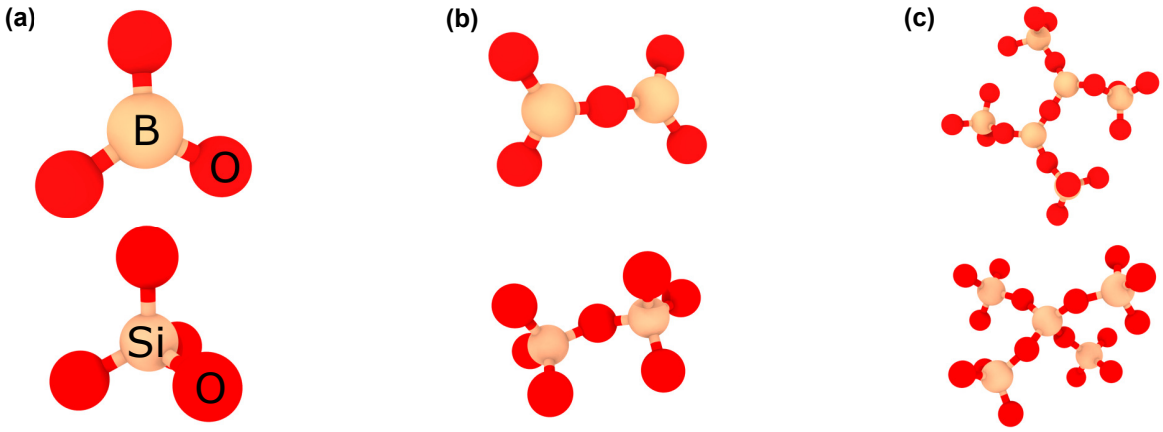

Figure. 2.2: a Boron triangles and silicon tetrahedron, b two triangles (tetrahedra) linked by bridging oxygen, and c a triangle (tetrahedron) surrounded by three (four) other triangles of tetrahedra.

These criteria allow us to make several predictions about the glass's local structure and the possibility of vitrification of the elements. Therefore, oxides having the following formulas A_2O, AO (A is cation and O is oxygen), cannot satisfy these rules, mainly rule 1 and 3, so they cannot be suitable glass formers (e.g., Na_2O). Oxides A_2O_3 satisfy these rules if the oxygen atoms form triangles around cation A (e.g., B_2O_3). The oxides AO_2 and A_2O_5 can satisfy these rules and, therefore, form glassy systems if four oxygen atoms surround each cation A (e.g., SiO_2 and P_2O_5) see the Table. 2.1. Zachariasen's predictions, which are confirmed experimentally, have given this model great importance. Following these rules, Zachariasen also classified the oxides into three major categories (Table. 2.1):

- The network-forming oxides of glass are the components that form a glass network and polymerize the network.
- Intermediate oxides can be both formers and modifiers, depending on their chemical compositions.
- Modifying oxides do not participate in creating the glassy network. Therefore they depolymerize it by breaking the bonds. They are essentially alkaline or alkaline earth. If necessary, they balance the charge within the glass network.

Table 2.1: Classification of oxides according to Zachariasen.

Formers	Intermediaries	Modifiers
SiO_2	Al_2O_3	Li_2O
GeO_2	PbO	Na_2O
B_2O_3	ZnO	K_2O
P_2O_5	CdO	CaO
As_2O_3	TiO_2	BaO
V_2O_5	-	-

Dietzel extended the network theory based on the considerations made by Goldschmidt [50, 52], where the interaction forces between anions and cations were taken into consideration in the solidification process. Based on these physical interactions, Dietzel introduced the term field strength (FS), which is defined as,

$$FS = \frac{Z_c}{(r_a + r_c)^2}, \tag{2.1}$$

where Z_c, r_a, and r_c are the valence of the cations, anion radius, and cation radius, respectively. Following the FS as a parameter, compounds that have an FS between $\approx$ 0.1 to 0.4 are considered glass network modifiers, glass network formers have FS that is around one order of magnitude higher $\approx$ 1.4 to 2, and finally, intermediates have an FS between $\approx$ 0.5 to 1.0. This rule aligns with Zachariasen's classification of oxides as network formers, network modifiers, and intermediates. A similar classification was made by the electronegativity concept proposed by Pauling [53].

Further development of the network theory was made by Smekal [49], Weyl [49], Stevels [49, 54], and many others which I will briefly summarize their contributions and findings:

- Smekal [49] related the glass formation to the type of chemical bonding, in which he regarded glasses as substances formed by mixed chemical bonding. Thus materials with ionic bonding typically have low melting temperatures and crystallize quickly due to the non-directional nature of the ionic bonds. On the other hand, materials with mixed bonding, e.g., quartz, have a high melting temperature and high viscosity in the melting range; thus, the glass formation is easy.

- Weyl [49] proposed the screening theory, where he stressed the importance of the residual valence forces as promoted by polarization and deformation of SiO_4 , BO_3, PO_4 , or BeF_4 to irregular networks. In the case of a highly charged cation, if the cation charge is fully screened, such as S by F in SF_6, the glass formation will not occur. In the case of silicate glasses, if a high content of modifiers is present in the melt, e.g., Na_2O, the silicon ions will be saturated in coordination and then isolated, and electron-neutral SiO_4 complexes will form, which will give rise to crystals precipitation. On the other hand, when the concentration of modifiers is relatively low, the degree of polymerization, and therefore glass formation, will be determined by the ratio Si:O.

- Stevels [49, 54] developed a plausible theory for the existence of the so-called "invert glasses". The invert glasses have a higher content of the modifiers than glass formers, and the glass backbone is depicted by the modifiers network rather than the glass former network. He also introduced the parameter Y = 8 - 2(O:Si), related to the degree of polymerization (e.g., of SiO_4 units). This parameter indicates the number of BO per SiO_4 tetrahedron. Thus Y = 4 for O/Si = 2, which leads to the formation of a 3-dimensional network, Y = 3 for O/Si = 2.5 (e.g., Na_2O-$2SiO_2$), the tetrahedra are connected at three corners; Y = 2 for O/Si = 3 (e.g., Na_2O-SiO_2), which corresponds to a 2-dimensional network made out of SiO_4 chains. However, in the case where $Y < 2$ it was expected that the glass could not form. But Stevels and Trapp [49] synthesized glasses with $Y < 2$, i.e., an SiO_2 content < 50 % (e.g., (mol%) $15Na_2O$, $15K_2O$, 15CaO, 15BaO, $40SiO_2$). These glasses are what we call invert glasses. The possible reasons that glass forms in these compositions are attributed to the high degree of disorder, which Dietzel's FS concept can also describe, where we have so many competitors for the oxygen ions in an "invert glass" in a way that no crystalline compound can be precipitated or formed.

2.3 Silicate and phosphate glasses

Silica and silicates

Silica is an archetypal glass former, which has been the subject of several interesting studies to date, both from an experimental [55–62] point of view as well as theoretical modeling and numerical simulations [19, 21, 61, 63, 64]. It is also one of the basic constituents of glasses used in several industrial applications, thanks to its abundance in nature and its physical and chemical properties, such as its high corrosion resistance, low thermal expansion coefficient, and good electrical insulation compared to other glasses [57–62].

On the structural side, silica is one of the glasses with the simplest structure, but it is not well known beyond its local structure. The silica network is made of SiO_4 tetrahedra connected by oxygen atoms located at the corners, and each oxygen connecting two tetrahedra is called bridging oxygen (BO). In pure silica, almost all oxygen atoms are bridging except for a few rare defects (see Fig. 2.3) that might result from the processing of the glass [65].

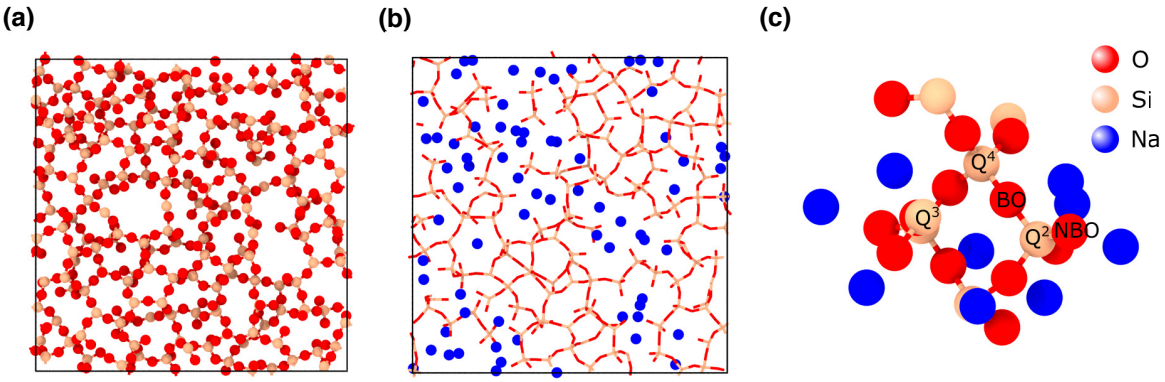

Figure. 2.3: a silica glass structure, b sodium silicate structure (20% Na_2O), and c shows nonbridging oxygen (NBO), bridging oxygen (BO), and some of the Q^n.

In addition, the connection of two neighboring tetrahedra is defined by the Si–O–Si bond angle, which is larger and more flexible than the O–Si–O bond angle. Therefore, the Si–O distance and the O-Si-O angles that define a SiO_4 tetrahedron are relatively well defined; the lattice disorder comes mainly from the Si-O-Si angle, which connects two tetrahedra, and from the dihedral angle, which defines the relative orientation of two neighboring tetrahedra.

Nevertheless, high purity silica has limited industrial use in advanced fields such as astronomical mirrors or optical fibers [61]. Regardless of the difficulty of obtaining pure silica, the high glass transition temperature (T_g) of silica $T_g \approx 1400$ K [64] implies the use of a significant input of energy to be able to shape it. Considering the difficulty of carrying out a quenching from a high temperature, the industrial glasses are generally a mixture of silica and other compounds. The addition of modifiers (e.g., alkali metals) to the silica network (backbone) help in reducing the glass transition temperature by depolymerization of the glass network through breaking the Si–BO–Si bonds to form Si–NBO bonds with NBO is the non-bridging oxygen defined as oxygen atoms that are not linking two neighboring tetrahedra.

Phosphate glasses

Phosphate glasses have a lower glass transition temperature, and higher thermal expansion coefficients compared to borate and silicate glasses [66]. Also, they play an important role as bioactive materials [67–69], and as a solid-state ion conductor [70–72].

Low glass transition temperatures are usually associated with high thermal expansion coefficients and have a clear relationship with the two main structural factors: the modifier cations' field strength and the polymerization degree of the glass-forming network. The less interconnected network in phosphate glasses resulting from the double P=O bond of the PO_4 building units has a tremendous impact on the T_g and simultaneously on the thermal expansion of the glass.

Phosphorus has different bonding configurations and plays a vital role in inorganic chemistry, and biochemistry [73]. Phosphorous is mainly found in oxidation states III and

V. When combined with oxygen; phosphorous gives rise to six oxide structures, among which the phosphorous pentoxide, P_4O_{10}, is the most important. P_4O_{10} is so defined because it forms molecular structures of four PO_4 units connected to form a ring, with each phosphorous having three BO and one double-bonded O called terminal oxygen [74]. Similarly, the structure of P_4O_{10} glass is described as a three-dimensional network of connected PO_4 tetrahedra [73]. The materials having phosphorus V are usually stable against the oxidation state +3, which is due to the formation of a double phosphorous oxygen bond, while polymeric forms of P_4O_{10} form H_3PO_4 easily, and from here derives the extremely high dissolution tendency of phosphate glasses in water.

As shown previously, P_2O_5 fulfills the condition to form a glass, and it was classified as a network-former by Zachariasen [51] and had the highest value of ionic field strength (2.1) as reported by Dietzel [52]. When modifier oxides are added to P_2O_5, a quite broad glass-forming range can be attained in most combinations; in the MgO-P_2O_5 system, for instance, the modifier oxide amount may reach 60 mol%, while in ZnO-P_2O_5 it can be as high as 64.8 mol% [73]. After adding a modifier oxide to the network of P_2O_5, P–O–P bonds break and form negatively charged single-bonded oxygens ($P–O^-$), whose charges are compensated with the modifier cations. Thilo classified phosphate compositions into ultraphosphates (O/P ratio < 3), polyphosphates (O/P > 3) and metaphosphates for the case with O/P = 3 [75].

Glassy P_2O_5 is formed by Q^3 groups where the doubly bonded phosphorous oxygen bonds are named terminal bonds and regarded as NBOs. The fact that there is a presence of these terminal bonds makes the network weaker and highly hydrophilic. Adding a modifier breaks the P–BO–P bonds to form P–NBO bonds where the terminal oxygen atoms are linked to the modifiers [74]. When the metaphosphate composition is reached, only chains or large rings of Q^2-type groups remain. With further increase of the modifier content, the Q^2 are converted to Q^1, and the structure is depolymerized until orthophosphate.

Q^n population

The glass network former such as Si or P is always bonded to four BOs in the case of Si, and three BOs and one terminal oxygen in the case of P [74], and when doped by a modifier, the average number of NBOs bonded to Si or P increases while that of BO increases. The number of BOs in each Si or P tetrahedron is characterized by Q^n units (n = 0..4) (see Fig. 2.3), a Q^n unit corresponds to a T atom surrounded by n BO atoms. Hence, a unit Q^0 corresponds to a T atom surrounded by 4 NBOs which refer to an isolated tetrahedron, while the unit Q^4 represents the basic unit of pure silica glass (Glass with a fully connected structure). The statistics of these units can be quantitatively determined by atomistic simulations[35, 36] or experimentally using nuclear magnetic resonance (NMR) [74, 76]. In addition to that, it was shown that the distribution of Q^n units is not random, and it follows the rule: when small amounts of modifier dope the glass, the Q^4 are converted to only Q^3 up to the composition where MO/TO = 0.5, which is equivalent to 33.3 mol % of MO, at this composition all Q^4 units are converted to Q^3. Further increase of the modifier content leads to the conversion of Q^3 sites to only Q^2, etc. Naturally, this affects the connectivity of the glass network. For instance, a glass structure made of Q^2 units is dominated by chains of network former

tetrahedra [74].

2.4 Anisotropy in glasses

The dependence of the material properties on the direction of observation is called anisotropy. Commonly, melt-quenched glasses are regarded as isotropic materials as reported in the literature [77–79]. However, it has been shown that for melt-quenched glasses, the properties showed no dependence on the direction of the observation or measurement [77–79]. The origins of the isotropic nature of glasses are due to their disordered structure that is similar to that of the supercooled liquid [77–79]. However, when processed accordingly, structural anisotropy or poling, associated with the alignment of super-structural motifs, can be induced through processing in mechanical or electrical fields[1–3, 80, 81]. This is demonstrated mainly through optical birefringence, which visualizes residual or transient mechanical stress embedded in a glass object. Another example, homogeneous anisotropy, can be induced in glasses by fiber drawing [1, 3, 80, 82]. Such anisotropy, caused by deformation of the viscous melt [60], is only reversible by thermal annealing.

On the other hand, glasses can also exhibit anysotropy only under mechanical load which is of elastic nature, e.g., as observed in stress-induced reversible birefringence [83]. Mechanical deformations can lead to persistent anisotropy that remains after removing the load and is then reflected, e.g., in the occurrence of residual stresses [84]. The transient anisotropy represents the initial response of the glass to the applied load and thereby defines the following mechanical reactions, which make it of fundamental importance. The atomic- or molecular-scale deformation mechanisms are a direct consequence of the presence of structural disorder, highly directional covalent bonds, and usually, the presence of interatomic interactions with reduced directionality [1]. On the other hand, the persistent anisotropy represents the anisotropy left in the structure after removing the load [1].

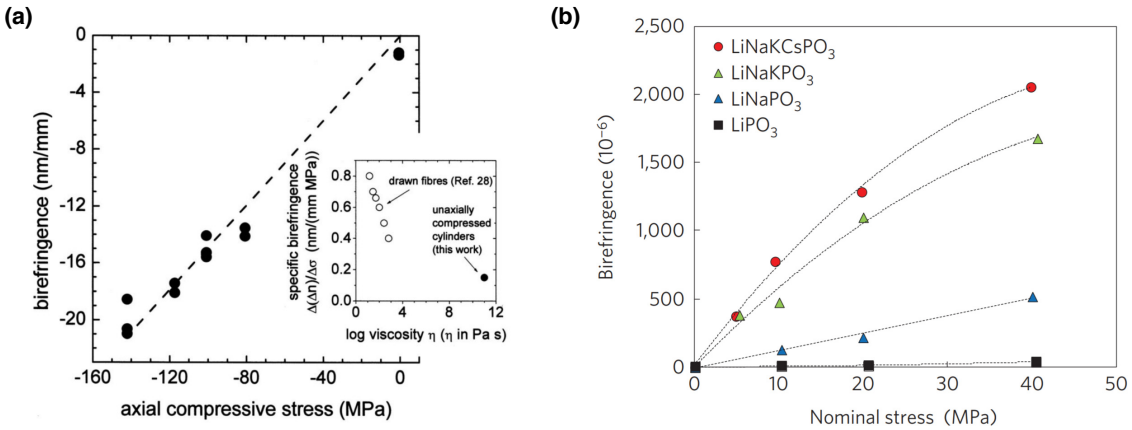

Figure. 2.4: (a) Birefringence as a function of the compressive stress of uniaxially compressed E-glasses given in Ref. [85]. (b) Relationship between birefringence and initial stress of alkali metaphosphate glasses as given in Ref. [1]. Figures are adapted from Refs. [1, 85].

Persistent anisotropy was also shown to be caused by the inhomogeneities in the glass,

such as regions rich in modifiers. These inhomogeneities either become aligned or deformed through the deformation process leading to an anisotropic response of the glass to the applied deformation[86]. However, many works highlighted and showed the presence of persistent anisotropy in the absence of inhomogeneities. Earlier experimental observations of optical anisotropy were suggested to be a result of frozen-in elastic deformation with the assumption that the glass structure consists of elastic and fluid units [87]. In the first systematic review given by Takamori and Tomozawa [88] on anomalous birefringence occurring in many oxide glasses, the anomalous birefringence was related to frozen-in strain and microstructural orientation. The structural origin of mechanically-induced anisotropy in metallic glasses was studied by subjecting the glasses to uniaxial tensile stress during creep. The X-ray diffraction results showed atoms in the unloaded glass have more nearest neighbor atoms in the direction perpendicular than parallel to the tensile axis [81]. Other studies on the anisotropy in oxide glasses showed that the anisotropy in, i.e., silica glass was shown to be due to the changes at the medium-range structure [60, 89]. By uniaxially compressing a silica glass at room temperature and unloading it, a remaining strain was observed [60]. The characterization of the structure using diffraction techniques showed that the structure became anisotropic as extracted from the first sharp diffraction peak deviations. Sato *et al.* proposed that the anisotropy was caused by directionality of the medium-range structure by the permanent densification [60]. Similar conclusions were also drawn by Champagnon *et al.* from Brillouin scattering experiments on uniaxially compressed silica glass [89].

As shown previously, a way of inducing anisotropy into the glass structure is through quenching under load, in which the glass will have frozen-in stress and/ or strain to lead to anisotropic properties. This led to a significant change in the glass fiber properties, such as polarization. The design of optical fibers with low signal loss and can maintain polarization is usually done by inducing birefringence to the fibers during the making process. Optical birefringence is an important optical property, especially for optical fibers. The high birefringence optical fibers are heavily used in telecommunications and other industrial applications such as fiber optic sensors to design optoelectronic and functional devices. The work of Wu *et al.* [85] showed that aluminoborosilicate corresponds to the E-glass composition uniaxially compressed from above the glass transition temperature and cooled under pressure to room temperature has led to glasses with considerable permanent birefringence. Moreover, they showed that the birefringence increased with the compressive stress, conjectured to be due to the preferential structure orientation in a preferred direction. The results of the dependence of the birefringence on the axial compressive stress are shown in Figure. 2.4a taken from Ref. [85]. Other work showed that the tensile strength of E-glass fibers is higher than the bulk glass samples of the same composition. This was attributed to the orientation of the glass structural units during the fiber drawing process [82].

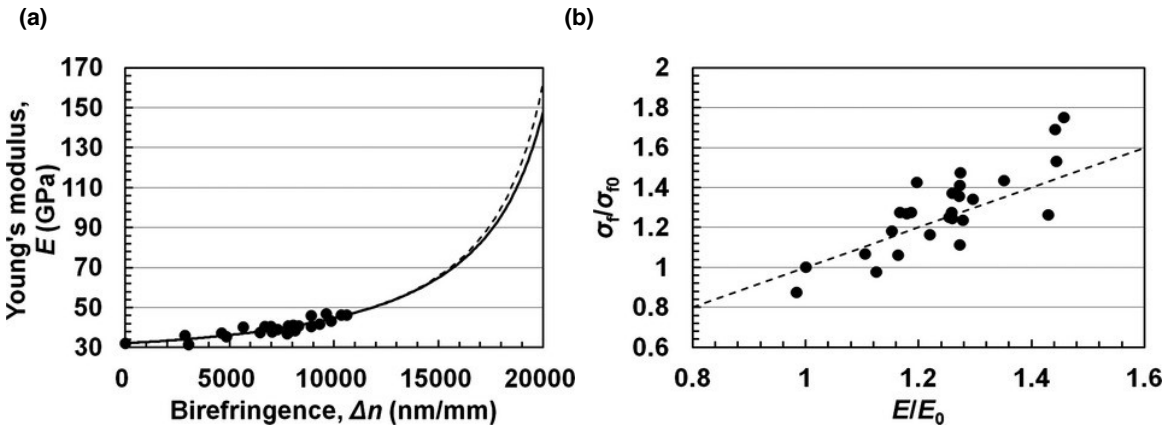

Figure. 2.5: (a) The values of the Young's moduli of $LiNaKCsPO_3$ metaphosphate glasses as a function of the birefringence. (b) The normalized strength as a function of the Young's moduli of $LiNaKCsPO_3$ metaphosphate glass fibers, where σ_{f0} and E_0 are the strength and Young's modulus of the isotropic glass fiber. Figures are from Ref. [80].

The work of Inaba *et al.* [1] on highly anisotropic metaphosphate glasses showed that combining the mechanical elongation from the supercooled liquid and a proper selection of the glass composition has led to the development of glasses with permanent anisotropy, and they show entropic shrinkage, a property that is usually observed in rubbers and organic polymers [1]. The increasing birefringence values quantified the anisotropy in the glass with the initial stress of different alkali metaphosphate glasses. The results are shown in Figure. 2.4b, where the birefringence increased with increasing stress. Moreover, the glasses with more alkali elements showed higher anisotropy at the same stress level [1]. The same group has done the investigation of the mechanical and structural properties of the same glasses, and they found that when compared to the isotropic glass fiber, the anisotropic glasses show an increase of Young's modulus and fracture toughness of isotropic glass fiber by 160 % and 140 %, respectively, when measured along the drawing axis [80] (See Figure. 2.5a and b. The origin of the observed entropic shrinkage and increase of the mechanical properties of these anisotropic glasses was shown to be due to the alignment of –P–O–P– chains along the wire axis, leading to the orientation of strong P–O bond along the wire axis [1, 80, 90]. Similar conclusions were drawn from the work of Yang *et al.* [3], where the authors exploited the one-dimensional chain-like structure of metaphosphate glasses to make a hybrid fiber optical waveguide with tailored transverse anisotropy. They found that the transverse anisotropy can be controlled by controlling the material processing conditions (e.g., pressure). This observed anisotropy was shown to be due to the orientation of the phosphate chains. Although many authors developed anisotropic metaphosphate glasses by exploiting the one dimensional chain-like structure of theses glasses, none of them addressed the origins of this structural anisotropy at atomic scale and the differences between the ***transient*** and ***persistent*** anisotropy in metaphosphate glasses remained elusive to date, and will be addressed in the first part of this thesis.

2.5 Deformation behavior of glasses

The major drawback of glasses is their brittleness. In this section, we will briefly remind some basic concepts of the mechanics of glasses and give a short review on the state of the art of the deformation of oxide glasses. We introduce the deformation of a material subjected to tensile, compressive, and shear deformations. We can generally distinguish between brittle and ductile materials from the stress-strain curve. From the stress-strain curve, we can define the elastic regime as characterized by Young's modulus (E), the yield point where the non-linear deformation begins, the failure stress (strain) defined as the point where the stress reaches its maximum, and finally, the fracture points that is defined as the point where the stress goes to zero [91]. Brittle materials such as glasses show no or limited plasticity before failing, while in ductile materials such as metals, a necking is usually observed before breaking. The yield stress or yield strength separates the elastic and plastic regimes of material [91].

The different regimes in the stress-strain curve can be easily extracted from the change in its slope, defined as;

$$E_t = \frac{d\sigma}{d\epsilon}, \tag{2.2}$$

The value of E_t where ϵ is 0 is Young's modulus E. The Young's modulus is also called the elastic modulus and is used to quantify the stiffness of the materials, as materials with a larger Young's modulus are stiffer than materials with a lower young's modulus.

Elasticity and topology of glasses

The properties of the glasses are also linked to the glass typology through the topological constraint theory (TCT), or the rigidity theory [5, 92]. It is based on counting the number of constraints and degrees of freedom on each atom by making an analogy between the glass network made of the covalent bond and mechanical truss [92]. This theory has been used for many years to predict the properties of the glasses, such as the glass transition temperature [92, 93], hardness [92, 94, 95], and elastic moduli [92, 94]. Moreover, over the years, the TCT has been extended to consider the temperature and pressure in counting the constraints and degrees of freedom per atom [96]. Due to the success of TCT (and also temperature-dependent TCT), it is of great importance to highlight that until now, there is no model based on the topological aspects that successfully predict the elastic moduli of glasses or gives a relationship between the elasticity, and the glass topology [97]. This is mainly due to the complex structure of oxide glasses and might be because the medium-range topology of the glass is not included in the formulation of the TCT. This gives an idea of the complexity of getting a relationship between the structure and glass elasticity.

Non-linear elasticity of glasses

For a linearly elastic material, E_t is supposed to be equal to Young's modulus. This is mostly valid in the case of normal glasses. However, abnormal or anomalous glasses, such as silica glasses with high silica content, also exist. These glasses are known to exhibit

non-linear elastic behavior. Moreover, the anomalous glasses increase the elastic moduli with increasing temperature and decrease the elastic moduli with increasing pressure. The non-linear elasticity of inorganic glasses is usually observed in anomalous glasses, where Young's modulus increases with increasing stress. This behavior is proposed to be a consequence of the large free volume in the anomalous glasses (e.g., silica) which affects the response of the glasses to the deformation. Initially, the glass is deformed by the distortion of the bond angles, which are more flexible and easy to deform, leading to a relatively low Young's modulus. However, when this deformation mode reaches its limit, the glass will start rigidly deforming by stretching the bonds, which indeed leads to an increase of Young's modulus [63, 98].

For normal glasses, there is a less free volume which leads to a limited distortion of the bond angles, and as a consequence, Young's modulus decreases with increasing strain [91]. The glasses that exhibit non-linear elasticity do not follow Hooke's law; therefore, the fitting of the stress-strain curve has to be made using higher-order polynomial functions [62, 98–103]. Gupta *et al.* [98], used eq. 2.3 to describe the behavior of the glass fibers under tensile deformation. Therms containing powers of strain higher than three were excluded.

$$\sigma(\epsilon) = E_0\epsilon + (E_1/2)\epsilon^2 + (E_2/6)\epsilon^3 \tag{2.3}$$

In eq. 2.3, E_0 in the zero-strain Young's modulus is also known as second-order Young's modulus. E_1 and E_2 are the third and fourth-order Young's moduli, respectively. By differentiating eq. 2.3, we obtain the strain dependence Young's modulus as given in eq. 2.4.

$$E(\epsilon) = E_0 + E_1\epsilon + (E_2/2)\epsilon^2 \tag{2.4}$$

The eq. 2.4 depicts the non-linear elasticity of silica and silicate glasses [98] as it will be shown in the following chapters.

Strength, fracture, and plasticity of glasses

It is well known that glasses fail in a brittle manner when deformed well below the glass transition temperature [4, 104]. The first theoretical criterion for rupture was proposed by Orowan in 1949, which include therms of elastic modulus E, surface energy ζ, and interatomic distance r_0, is given by:

$$\sigma_{th} = \sqrt{\frac{E\zeta}{r_0}} \tag{2.5}$$

Theoretically, the strength of the glasses (e.g., for silica glass σ_{th} = 16.5 GPa) as predicted by Orowan's equation (eq. 2.5) is, unfortunately, well above its experimental strength (e.g., for silica glass σ_{exp} = 100 MPa) [105]. This huge difference between the theoretically calculated value and the experimentally measured one is argued to be caused by the presence of surface flaws, internal defects, and/ or the environment of measurement [4]. Moreover, it was evidenced that the strength of the glasses depends on the type and size of the glass object [106], e.g., glass fibers are stronger than flat glasses [4]. The tensile strength of glass

can be measured by performing a simple tensile test of glass fiber. However, this is not as easy as it sounds since they are difficult to grip the glass fiber; scientists usually use three- and four-point bending techniques to put a glass under tension by allowing the formation of tensile zones at the surface of inside the glass sample [105].

When subjected to tensile deformation, the glass deforms along the tensile axis, and a side deformation is also observed, which depends on the Poisson's ratio. The failure of glasses usually starts from the zones that are under tension. The failure of material depends essentially on its intrinsic properties, and it originates from the defect found in the glass generally at the surface but can also start from the internal defects [105]. While it is now possible to eliminate any type of defects, e.g., bubbles [105], microscopic defects such as dangling bonds or large rings [105] can strongly affect the fracture behavior of the glasses. When the crack nucleates at a critical defective zone, it expands at a low speed leading to the formation of a flat crack surface [105]. On the other hand, when the crack propagates at higher speeds, a larger surface area is needed to dissipate the internal strain energy, leading to the formation of a rough crack surface, and further expansion of the crack will result in crack multiplication or branching (See Figure. 2.6) [105, 107]. As mentioned above, by assuming that the glass is defect-free and fracture is ideal, i.e., involves the sequential breaking of individual bonds, then tensile strength values are related to the energy needed for bond cleavage, and the predicted theoretical strength is much higher than those observed.

When put in contact with a sharp object, e.g., diamond indenter in indentation experiments, oxide glasses (e.g., silica) show several types of cracking, such as Hertzian cone cracking and lateral cracking propagates parallel to the glass surface [108, 109]. Another type of crack that appears in the indented glass and that strongly affect glass strength is the radial crack that propagates perpendicular to the glass surface, e.g., half-penny and Palmqvist cracks [108, 110].making it crucial to not ignore this type of cracks when studying the long-term mechanical reliability of indented glass [108].

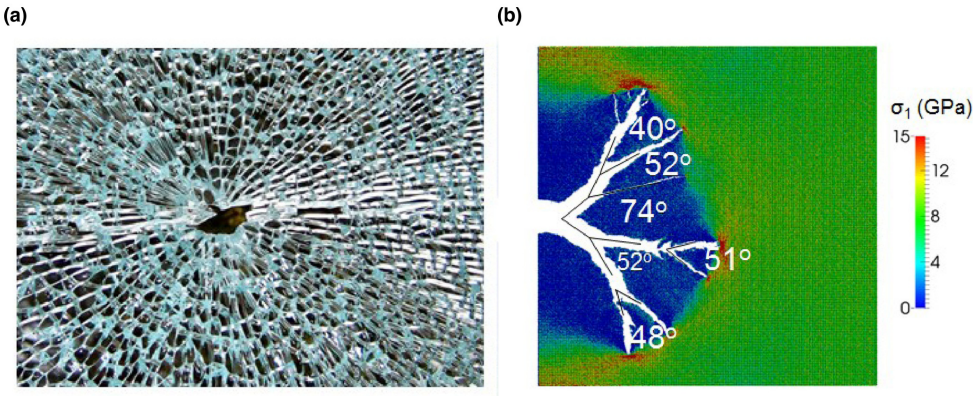

Figure. 2.6: (a) Real thermally tempered soda lime glass where radial cracks were initiated at the center and branches into a network that spans the whole sample. (b) Snapshot of the deformation morphology and first principal stress field during crack branching for silica glass containing around 20 million atoms subjected to biaxial far-field loading with an initial edge crack with a length of 5 nm modeled by Teter force field with a loading rate of 0.2 /ns. Figures are from Ref. [107].

By definition, plasticity is the non-reversible deformation of a solid subjected to an external force. In contrast to crystalline solids, where the motion of dislocations mainly mediates the plasticity [111], the plasticity in glasses is not governed by the same mechanism, which is due to the absence of a long-range order [111, 112]. Many studies showed that the local inelastic transformations represent the fundamental mechanism of plasticity in amorphous solids [113]. These transformations are known as shear transformation zone, which is represented by an ensemble of atoms moving cooperatively in a short time [113]. It is commonly known that oxide glasses are archetypal brittle materials. However, oxide glasses can show a plastic deformation behavior, e.g., at high compressive stresses.

Previous studies on silica glass fibers of diameters larger than 50 nm showed brittle fracture when subjected to tension [61, 114, 115]. In another study, using experiments and simulations, Luo *et al.* showed that silica glass fibers have a size dependence brittle-to-ductile transition, which is present when the diameters of the fiber are less than 18 nm [61]. The origin of this brittle-to-ductile transition was shown to be due to the volume/surface ratio of the nanofibers, where the glass fibers with small cross section area have enhanced ionic mobility compared at their surface compared to the bulk, which improves ductility by producing more bond-switching events per irreversible bond loss under tensile stress [61]. Effect of processing, such as cooling the glass under pressure, was also used to study the effect of the structure on the strength and plasticity of the oxide glasses. Using atomistic simulations, Yuan *et al.* [116] showed that tailoring the silica glass structure through pressure quenching enabled an increase in the glass ductility in the samples quenched under increasingly higher pressure. The brittle-to-ductile transition in densified silica glasses was attributed to the existence of 5-fold Si coordinated atoms, which play the role of defects that facilitate shear deformation and dissipation of the energy by converting back to the 4-fold coordination state during deformation [116]. Mantisi et al. [117] studied the effect of hydrostatic pressure on the plasticity of silica glass. They reported a decrease in the yield stress with increasing hydrostatic pressure. Taking plasticity in metals as a reference, the dislocations slipping along specific atomic planes is a volume-conservative mechanism of shear flow [111]. It is also expected that compact materials tend to show shear flow [111].

On the other hand, in oxide glasses, the plasticity happens through a more complex mechanism, the volume may not be conservative during the deformation value, and a combination of shear flow and densification may occur with different percentages. Moreover, due to their diverse composition, structure, and bonding nature, not all glass families are equal regarding permanent deformation. For example, some metallic glasses can deform in a similar way to metallic alloys, showing a large plastic deformation before fracture when subjected to tensile loading [118, 119]. This plasticity in metallic glasses is localized in shear bands, which remembers the preferential slipping plane mechanisms in metals [111]. Oxide-based glasses, e.g., silicate glasses, their deformation behavior under tensile loading at low temperatures, i.e., far below T_g is a brittle fracture in general. This fracture happens suddenly without evidence of permanent deformation before failure [111]. On the other hand, during compression, the behavior is a different story [111].

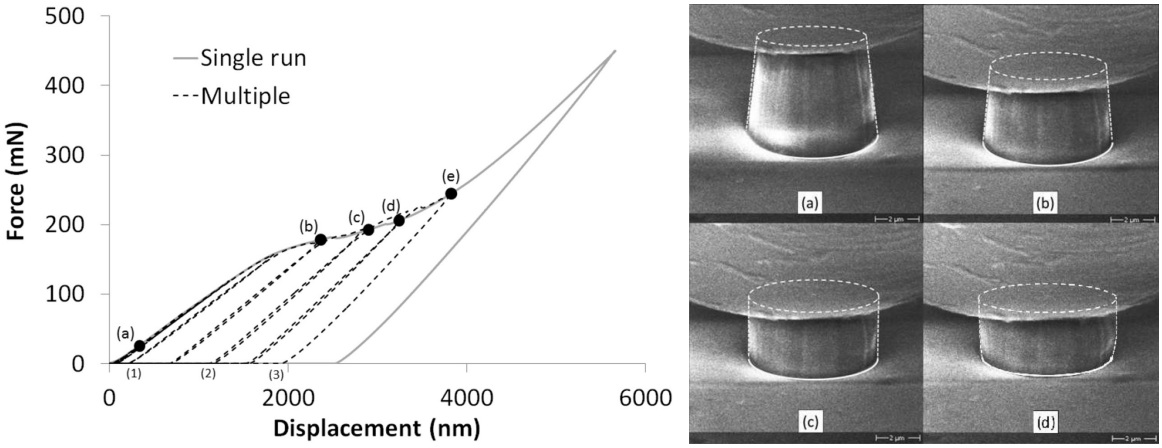

Figure. 2.7: (left) Load-displacement curves showing that the behavior of single run and multiple loading-unloading give similar results. (right) Shows the pillars deformation during straining. Inset letters (a), (b), (c) and (d) are related to the points of the load-displacement curve in. Figures are from Ref. [120].

Kermouch *et al.* studied the shear-hardening in silica glass. By using *in situ* SEM mechanical testing, they were able to compress silica pillars up to very large strains demonstrating the significant role of homogeneous shear flow [120]. The behavior of the silica pillars subjected to compression is shown in Figure. 2.7, where compression happened without crack nucleation or propagation. Motivated by the effect of the composition of the deformation behavior of silicate glasses, the same group led by Kermouche showed recently that the indentation-induced cracking in silicate glasses is mainly directed by shear flow, not by densification. They highlighted that the deformation of silicate glasses happens through shear flow instability and localization which could control the crack initiation [121]. These important results highlighted that the densification effect on the indentation response of silicate glasses is overrated, and its contribution is rather limited. The effect of the effect of initial flaws (e.g., cavities) on the deformation behavior of silicate glasses at atomic scale and how those flaws are affected by the composition and pre-deformation is either not well understood or not studied at all, which limits the development of oxide glasses. This will be addressed in the second part of this thesis.

2.6 Thesis motivation and objectives

In the work done in this thesis, I focused on investigating the role of the topology on the mechanical behavior of oxide glasses using atomistic simulations. The results are analyzed at an atomic level to explain the materials' behavior under load. The topology of the glasses was altered by either changing the composition or by applying an external load in the form of pre-deformations enabling us to address the following scientific questions.

- What are the origins of the anisotropy in metaphosphate glasses?
- What is the structural basis of anisotropy in metaphosphate glasses?

- What are the differences between the transient and persistent anisotropy in metaphosphate glasses?
- How does the type of the modifiers influences the structure and the structural anisotropy in metaphosphate glasses?
- What is the influence of the persistent anisotropy on the deformation behavior of the metaphosphate glasses?
- How does composition influence the deformation behavior of silica and sodium silicate glasses?
- How does the mechanical deformation and composition affect the silicate glasses structure and influence the formation of cavities (flaws)?
- How does the silicate glasses deformation mechanism depend on pre-deformation mode?

3 Methods

In this thesis, we studied the effect of the composition and pre-deformation on the structure and mechanical behavior of different oxide glasses using different loading conditions by molecular dynamics simulations. Moreover, many tools were used to analyze the structure of the glasses. In this chapter, we will briefly summarize the basics of molecular dynamics and give some details on the analysis tools.

3.1 Molecular Dynamics

Molecular dynamics simulation is a technique for describing the displacement of a classical many-body system in time. In this context, the word classical means that the motion of atoms and/or molecules obeys the laws of classical mechanics. Molecular dynamics simulations are based on solving Newton's equation, which describes the motion of atoms and molecules over time. Alder and Wainwright first used this simulation method in 1957 when they studied using MD simulations the phase transition behavior in a hard-sphere system [122]. MD is one of the most widely used simulations methods to study different materials properties (e.g., mechanical [104, 123–125], structural [36, 71, 125–127], thermodynamic [94, 128, 129], surface [127, 130, 131], and vibrational [97, 127, 132–134]) and it is well established in physics, chemistry, and materials science [35, 122, 135].

An introduction to the method and more detailed discussions, theoretical derivation, and algorithms are well described in detail in several books:

- Michael P Allen and Dominic J Tildesley. Computer simulation of liquids [136].
- Dennis C Rapaport. The art of molecular dynamics simulation [137].
- Wanda Andreoni and Sidney Yip. Handbook of Materials Modeling: Methods: Theory and Modeling [138].
- Daan Frenkel and Berend Smit. Understanding Molecular Simulation: From Algorithms to Applications [139].

Principle

Molecular dynamics simulations allow to study the motion of interacting atoms during a period of time, this is done by solving Newton's equations of motion. If we consider a system made of N atoms, the Newton's equation of motion can be written as follows

$$\vec{F}_i = \vec{m}_i \vec{a}_i \tag{3.1}$$

where $\vec{F}_i$ is the force, m_i is the mass, and $\vec{a}_i$ is the acceleration of the atom i, respectively. The determination of the forces is carried out from the interactions between the atoms

which are described by the interaction potential. Once the forces are obtained, positions and velocities can also be calculated by integrating the acceleration.

$$m\vec{a} = m\frac{d^2\vec{r}}{dt^2} = \vec{F}_i = -\vec{\nabla}_r U(r) \tag{3.2}$$

where $\vec{r}$ and U are the position vector is the interaction potential.

Many algorithms exist to integrate Newton's equations of motion, i.e., to calculate the atoms' trajectories. However, for a successful simulation, the algorithm used for the integration of the equations of motion should be fast with little memory requirements, allow the usage of a long timestep Δt, duplicate the classical trajectory as closely as possible, and conserve energy, momentum, time-reversibility[136].

The velocity-Verlet algorithm [140], which is a modification of the original Verlet algorithm [141], satisfies these requirements. The position and velocities are updated using the following equations:

$$\vec{r}(t+\Delta t) = \vec{r}(t) + \vec{v}(t)\Delta t + \frac{1}{2}\vec{a}(t)\Delta t^2 \tag{3.3}$$

$$\vec{v}(t+\Delta t) = \vec{v}(t) + \frac{\vec{a}(t) + \vec{a}(t+\Delta t)}{2}\Delta t \tag{3.4}$$

Periodic boundary conditions

The objective of molecular simulations is to provide information on the physical properties of a macroscopic system. These calculations are very time-consuming, limiting in most cases the size of the simulated system to only a few thousand to a few hundred of thousand particles. This number is far from the thermodynamic limit. For such small systems, it cannot be safely assumed that the choice of boundary conditions has a negligible effect on the properties of the system.

In order to simulate bulk systems, it is essential to choose boundary conditions that virtually mimic an infinite sample of the material. This is usually achieved by using the so-called periodic boundary conditions. The volume containing the N particles is treated as the primitive cell of an infinite periodic array of identical cells, as shown in Figure. 3.1. A given particle of the primitive cell interacts with all the other particles in this infinitely periodic system. Moreover, when an atom leaves the central box, one of its images will enter through the opposite side. There are no walls at the edge of the central box and no surface atoms. In molecular simulations, it is crucial to calculate the potential energy of the simulated system as accurately as possible and as quickly as possible. However, it is almost impossible to simulate systems of experimental size because they consist of an almost infinite number of atoms. The concept of "Minimum Image Convention (MIC)" is introduced to solve this problem.

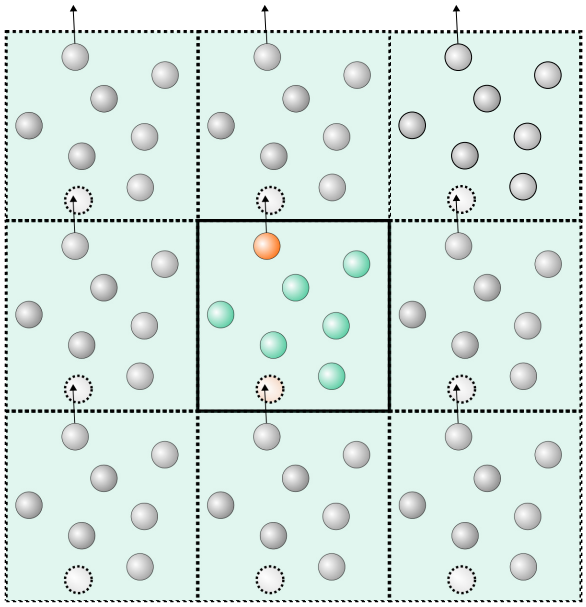

Figure. 3.1: A two-dimensional sketch of periodic boundary conditions. Atoms can enter and leave each box on each of the four edges. In a three-dimensional example, the atoms would be free to pass through one of the six cubic faces.

The MIC implies that each particle should interact at most with just one image of every other particle in the system, which is repeated infinitely via periodic boundary conditions. Moreover, when a cutoff distance is used, the interactions between the atoms far from each other are switched off, e.g., the separation distance is larger than the cutoff.

Statistical ensembles

Statistical mechanics is one of the most important theories in physics. It was established initially in the second half of the nineteenth century by Clausius, Maxwell, Boltzmann, and Gibbs.

In statistical physics, the notion of statistical or thermodynamic ensembles is introduced by Josiah Willard Gibbs in 1878 [142, 143]. An ensemble combines all possible systems with different molecular or atomic states but has the same macroscopic or thermodynamic state. Also, we should stress that the concept of ensembles in statistical mechanics is only theoretical. There are different ensembles with different characteristics.

- The microcanonical ensemble (NVE): this is a thermodynamic state characterized by a fixed number of atoms, N, a fixed volume, V, and fixed energy, E. A microcanonical ensemble corresponds thermodynamically to an isolated system.
- Canonical ensemble (NVT): it describes a system with a given number of particles N, a constant volume V and a constant temperature T. This is achieved by assuming that the system at equilibrium interacts with a much larger system called a ”heat bath or thermostat” which provides the amount of energy needed to keep the temperature of the subsystem constant.

- The isobaric-isothermal ensemble (NPT) or Gibbs ensemble: describes a system with a given number of particles N, a constant pressure P, and a constant temperature T. This is the most common ensemble used in molecular simulations because it reproduces the behavior of a material under real conditions of pressure and temperature.
- The isobaric-isoenthalpic ensemble (NPH) describes a system with a given constant number of particles N, a constant pressure P, and a constant enthalpy H.
- The grand canonical ensemble (μVT): a collection of systems, each of which can exchange energy and particles with a large reservoir. This fixes the temperature of the system and a quantity known as the system chemical potential μ.
- grand isothermal-isobaric ensemble (μPT): it describes a system that exchanges energy, particles, and volume with its surroundings. This keeps a constant pressure P, chemical potential μ, and temperature T.

The notion of statistical or thermodynamic sets is well detailed in several books, for example,

- Statistical mechanics by Donald A. McQuarrie [144].
- Concepts in thermal physics by Stephen J Blundell and Katherine M Blundell [145].
- Fundamentals of statistical and thermal physics by Frederick Reif [146].
- Statistical Mechanics An Introductory Graduate Course by John Berlinsky and Arthur Brooks Harris [147].
- Statistical Mechanics: From Thermodynamics to the Renormalization Group by James H. Luscombe [148].

3.2 Interatomic potentials

The importance of interatomic forces in nature is challenging to estimate. However, it is sufficient to say that the existence of liquids and solids is due to interatomic interactions. Without interatomic interactions, our world would be a uniform ideal gas. Knowing and understanding the physics of interatomic interactions is necessary to solve many problems in physics, chemistry, and biology. The nature of the interatomic interactions determines the thermodynamic properties of solids and liquids and their kinetic characteristics (coefficients of thermal conductivity, diffusion, etc.). Different semi-empirical or empirical interatomic potential models are often used with parameters obtained by fitting to experimental data or data obtained by *ab initio* to perform atomic-scale simulations. In this thesis, the Born [149] model of solids is the basis for calculating the forces acting on atoms. In this model, particles are treated as charged points that interact with Coulomb interactions and

a short-range potential describing the interaction between pairs of atoms. Short-range potentials are usually given in terms of parameterized analytical functions, which include both a repulsive term due to the overlap of electrons and an attractive term in the form of a dispersion term or Van der Waals interactions. We will briefly present the form of potential that we used to obtain the structural and physical properties of the glasses studied.

PMMCS force field

We used the well-established potential developed by Pedone *et al.* [150]. The functional form of the potential is given by:

$$U_{ij}(r) = \frac{z_i z_j e^2}{r} + D_{ij}[\{1 - e^{-a_{ij}(r-r_0)}\}^2 - 1] + \frac{C_{ij}}{r^{12}} \tag{3.5}$$

Where i and j are atoms (O, Si, P, Na, Ca, or Mg), r is the distance between atoms i and j, z_i and z_j are the effective charges of atoms i and j. D_{ij}, a_{ij}, r_0 and C_{ij} are potential parameters. The first term of the eq. 3.5 describes the long-distance electrostatic interaction between atoms, the second is a short-range Morse function which is generally used in modeling bound interactions in covalent systems, and the last term represents a repulsive contribution necessary to model the interaction at high temperature and pressure [150]. As mentioned in the literature, this potential gives realistic agreement with the available experimental data [63, 150–155]. The potential parameters and partial charges are given in reference [150] and Table. 3.1.

Table 3.1: PMMCS potential parameters. The effective charges are given as superscripts. All parameter are taken from reference [150].

	D_{ij} (eV)	a_{ij} ($Å^{-2}$)	r_0 ($Å$)	C_{ij} (eV $Å^{12}$)
$Na^{0.6}$–$O^{-1.2}$	0.023363	1.763867	3.006315	5.0
$Mg^{1.2}$–$O^{-1.2}$	0.038908	2.281000	2.586153	5.0
$Ca^{1.2}$–$O^{-1.2}$	0.030211	2.241334	2.923245	5.0
$P^{3.0}$–$O^{-1.2}$	0.831326	2.585833	1.800790	1.0
$Si^{2.4}$–$O^{-1.2}$	0.340554	2.006700	2.100000	1.0
$O^{-1.2}$–$O^{-1.2}$	0.042395	1.379316	3.618701	22.0

Damped shifted force model

Atomistic simulations of oxide glasses require dealing with atomic sites with either full or partial charges. A proper evaluation of the electrostatic interactions is necessary to obtain meaningful results. These type of charge-charge long-range interactions ($U^{qq}(r) \sim r^{-1}$) are the most computationally demanding compared to short-range interactions [136]. Many methods to solve these long-range interactions, such as; Ewald summation, include the interaction of an ion with all its periodic images [136]. The Ewald method was further optimized by assigning the charges to a fine regular mesh, making it possible to calculate

these long-ranged interactions efficiently using a fast Fourier transform. An example of methods using this approach is the particle-particle particle-mesh [136]. For more details about these methods, the reader can refer to the following literature [136, 156, 157].

The simulations of large samples using the above mentioned methods are still computationally demanding. Therefore, efforts were devoted to developing more efficient methods to deal with the long-range forces. Wolf et al. [156] proposed a cutoff-based technique where the Coulomb energy function is replaced by a damped distance-dependent energy function [59, 136, 156]. This pairwise summation is formulated in a way that ensures that charge neutrality. However, this method suffered from a drawback that the potential and forces are not continuous at the cutoff leading to poor convergence and energy drift in molecular dynamics simulations. This drawback was corrected by Fennel et al. [157] where they proposed a damped shifted force (DSF) version of the Wolf method where both energy and force are continuous at the cutoff. The damping function is needed for fast convergence, while the complementary error function is chosen to mimic the screening used in the Ewald method. The potential energy and forces of the DSF method are given below:

$$U_{DSF}(r) = q_i q_j \left[\frac{erfc(\alpha r)}{r} - \frac{erfc(\alpha R_c)}{R_c} + \left(\frac{erfc(\alpha R_c)}{R_c^2} + \frac{2\alpha}{\pi^{1/2}} \frac{exp(-\alpha^2 R_c^2)}{Rc} \right) (r - R_c) \right], r \leq R_c, \tag{3.6}$$

$$F_{DSF}(r) = q_i q_j \left[\left(\frac{erfc(\alpha r)}{r^2} + \frac{2\alpha}{\pi^{1/2}} \frac{exp(-\alpha^2 r^2)}{r} \right) - \left(\frac{erfc(\alpha R_c)}{R_c^2} + \frac{2\alpha}{\pi^{1/2}} \frac{exp(-\alpha^2 R_c^2)}{R_c} \right) \right], r \leq R_c, \tag{3.7}$$

with α is the damping parameter, r is the distance between two atoms, and R_c is the cutoff radius. In all simulations, a cuttoff radius of 8.0 Å was chosen with α = 0.25 Å^{-1}.

3.3 Simulation setup

Sample preparation

The glasses were prepared by following the conventional melt-quenching technique. First, we put N atoms in the simulation box to satisfy the glass chemical formula and apply periodic boundary conditions in all directions. The simulation box volume is fixed to reproduce the experimental density of glass at ambient temperature and pressure and is given in Table. 3.2 for all samples. Next, the systems were equilibrated in the canonical ensemble (NVT) at a high temperature (T = 5000 K) for 500 ps, and this time is sufficient to bring the systems to the liquid state and to obtain an equilibrated liquid as well as to ensure that each system loses the memory of its initial configuration for the used interatomic potential. The second step is linear cooling from high temperature (T = 5000 K) to room temperature (T = 300 K) with a cooling rate of 1 K/ps while keeping the volume fixed. However, cooling under fixed volume conditions results in glasses containing an amount of residual stress that must be removed, for which the system has been equilibrated at room temperature and zero pressure in the isobaric-isothermal (NPT) ensemble for 1 ns to release the residual

stress and another 100 ps in the NVT ensemble for statistical averaging over 100 configurations each separated by 1 ps. The temperature and pressure controls were assigned using the Nosé-Hoover thermostat and barostat [158, 159] using the coupling constants given in Table. 3.3. The equations of motion were solved via the velocity-Verlet algorithm with a timestep Δt = 1 fs.

Table 3.2: Details about the compositions studied in this thesis. Glass composition, final simulation box lengths X, Y, and Z in nm, number of atoms (N), the density of the glass samples at the end of the simulations given in g/cm^3, and the experimental density which was used as the starting density is also provided.

Sample	X (nm)	Y (nm)	Z (nm)	N	Density (g/cm^3)	Density$_{Exp}$ (g/cm^3)
50Na_2O-50P_2O_5	11.23	11.23	11.23	108000	2.58	2.53 [160]
50MgO-50P_2O_5	11.31	11.31	11.31	108000	2.51	2.44 [161]
50CaO-50P_2O_5	11.45	11.45	11.45	108000	2.63	2.65 [161]
SiO_2	17.79	17.79	17.79	375000	2.22	2.20 [162]
5Na_2O-95SiO_2	17.58	17.58	17.58	375000	2.30	2.23 [162]
10Na_2O-90SiO_2	17.44	17.44	17.44	375000	2.36	2.29 [162]
15Na_2O-85SiO_2	17.35	17.35	17.35	375000	2.40	2.33 [162]
20Na_2O-80SiO_2	17.30	17.30	17.30	375000	2.44	2.38 [162]

Table 3.3: Coupling constants of the thermostat (C_T) and barostat (C_B) used in our simulations and all given in fs.

Sample	C_T	C_B
50Na_2O-50P_2O_5	50	700
50MgO-50P_2O_5	60	700
50CaO-50P_2O_5	80	800
SiO_2	100	1000
5Na_2O-95SiO_2	100	1000
10Na_2O-90SiO_2	100	1000
15Na_2O-85SiO_2	100	1000
20Na_2O-80SiO_2	100	1000

Mechanical deformations

Using MD simulations, the glasses were deformed to study the mechanical behavior of the materials and in the following we will briefly describe the loading procedure in each loading mode. The pristine glass (Figure. 3.2a) and other pre-deformed glasses are shown in Figure. 3.2.

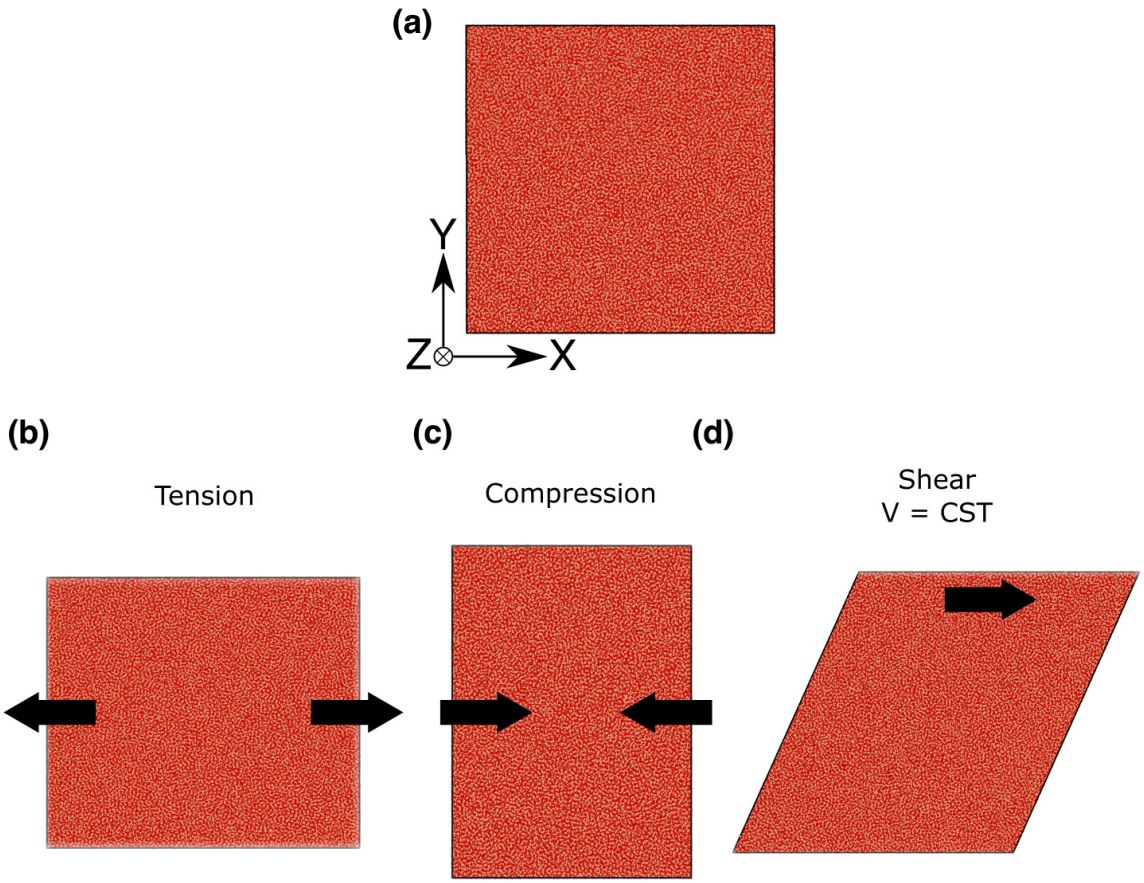

Figure. 3.2: Illustration of (a) pristine glass, (b) tensile, (c) compressive, and (d) constant volume shear deformations. The tensile and compressive simulations are performed along the x-axis while shear is applied by tilting the y-axis along the x-direction.

Tensile and compressive deformartion

The simulated tensile deformation was applied by homogeneously uni-axially straining the glass along one direction at a constant engineering strain rate. To account for Poisson's contraction, the pressure along the orthogonal axis to the loading direction was controlled using the Nosé-Hoover barostat, and it was set to be fluctuating around 0 MPa. This process is schematically shown in Figure. 3.2b.

Like tensile loading, the simulation box was homogeneously strained along one direction at a constant engineering strain rate in compression. Poisson's contraction was considered by controlling the pressure along the orthogonal axis to the loading direction using the Nosé-Hoover barostat, and it was set to be fluctuating around 0 MPa. This process is schematically shown in Figure. 3.2c.

Constant volume shear

The simple shear deformation was performed by tilting the y-axis of the simulation box along the x-direction at a constant engineering strain rate with the volume fixed. The shear strain is then defined as the change in angle between $y-$axis and x-axis of the simulation box. This process is schematically shown in Figure. 3.2d.

3.4 Structure analysis

Partial distribution function

The partial distribution function (PDF) is used to describe the local atomic structure of glasses. The PDF, which is defined as the probability of finding an atom of type j far from the atom of type i, is given by [36, 136, 137]:

$$g_{ij}(r) = \frac{1}{4\pi r^2 \rho_j} \left[\frac{dN_{ij}(r)}{dr} \right], \tag{3.8}$$

where i, j are atom types and $N_{ij}(r)$ represents the average number of atoms of type j in the sphere centered on atoms of type i of radius r (figure 3.3 is an example of a PDF of the O-O pair in a silica glass). Alternatively, we can also get an overview of the order in the glasses by determining the coordination number N_{ij} in the first coordination sphere. The coordination number N_{ij} is the number of atoms of type j around atoms of type i and it is calculated by integrating the RDF from zero to its first minimum r_{min} delimiting the first neighboring sphere,

$$N_{ij}(r_{min}) = 4\pi\rho \int_0^{r_{min}} g_{ij}(r) r^2 dr. \tag{3.9}$$

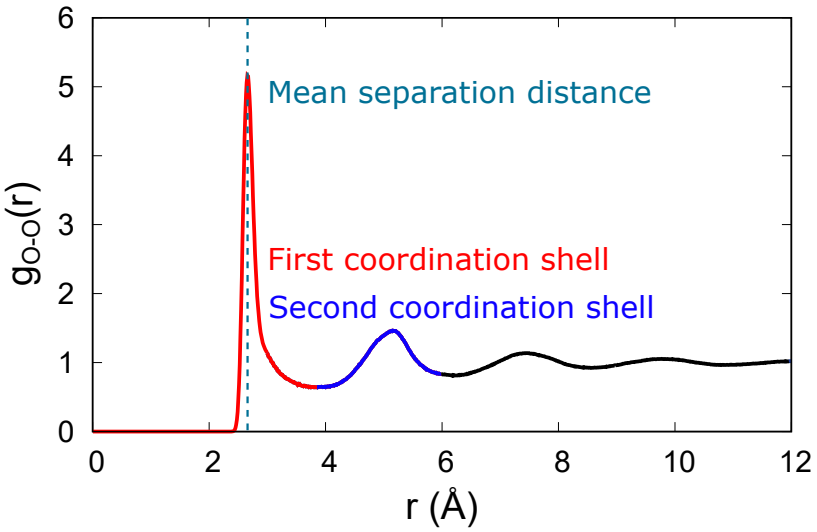

Figure. 3.3: Example of partial distribution function of the O-O pair as a function of the distance of the separation in a simulated silica glass.

Projected partial distribution function

The partial distribution function is defined as a probability of finding an atom of type j far away from a central atom of type i in a spherical volume. The PDF by definition is isotropic; therefore, it can not capture the signature of an anisotropic local structure. Thus to capture the directionality of short-range order, the RDF must be expanded onto a suitable higher order spherical harmonics. Particularly, we take the following expansion into spherical harmonics $Y_{lm}(\theta, \phi)$

$$g(r) = \sum_{l=0}^{\infty} \sum_{m=-l}^{l} g_{lm}(r) Y_{lm}(\theta, \phi), \tag{3.10}$$

where g_{lm} are the expansion coefficients [163–167]. In an uniaxial deformation, the deformation axis will be the symmetry axis. By checking the spherical harmonic functions, the Y_2^0 was the best to capture this behavior. The expansion coefficients of the PDF into the Y_2^0 spherical harmonic is given as,

$$g_{20}^{\alpha\beta} = \frac{\sqrt{15}V}{\sqrt{16\pi}N_\alpha N_\beta} \left\langle \sum_{i}^{N_\alpha} \sum_{j \neq i}^{N_\beta} \delta(|r_i^\alpha - r_j^\beta| - r) \frac{2(z_i^\alpha - z_j^\beta)^2 - ((x_i^\alpha - x_j^\beta)^2 + (y_i^\alpha - y_j^\beta)^2)}{(r_i^\alpha - r_j^\beta)^4} \right\rangle, \tag{3.11}$$

with α and β are atom types, N_α and N_β are number of atoms of type α and β, V is the volume of the simulation box, x, y, and z represent atomic position in Cartesian coordinates. This function gives a negative or positive signature. For example, it is positive when there are more bonds between atom types α and β of length $\langle |r_i - r_j| \rangle$ oriented along the loading axis than perpendicular to it, and negative when and negative when there are more bonds of a particular length perpendicular to than along the loading axis.

Angular distribution function

The angular distribution function (ADF) represents the probability of finding two distinct atoms at a distance $r < r_{\min}$ forming an angle with a central atom[36, 168]. For example, Figure. 3.4 shows angles of type O_2-Si-O_3, O_1-Si-O_2, and O_1-O_2-O_3 for two tetrahedra with Si centers and which are connected by bridging oxygen (BO) O_2. If θ is the angle between the bonds *i-j* and *j-k* bonds, the angular distribution function g(θ) is obtained as a histogram distribution of the angles determined as follows :

$$\theta_{ijk} = \arccos\left(\frac{r_{ij}^2 + r_{ik}^2 - r_{jk}^2}{2 r_{ij} r_{ik}}\right), \tag{3.12}$$

$$P(\theta) = \frac{n}{N}, \tag{3.13}$$

where r_{ij} corresponds to the distance between two atoms, n is the number of angles *i-j-k* at angles θ in a sphere of radius $r_{\min}$ determined from the RDF, and N is the total number of angles *i-j-k* in the same sphere. In this study, the ADF is used to estimate the angle between the inter- and intra-tetrahedral units of the systems (figure 3.4 shows an example of the angular distribution function of the O-Si-O angle obtained from a silica glass).

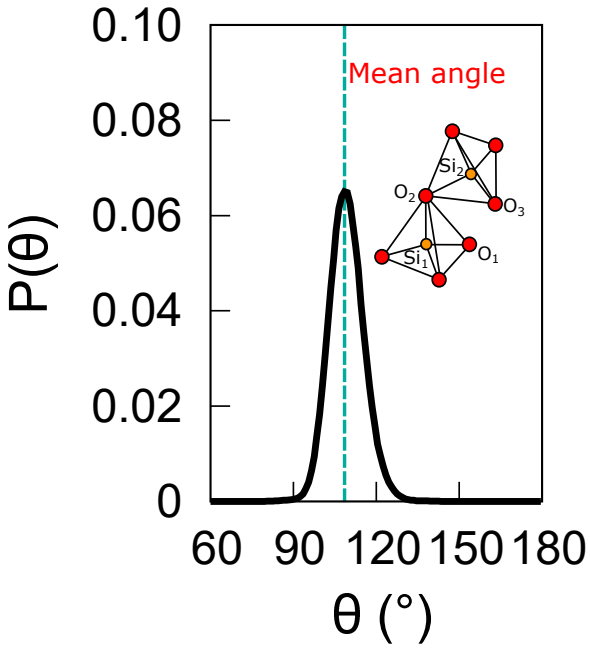

Figure. 3.4: Angular distribution function of the O-Si-O angle obtained from silica glass. The inset show schematically two linked tetrahedra centered on Si atoms.

Chain analysis

The metaphosphate glasses have a chain-like structure and a [Oxygen]/[Phosphorous] = 3. The approach to identifying the chains in the metaphosphate glasses is as follows. First, all atoms were deleted except P atoms, and then we used the minimum of the P–P radial distribution function to define the P–P separation distance. A chain is identified if a succession of at least three atoms is found. Atoms are members of the same chain if their separation distance is less or equal to the minimum of the P–P RDF. This procedure was performed using the RINGS code [169].

When the chains are identified, the end-to-end vector of each chain is computed. The tortuosity parameter was calculated and is defined as:

$$\tau = \frac{C}{L}, \tag{3.14}$$

where C is the length of the end-to-end vector and L is the actual length of the chain. The distribution of the tortuosity parameter τ for the sodium metaphosphate glass is given as a showcase in Figure. 3.5, other glasses show similar behavior. All chains with a tortuosity parameter lower than 1.5 are selected for further analysis. Next, the angle between each end-to-end vector of the selected chains and the loading axis was calculated. Finally, the mean angle is calculated as an average from the angles of the end-to-end and the loading axis.

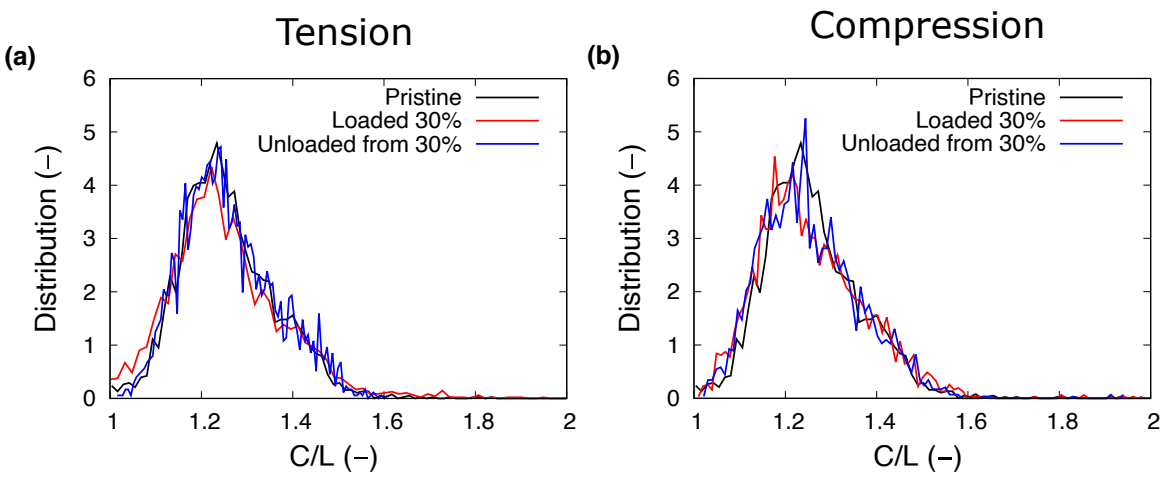

Figure. 3.5: Distribution of tortuosity parameter for pristine, loaded, and unloaded sodium metaphosphate glass containing 108000 atoms. (a) Tension and (b) compression. The deformation was performed at room temperature and using a strain rate of 5×10^8 s^{-1}.

Anisotropy index

In order to quantitatively measure the structural anisotropy, a simple scalar quantity such as coordination is not enough as it was previously shown for granular media [170] and at least a second-order tensor internal variable that characterizes the geometry packing is needed [170]. A natural choice for this tensor-valued internal variable in the fabric tensor, which is defined as the ensemble average of the dyadic product of all contact normals F = $< \vec{n} \otimes \vec{n} >$. For the metaphosphate glasses, each phosphorous atom is encaged in a tetrahedron of four oxygen atoms forming a PO_4 unit. These tetrahedra are linked through bridging oxygen atoms. The fabric tensor in metaphosphate glasses is built from the contacts between neighboring tetrahedra, and for all P-O-P triplets, a unit vector $\vec{n}$ is considered, which connects all P-P nearest neighbors (connect all neighboring tetrahedra. The fabric tensor is then normalized through the contacts in a way that provides a tensor of unit trace (tr(F)=1), meaning that the sum of the eigenvalues (λ_i) is 1.

Based on this logic Rountree et al. [2] introduced an new parameter called anisotropy index (α)defined as follows:

$$\alpha = \sqrt{\frac{3}{2}\sum_{i=1}^{3}(\lambda_i - \frac{1}{3})^2} \tag{3.15}$$

Thus for glass with an isotropic structure, all three eigenvalues are equal, and $\alpha = 0$. The prefactor in eq. 3.15 was chosen to return a value of 1 when the structure is fully anisotropic.

Bond statistics

During the deformation process of the glasses, atoms change their bonding topology to adapt to the imposed strain or stress. Therefore, statistically quantifying the atoms that have changed their neighbors and locally visualizing them is of utmost importance.

Following the work of Luo *et al.* [61], the number of atoms with new, switched, or broken bonds were determined. This was done by comparing the neighbors of each atom in the deformed configuration with the undeformed glass configuration and finding the differences in bonding topology between them. Each atom in the simulation box has a unique ID that does not change during the simulation. We use this ID to identify and compare a deformed configuration to the pristine glass. The change in the atoms' bonding topology is computed by the change in the number of the nearest neighbors identified by the first minimum of the RDF (e.g., r = 2 Å for Si-O for silicate glasses). We distinguish between four types of atoms depending on the type of change in their neighbors. Atoms with unchanged bonding topology are the atoms with no change in their nearest neighbors. Atoms with broken bonds, which means that the number of nearest neighbors decreased compared to the reference configuration, atoms that have a new bond have an increased number of neighbors compared to the reference configuration, and atoms with no change in the number of neighbors, but at least one nearest neighbor has changed (different ID) are considered as atoms with switched bonds.

Local strain and nonaffine deformation

The strain is a relative measure and can be calculated locally at the atomic scale if a reference configuration is known. In this thesis, von Mises strain was calculated by getting an affine transformation matrix to the relative neighbors within a cutoff through least-square fitting [171]. Based on this simple yet complex definition of the atomic strain, a reference configuration is always needed. Therefore, in all strain calculations, the pristine glass was chosen as a reference configuration even for the pre-deformed sample. Details of the strain calculation can be found in Ref. [171, 172] and are briefly summarized as follows:

1. Calculation of the particle displacement vectors from the differences between the current and reference particle positions.
2. These vectors are used to calculate the atomic deformation gradient tensor.
3. The results from strep two are used to derive an atomic Green-Lagrangian strain tensor.
4. The von Mises local shear invariant and the hydrostatic strain measure are calculated based on the results from step three.

$$\{d_{ji}^0\} \rightarrow \{d_{ji}\}, \forall j \in N_i^0, \tag{3.16}$$

where d's are vectors of ceparation between atom j and i given as $d_{ji} \equiv x_j - x_i$, the subscript 0 indicate the reference configuration [171], and N_i^0 is the total number of neighbors of atom i within a cutoff (the cutoff values will be given in the upcomming chapters when this analysis will be used). In the reference configuration the local transformation matrix J_i is obtained by minimizing,

$$\sum_{j \in N_i^0} |d_{ji}^0 J_i - d_{ij}|^2 \rightarrow J_i = \left(\sum_{j \in N_i^0} d_{ji}^{0T} d_{ji}^0 \right)^{-1} \left(\sum_{j \in N_i^0} d_{ji}^{0T} d_{ji}^0 \right). \tag{3.17}$$

For each J_i, the local Lagrgian strain matrix is computed as:

$$\eta_i = \frac{1}{2}(J_i J_i^T - I), \tag{3.18}$$

where η_i, J_i, J_i^T, and I are the Lagrangian strain matrix, the local transformation matrix, the transpose of the local transformation matrix, and the identity matrix, respectively.

Finally, the local shear strain invariant η_i^{Mises} of atom i is computed as follow:

$$\eta_i^{Mises} = \sqrt{\eta_{yz}^2 + \eta_{xz}^2 + \eta_{xy}^2 + \frac{(\eta_{yy} - \eta_{zz})^2 + (\eta_{xx} - \eta_{zz})^2 + (\eta_{xx} - \eta_{yy})^2}{6}}, \tag{3.19}$$

Using molecular dynamics simulations, we can access details at the atomic scale and overview how atoms behave during loading and unloading deformations. This is helpful to see if there are any localized irreversible deformed regions. For this, we need to locate the regions with nonaffine atomic displacements, meaning the displacements deviate from the displacements described by a linear strain field. The current atomic configuration needs to be compared with a reference configuration to obtain these regions with a nonaffine displacement. The neighbors of each particle are defined by defining a sampling radius, and this sampling radius was chosen to be large enough to give a smooth visualization and small enough to resolve local events. The local strain is then calculated from the displacements of the neighboring particles to the central one and relative displacements that they would have if they were in a region of uniform strain. More details about the calculation of the nonaffine displacements are given in Ref. [173].

Strain localization

The strain localization parameter (Ψ_{strain}) proposed by Cheng *et al.* [174] was calculated during all deformation stages using Eq. (3.20).

$$\Psi_{strain} = \sqrt{\frac{1}{N} \sum_{i=1}^{N} (\eta_i^{Mises} - \eta_{ave}^{Mises})^2}, \tag{3.20}$$

where η_{ave}^{Mises} is the average von Mises strain over all atoms in the simulation box [174] and N is the total number of atoms in the simulation box. The strain localization parameter, Ψ_{strain}, is used to evaluate the deviation of strain distribution from the homogeneous behavior. Large values of this parameter indicates large variation in the atomic strain during the deformation process. To the best of our knowledge, this is the first study to apply this analysis to study the deformation of oxide glasses.

Part I

Metaphosphate glasses

4 Results

In this chapter, we used molecular dynamics simulations to investigate how mechanical deformations lead to anisotropic metaphosphate glass structure, the structural origin of this anisotropy in metaphosphate, and how the mechanical properties are affected by the anisotropic structure and composition of the glass. The glasses contain 108000 atoms prepared using the procedure described in Chapter. 3, with 10^{12} K/s as a cooling rate and deformed at room temperature (300 K) using a strain rate of 5×10^{8} s^{-1}.

4.1 Structure of pristine metaphosphate glasses

To begin with, we investigated the local structure around the cations in the metaphosphate glasses. The radial distribution and angular distributions are used to do so. All the data for structural properties is obtained at 300 K using 108000 atoms as system size and prepared following the cooling procedure presented in section. 3.3.

Figure. 4.1a shows the radial distribution function for the P–O pair in the three metaphosphate glasses studied here. The position of the first peak of this distribution indicates the mean separation distance, which is around 1.52 Å; this position is not dependent on the type of modifier present in the glass network (See Table. 4.1). The P–O first peak contains both P–NBO and P–BO bonds found in PO_4 tetrahedra as shown for the sodium metaphosphate glass in the inset of Figure. 4.1a. The P–NBO bond is shorter than the P–BO bonds and centered at 1.48 and 1.56 Å, respectively. Experimentally, the reported difference between P–NBO and P–BO is around 0.1 Å [175] and the one reported here is around 0.08 Å, in good agreement with the experiments [175] and other MD simulations [176].

In the same figure, we plotted the cumulative coordination number (CN), which is the variation of the number of O around P as a function of the distance. The cumulative CN increases with the beginning of the P–O RDF until it reaches a value around 4.1; then, a plateau is observed and increases again at larger separation distances. The plateau found in the cumulative CN indicates a well-defined first coordination shell with a mean coordination number around 4.1 found at a distance of 2.1 Å. Most of the P atoms have four-fold coordination with the presence of some five- and six-fold coordinated P atoms that are considered as a defect arising from the high cooling rate used to prepare the glass, which is a common type of defect observed in glasses prepared by MD simulations [176]. The fraction of each phosphorous species is given in Table. 4.2.

In Figure. 4.1b, we plotted the O–O RDF, which shows a first peak centered around 2.5 Å, the first minimum around 2.75 Å, and a cumulative CN around 4, indicating that each O atom has four atoms in its first coordination shell. Figure. 4.1c shows the P–P RDF and cumulative CN where the position of the first peak is centered around 3.15 Å and can be seen as the separation distance between two phosphorous tetrahedra. The cumulative CN shows a plateau around a value of two, which is consistent with the fact that the metaphosphate glasses are made by PO_4 chains meaning that most of the P atom should have two other P atoms in its first neighboring shell. Figure. 4.1d depicts the X–O RDFs, where X

stands for Na, Mg, or Ca. As stated in the previous chapters, magnesium has the highest field strength, followed by calcium and then sodium. The behavior of the X–O mean separation distance correlates negatively with the field strength, as magnesium has the shortest bond length, followed by calcium and then sodium, with sodium and calcium having close enough bond lengths. Similar to the bond length, the mean coordination increases with increasing cation field strength, and we have magnesium showing a mean CN of around 4.3, calcium around 6, and sodium is also coordinated by around 6 oxygen atoms.

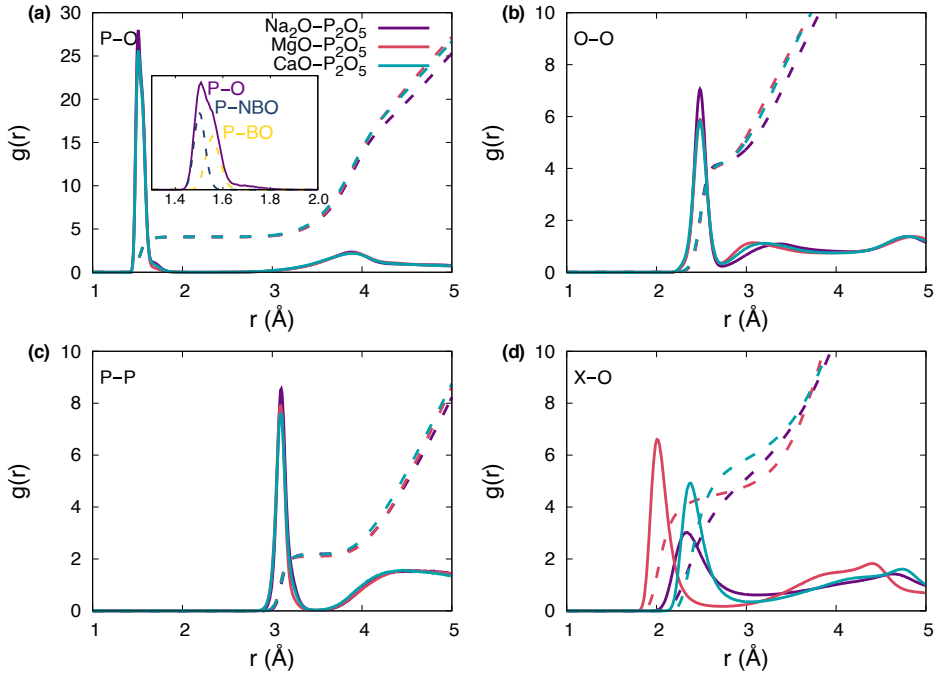

Figure. 4.1: Pair distribution functions (solid lines) for (a) P–O, (b) O–O, (c) P–P, and (d) X–O (where X is Na, Mg, and Ca). The dashed lines stand for the cumulative coordination number.

The bond angle distribution (BAD) details the angle in the first coordination shell and neighboring coordination shells. Thus, we can define the polyhedra shape that makes the glass and how they are connected. The distributions of O–P–O angles for all metaphosphate glasses are shown in Figure. 4.2a, where we see a well-defined peak at angles around

Table 4.1: Short-range structural parameters of the MD prepared metaphosphate glasses at 300 K. The cutoffs to calculate the mean coordination numbers were set to 2.1 Å for the P–O and 3.5, 2.75, 3.166, 2.534, 2.951 Å for the P–P, O–O, Na–O, Mg–O, and Ca–O pairs, respectively. The bond lengths are given with an error of ± 0.002 Å.

Glass systems	P–O		P–P		O–O		M–O	
	r_{ij}	N_{ij}	r_{ij}	N_{ij}	r_{ij}	N_{ij}	r_{ij}	N_{ij}
Na_2O-P_2O_5	1.508	4.097	3.101	3.10	2.19	4.191	2.331	5.604
MgO-P_2O_5	1.508	4.053	3.093	3.09	2.10	4.137	2.013	4.350
CaO-P_2O_5	1.508	4.091	3.093	3.09	2.18	4.189	2.376	5.730

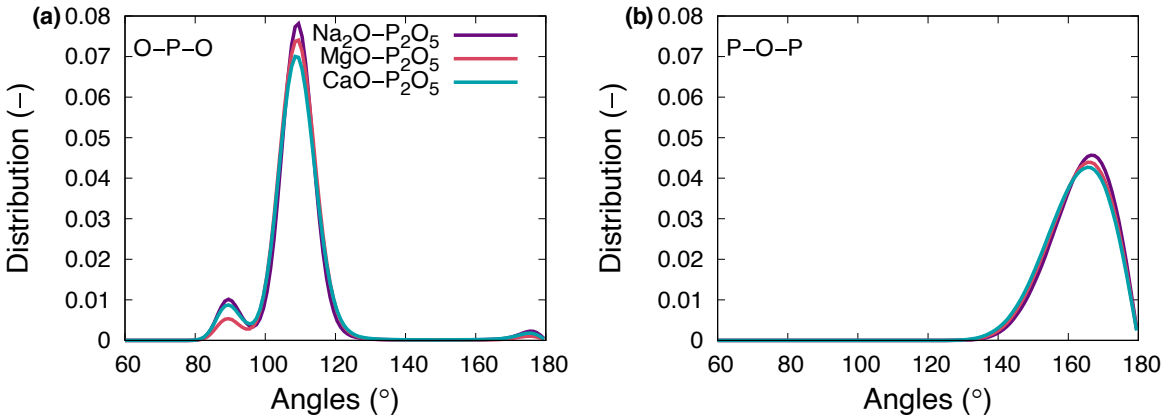

Figure. 4.2: Bond angle distributions obtained of (a) O–P–O and (b) P–O–P in the simulated metaphosphate glasses at 300 K.

Table 4.2: Phosphorous species, NBO, and BO fractions in the pristine glass samples at 300 K.

Glass	P^4 (%)	P^5 (%)	P^6 (%)	NBO (%)	BO (%)
$Na_2O–P_2O_5$	93.22	4.21	2.57	63.55	36.45
$MgO–P_2O_5$	95.77	3.42	0.81	64.98	35.02
$CaO–P_2O_5$	93.12	5.09	1.79	63.77	36.23

110°. Moreover, due to the presence of some P atoms with a coordination number larger than 5 we also observe the presence of two other peaks at angles centered around 90° and 170°, respectively. The intensity of the additional peaks correlates negatively with the cation field strength, indicating that the glasses containing high field strength modifiers tend to have a lower number of P atoms with a coordination number of more than 4. In addition to that, the main peak centered around 110° clearly shows that the local structure of the glasses is mainly built up by PO_4 tetrahedra. The angle between these tetrahedra is captured by the P–O–P angular distribution as shown in Figure. 4.2b, where there is only one peak centered on angles around 165° with a broad distribution. This distribution shifts slightly toward smaller angles with increasing modifiers' field strength.

The Q^n distribution gives the number of BO in each phosphorous polyhedron, with n being the number of BO per polyhedron. This distribution for the pristine glasses is given in Table. 4.3 where we can see that as expected Q^1, Q^2, and Q^3 presents the majority of the Q^ns in the simulated glasses. This is consistent with the fact that metaphosphate glasses have a chain-like structure made by linked tetrahedra ion in the form of Q^2 and ended by Q^1 tetrahedra. The Q^3 represents the cross-linking of two chains. Moreover, glasses with modifiers with high field strength tend to have more Q^2 units, thus indirectly implying that those glasses have longer chains.

The metaphosphate glasses are made by tetrahedra linked to form a chain-like structure at the medium range level. Thus, it is vital to probe the medium-range order of these glasses and understand how the chain length is distributed and the effect of the modifier type on the chain length distribution. The chain length distribution is calculated as de-

Table 4.3: Q^n distribution fractions in the pristine glass samples at 300 K.

Glass	Q^0 (%)	Q^1 (%)	Q^2 (%)	Q^3 (%)	Q^4 (%)	Q^5 (%)	Q^6 (%)
Na_2O–P_2O_5	4.15	24.86	38.22	21.89	5.16	3.23	2.49
MgO–P_2O_5	2.42	23.66	45.3	22.0	4.02	1.85	0.75
CaO–P_2O_5	3.67	23.90	40.10	22.41	5.2	3.09	1.63

picted in section. 3.4 and is shown in Figure. 4.3a for the three metaphosphate glasses we studied. We can tell that most chains are made of 3, 4, 5, and 6 PO_4. In the magnesium metaphosphate glass, we observe that the fraction 5, and 6 membered chains are higher than in sodium metaphosphate or calcium metaphosphate glasses. This is seen in Figure. 4.3b, where the magnesium metaphosphate glass contains chains larger than calcium and sodium metaphosphate glasses. The behavior of the average chain length generally increases with increasing modifiers' field strength. The chain length distribution is consistent with previous MD work of different glass compositions, but with similar content of modifiers [24].

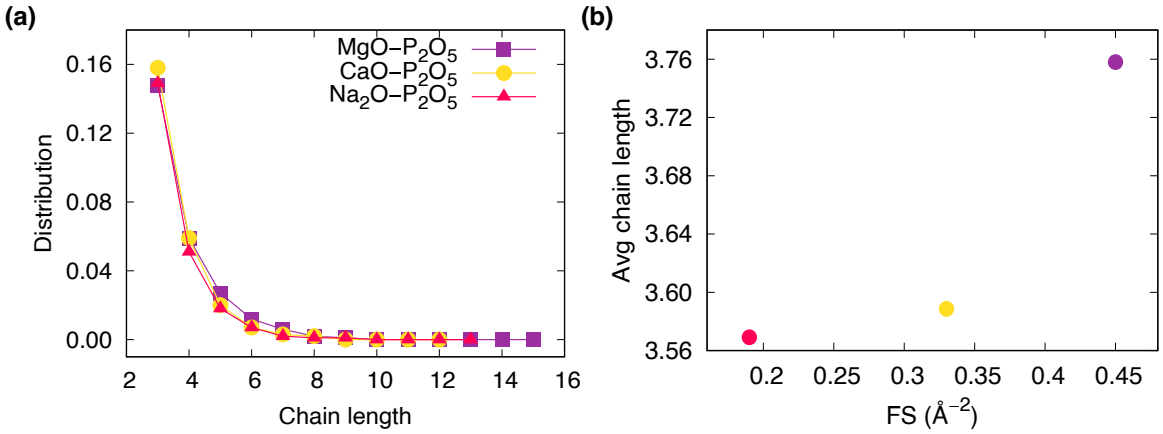

Figure. 4.3: (a) Chain length distribution given as the number of tetrahedra in each chain and (b) average chain length as a function of the modifiers field strength (FS) in the pristine metaphosphate glasses.

4.2 Deformation behavior of metaphosphate glasses

The metaphosphate glasses studied in this thesis are subjected to tensile or compressive deformation to investigate their mechanical behavior, explain the deformation mechanisms, and understand the processes that lead to the transient and persistent structural anisotropy. The glasses were deformed using the protocol described in section. 3.3. All glasses are subjected to deformations at 300 K using a strain rate of 5.0×10^8 s^{-1}, 108000 as system size, and a cooling rate of 10^{12} K/ps.

Tensile tests on metaphosphate glasses

The stress-strain curves of Na_2O–P_2O_5, MgO–P_2O_5, and CaO–P_2O_5 glasses are shown in figure 4.4a during uniaxial tension along the x-axis. During the loading, all the samples deform elastically at low strains, yield, and then show a plastic plateau with a low softening behavior at larger strains. The sodium metaphosphate glass shows the lowest Young's modulus (37 $\pm$ 0.1 GPa), followed by that of calcium metaphosphate (60 $\pm$ 0.1 GPa) and then magnesium metaphosphate (63 $\pm$ 0.1 GPa). The values of Young's modulus are consistent with experimental measurements (35.7 GPa, 53.9 GPa, 55.5 GPa for Na_2O-P_2O_5, MgO-P_2O_5, and CaO-P_2O_5, respectively) [161, 177]. However, in experiments, the values of Young's modulus of calcium metaphosphate glasses are higher than that measured for the magnesium metaphosphate glass [161]. The maximum stress in tension and compression scales are as follows, NaPO $<$ CaPO $<$ MgPO. The tensile yield stresses (strains) calculated from the 0.2% rule are as follows 950 MPa (2.7 %), 1808 MPa (3.1 %), and 1580 MPa (2.8 %) for Na_2O-P_2O_5, MgO-P_2O_5, and CaO-P_2O_5, respectively .

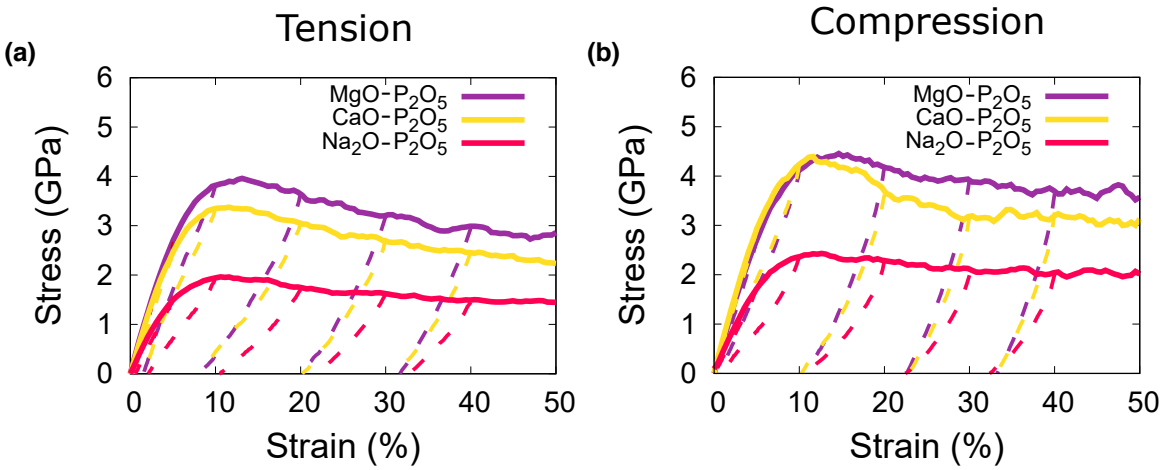

Figure. 4.4: Stress-strain curves during tension (a) and compression (b) for Na_2O-P_2O_5, MgO-P_2O_5, and CaO-P_2O_5 during loading (solid lines) and unloaded from 2.5%, 5%, 10%, 20%, 30%, and 40% (dashed lines). The strain rate is 5.0 $\times$ 10^8 s^{-1} along the x-axis at a constant temperature of 300 K and using 108000 atoms as a system size.

The unloading to zero stress was performed starting from different values of the strain: 2.5%, 5%, 10%, 20%, 30%, and 40%. All unloaded samples show a plastic deformation as observed by the remaining plastic strain ϵ_{pl} except in the case of the samples unloaded from 2.5% and 5%. As shown in Figure. 4.4a, for strain higher than 8% corresponding to a stress of about 3 GPa in tension, the glass shows permanent macroscopic plastic deformation. After unloading the glasses, the plastic strain of magnesium metaphosphate and calcium metaphosphate glasses shows similar values, while those for sodium metaphosphate are always higher. It is worth stressing that magnesium and calcium are alkaline earth metals, while Na belongs to the alkali metals family.

Compression tests on metaphosphate glasses

The stress-strain curves of Na_2O–P_2O_5, MgO–P_2O_5, and CaO–P_2O_5 glasses during uniaxial compression along the x-axis are depicted in figure 4.4b. During the loading of the glasses, all the samples have an elastic deformation at low strains and show a plastic plateau at larger strains. In the case of calcium metaphosphate glass, a clear stress drop was observed after yielding, where the stress drops from around 4.4 GPa to 3 GPa when the strain is around 30%. The stress drop is not visible in the other glass samples. The yield stress in compression scales is as follows NaPO $<$ CaPO $<$ MgPO.

The unloading to zero stress simulations was performed starting from different values of the maximum strain: 2.5%, 5%, 10%, 20%, 30%, and 40%. In all samples, we observed a remaining plastic strain ϵ_{pl} except for unloading from 2.5% and 5%. As shown in Figure. 4.4b, for strain higher than 8% corresponding to a stress of about 3.5 GPa in compression, the glass shows permanent macroscopic plastic deformation as depicted by the finite measured plastic strains. It is observed that the stresses in compression are higher than those in tension, indicating a tension-compression asymmetry.

Tensile tests on pre-deformed metaphosphate glasses

The mechanical behavior of the glasses already subjected to mechanical loading, i.e., tension or compression, will be presented in the following. All deformations are performed at 300 K and using the samples with 108000 atoms, cooled with a quenching rate of 10^{12} K/s and deformed using a constant strain rate of 5×10^8. The pristine glass samples deformed in tension or compression along the x-axis will be referred to as pre-tension or pre-compression. These pre-deformed glasses that were unloaded from different maximum strains are reloaded back in tension along different directions, i.e., x, y, or z

In Figure 4.5, we show the tensile stress-strain curves of the metaphosphate glass samples pre-deformed in tension (Figure 4.5(a, c, and e)) or compression (Figure 4.5(b, d, and f)) along the x-axis and unloaded back to 0 MPa from different strains, i.e., 10, 20, 30, 40%. The reloading in tension is performed along the same direction as the pre-loading, i.e., x-direction. The stress-strain curves of the pristine metaphosphate glasses obtained from a tensile test along the x-axis are also provided in the plot for comparison. Similar deformation behavior is observed for all glasses, where Young's modulus decreases with increasing the plastic strain (unloading strain). However, if we compare the samples pre-deformed in tension with those pre-deformed in compression, it is obvious that the ones pre-deformed in compression have a lower Young's modulus, as highlighted below. Figure. 4.6 shows the values of Young's modulus as calculated from the stress-strain curves along the x-, y-, and z-direction. The values of Young's modulus are normalized to the one of the pristine glass. When the reloading is performed along the same direction as the pre-deformation (x-axis), both pre-deformation modes decrease Young's modulus compared with the pristine glass. However, as can be noticed in Figure. 4.6, pre-deforming in tension resulted in higher Young's modulus values compared to the pre-compression also, the rate of the decrease is different in both pre-deformation modes.

The Young's modulus along the orthogonal directions to the pre-deformation axis showed

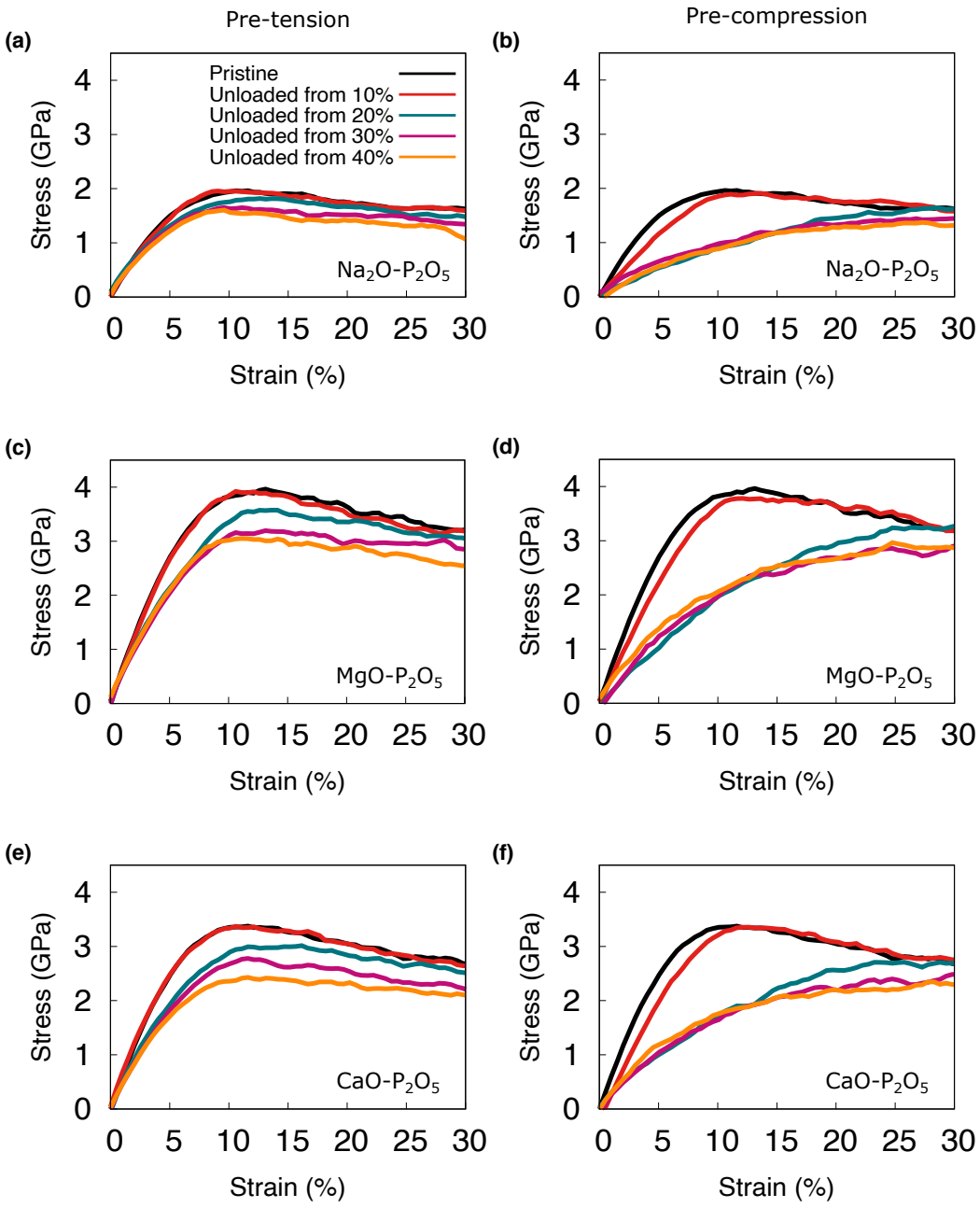

Figure. 4.5: Pristine vs pre-deformed tensile stress-strain curves of sodium metaphosphate glass. (a) For the samples pre-deformed in tension along the x-direction and unloaded from different maximum strains and (b) for the samples pre-deformed in compression along x-direction and unloaded from different maximum compressive strains. The the reloading is along the $x-$axis. The glasses were at 300 K using a strain rate of $5\times10^{8}\text{s}^{-1}$.

a strong decrease when the glass was pre-deformed in tension. In contrast, Young's modulus of the glasses pre-deformed in compression and reloaded in tension along the orthogonal directions to the pre-deformation axis showed a decrease compared to the pristine glass for the case of Na_2O-P_2O_5 and CaO-P_2O_5, while those of MgO-P_2O_5 glasses stayed almost

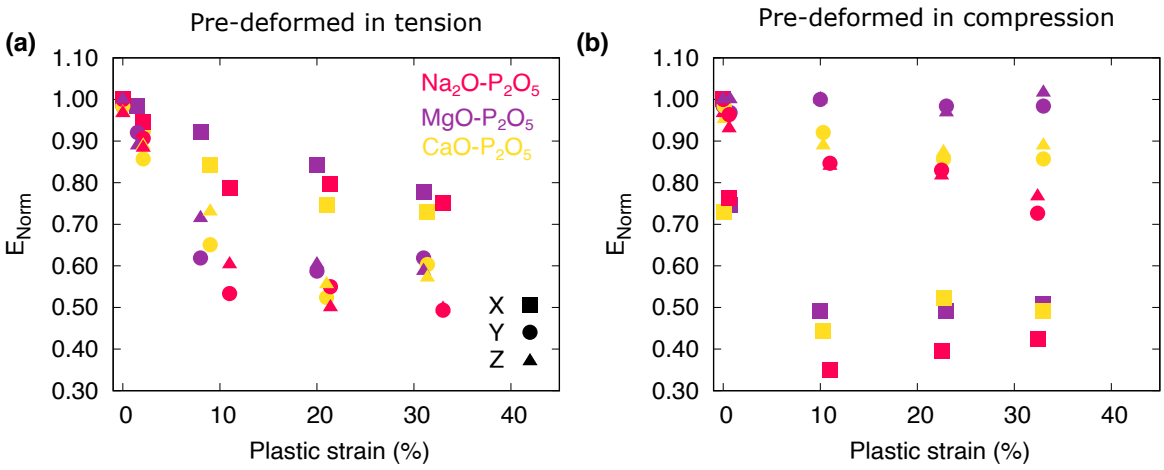

Figure. 4.6: Normalized Young's modulus as a function of the plastic strain of pristine and pre-deformed glasses. (a) for the samples pre-loaded in tension along x-direction, unloaded to zero strain, and reloaded in tension. (b) the samples pre-loaded in compression along x-direction unloaded to zero strain, and reloaded in tension. Young's modulus is normalized with respect to the values found for the pristine glasses. The glasses were at 300 K using a strain rate of $5\times10^8 s^{-1}$.

constant. For the yield and flow stresses, they follow the same trend as Young's modulus as shown for sodium metaphosphate in Figure. 4.5

In Figure. 4.7, we show the direction-dependent stress-strain curves during the tensile test of the samples pre-deformed up to 20% strain in tension and compression and unloaded to zero stress state, respectively. The stress-strain curve of the pristine glass subjected to tension along the $x-$axis is also given as a reference. The response of the glasses pre-deformed in tension and reloaded in tension is similar to the pristine glass with a reduction of Young's modulus and yield and flow stresses. The tensile stress-strain response along the orthogonal directions (y- and z-axis) to the tensile pre-loading axis (x-axis) showed a considerable reduction of Young's modulus and the elastic regime in general, with a decrease in the yield stress. The sample pre-deformed in compression showed a reversed behavior compared to those pre-deformed in tension. The Young's modulus and yield stress were significantly decreased in the glass reloaded in the same direction as the pre-compression. In contrast, the orthogonal directions slightly decreased Young's modulus and yield stress.

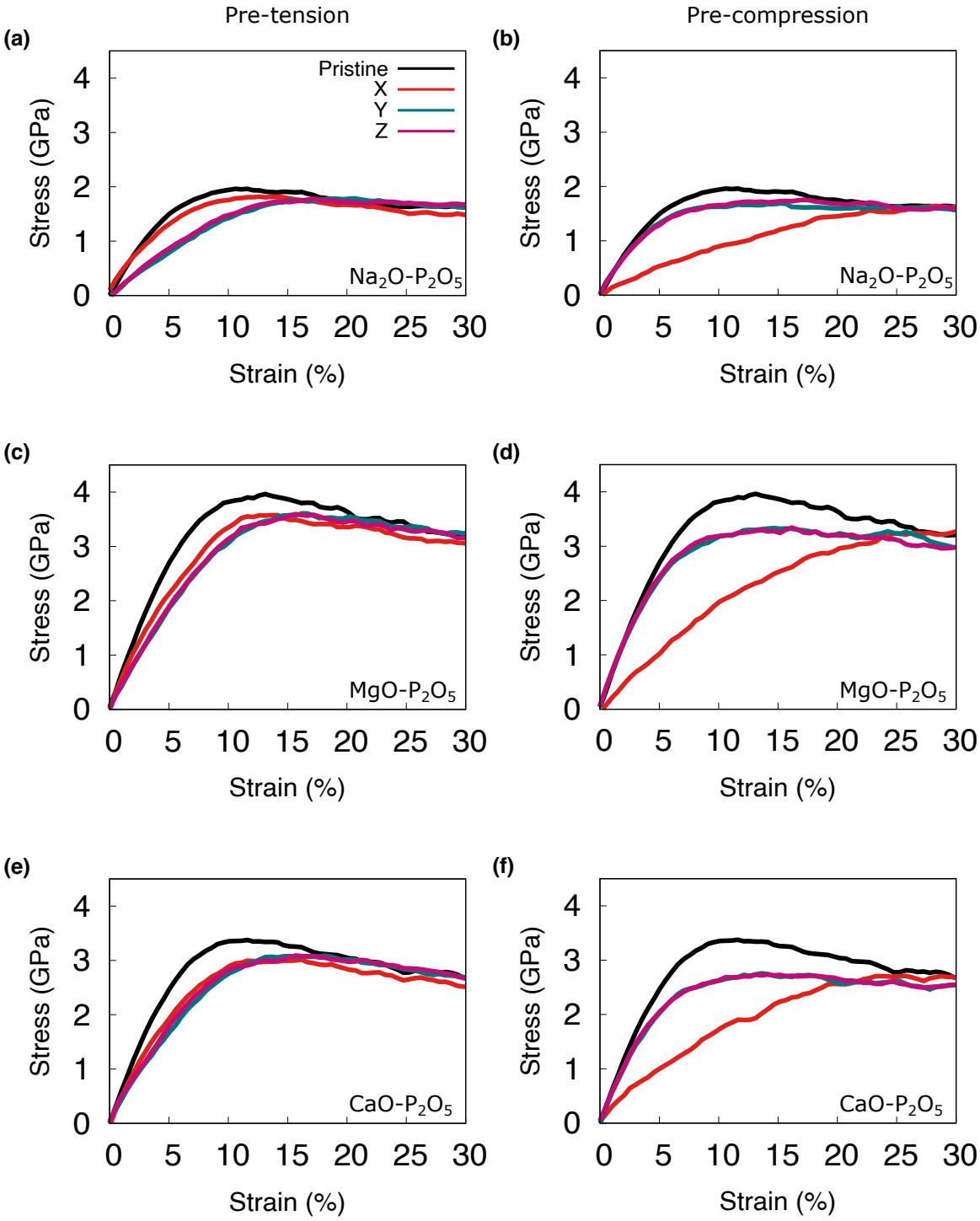

Figure. 4.7: Pristine vs pre-deformed tensile stress-strain curves of sodium metaphosphate glass. (a) For the samples pre-deformed in tension and unloaded from 20% strain and (b) for the samples pre-deformed in compression and unloaded from 20% compressive strain. The reloaded samples were loaded along $x-$, $y-$, and $z-$axis. The glasses were at 300 K using a strain rate of $5\times10^{8}\text{s}^{-1}$.

4.3 Structure of pre-deformed metaphosphate glasses

RDF, BAD, Chains

The structural analysis at short- and medium-range levels of the pre-deformed metaphosphate glasses studied in this work will be presented in this section. The P–O radial distribution functions of the samples loaded to and unloaded from different strain values are shown in Figure. 4.8, where (a and b) are for sodium metaphosphate, (c and d) are for magnesium metaphosphate, and (e and f) are for calcium metaphosphate glasses. The RDFs of the samples obtained at a strain ϵ_x during the loading are shown in solid lines, while those obtained after the unloading to 0 MPa from a strain ϵ_x are shown in dashed lines. In the P–O RDFs, only the first peak, which defines the first coordination shell, is shown. As can be seen in the plots, the P–O RDF is almost not affected by the loading mode or the strain level, and it stayed similar to the one of the pristine glass. The effect of the composition stayed the same as discussed above for the pristine glasses.

Figure. 4.9 depict the P–P RDF for all metaphosphate glasses studied and for different loading states and mode. In Figure. 4.9, (a and b) are for sodium metaphosphate, (c and d) are for magnesium metaphosphate, and (e and f) are for calcium metaphosphate glasses. Similar to the P–O RDF, we only show the first peak of the P–P RDF, which highlights the distribution of the separation distances between two neighboring tetrahedra. Minor changes were observed as a function of the loading state (loaded or unloaded) compared to the pristine glasses—these changes were more visible in compression than in tension.

The bond angle distribution functions of the intra- and inter tetrahedral angles O–P–O and P–O–P are shown in Figure. 4.10. The ADFs are extracted at different strains during the loading and for the glasses unloaded to 0 MPa from those strains in both tension and compression. In Figure. 4.10, (a and b) are for sodium metaphosphate, (c and d) are for magnesium metaphosphate, and (e and f) are for calcium metaphosphate glasses. The BADs provide us with details on the angle in the first coordination shell and neighboring coordination shells, which enables us to properly define the polyhedra's shape that makes the glass and how they are connected. The distributions of O–P–O angles for all metaphosphate glasses show a well-defined peak at angles around 110°. The height of the peak is the highest for the pristine glass and decreases with increasing the loading strain. The samples unloaded from 10% the pristine glass BAD is recovered, while for other strains, the BADs are slightly different from the pristine glasses. The angle between these tetrahedra is captured by the P–O–P angular distribution as shown in Figure. 4.10, where there is only one peak centered on angles around 165°, with a broad distribution. This distribution shifts slightly toward smaller angles in the unloaded samples, and the shift is more pronounced with increasing unloading (or plastic) strain. The change of the P–O–P BADs is more pronounced in the case of loading in compression than in tension, and the same observation is also valid for the unloaded samples. The effect of the composition showed that the change is similar in different compositions, with a difference being in its magnitude, where the change of P–O–P BADs was more pronounced in CaO-P_2O_5 than in the other two glasses.

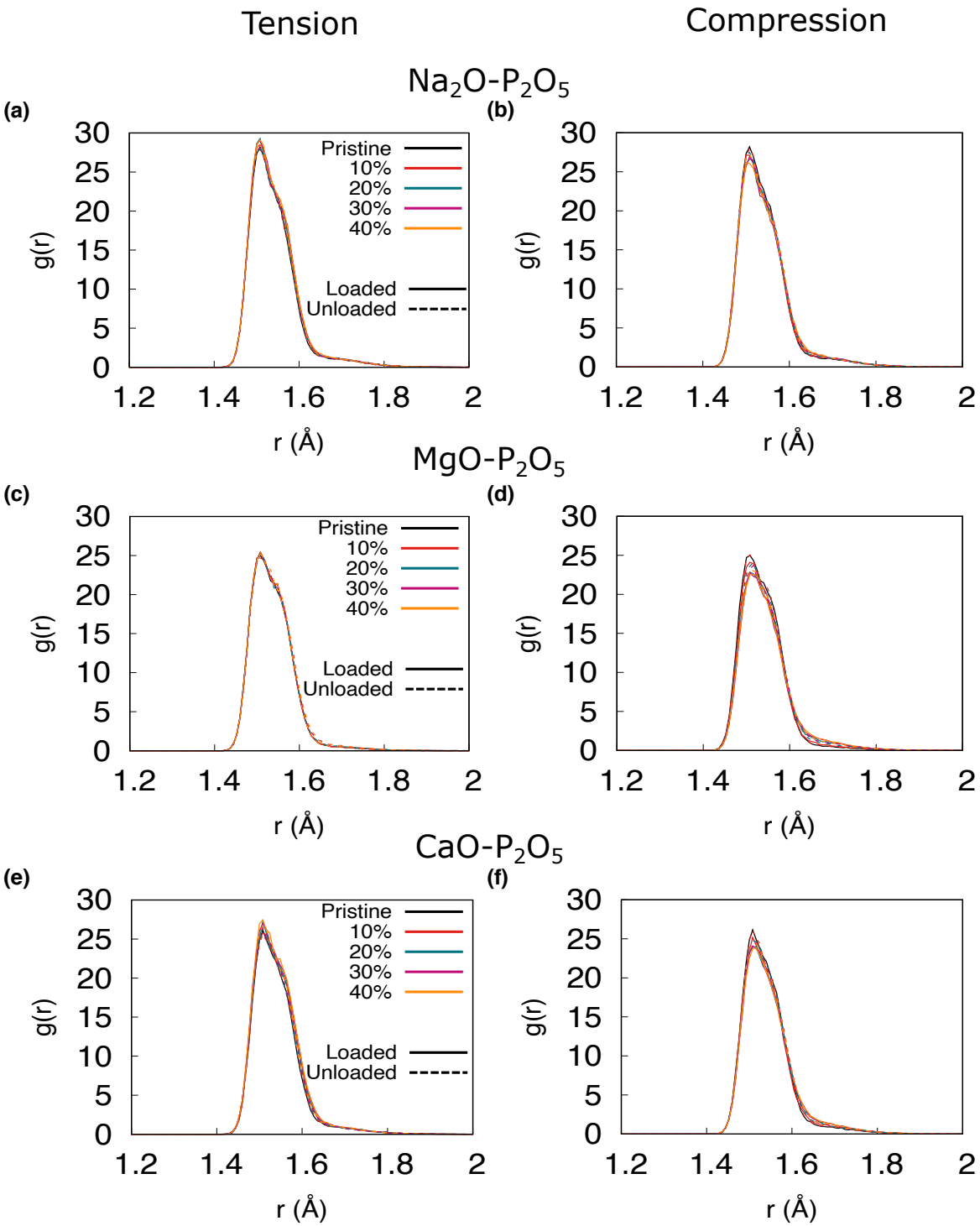

Figure. 4.8: Pair distribution functions for P–O for the loaded (solid lines) and unloaded (dashed lines) sodium magnesium, and calcium metaphosphate glass samples in both (a) tension and (b) compression. The glasses were deformed along the $x-$axis at 300 K using a strain rate of $5\times10^{8}\mathrm{s}^{-1}$.

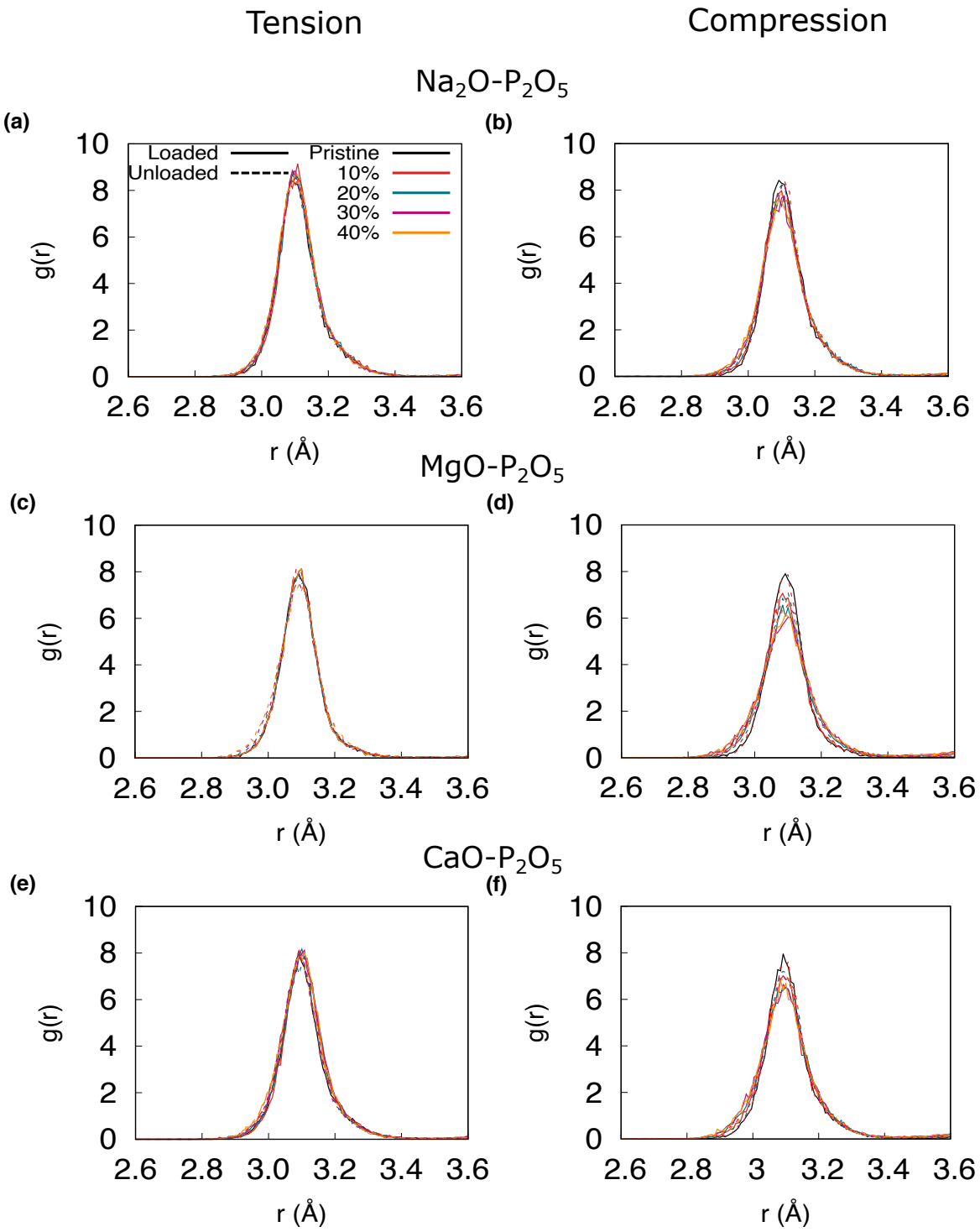

Figure. 4.9: Pair distribution functions for P–P for the loaded (solid lines) and unloaded (dashed lines) sodium magnesium, and calcium metaphosphate glass samples in both (a) tension and (b) compression. The glasses were deformed along the $x-$axis at 300 K using a strain rate of $5\times10^{8}\mathrm{s}^{-1}$.

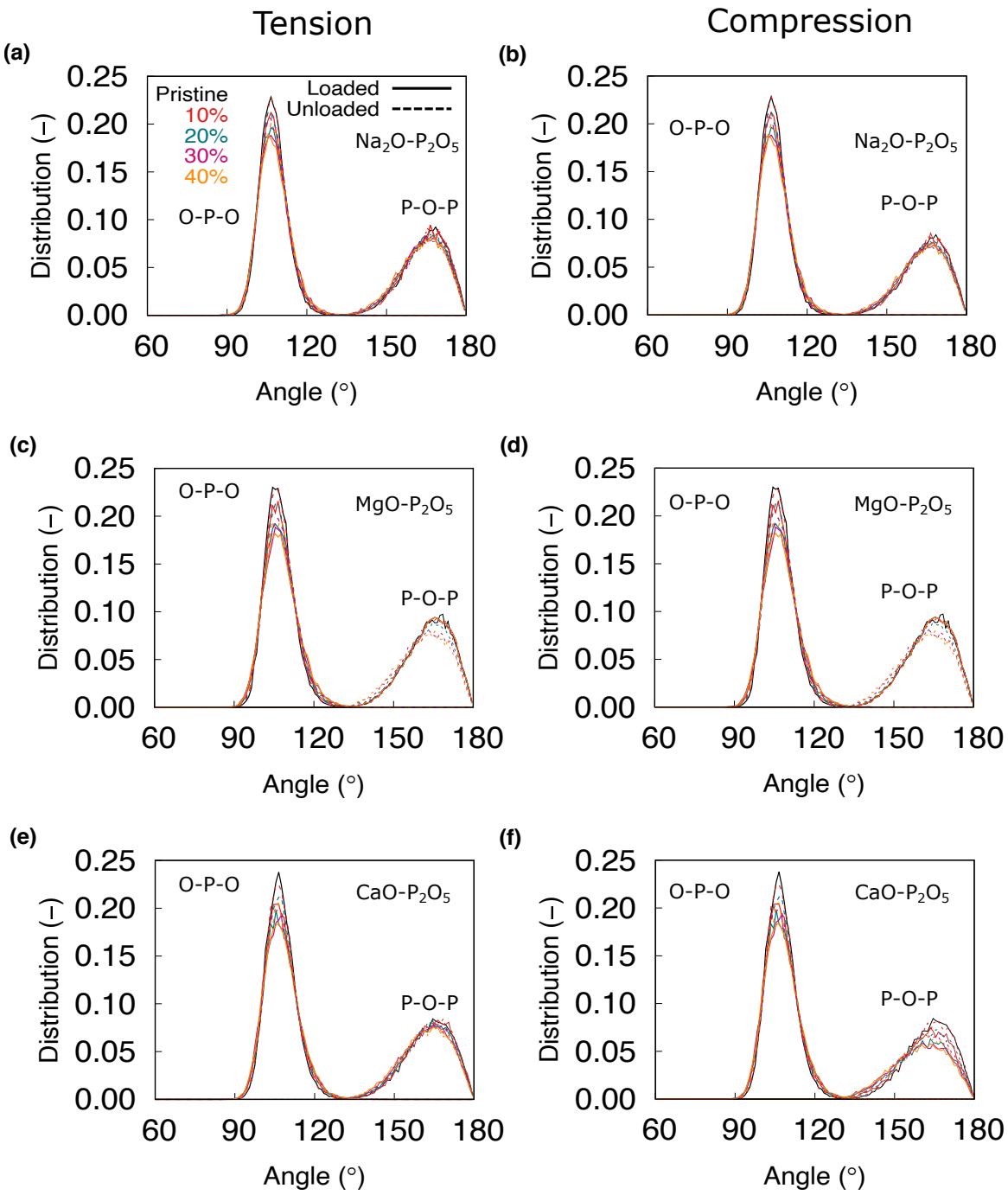

Figure. 4.10: Angular distribution functions for O–P–O for the loaded (solid lines) and unloaded (dashed lines) sodium magnesium, and calcium metaphosphate glass samples in both (a) tension and (b) compression. The glasses were deformed along the $x-$axis at 300 K using a strain rate of $5\times10^{8}\mathrm{s}^{-1}$.

In Figure. 4.11 we show the chain length distribution of the simulated metaphosphate glasses. The chain length is given as the number of PO_4 tetrahedra in each chain. As

can be seen in the figure, the structure of the metaphosphate glasses is mainly buildup by short phosphate chains with a length of 3 to 5 tetrahedral units. The chain length distributions for the loaded and unloaded samples look almost the same; however, looking at the mean chain length, we can notice the differences, where the mean chain length increases/decreases with the increase of the strain and increases/decreases in the unloaded glasses. This behavior is observed during both tension and compression.

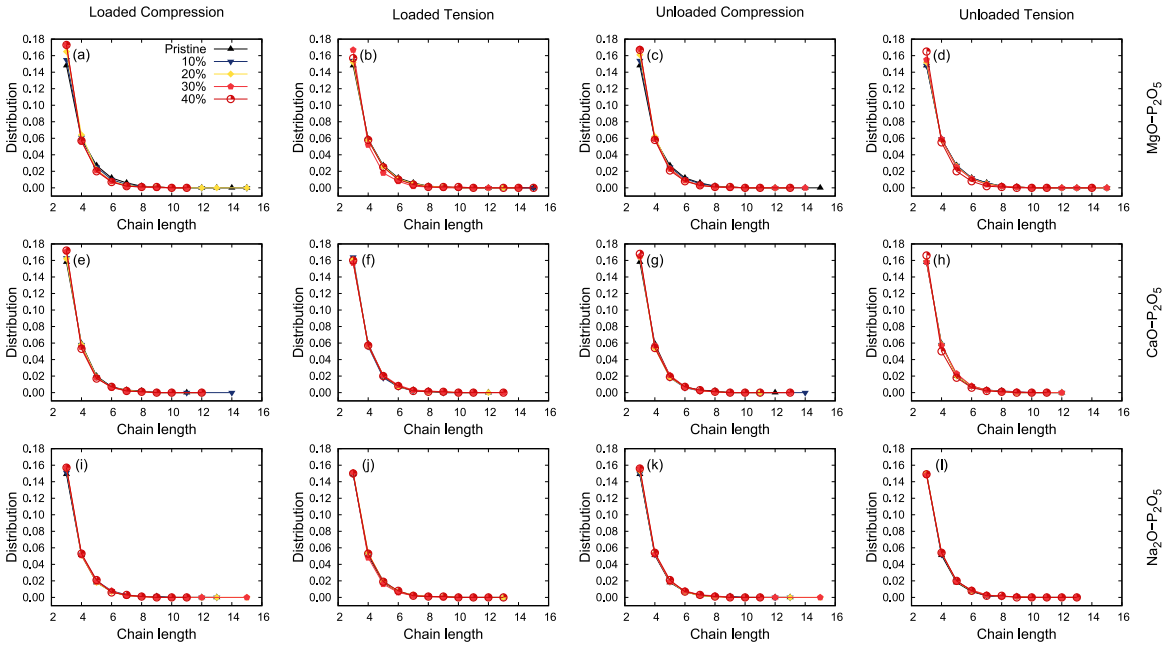

Figure. 4.11: Chain length distribution for the pristine, loaded to, and unloaded from different strains, where the strains are 10%, 20%, 30%, and 40%. The glasses are either loaded in tension or compression along the x-axis. The first row is for MgO-P_2O_5 glasses, second row is for CaO-P_2O_5 glasses, and third row is for Na_2O-P_2O_5. The glasses were deformed along the $x-$axis at 300 K using a strain rate of $5\times10^8 s^{-1}$.

The mean chain length was calculated from the chain length distribution and is shown in Figure. 4.12. At a strain ϵ, a configuration is extracted, and the chain length distribution is calculated following the method described in Section. 3. During the loading in tension (Figure. 4.12a), the behavior of the mean chain length with strain is unclear and shows a strong dependence on the composition. For the MgO-P_2O_5 glass, fluctuation exists, but all mean chain length values are lower than those recorded for the pristine glass. For the CaO-P_2O_5, the situation is a bit different where the fluctuations of the mean chain length values are around the value found for the pristine glass. The Na_2O-P_2O_5 glass show almost a similar behavior to that found for the CaO-P_2O_5 with a difference at 30% strain. The behavior of the mean chain length during compression (Figure. 4.12b) is much more straightforward and shows mostly a decrease, where the values of the mean chain length are lower than those found for the pristine glasses and generally decrease with increasing strain.

The values of the mean chain length for the unloaded glasses from both tension and compression are shown in Figure. 4.12c and d, where the mean chain length is plotted as

a function of the plastic strain. In the case of the unloading from different tensile strains (Figure. 4.12c), the mean chain length of the $MgO\text{-}P_2O_5$ decreases with increasing plastic strain, while that of $CaO\text{-}P_2O_5$ and $Na_2O\text{-}P_2O_5$ show a slight change compared to the pristine glass samples, which highlight the effect of the composition of the deformation behavior of these glasses. Similarly, the unloading from different strains in compression, as shown in Figure. 4.12d, resulted in a decrease of the mean chain length as a function of the plastic strain for the $MgO\text{-}P_2O_5$ glass, while the $CaO\text{-}P_2O_5$ and $Na_2O\text{-}P_2O_5$ glasses did not show and considerable change.

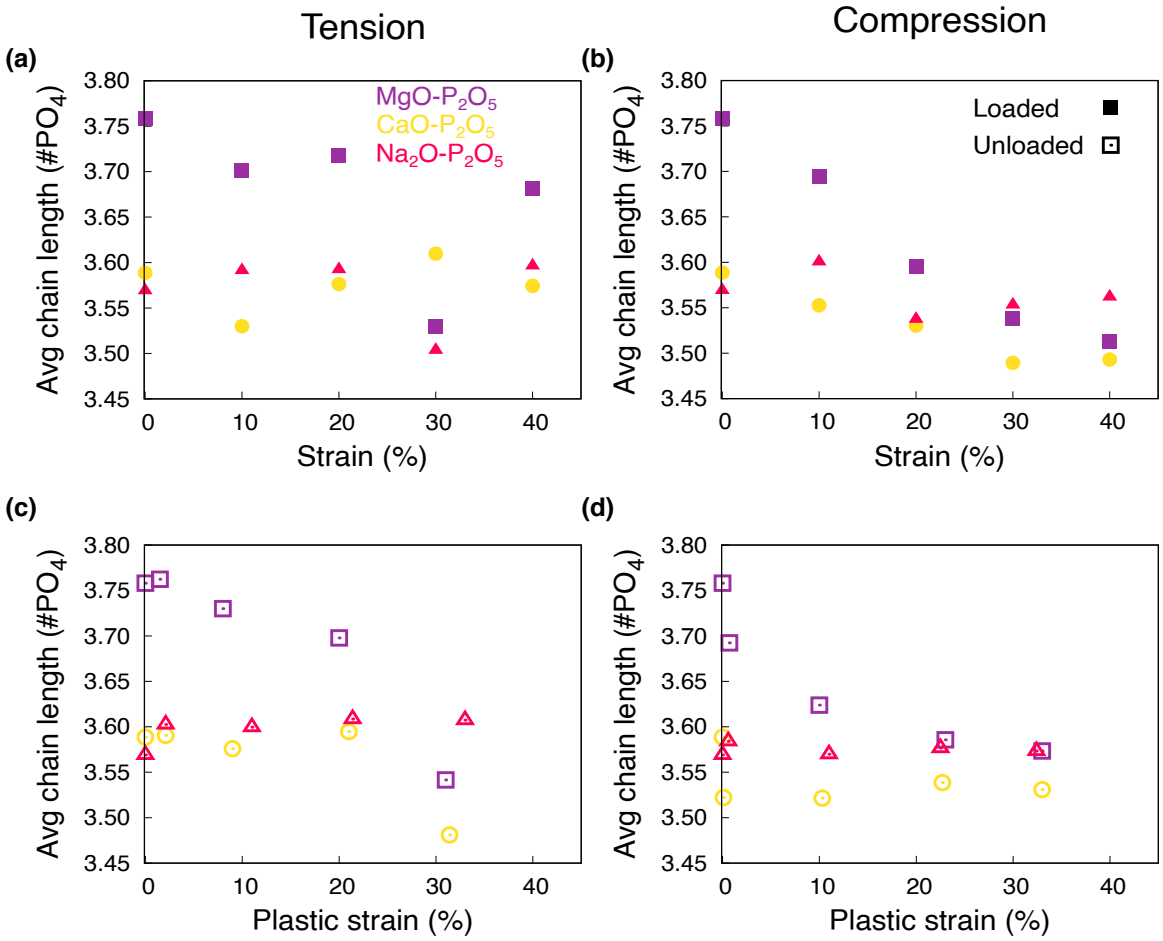

Figure. 4.12: Mean chain length of the three simulated metaphosphate glasses. (a and b) are for configurations extracted at different maximum strains during the loading (close symbols), while (c and d) are for the stress free unloaded configurations from the same maximum strain (open symbols). The glasses were deformed along the $x-$axis at 300 K using a strain rate of $5\times10^8 s^{-1}$.

Structural anisotropy

The change of the structural anisotropy during the deformation was tracked quantitatively by using the same anisotropy index as depicted in Section. 3. The anisotropy index-strain curves during loading and unloading tests are shown in Figure. 4.13a and b for tensile and

compressive loading. The anisotropy index increases during the loading in both tension and compression, proportional to the stress in the elastic regime. Although, after yielding, we observed a decrease of the anisotropy index in both tensile and compressive loading; however, the decrease was more pronounced in the case of tension than the one in compression; this is due to the different deformation mechanisms in these loading modes and will be discussed in later sections. The anisotropy index decreases during the unloading process and reaches its minimum α_p (α_p stands for persistent anisotropy index) when the stress is around 0 MPa. Moreover, when unloading from 2.5% or 5% of the maximum strain, the system's original state is recovered, and no visible differences between the pristine glass and the unloaded one are observed. Additionally, unloading from higher maximum strains ($\epsilon > 8\%$), we observe an apparent increase of α_p. Similar behavior was observed for all glass samples irrespective of the modifier used in the glass. The modifier's effect was observed in the level of the anisotropy achieved, which was also related to the stress level experienced by the samples. For example, the Na_2O-P_2O_5 showing the lowest yield and flow stress values followed by CaO-P_2O_5 and then MgO-P_2O_5, we see similar behavior in the anisotropy index-strain curves.

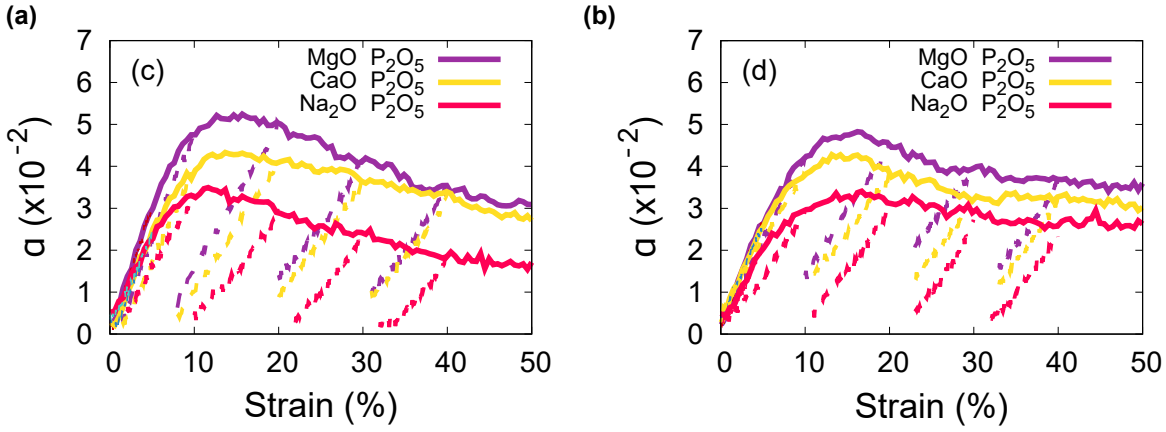

Figure. 4.13: Anisotropy index as a function of the strain during loading (solid lines) along the $x-$axis and unloading (dashed lines) for Na_2O-P_2O_5, MgO-P_2O_5, and CaO-P_2O_5 glasses at 300 K and using a strain rate of 5.0×10^8 s^{-1}. (a) tension and (b) compression.

The results summarizing the behavior of α_p with the plastic strain are shown in Figure. 4.14a and b for tension and compression, respectively. Figure. 4.14 shows that when the glass is plastically deformed, a significant anisotropy persists even after unloading to 0 MPa stress state. The persistent anisotropy values strongly depend on the glass composition, highlighting that by tuning the composition, we can tailor the glass structural anisotropy. Moreover, the values of persistent anisotropy observed do not show a clear correlation with the plastic strain, where they increase with increasing plastic strain up to strains around 20% in tension and 23% in compression and then decrease with further increase of the plastic strain. This indicates a change in the glass structure which is further discussed in the coming chapter. The Na_2O-P_2O_5 as expected showed the lowest persistent anisotropy compared to the other glass samples. The persistent anisotropy observed is quantitatively more pronounced in compression than in tension.

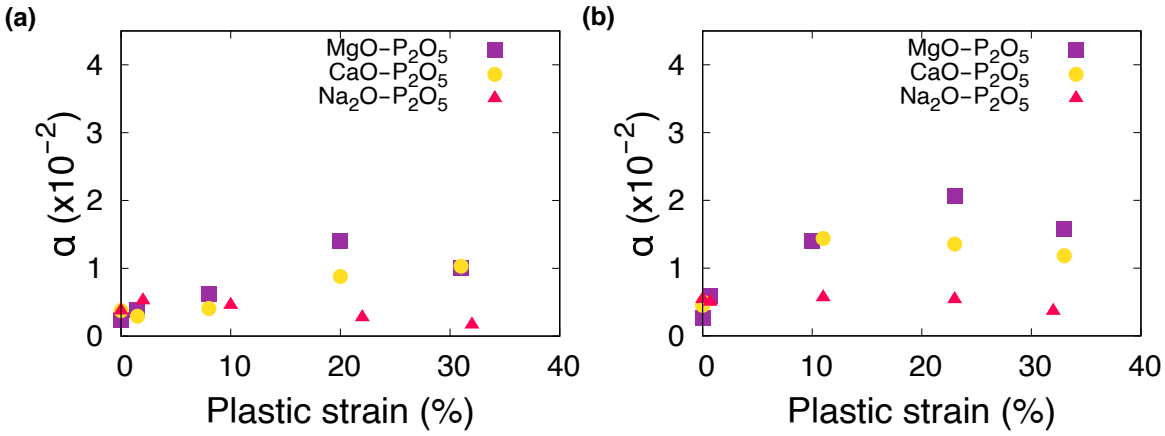

Figure. 4.14: Anisotropy index as a function of the plastic strain for Na_2O-P_2O_5, MgO-P_2O_5, and CaO-P_2O_5. The glasses were deformed along the $x-$axis at 300 K using a strain rate of $5\times10^8 s^{-1}$. (a) tension and (b) compression.

Directional structure

Projected RDF onto spherical harmonics: The comparison between the RDFs and ADFs at different stages of the deformation showed some minor changes indeed. However, no information on the anisotropic structure was obtained. Therefore, these functions can not be used to understand the structure of an anisotropic glass and to highlight the origins of its anisotropy. For these reasons, we refer to the projection of the radial distribution function onto higher-order spherical harmonics. In the case of axial symmetry, as in the case of uniaxial tension and compression, the spherical harmonic Y_2^0 is the most suitable function. The details and equation of the expansion of the RDF on spherical harmonics are found in the Method chapter Section. 3. In Figure. 4.15, Figure. 4.16, and Figure. 4.17, we show the coefficients of the projected RDF on spherical harmonics Y_2^0 of P–O pair in the sodium metaphosphate, magnesium metaphosphate, and calcium metaphosphate glasses. The Figure. 4.15a and b, we compare the projected RDF of the pristine sample with the loaded samples by tension and compression at different load levels. During tension, we observe the presence of two peaks at around 1.48Å and 1.56Å. The peak found at a shorter distance is of negative values, while that found at larger distances is positive. On the contrary, in compression, the peak found at a shorter distance is positive, while that found at a larger distance is of negative values. The position of the peaks is the same as in tension. Another noticeable observation is that the intensity of the peaks increases with increasing strain. The same behavior was found for the other glasses, as shown in Figure. 4.17 and Figure. 4.16. The almost straight line of the pristine glass indicates that the glass structure is isotropic, and no preferential short-range orientation is present in the glass. However, with increasing load, the observed positive peaks indicate that the structure becomes more anisotropic than the pristine glass samples, and a preferential bond alignment is present. The positive peaks indicate that more bonds are found in the direction parallel to the loading axis, while the negative one indicates that more bonds are found in the orthogonal axes to the loading axis. The peaks in tension and compression are reversed.

Figure. 4.15c and d show the projected RDF of the pristine sodium metaphosphate glass with that of the glasses pre-deformed and unloaded from different maximum strains to 0 MPa stress state. After unloading from different maximum strains, no change in the positions of the peaks was observed in the P–O projected RDF; however, their intensity decreased as compared to the loaded systems. The projected P–O RDF shows the same behavior in the sample loaded in compression. The only difference is now the first peak centered around 1.48Å is of positive values, while the one centered on 1.56Å is of negative values. During the unloading from different maximum strains, these peaks persist and show a reduced intensity compared to the loaded samples. These changes are highlighted in Figure. 4.18, where we only focus on the projected RDF of the pristine glass, the sample loaded up to 20%, and unloaded from 20% strain to 0 MPa. The P–P projected RDF given in Figure. 4.19 shows a flat line in the pristine glass and only one peak centered around 3.1Å. This peak is of positive values in tension and is negative in the compressed samples. Like the projected RDF of the P–O pair, the projected P–P RDF peaks persist in the unloaded glasses and show a reduced intensity.

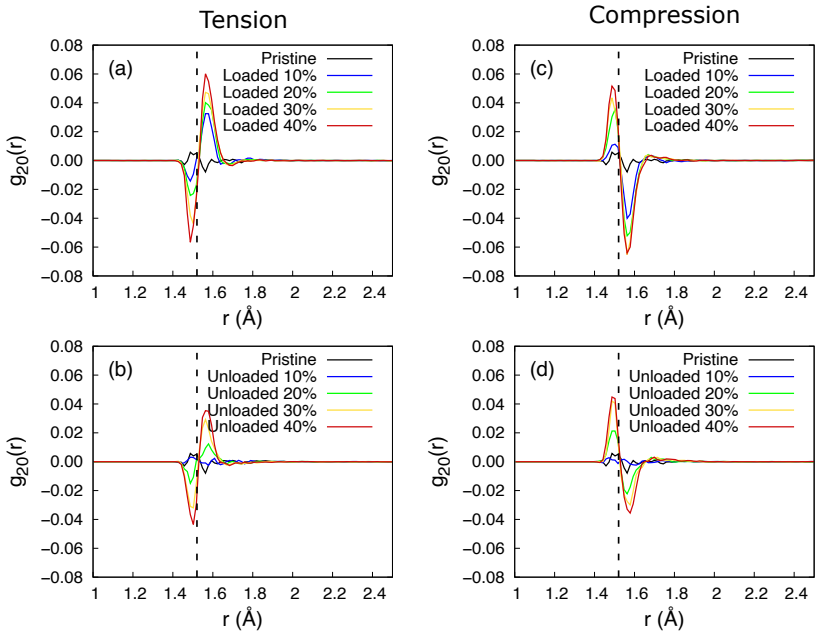

Figure. 4.15: Projection of P–O pair distribution functions on Y_{20} spherical harmonic in Na_2O-P_2O_5 glass. (a - b) corresponds to tensile deformation during loading and unloading, respectively. (c - d) corresponds to compression during loading and unloading, respectively. The inset in the figure (a) show a sketch of Y_{20} spherical harmonic. The glasses were deformed along the $x-$axis at 300 K using a strain rate of $5\times10^8 s^{-1}$.

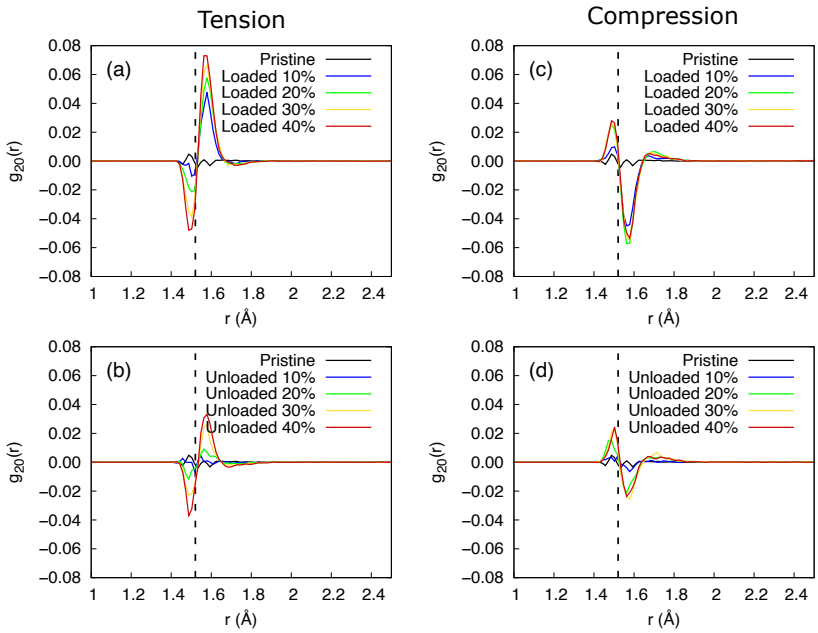

Figure. 4.16: Projection of P–O pair distribution functions on Y_{20} spherical harmonic in MgO-P_2O_5 glass. (a - b) corresponds to tensile deformation during loading and unloading, respectively. (c - d) corresponds to compression during loading and unloading, respectively. The inset in the figure (a) show a sketch of Y_{20} spherical harmonic. The glasses were deformed along the $x-$axis at 300 K using a strain rate of $5\times10^8 s^{-1}$.

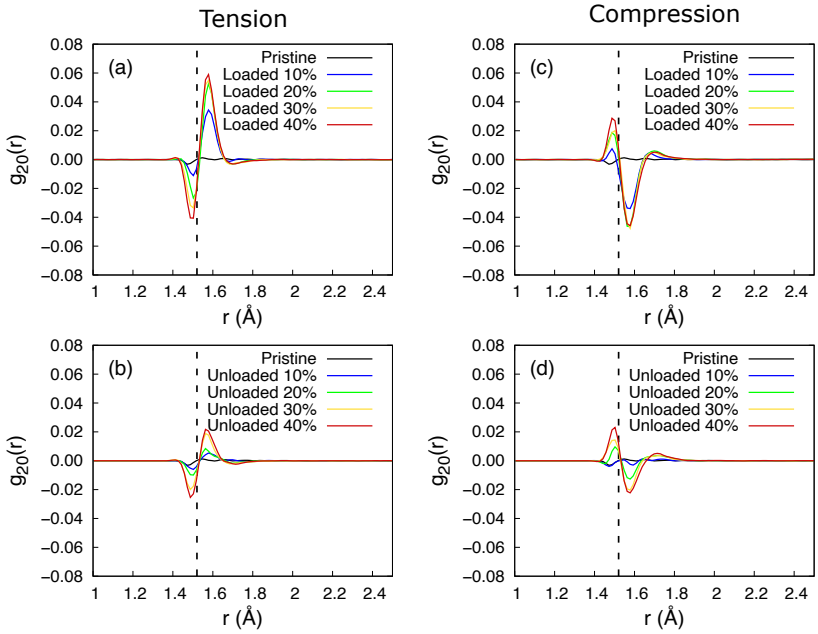

Figure. 4.17: Projection of P–O pair distribution functions on Y_{20} spherical harmonic in CaO-P_2O_5 glass. (a - b) corresponds to tensile deformation during loading and unloading, respectively. (c - d) corresponds to compression during loading and unloading, respectively. The inset in the figure (a) show a sketch of Y_{20} spherical harmonic. The glasses were deformed along the $x-$axis at 300 K using a strain rate of $5\times10^8 s^{-1}$.

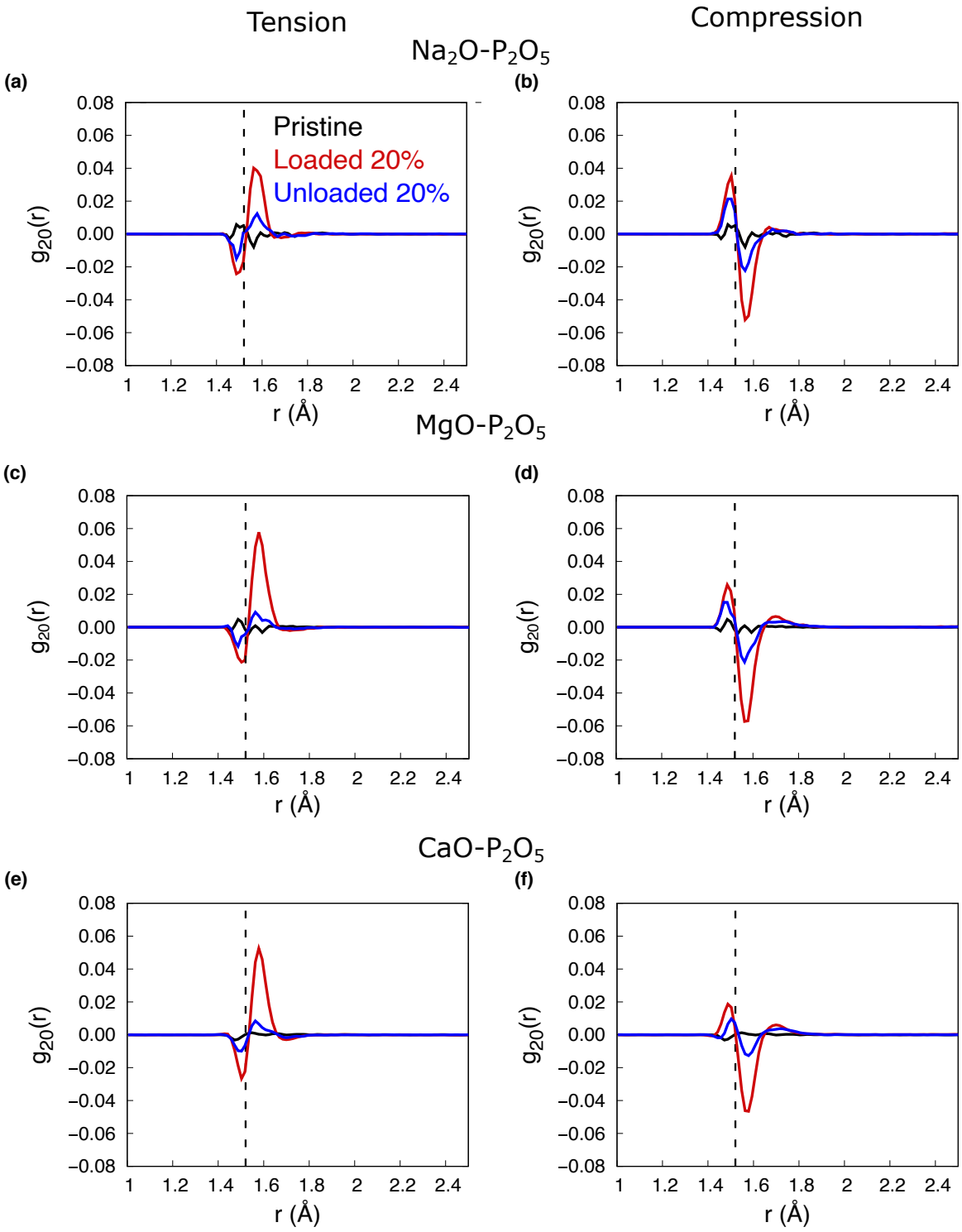

Figure. 4.18: Projection of P–O pair distribution functions on Y_{20} spherical harmonic in (a) Na_2O-P_2O_5, (b) MgO-P_2O_5, and (c) CaO-P_2O_5 glasses. Left column is for tensile deformation and right column is for compressive deformation. The glasses were loaded up to 20% strain and subsequently unloaded to 0 MPa. The dashed lines indicate the position of the mean P–O bond length. The glasses were deformed along the $x-$axis at 300 K using a strain rate of $5\times10^8 s^{-1}$.

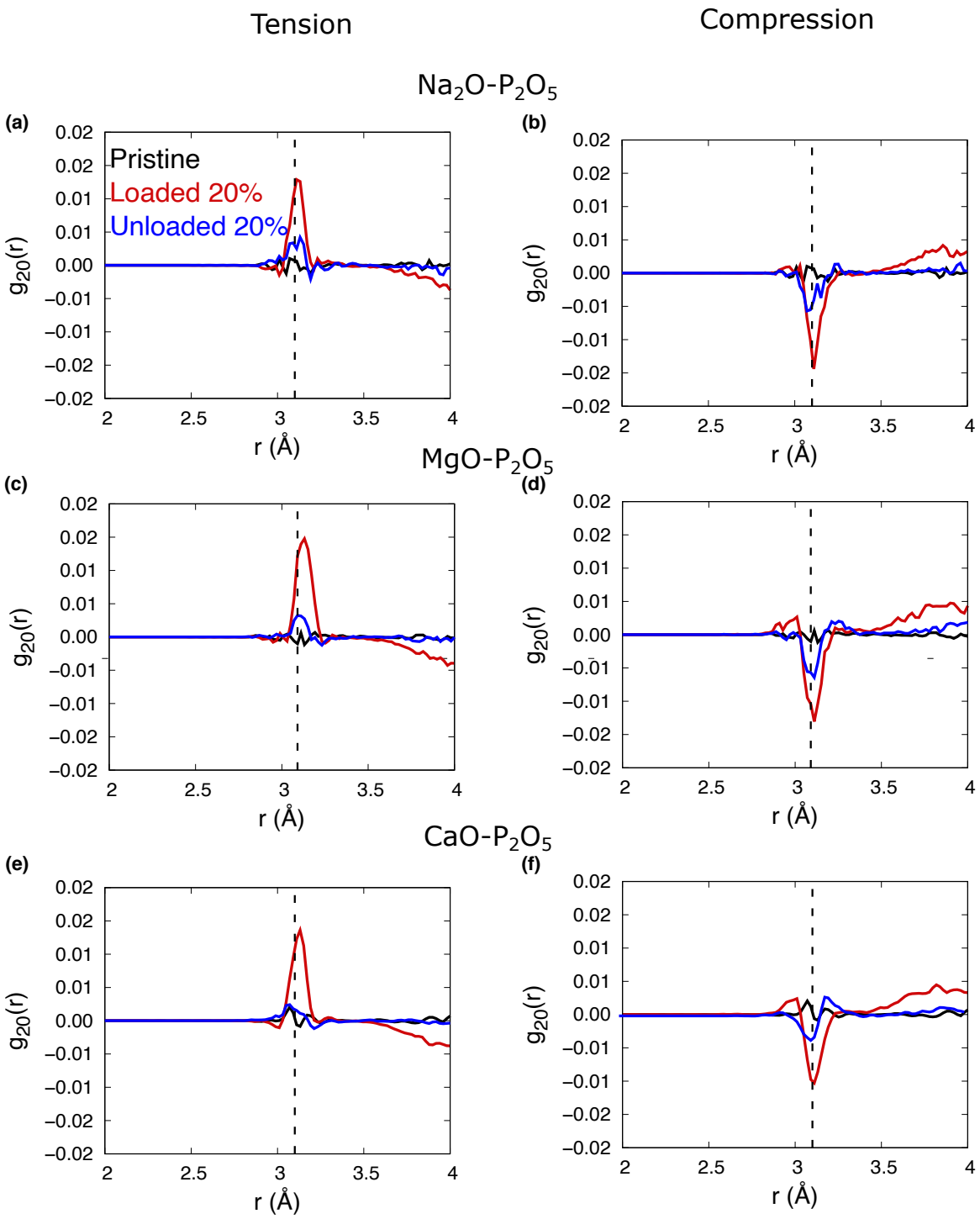

Figure. 4.19: Projection of P–P pair distribution functions on Y_{20} spherical harmonic in (a) Na_2O-P_2O_5, (b) MgO-P_2O_5, and (c) CaO-P_2O_5 glasses. Left column is for tensile deformation and right column is for compressive deformation. The glasses were loaded up to 20% strain and subsequently unloaded to 0 MPa. The dashed lines indicate the position of the mean P–P bond length. The glasses were deformed along the $x-$axis at 300 K using a strain rate of $5\times10^8 s^{-1}$.

Chains orientation: Figure 4.20 shows the mean angle between the chain's end-to-end vectors and the loading axis in the metaphosphate glasses studied in this thesis for the loaded samples at different maximum strains and unloaded samples from different maximum strains in tension, the values of the mean angles are shown as the difference between mean angle found in the pristine glass and the mean angle at a strain ϵ. In Figure. 4.20a, we can see that when deformed in tension, the chains tend to orient themselves to be aligned with the loading axis, as indicated by the decrease of the mean angle between the chain's end-to-end vectors and the loading axis. On the other hand, when unloading from strains within the elastic regime, the chains show no difference in the angles with the loading axis compared to the pristine glass. Moreover, unloading from higher strains, the chains tend to keep their new orientation with the loading axis as shown in Figure. 4.20b.

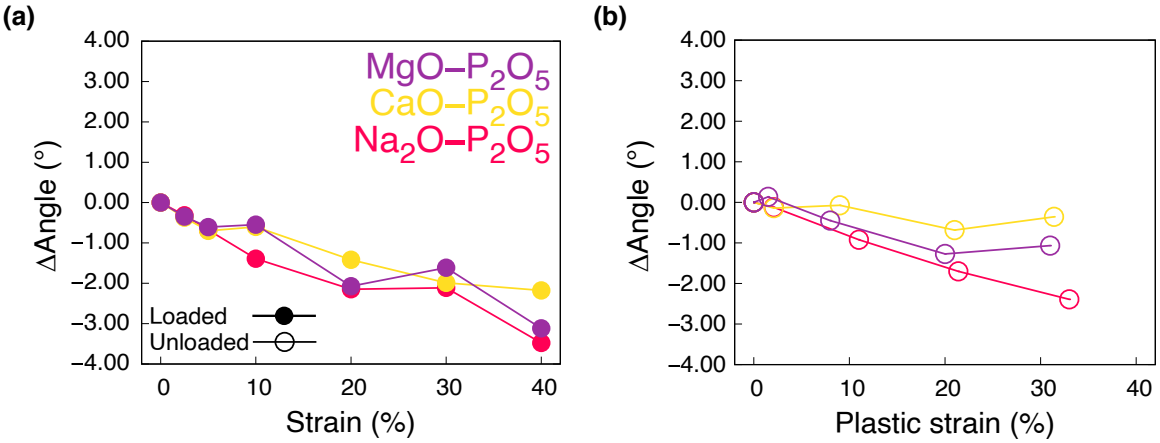

Figure. 4.20: The difference between the mean chains end-to-end vectors angle in the loaded (a) or unloaded (b) glasses in tension and the pristine metaphosphate glasses. The ΔAngle = Angle_L - Angle_P, where Angle_L is the mean angle between the chain end-to-end vectors and the loading axis in the loaded sample and angles_P is the mean angle between the chain end-to-end vectors and the loading axis in the pristine glass. For the loaded sample (a), the mean angle difference is plotted as a function of the strain before unloading. The mean angles difference are plotted for the unloaded samples as a function of the remaining plastic strain after unloading to zero stress. Closed dots denote loaded samples, and open dots stand for unloaded samples. The lines in both figures are guides for the eyes. The glasses were deformed along the $x-$axis at 300 K using a strain rate of $5\times10^8 s^{-1}$.

Figure. 4.21 shows the mean angle between the chain's end-to-end vectors and the loading axis in the metaphosphate glasses studied for the loaded samples at different maximum strains and unloaded samples from different maximum strains in compression, the values of the mean angles are shown as the difference between mean angle found in the pristine glass and the mean angle at a strain ϵ. In Figure. 4.21a, we can see that when deformed in tension, the chains tend to orient themselves perpendicular to the loading axis, as indicated by the increase of the mean angle between the chain's end-to-end vectors and the loading axis. When unloading from strains within the elastic regime, the chains show no difference in the angles with the loading axis compared to the pristine glass. The unloading from higher strains leads to a persistent alignment of the chains with the loading axis, as shown in Figure. 4.21b.

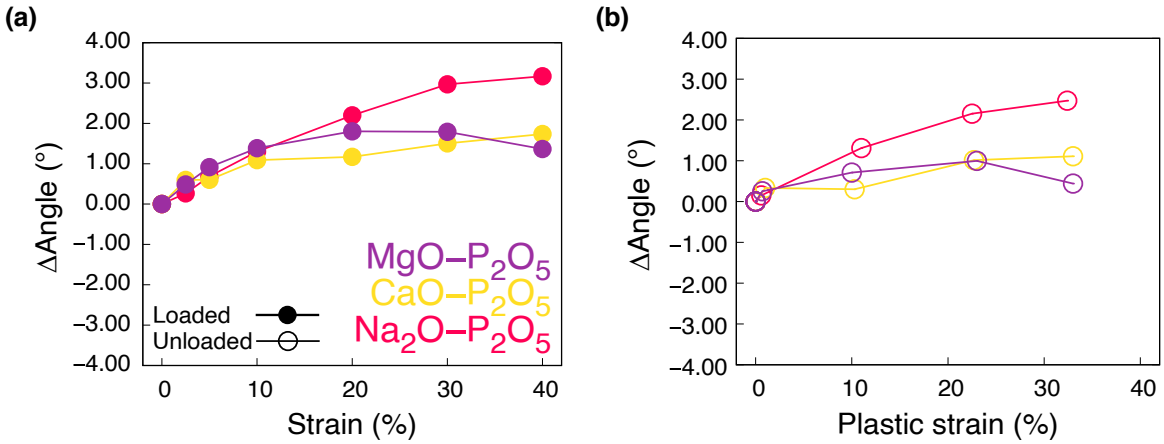

Figure. 4.21: The difference between the mean chains end-to-end vectors angle in the loaded (a) or unloaded (b) glasses in compression and the pristine metaphosphate glasses. The ΔAngle = Angle_L - Angle_P, where Angle_L is the mean angle between the chain end-to-end vectors and the loading axis in the loaded sample and angles_P is the mean angle between the chain end-to-end vectors and the loading axis in the pristine glass. For the loaded sample (a), the mean angle difference is plotted as a function of the strain before unloading. The mean angles difference are plotted for the unloaded samples as a function of the remaining plastic strain after unloading to zero stress. Closed dots denote loaded samples, and open dots stand for unloaded samples. The lines in both figures are guides for the eyes. The glasses were deformed along the $x-$axis at 300 K using a strain rate of $5\times10^{8}\text{s}^{-1}$.

5 Discussion

The upcoming sections are reserved for discussing the structural origins of the deformation-induced structural anisotropy and its influence on the mechanical properties of the metaphosphate glasses. The mechanisms of how the mechanical load at room temperature makes the glass structure anisotropic will also be discussed. We will focus on the effect of the modifier type and loading mode. Also, the effect of the simulation parameters on the mechanical behavior of the pristine glasses will be discussed at the end of this chapter.

5.1 Glass structure

The obtained metaphosphate glass structures as depicted by the RDF, BAD, the oxygen species, Q^n distribution, and the chain length distribution are consistent with previous simulations using similar and different interatomic potentials [176]. Moreover, the data of the P–O, P–NBO, and P–BO bond length, as well as the O–P–O bond angle, are in good agreement with experimental measurements by Hoppe et al. [175]. The values of the P–NBO that is 1.48 Å and that of P–BO 1.56 Å are similar to the ones measured using neutron diffraction [175, 178] where the differences between P–NBO and P–BO obtained from our simulations is 0.08 Å and the one obtained from experiments is 0.1 Å [175]. The calculated P–P bond lengths are around 3.1 Å is a bit higher than the experimentally measured one, which is around 2.95 $\pm$ 0.1 Å [179]; the P–P coordination number from our MD simulation was found to be around 3.1, and the one found experimentally is around 3.0 [180]. The O–O pair distance as obtained from our MD simulations depend on the composition and is around 2.19 Å for Na_2O–P_2O_5, 2.1 Å for MgO–P_2O_5, and 2.18 for CaO–P_2O_5. Experimental values of the O–O pair for the MgO–P_2O_5 were around 2.25 Å as measured by X-Ray diffraction [179], which is a bit higher than the one obtained from our MD results. The M–O bonds length obtained from our MD results were found to be 2.331 Å for Na–O, 2.013 Å for Mg–O, and 2.376 Å for Ca–O. These values are in a good agreement with the ones obtained experimentally where, Na–O is 2.38 $\pm$ 0.3 Å [181, 182], Mg–O is 1.97 $\pm$ 0.2 Å [179, 183], and Ca–O is 2.39 $\pm$ 0.3 Å [181]. The coordination number of the M–O pairs are also consistent with the experimental findings in the literature, where CN_{NaO}^{EXP} is 5.0 $\pm$ 0.4 and CN_{MgO}^{EXP} 4.0 $\pm$ 0.1[179, 184]; and the ones from MD are CN_{NaO}^{MD} = 5.604 and CN_{MgO}^{MD} = 4.35. The mean O–P–O and P–O–P angles were also found to be in good agreement with the experimental data [179]. These similarities between the values obtained using atomistic simulations and the experiments show that the interatomic potential accurately reproduces the simulated glasses' short-range and near medium-range structures at equilibrium and at 300 K.

The number of BO and NBO in the glass gives an overview of the connectivity of the glass and how connected the structure is. Also, the distribution of this NBO per tetrahedron as given by the Q^n species give a picture of the near medium-range structure. The dominant Q^n units are the Q^2 followed by Q^1 and Q^3, with a minor presence of other units. Because we are simulating metaphosphate glasses, the structure should be mainly built by long chains in the form of Q^2 units terminated by Q^1 units. The Q^3 present the intersec-

tion of chains which was also observed in experiments [161]. The presence of the other units, such as Q^4, Q^5, and Q^6 might be due to the high cooling rate used in this work and in MD simulations. This behavior was verified that is due to the cooling rate for silicate glasses, where a decrease of the cooling rate had led to obtaining a glass structure much more consistent with the experimentally observed structure as depicted by the structural parameters such as the Q^n units [65, 185].

Currently, it is impossible to extract the chain length distribution from experiments, and we are not aware of any work that quantitatively extracted the chain length distribution in a metaphosphate glass. However, obtaining the chain length distribution should be possible using glass structures generated by MD simulations and some analysis tools. By removing all atoms from the glass sample except for the phosphorous atoms and using the first minimum of the P–P radial distribution function, we can find linked P atoms, and a succession of P atoms larger than two is considered a chain. The obtained results were found to be in line with the previous simulation of other glasses [24]. The glasses were generally made by chains of length lower than 6 PO_4 units. Moreover, from the chain length distribution, it is a bit hard to extract the differences between the three simulated glasses (See Figure. 4.3a). For this reason, we calculated the mean chain length, which was plotted as a function of the modifier's field strength (See Figure. 4.3b), and we found that the glasses with higher field strength show higher values of the mean chain length. This behavior can be explained by the fact that modifiers with high field strength tend to have a role similar to that of the glass formers [36] and thus stabilizing the glassy network and allowing for the formation of longer chains. The values of the anisotropy index for the pristine glasses were almost zero, suggesting that the melt-quenched glass obtained are isotropic. This isotropic structure was confirmed by the absence of any residual peaks in the projected RDF function.

5.2 Origin of the structural anisotropy

In this section, the changes in the structure when the glasses are subjected to tension or compression are discussed based on the already presented results. The deformations are performed at 300 K, and we will focus only on the samples containing 108000 atoms and deformed using a strain rate of 5×10^8 s^{-1}. During the discussion, we generally distinguish between the structural anisotropy when the samples are under stress *transient* anisotropy and the structural anisotropy in the stress-free unloaded samples, referred to as *persistent* anisotropy. Moreover, the origins of the structural anisotropy in metaphosphate glasses will be discussed in the short-range structure, where we will focus only on the P–O bonding state; and at both near and extended medium-range order, where the linkage between neighboring tetrahedra will be taken into account and also the chain structure.

As shown in the previous chapter, during both tension and compression, the structure exhibit structural transient anisotropy at all structural level, which we mentioned earlier (See Figure. 4.18, Figure. 4.19, Figure. 4.20, and Figure. 4.21). Therefore, the anisotropy index α, as it was calculated using the eigenvalues of the fabric tensor extracted from each neighboring PO_4 tetrahedra, is used to quantify the level of the anisotropy experienced by

the glass. However, the fact that α is a scalar value is not of much help as it will not give us any insights into the directional structure (See Figure. 4.13). For this reason, other analyses were performed to extract directional short- and medium-range structures, such as using the projected RDFs on spherical harmonics and computing the angle between the chain's end-to-end vectors and the loading axis.

The glass showed plasticity in both tension and compression, with higher strength stress in compression than in compression (See Figure. 4.4). The obtained yield stress (strains) in tension are as follows 950 MPa (2.7%), 1808 MPa (3.1%), and 1580 MPa (2.8%) for Na_2O-P_2O_5, MgO-P_2O_5, and CaO-P_2O_5, respectively. However, in compression, the yield stress (strain) was 1011 MPa (2.9%), 1950 MPa (3.4%), and 1760 MPa (3%) GPa for MgO–P_2O_5, CaO–P_2O_5, and Na_2O–P_2O_5, respectively. These differences in the yield stress indicate a tension-compression asymmetry. The stress-strain curves of the metaphosphate glasses during tension and compression during loading and unloading are divided into four main regions. (I) the elastic region, (II) the region between the end of the elastic limit and the maximum stress, (III) the region of flow, and (IV) the unloading regime, including the unloaded stress-free state. Within the first region, if the samples are unloaded, the initial glass structure is recovered on average; the deformation in this region is mainly dominated by P–O bond stretching or contraction and P–O–P bond angle bending. The changes in the P–O bond length, O–P–O, and P–O–P bond angle during tension and compression are summarized in Figure. 5.1 for all glasses and schematically explained in Figure. 5.2. During tension the P–O bond (See Figure. 5.1a) tend to elongate slightly and increases by around 0.0011 Å for Na_2O–P_2O_5, 0.003 Å for MgO–P_2O_5, and 0.002 Å for CaO–P_2O_5. Within the elastic regime, the P–O bond length increases; however, after yielding, the P–O bond length keeps fluctuating around the same value. In the loading during compression (See Figure. 5.1b), the P–O bond length behaves differently as it initially decreases in the elastic regime and then increases after yielding and reaches a steady state. In Figure. 5.1c and d, we tracked the change of the O–P–O means angle, and it is obvious that it is almost not affected by the applied strain. Figure. 5.1e and f show the change of the mean P–O–P angle during tension and compression, where in both cases it decreases win increasing strain, although in tension, the values of P–O–P angles increase first until the yield strain, then decreases again. These changes indicate that the O–P–O bond angle is energetically less favorable than changing the P–O bond length or P–O–P bond angles. The change during compression is more visible than during tension, and the sample with the modifier having the highest field strength showed more change of these measured properties.

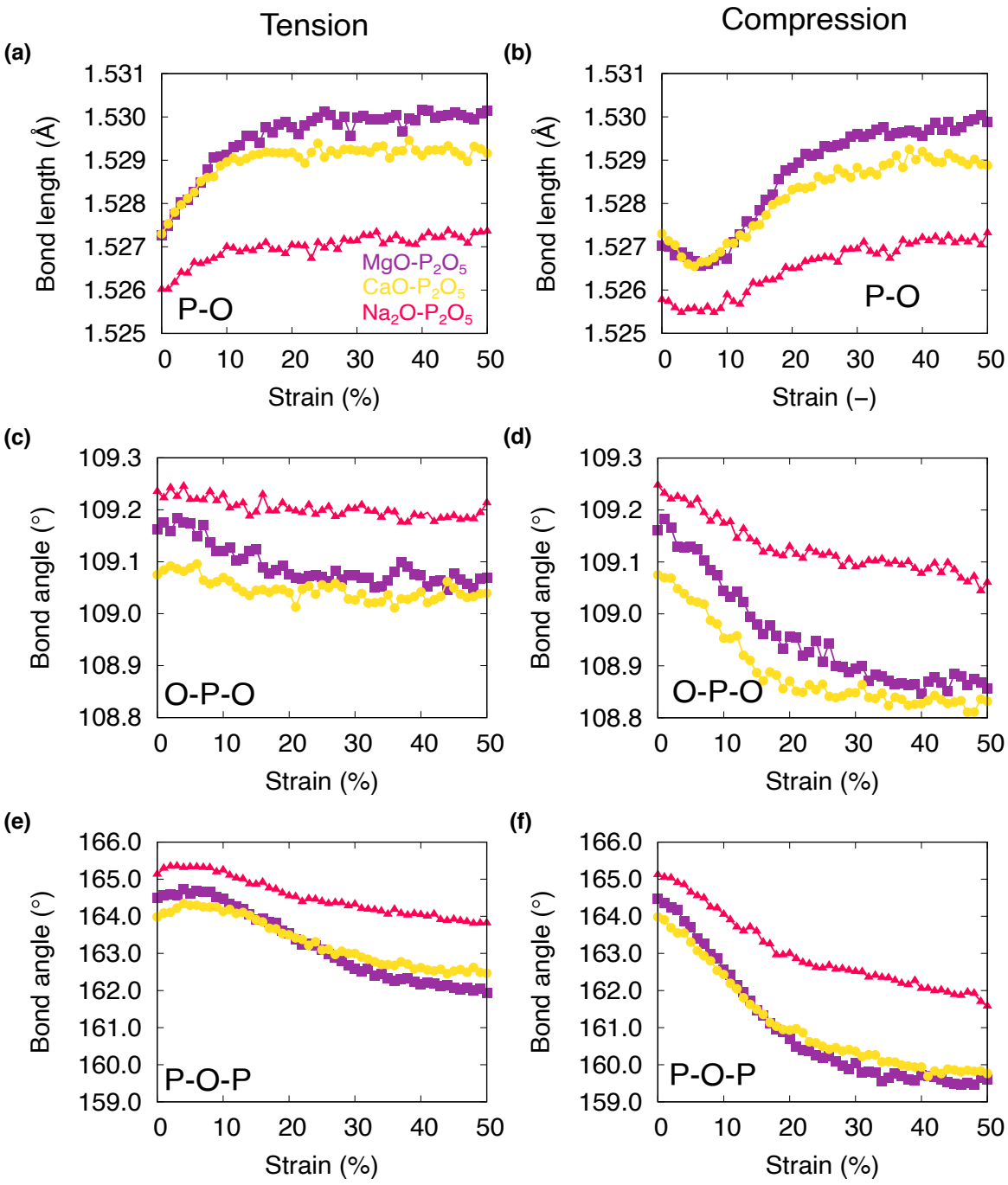

Figure. 5.1: Characterization of the deformation modes of the P–O network during tension (left) and compression (right). The curves present the mean values of the P–O bond length (a) and (b), the O–P–O bond angle (c) and (d), and the P–O–P bond angle (e) and (f). The glasses were deformed along the $x-$axis at 300 K using a strain rate of $5\times10^{8}\mathrm{s}^{-1}$.

However, looking only at the changes in the mean bond length and angle is less insightful as much more happens during the deformation and gives no details about the

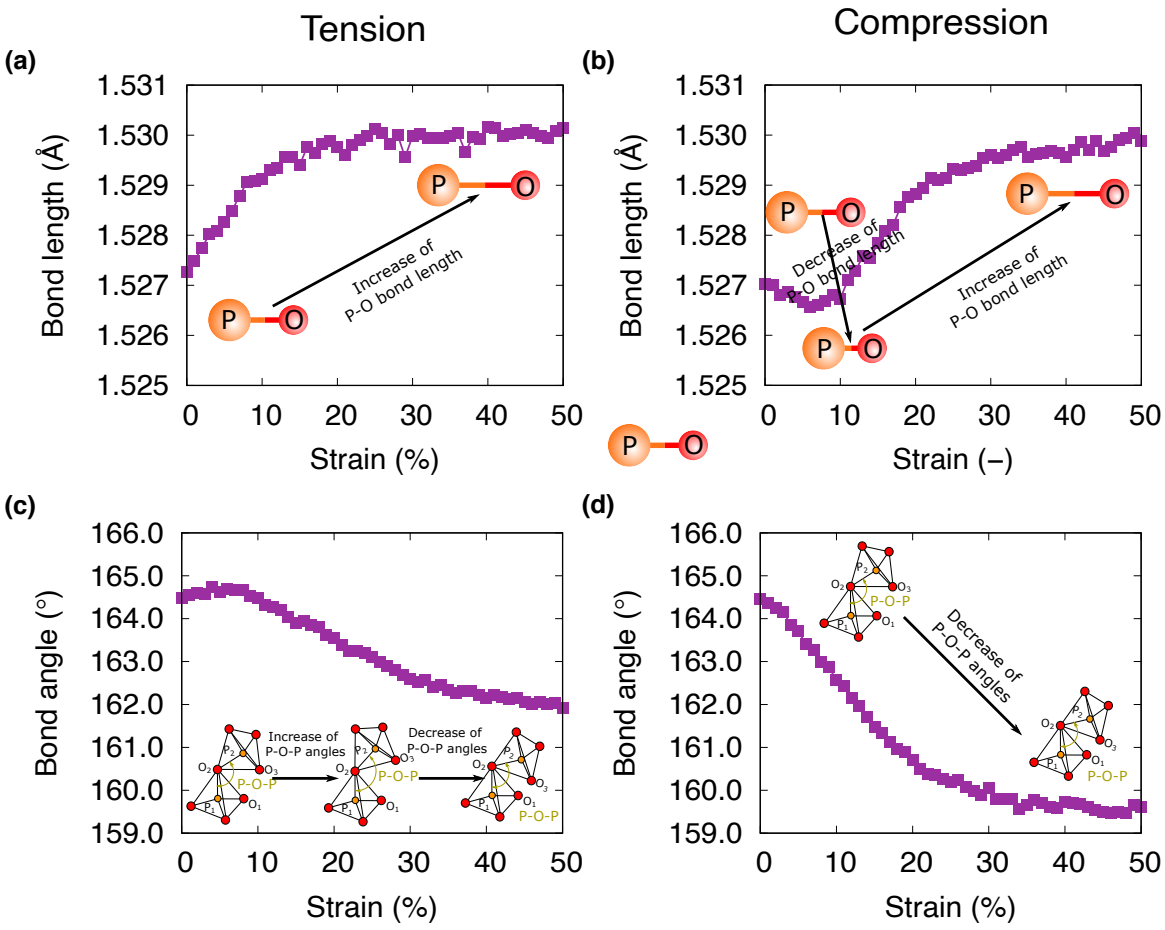

Figure. 5.2: Schematic illustrating the evolution of the averaged P–O bond and P–O–P angles during straining in (a) and (c) tension, and (b) and (d) compression. The schematics are for the magnesium metaphosphate glass but are valid for all metaphosphate glasses studied here. The glasses were deformed along the $x-$axis at 300 K using a strain rate of $5\times10^{8}\mathrm{s}^{-1}$.

anisotropic structure. Within the elastic regime, the shorter P–O bonds, which correspond to the P–NBO (See Figure. 4.1), are perpendicular to the loading axis in tension and are along the loading axis in compression (See Figure. 4.18). On the other hand, the longer P–O bonds corresponding to the P–BO bonds are oriented along the tensile and perpendicular to the compression axis (See Figure. 4.18). The amount of the oriented P–O bond increases with increasing the loading strain in both tension and compression, which highlights that further alignment is happening with strain and is captured using the $g_{20}(r)$ as shown in Figures. 4.15, 4.16, and 4.17. When Unloaded from a specific strain, especially larger strains, some of the already oriented bonds tend to keep their new orientation, leading to an anisotropic short-range bonding where short and long P–O bonds orient themselves in orthogonal to the loading direction depending on the loading mode. This is consistent with the available experimental data [74, 90], which showed that the P–NBO distance is shorter than the P–BO distance in a potassium metaphosphate glass. The fact that the P–NBO bond is perpendicular (parallel) to the tensile (compression) axis is another

evidence that the chains are aligned along (perpendicular to) the tensile (compression) axis (see Fig. 5.3).

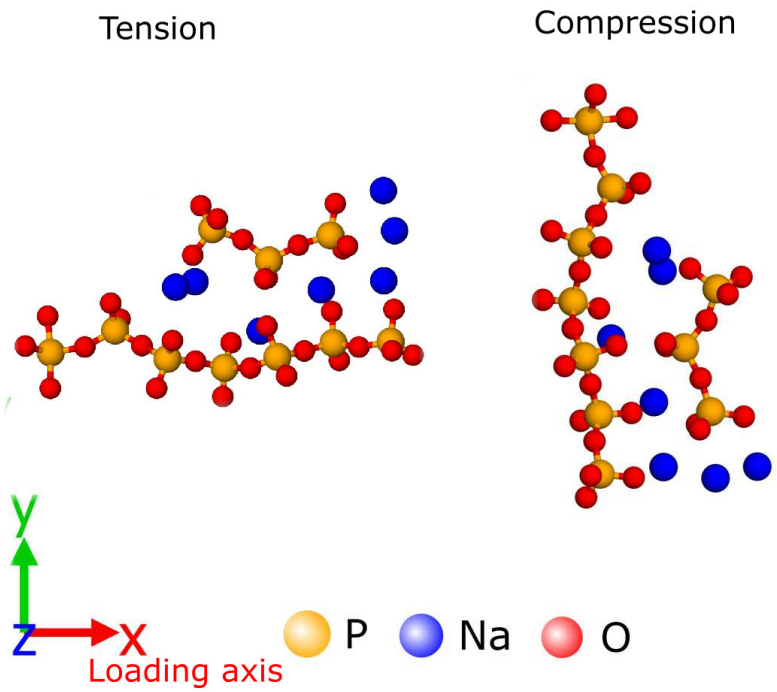

Figure. 5.3: Sketch showing of two selected chains during a tensile (left) and compressive (right) tests of Na_2O–P_2O_5 (red: O atoms, orange: P atoms, and blue: Na). The snapshot shows that weak Na links the chains–NBO bonds perpendicular to the tension loading axis and along the compression axis. In contrast, the strong P–BO bonds are aligned along the deformation axis during tension and perpendicular to the compression. The glasses were deformed along the $x-$axis at 300 K using a strain rate of $5\times10^8 s^{-1}$.

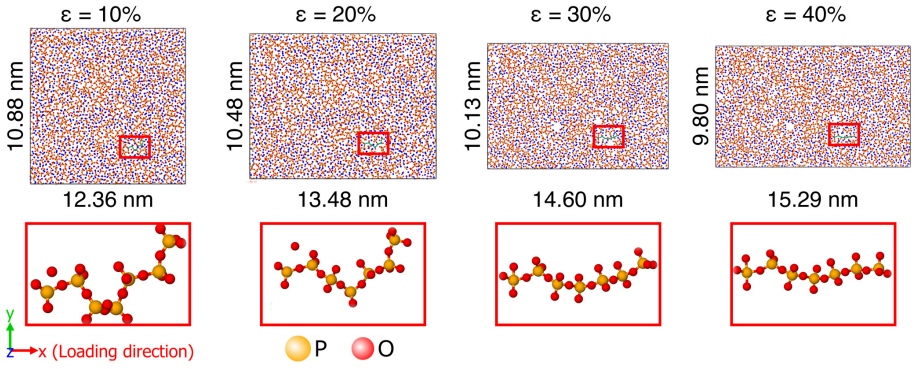

Figure. 5.4: Snapshots at different strains during tensile deformation test of Na_2O–P_2O_5 glass (red: O atoms, orange: P atoms, and blue: Na) and a single chain is highlighted in green in the red box (Top row). The bottom row shows a zoomed-in snapshot of the chain highlighted in the top row and shows that it orients to be aligned with the deformation axis. The glasses were deformed along the $x-$axis at 300 K using a strain rate of $5\times10^8 s^{-1}$.

If we move to the next structural level, we find the near medium-range structure as depicted by the P–P pairs or the separation between the center of two neighboring tetrahedra. Most of the P–P pairs within the first coordination shell tend to be oriented along the loading axis in tension and parallel to it in compression, indicating an anisotropic structure at the inter-tetrahedral level. The metaphosphate glasses are essentially made of –P–O–P– chains, and the orientation of the P–P pairs indicates that the –P–O–P– chains should be aligned along the tensile perpendicular to the compression axis. This is, in fact, the case as shown in Figure. 4.20 and Figure. 4.21, where the mean angle between the chains end-to-end vectors and the loading axis decreases on average by around 5° for the samples loaded in tension and increases around by 5° in the case of compression. The behavior of a selected chain during a tensile test of Na_2O–P_2O_5 glass at 300 K is shown in Figure. 5.4, similar observations are also seen for the other glasses. Moreover, during compression, the chains tend to be aligned along the orthogonal directions to the loading axis (See Figure. 5.3b for a schematic representation). When unloaded from larger strains, the chains tend to keep their orientation and only get reduced by a small value. These explanations are valid for all glasses studied in this chapter. The composition effect affects only the level of the anisotropy observed in the glass or the level of the orientation of the chains, which indeed affect the mechanical properties and will be discussed in the upcoming paragraphs. As a summary of this section, the persistent and transient anisotropy in the metaphosphate glasses are of similar origins and are due to the changes at the tetrahedral level, where the alignments of P–O bonds and P–P pairs lead to an alignment of the -P–O–P– chains. The alignment depends on the loading mode, while its magnitude is strongly influenced by the type of modifier used in the glass. Glasses containing modifiers with lower FS have weaker interchain links, allowing easy orientation and relaxation, resulting in lower levels of structural anisotropy. These results agree with experimental observations where many authors conjectured the alignment of the chains as the origin of the observed optical and mechanical anisotropy in metaphosphate glasses [80, 90]. This indeed helps in tuning the composition to design new functional glasses for advanced applications.

5.3 Mechanical behavior of isotropic and anisotropic metaphosphate glasses

The calculated Young's modulus for the three metaphosphate glasses showed a good agreement with the experimental data reported in the literature [161, 177]. Moreover, the increase of Young's modulus with FS is consistent with previous studies for different glasses [36, 186]. This increase of Young's modulus with FS is linked to the degree of ionicity of the modifier–oxygen bonds, as higher field strength indicates that the bond has a lower ionic character, thus, a higher bond strength [52]. Therefore, the sample with high FS modifiers has tighter bonding and is supposed to show a higher Young's modulus than those containing modifiers with lower FS [36, 80]. Similarly, the yield stress and flow stress increase with increasing FS and are higher in compression than in tension leading to a tension-compression asymmetry. We attribute the observed tension-compression asymmetry in the yield stress and flow stress for all glasses to the orientation mechanism of the chains.

During tension, the chains tend to orient themselves along the loading axis. However, they tend to be perpendicular to the loading axis during compression. This is because the chains are linked to each other through modifier–oxygen bonds, as shown in Figure. 5.3. These bonds can be easily deformed or broken, showing no directionality. Thus, when we perform a tensile test, these bonds break easily, allowing the chains to be oriented parallel to the loading axis and release stress. In contrast to that, during compression, the deformation process starts by reducing the P–O bond length and the P–O–P bond angles, which are more resistant to deformation than the X–O bonds and X–O–X angles [36, 187–189], then the chains reorient to be orthogonal to the compression axis. This leads to higher yield stress and flows stresses in compression than in tension. This is explained by the structure requiring more force to be compressed than stretched. The anisotropy index also shows a tension-compression asymmetry, which is a consequence of the chain orientation and the level of alignment of the chains. Moreover, the persistent anisotropy increased with the plastic strain up to around 20% in tension and around 24% in compression, then it decreased at higher plastic strains. One possible reason for this behavior is that the chains reach their maximum elongation at larger strains and break to form smaller chains. The breaking of these chains leads to structural relaxation indicated by decreased stress in both tension and compression.

Now having established the fact that the anisotropic metaphosphate glasses can be produced using MD simulations and that the –P–O–P– chains exhibit specific orientation with respect to the loading axis, we now focus on exploring whether these details can be used to decipher the mechanisms of the deformation of metaphosphate glasses. The Young's modulus and yield stress of the pre-deformed glasses showed an anisotropic behavior. Experimental findings on highly anisotropic metaphosphate glasses produced through wire drawing showed that the young's modulus calculated along the wire drawing is higher than that along the orthogonal direction to it [80]. Our results of these metaphosphate glasses pre-deformed at room temperature showed similar behavior (See Figure. 4.6a and b), where Young's modulus of the glasses pre-deformed in tension and reloaded in tension showed higher values when measured in the same direction as the pre-loading. The young's modulus and yield stress decreased with increasing plastic strains. The decrease of these macroscopic properties compared to the pristine glasses is linked to the fact that there is a residual plastic strain after unloading the glasses. This plastic strain is due to the stretched chains for the pre-deformation in tension or chains oriented perpendicularly to the loading axis in pre-compression, as shown by the snapshot in Figure. 5.3. Therefore, the samples pre-deformed in tension were expected to show higher Young's modulus and yield stress than those pre-deformed in compression. This is also linked to the bond strength; the P–O bond has a higher strength than the modifier–O bonds [188, 189]. Therefore, when the chains are aligned along the deformation axis and when a tensile test is performed, we will be stretching the P–O bond more than the modifier–O bond, while when the chains are oriented in a perpendicular direction to the tensile axis, the modifier–oxygen bonds are stretched, and the glass is easily deformed. As a result, Young's modulus and yield stress show higher values for the glasses pre-deformed in tension than those pre-deformed in compression.

5.4 Effect of the simulation parameters

Molecular dynamics simulations enable us to study the properties of the materials at an atomic scale, where mechanistic understanding can be achieved by tracking atomic movement. However, MD simulations are limited by the time and scale that can be adequately simulated. Hence, it is essential to check that the studied properties and the obtained mechanisms are not dependent on the simulation parameters, such as the system size, cooling rate, strain rate, etc. Moreover, some properties of glasses do not show a strong size dependency, or they are size-independent, e.g., short-range structural properties. In the following section, we will discuss the influence of these parameters on the deformation behavior of sodium metaphosphate glasses. The observations, discussion, and conclusions also hold for the other metaphosphate glasses.

System size

To check for the effect of the system size on the mechanical behavior of sodium metaphosphate glass and boundary effects. In contrast to the structural properties that can be studied using a few thousand atoms, the mechanical properties, especially the fracture behavior, strongly depend on the samples' size. This is because these properties do not depend on local events only but also on the collective processes that include atoms beyond the first coordination shells [91]. Three sodium metaphosphate glasses with different sizes were simulated using MD simulations and cooled using the same cooling rate of 1 K/ps. The samples contain 54000, 108000, and 216000 atoms. After the cooling and the low-temperature equilibration, the pristine glasses were subjected to tensile and compressive deformations using 5×10^{8} s^{-1} as a strain rate. The results that compare the three different sizes are shown in Figure. 5.5. The results do not show any finite size effects for the studied system sizes. The elastic regime was found to be independent of the size of the simulation box. Moreover, no fracture was observed for all sample sizes up to 50% strain. Minor differences were observed in the values of the flow stress in tension. The stress drop is also observed during compression, not dependent on the system size for the sizes studied here. The fact that the samples deform plastically can be related to the presence of the Na atoms, making the glass more flexible than pristine glass.

Cooling rate

Another parameter that affects the mechanical behavior of glasses is the cooling rate. Glasses with different thermal histories are mainly cooled using two cooling rates, which are 10^{12} K/s and 10^{13} K/s. The sample size used for the cooling rate study contained 108000 atoms. The cooling procedure is the same as the one described in Sec. 3. Due to the limited time scale in MD simulations, it is commonly known that higher cooling rates are used during the cooling simulations [35, 40]. The influence of the cooling rate on the deformation of sodium metaphosphate during tension and compression is shown in Figure. 9.22. The stress-strain curves of the samples cooled using the above-mentioned cooling rates. We observed that there is an increase in the elastic regime for lower cooling rates, and higher

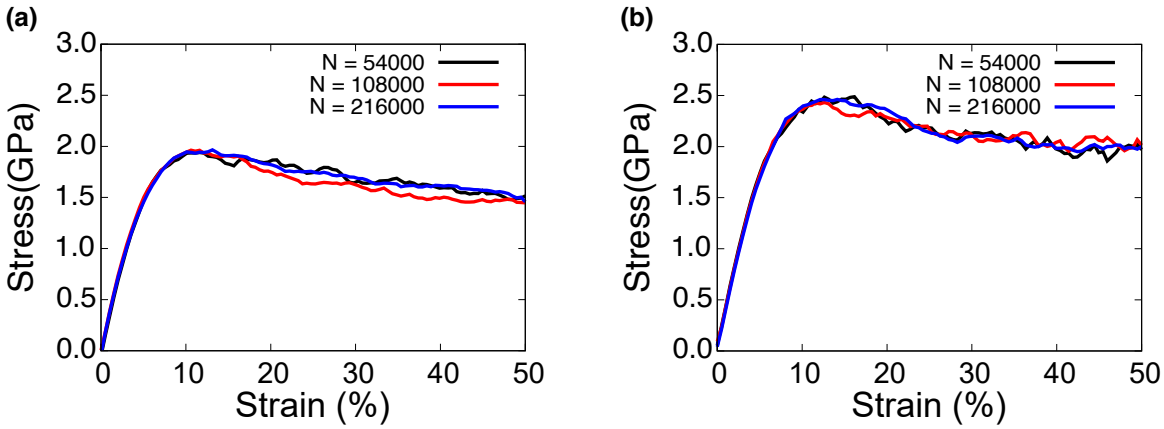

Figure. 5.5: Tensile (a) and compressive (b) stress-strain curves of sodium metaphosphate glass of different sizes deformed along the $x-$axis at room temperature, using a strain rate of $5\times10^{8}s^{-1}$. Theses samples used for these deformation are cooled using 1 K/ps as a cooling rate.

values of the strength were measured, 2.0 GPa for 10^{12} K/s and 1.7 GPa for 10^{13} K/s for the glasses deformed in tension. Same observations were also seen for the compressive loading, where there is a reduction in the elastic regime and an increase of the maximum stress obtained with decreasing the cooling rate, i.e., 2.5 GPa for 10^{12} K/s and 2.3 GPa for 10^{13} K/s. Moreover, the tension-compression asymmetry was also observed in the cooled using different cooling rates. It is worth stressing that the results obtained using different cooling rates are in good agreement with the data obtained for other glasses and using a wider range of cooling rates [91].

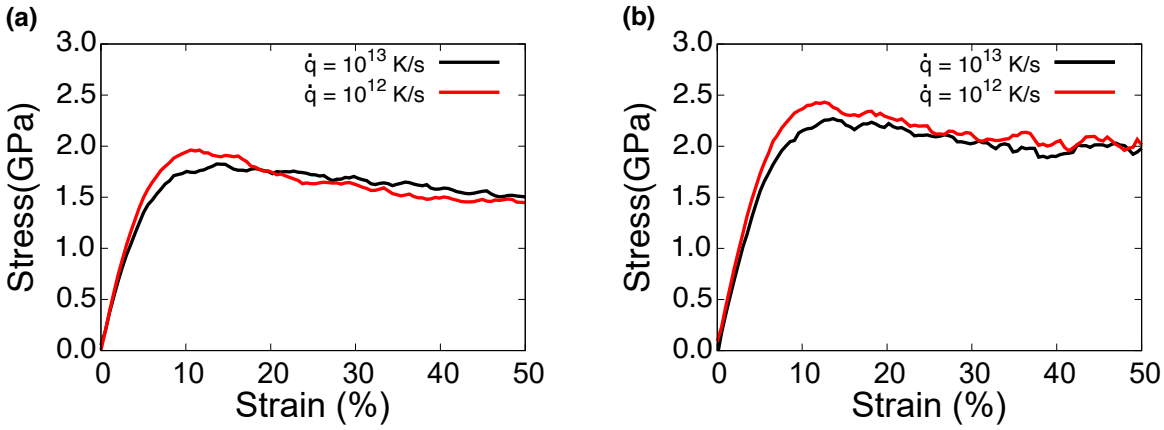

Figure. 5.6: Tensile (a) and compressive (b) stress-strain curves of sodium metaphosphate glass deformed at room temperature, using different strain rates. The sample used for these deformations is the sample containing 108000 atoms and cooled using 1 K/ps as a cooling rate.

Deformation temperature

Similar to previous sections, the sodium metaphosphate glass containing 108000 atoms was used to investigate the mechanical behavior of the glasses at different temperatures. The glasses were prepared using 10^{12} K/s as a cooling rate and deformed in tension and compression using a strain rate of 5×10^{8} s-1 at different temperatures, i.e., T_1 = 300 K = 0.29 T_g , T_2 = 500 K = 0.48 T_g, T_3 = 700 K = 0.67 T_g, and T_4 = 900 K = 0.86 T_g all these temperature are bellow T_g, with T_g = 1040 K $\pm$ 20 K. Generally speaking, brittle materials becomes more ductile with the increase of the temperature [91]. The effect of the temperature on the stress-strain curves during tension and compression is shown in Figure. 5.7 for the sodium metaphosphate glass. As seen for both tension and compression, the elastic regime becomes smaller with increasing temperature. The maximum stress also decreases with increasing the deformation temperature, and the tension-compression asymmetry is still present at higher deformation temperatures. Moreover, the flow stress at larger strains decreases with increasing temperature, and the stress drop disappears with the increase of the deformation temperature. The above-observed behavior can be explained by considering the atomic movement and reorganization of the glass network. With the increase of the deformation temperature, atoms start to move very fast and have enough kinetic energy to jump higher energy barriers, thus escaping from their local constraints defined by the surrounding environment. This diffusion enables structural rearrangements that weaken the bond, and from another side, the glass can accommodate a larger deformation.

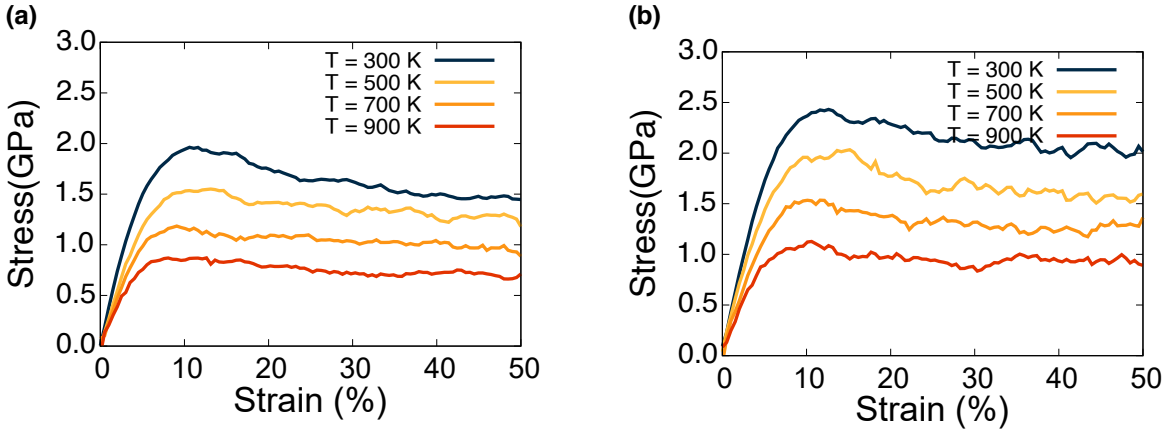

Figure. 5.7: Tensile (a) and compressive (b) stress-strain curves of sodium metaphosphate glass at different temperatures bellow T_g. The sample used for these deformation is the sample containing 108000 atoms, cooled using 1 K/ps as a cooling rate, and the deformation rate was fixed at $5\times10^{8}s^{-1}$.

Deformation rate

Another parameter that can affect the mechanical behavior of the materials is the strain rate. In MD simulations of materials deformations, we usually use a strain rate higher than the ones used experimentally by a few orders of magnitudes due to the limited time and computational power. To investigate the effect of the strain rate of the stress-strain curves,

we deformed the sodium metaphosphate glass containing 108000 atoms at 300 K using two strain rates, i.e., 1×10^{9} s^{-1} and 5×10^{8} s^{-1}. The results of uniaxial tension and compression using these strain rates are shown in Figure. 5.8. The elastic regime was unaffected by the strain rate used to perform the deformation in both deformations. However, we observed that the maximum stress achieved was lower for the lower deformation rate. Although the differences are minor, they are in good agreement with the previous observations from both MD simulations of oxide glasses [190] and experiments [191]. The observed change in the maximum stress can be explained by the fact that by using high strain rates, the structure will not have enough time to adapt to the applied strain, and higher stresses will be achieved as the time for stress relaxation is not enough [190].

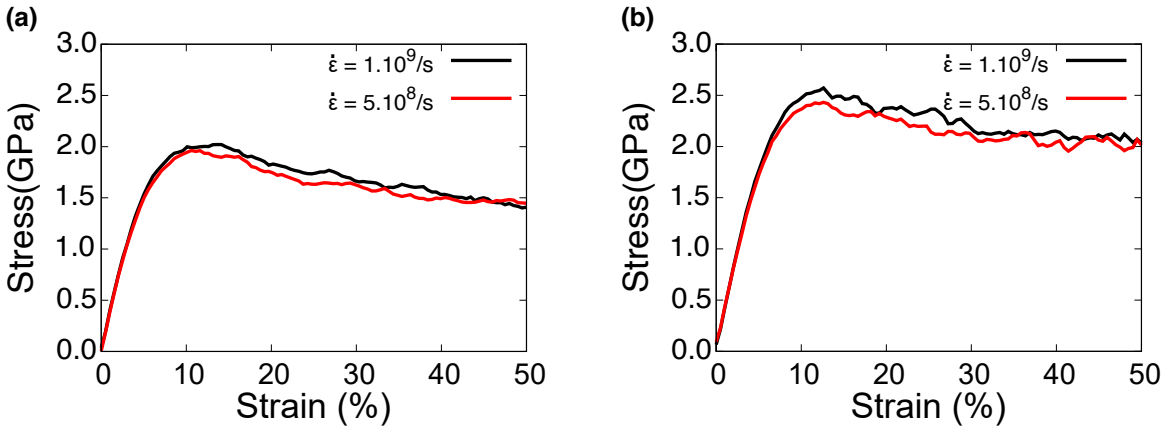

Figure. 5.8: Stress-strain curves of sodium metaphosphate glasses deformed with different strain rates. The sample used for these deformation is the sample containing 108000 atoms and cooled using 1 K/ps as a cooling rate. The stress-strain curves were obtained with the application of (a) tension or (b) compression.

6 Conclusions

In this part of the work, the origins of the deformation-induced structural anisotropy and the mechanical behavior of isotropic and anisotropic metaphosphate glasses were studied. The effect of the modifier type on the deformation and structural anisotropy was also investigated. From this work, we conclude that:

- The presence of modifiers with high field strength within the glass network leads to higher mechanical properties when compared to the glass with the same low field strength modifiers content. This is because with modifiers having higher field strength, the average bond strength of the glass increases. This behavior was nicely observed in our MD simulations.
- The origin of the structural anisotropy was discussed at different levels. At the short-range structure, this structural anisotropy originates from the P–O bonds' alignment that depends on the loading mode (tension or compression). The P–NBO bonds are perpendicular (along) the tensile (compression) axis, while P–BO bonds are along (perpendicular) to the tensile (compression) axis. The next structural level involving neighboring tetrahedra is captured by the orientation of the P–P bonds, which are oriented along the tensile axis and orthogonal to the compression axis. These short-range alignments of the P–O and P–P bonds lead to the changes at the medium-range order as captured by the orientation of the chains to be along the tensile axis and orthogonal to the loading axis.
- The transient and persistent anisotropy observed in all glasses were shown to have the same origin but with different intensities. When unloaded from different maximum strains, the P–O bonds and chains tend to keep their orientation, leading to persistent structural anisotropy in the stress-free pre-deformed glass.
- Persistent anisotropy is more pronounced after compression than after tension because larger flow stresses were achieved in compression than in tension.
- Glasses containing higher field strength modifiers showed more anisotropy than the glasses containing low field strength modifiers.
- The mechanical behavior of the anisotropic glasses was also evaluated. It showed that Young's modulus in anisotropic glasses obtained by either pre-tension or pre-compression is lower than the pristine glass due to stretching the structure as indicated by the remaining plastic strain. Furthermore, the glasses where the anisotropy was induced by pre-tension showed a higher Young's modulus than the glasses where the anisotropy was induced by pre-compression when measured in the same direction as the pre-deformation.

7 Outlook

In an open chain-like glass, i.e., metaphosphate glasses, we demonstrated that the observed transient and persistent anisotropy at room temperature have the same origin but different intensities. When unloaded from different maximum strains, the P–O bonds and chains tend to keep their orientation, leading to persistent structural anisotropy in the stress-free pre-deformed glass. Furthermore, the modifiers were shown to strongly influence the transient and persistent anisotropy level. A complete picture of the effect of different oxides on structural anisotropy is still missing.

Understanding the origins of the structural anisotropy in a modifier-free mixed glass former glasses and glass with different modifiers (mixed modifier effect) should be a must to obtain a clear picture of the origins of the anisotropy and the effect of each oxide on it. This will include studying glasses with mixed structural units such as rings and chains. This can be achieved by varying the modifier content from a rings-based structure to a chain-based structure, passing by mixed rings and chains structures with different dominance. Furthermore, the effect of the glass former on the anisotropy can be done by studying the deformation-induced anisotropy in pure glasses formers, i.e., SiO_2, GeO_2, B_2O_3, P_2O_5, ... Also glasses containing two or more glass former should be interesting to investigate such as phopshosilicate, or borosilicate glasses.

Part II

Silicate glasses

8 Results

The deformation behavior of pure silica and binary sodium silicate glasses under tensile, compressive, and shear loading was investigated using large-scale molecular dynamics simulations. The samples were prepared following the protocol described in Chapter. 3. All samples contain 375000 atoms initially placed in cubic boxes to match the experimental density (See Table. 3.2) and cooled using 1 K/ps as a cooling rate. The effect of the pre-deformation mode on the tensile deformation behavior of silica and silicate glasses is investigated.

8.1 Structure of pristine silicate glasses: effect of sodium content

The glass transition temperature (T_g) of the simulated sodium silicate glasses decreased with increasing sodium content. The T_g values were measured from the change of the potential energy during the cooling and are defined as the intersection point of the fitted slops at high and low temperatures. The value of T_g of all glasses are as follows with experimental values [192, 193] given between parenthesis: 3000 K (1450 K) for silica glass, 2700 K (863 K) for the sample with 5 mol% of Na_2O, 2510 K (832.4 K) for the sample with 10 mol% of Na_2O, 2350 K (805.1 K) for the sample with 15 mol% of Na_2O, and 2120 K (769.8 K) for the sample with 20 mol% of Na_2O. The T_g values of the simulated samples are given with an error of $\pm$ 20 K. The decreasing T_g values ate consistently with experimental data [192].

The local atomic structure in the studied silicate glasses is investigated using the radial distribution and bond angle distributions. The data for structural properties is obtained at 300 K using 10^{12} K/s as a cooling rate. Figure 8.1a shows the radial distribution function for Si–O pair with changing Na_2O concentration up to 20 mol%. The position of the first peak of this distribution indicates the mean separation distance, which is around 1.61 Å this position is almost independent of the Na_2O concentration present in the glass. In the same figure (Figure. 8.1a), we plotted the cumulative coordination number (CN(r)), which is the variation of the number of O atoms around Si atoms as a function of the distance. The cumulative CN increases with the beginning of the Si–O RDF until it reaches a value around 4.0; then, a plateau is observed and increases again at larger separation distances. The plateau found in the cumulative CN indicates a clear, well-defined first coordination shell with a mean coordination number $\approx$4.0 found at a distance of 2.0 Å. Most Si atoms have four-fold coordination with the presence of some three- and five-fold coordinated Si atoms that are considered as a defect arising from the high cooling rate used to prepare the glass, which is a common type of defect observed in glasses prepared by MD simulations [65, 194].

In Figure. 8.1b, we plotted the O–O RDF, which shows a first peak centered around 2.65 Å, the first minimum around 2.95 Å, and a cumulative CN around ranging from 6.14 for silica glass to 5.49 for sodium silicate glass containing 20 mol% of Na_2O, indicating that each O atom has N O atoms in its first coordination shell. Figure 8.1c shows the Si–Si

RDF and cumulative CN where the position of the first peak is centered around 3.22 Å and can be seen as the separation distance between two SiO_4 tetrahedra. The cumulative CN shows a plateau around a value of 4.0 for silica glass and decreases with increasing Na_2O content. These values are consistent with the fact that with the addition of Na_2O to the glass, the network becomes less connected and the number of neighboring SiO_4 decreases [78, 150]. Figure. 8.1d depicts the Na–O RDFs. The behavior of the Na–O mean separation distance is seen to slightly increase with increasing Na_2O content (See Table. 8.1). Similar to the bond length, the Na–O mean coordination number increases with increasing sodium content, with a mean CN of around 5.21 for the glass containing 5 mol% of Na_2O to 5.56 for the glass containing 20 mol% of Na_2O. The data for the mean separation distance and the mean coordination numbers are given in Table. 8.1.

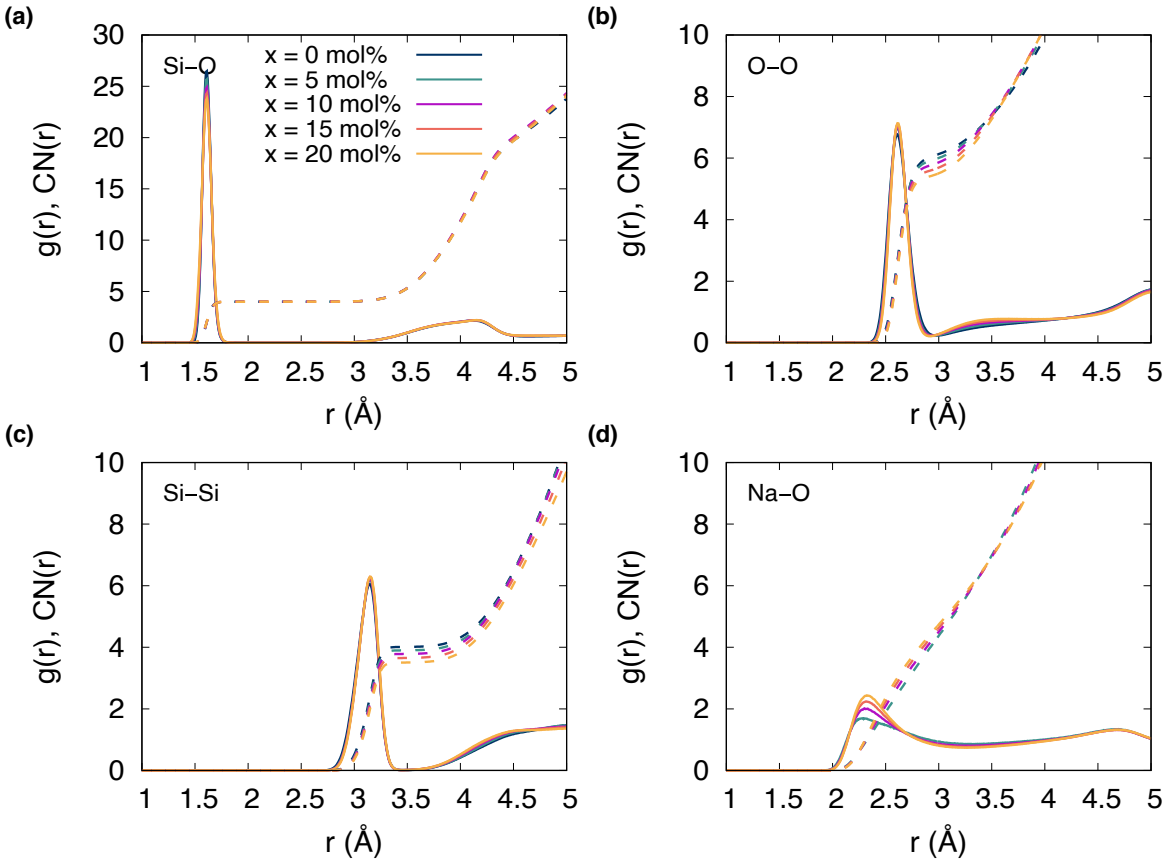

Figure. 8.1: Pair distribution functions (solid lines) and cumulative coordination number (dashed lines) of (a) Si–O, (b) O–O, (c) Si–Si, and (d) Na–O, for all pristine glasses with different Na_2O content at 300 K prepared using a cooling rate of 1 K/ps.

The bond angle distributions (BAD) provide details on the angle in the first coordination shell and neighboring coordination shells. Thus, we can define the shape of the polyhedra that make the glass and the connection among them more precisely. The distributions of O–Si–O angles for all glasses are shown in Figure. 8.2a, where we see a well-defined peak at angles around 108.5°. The peak centered around 108.5° clearly shows that the

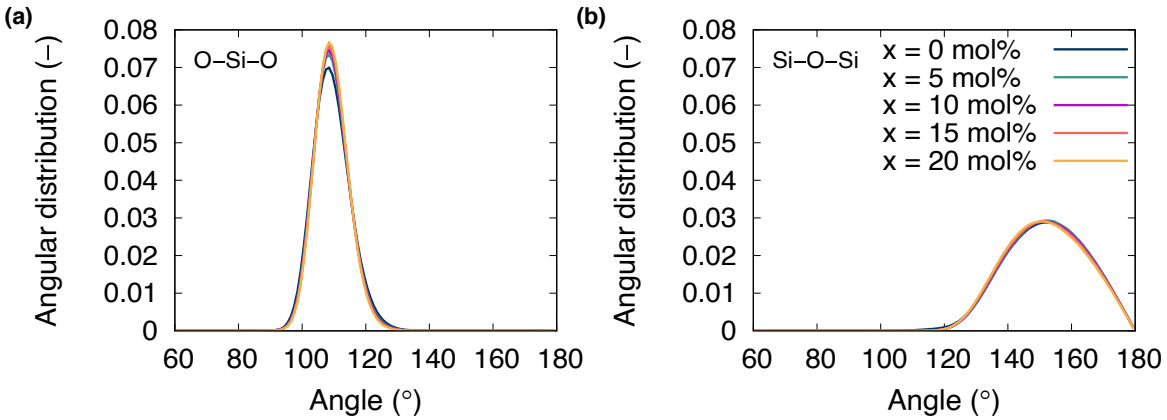

Figure. 8.2: Bond angle distributions of (a) O–Si–O, and (b) Si–O–Si for all pristine glasses with different Na_2O content at 300 K prepared using a cooling rate of 1 K/ps.

Table 8.1: Short-range structural parameters of pristine glasses obtained from molecular dynamics at 300 K and using a cooling rate of 1 K/ps. The cutoffs to calculate the mean coordination numbers were set to 2.0 Å for the Si–O and 3.2, 3.0, and 3.5 Å for the Na–O, O–O, and Si–Si pairs, respectively.

x (mol%)	Si–O		Na–O		O–O		Si–Si	
	r_{ij}	N_{ij}	r_{ij}	N_{ij}	r_{ij}	N_{ij}	r_{ij}	N_{ij}
0	1.609	4.00	—	—	2.610	6.14	3.142	4.019
5	1.608	4.00	2.267	5.21	2.610	5.98	3.149	3.915
10	1.611	4.00	2.308	5.40	2.614	5.83	3.141	3.792
15	1.612	4.00	2.315	5.45	2.614	5.69	3.150	3.665
20	1.611	4.00	2.317	5.56	2.615	5.46	3.153	3.503

local structure of the glasses is mainly built up by SiO_4 tetrahedra. The angle between these tetrahedra is given by the Si–O–Si as shown in Figure. 8.2b, where there is one peak centered on angles around 151° with a broad distribution. This distribution shifts slightly toward lower angles with increasing Na_2O content.

Now we focus on the distribution of the oxygen species, four types of oxygen atoms are generally found in glasses, which are free oxygen (FO), non-bridging oxygen (NBO), bridging oxygen (BO), and oxygen triclusters (TBO) [36]. To find the percentages of NBO and BO, we used the first minimum of the Si–O RDF. The free oxygen and triclusters were not found in our simulated sodium silicate glasses. In Table. 8.2, we present the percentage of NBO and BO as a function of the sodium content. We can see that with the increased sodium content, the percentage of NBO increases while that of BO decreases, indicating depolymerization of the network. This is in good agreement with experiments [195].

The Q^n distribution in silicate glasses gives the probability that a silicon atom is connected to n BO, with n = 0, 1, 2, 3, 4; and in some cases, in the stress-free, as cooled glass, minor n = 5 and 6 might be present within the network and are considered as defects due

to the high cooling rate [65]. The percentage of each Q^n in all glasses studied here is shown in Table. 8.3. For the distribution of the Q^n in sodium silicate glasses, the behavior is a bit different compared to experiments, as it is common always to have more Q^4 than in experiments [196]; however, the general trend is similar and is consistent with other MD simulations using different interatomic potentials [65, 91]. Moreover, the values of Q^n are strongly dependent on the cooling rate used in the glass preparation. Because the differences between the cooling rates used in MD are several orders of magnitude higher than the experimental ones, it should be evident that the depolymerization of the network is different from that observed experimentally. Earlier studies showed for sodium silicate glasses that the percentage of Q^3 increases with decreasing quench rate while that of Q^4 decreases [65].

Table 8.2: Silicon species, NBO, and BO fractions in the pristine glass samples at 300 K and prepared using a cooling rate of 1 K/ps.

x (mol%)	Si^4 (%)	Si^5 (%)	NBO (%)	BO (%)
0	99.850	0.150	0.0	100.0
5	99.823	0.177	5.047	94.954
10	99.839	0.161	10.453	89.579
15	99.871	0.129	16.157	83.843
20	99.899	0.101	22.175	77.825

Table 8.3: Q^n distribution fractions in the pristine glass samples at 300 K and prepared using a cooling rate of 1 K/ps.

Glass	Q^1 (%)	Q^2 (%)	Q^3 (%)	Q^4 (%)	Q^5 (%)
0	0.0	0.0	0.0	99.85	0.150
05	0.00	0.196	09.965	89.663	0.176
10	0.02	1.214	19.585	79.022	0.161
15	0.11	3.198	28.437	68.131	0.125
20	0.44	6.387	35.792	57.286	0.098

8.2 Influence of sodium content on deformation behavior of silicate glasses

Tensile deformation

The stress-strain response of pure silica and sodium silicate glasses containing different sodium content during tensile deformation at room temperature is shown in Figure. 8.3a. The glass exhibited an elastic behavior followed by a sudden stress drop after reaching the maximum stress (see Figure. 8.3a). The elastic modulus of these glasses showed that with the increase of Na_2O content, the glass becomes less stiff, as seen in Figure. 8.3b. The tensile strength σ_{max} is around 11.8 GPa for silica glass, which is consistent with experimental data reported in the literature for silica glass fibers (12.6 GPa) [197] and decreases to around 5 GPa with increasing Na_2O content up to 20 mol%. With the addition of sodium, the fracture behavior shows more plasticity before failing, and the failure strain also increases. The values of σ_{max} and failure strain are in a good agreement with the data in the literature, (σ_{max} = 12.6 GPa, ϵ_f = 0.18) for silica glass fibers [197].As shown in Figure. 8.3a, the glasses show increasing plasticity with increasing sodium content. The sodium silicate glasses show a more plastic behavior compared to SiO_2 or $5Na_2O$–$95SiO_2$ glasses. Unloading simulations starting from different strains to zero stress were performed and are depicted in Figure. 8.3a. The unloading to zero stress has been performed starting from different values of the strain: 2.5%, 10%, and 14% for silica glass and 15% for silicate glasses. In all samples, we observed a remaining plastic strain ϵ_{pl} except for unloading from 2.5% as shown in Table. 8.6.

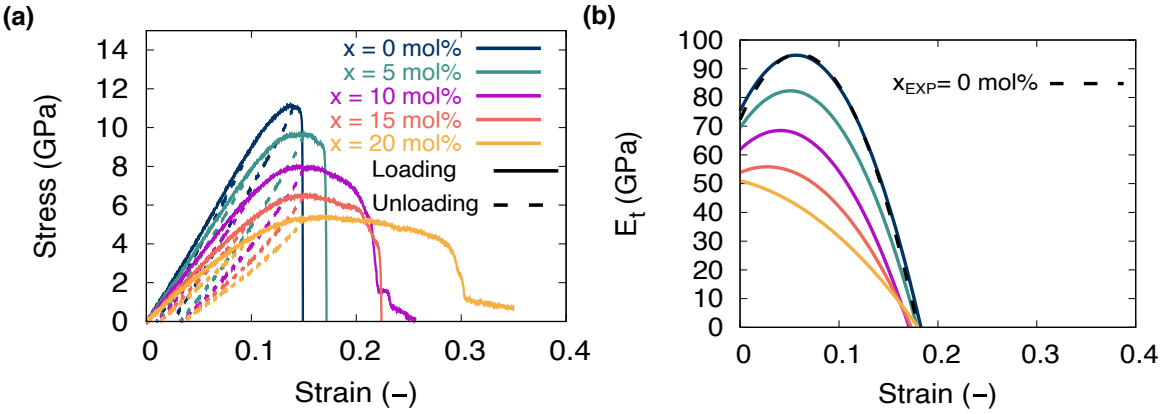

Figure. 8.3: Stress-strain curves (a) of pristine silicate glasses with increasing sodium content subjected to a tensile test along x-axis at 300 K using a strain rate of 10^8 s^{-1}. The dashed lines in (a) stand for unloading curves from different strains. Unloading curves are plotted but not very visible due to the busy plots. (b) Strain-dependent tangent modulus was obtained by fitting the stress-strain curves by a third order polynomial function up to 14% tensile strain (see text for details). The values larger than 14% strain are extrapolated from the equation, and the correlation factor R^2 in all glasses was higher than 0.97. The dashed black curve in (b) shows the experimentally extracted tangent modulus of silica glass fibers [98].

Focusing on the tangent modulus (E_t) shown in Figure. 8.3b and calculated by fitting the

stress strain curves by a third order polynomial function up to a strain equal to 14%. The fitting strain value was chosen to provide the best fit to eq. 8.2. Then a differentiation of the fitted functions leads to the evolution of E_t with strain as in equation 8.1,

$$E_t = \frac{d\sigma}{d\epsilon}, \tag{8.1}$$

where σ is the stress in the deformation direction and ϵ is the strain, the zero-strain limit of E_t results in the values of the Young's modulus as given by equation 8.3.

$$\sigma(\epsilon) = E_0\epsilon + \frac{E_1}{2}\epsilon^2 + \frac{E_2}{6}\epsilon^3, \tag{8.2}$$

$$E = \lim_{\epsilon \to 0} E_t(\epsilon), \tag{8.3}$$

The dependence of E_t on the strain and composition is depicted in Figure. 8.3b where we can see that the composition strongly affects the tangent modulus of silicate glasses. The silica sample compares well with the experimental data from Gupta and Kirkjian [98] (See Figure. 8.3b). For the pure silica glass, E_t increases with increasing strain up to around 7%, then decrease to zero. The tangent modulus showed a maximum of 99 GPa at around 7% from both experiments and our simulations (See Figure. 8.3b). This behavior was observed experimentally by Gupta [98](See Figure. 8.3b) and also from atomistic simulations by Pedone *et al.* [63]. The Young's modulus obtained by Gupta and Kirkjian [98] at zero strain is 72 GPa, which is in good agreement with Young's modulus obtained from our simulations, 75 GPa for silica glass. With increasing sodium content, the hardening observed in the tangent modulus-strain disappears, which is consistent with the data found in the literature [78]. This change in the behavior of the tangent modulus will be discussed in the following sections. The stress-strain curves of sodium silicate glasses with increasing Na_2O content are shown in Figure. 8.3a. The glasses show increasing ductility with increasing sodium content.

Table 8.4: Young's modulus (E) calculated from tension, and compression, shear modulus (G), strength (σ_{max}) in tension , compression, and shear; flow stress (σ_{flow}) in compression and shear, and Poisson's ratio (ν), for the pristine glasses. Experimental values are given in parenthesis.

	Tension		Compression			Shear			
x (mol%)	E (GPa)	σ_{max} (GPa)	E (GPa)	σ_{max} (GPa)	σ_{flow} (GPa)	G (GPa)	σ_{max} (GPa)	σ_{flow} (GPa)	ν
0	79.34 (71.99 [198])	11.13 (12.77 [198])	78.76	7.39	7.21	34.00	6.31	4.15	0.163 (0.16 [199])
5	72.43 (—)	9.7	71.69	6.69	6.51	30.00	5.27	3.84	0.201 (—)
10	65.94 (62.11 [198])	8.01	63.36	5.83	5.68	26.71	4.18	3.46	0.21 (0.18 [199])
15	57.39 (59.06 [198])	6.51	56.96	5.09	4.96	23.21	3.39	3.05	0.232 (0.196 [199])
20	53.15 (57.49 [198])	5.4	52.05	4.43	4.34	21.45	2.84	2.61	0.23 (0.213 [199])

Compressive deformation

The stress-strain response of silica glass subjected to compressive loading is shown in Figure. 8.4. The glass exhibited a non-linear elasticity, then yielded followed by plastic flow up to 50% strain (see Figure. 8.4a). The yield stress in compression calculated using the

0.2% rule was found to be around $\sigma_y = 7.4$ GPa, which is consistent with experimental data reported in the literature for silica glass nanopillars ($\sigma_{y,exp} = 7$ GPa) [120]. Moreover, a small strain hardening was observed due to the densification of the silica glass. The unloading to zero stress has been performed starting from different strain values: 2.5%, 5%, 16%, and 25%. In all samples, we observed a remaining plastic strain ϵ_{pl} except in the case of unloading from 2.5% and 5% as shown in Table. 8.8. In the case of compression, we used the stress over strain instead of the tangent modulus to investigate the non-linear behavior of the stress-strain curves of the silicate glasses. This was plotted as a function of the Na_2O content is in Figure. 8.4b. The behavior of the stress over strain during compression decreases with increasing strain. The effect of Na_2O content shows that the tangent modulus generally decreases with increasing Na_2O content.

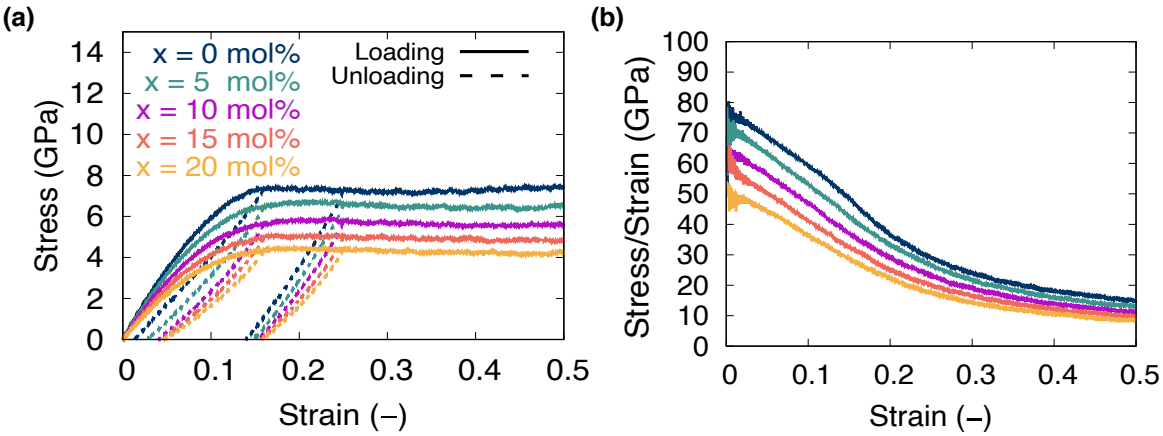

Figure. 8.4: Stress-strain curves (a) of pristine silicate glasses with increasing sodium content subjected to compression along x-axis at 300 K using a strain rate of 10^8 s^{-1}. The dashed lines in (a) stand for unloading curves from different strains. Unloading curves are plotted but not very visible due to the busy plots. (b) Strain-dependent stress over strain is used to highlight the nonlinear stress-strain curves of sodium silicate glasses during compression.

Shear deformation

Results of silica glass under shear deformation will be presented in this section. The s of silicate glasses subjected to shear loading by tilting the y-axis along the x-direction are shown in Figure. 8.5a. The glasses exhibited a linear elastic deformation, then yielding followed by plastic flow up to 50% strain (see Figure. 8.5a). The values of the maximum stress in shear were found to be around σ_{max} is around 6.31 GPa for silica glass and decreases to 2.84 GPa in the glass with 20 mol% of Na_2O. For the pure silica glass, a substantial stress drop was observed immediately after reaching maximum stress, with stress dropping from 6.31 to 4.15 GPa. The stress drop becomes less pronounced with increasing sodium content, and it does not exist in the case of the glass with 20 mol% of Na_2O. Moreover, the stress values after the stress drop for all glasses are close to each other and range from 4.15 GPa for silica to 2.61 GPa for the sample with 20 mol% of Na_2O. The shear moduli were evaluated by fitting the stress-strain curves with a linear function in the small strain regime

(0.5%) and are shown in Table. 8.4; the shear modulus decreases from 34.0 GPa for silica glass to 21.45 GPa for the glass with 20 mol% of Na_2O. The values of the calculated shear modulus are close to the experimental ones [63, 150]. The unloading to zero stress has been performed starting from different values of the strain: 2.5%, 5.0%, 22%, and 33%. In all samples, we observed a remaining plastic strain ϵ_{pl} except in the case of unloading from 2.5% and 5% as shown in Table. 8.10. Similar to compression, the tangent modulus during the shear deformation was extracted by using the same procedure, that is, by dividing the stress over the strain during shear deformation and is depicted in Figure. 8.5b. The stress over the strain in silica glass shows a plateau up to 15% strain, then start to decrease with increasing strain. The addition of Na_2O makes the tangent modulus decrease with increasing strain. This interesting composition dependence tangent modulus will be discussed later.

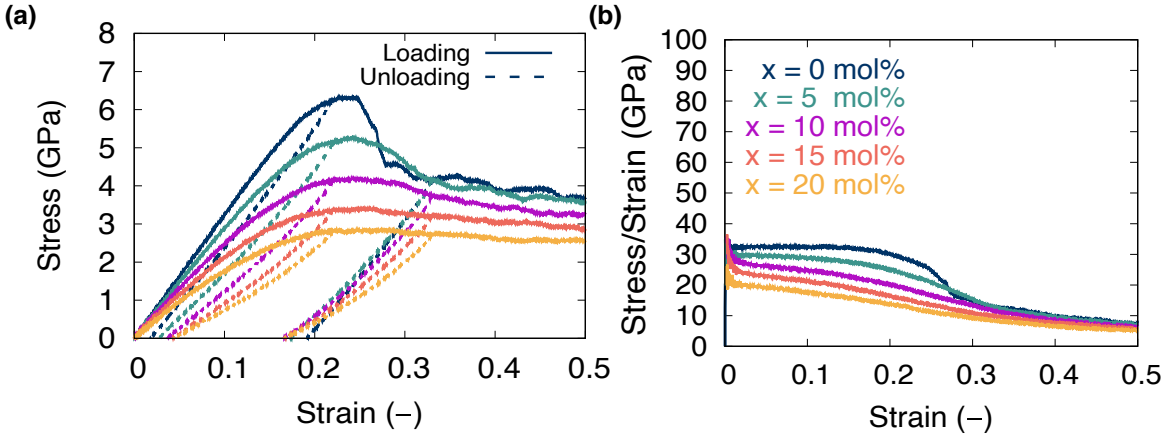

Figure. 8.5: Stress-strain curves (a) of pristine silicate glasses with increasing sodium content subjected to a simple shear deformation by tilting the y-axis along the x-direction at 300 K using a strain rate of 10^8 s^{-1}. The dashed lines in (a) stand for unloading curves from different strains. (b) Strain dependent stress over strain which is used to highlight the non linear stress-strain curves of sodium silicate glasses during shear deformation.

Change of the glass structure during and after the deformation

The deformation of silicate glasses is accompanied by a change in the bonding topology. From knowing that the silicate glass structure, which is made of SiO_4 tetrahedral units, we can distinguish three changes in the structure due to the applied load; these changes can happen individually or at the same time. I) change in the Si–O bond length and O–Si–O bond angle, which results in a distortion of the SiO_4. II) Change of the Si–O–Si bond angle, the angles between two tetrahedra. III) Rotation of SiO_4 tetrahedra usually happens through a bond switching mechanism. From the changes mentioned above in the local structure, one can understand that some of these changes also happen at different deformation stages, and the level of the change will depend on the loading mode.

The results of average Si–O bond length, O–Si–O, and Si–O–Si bond angle calculated as a function of the strain during the different deformation modes and for all glasses are

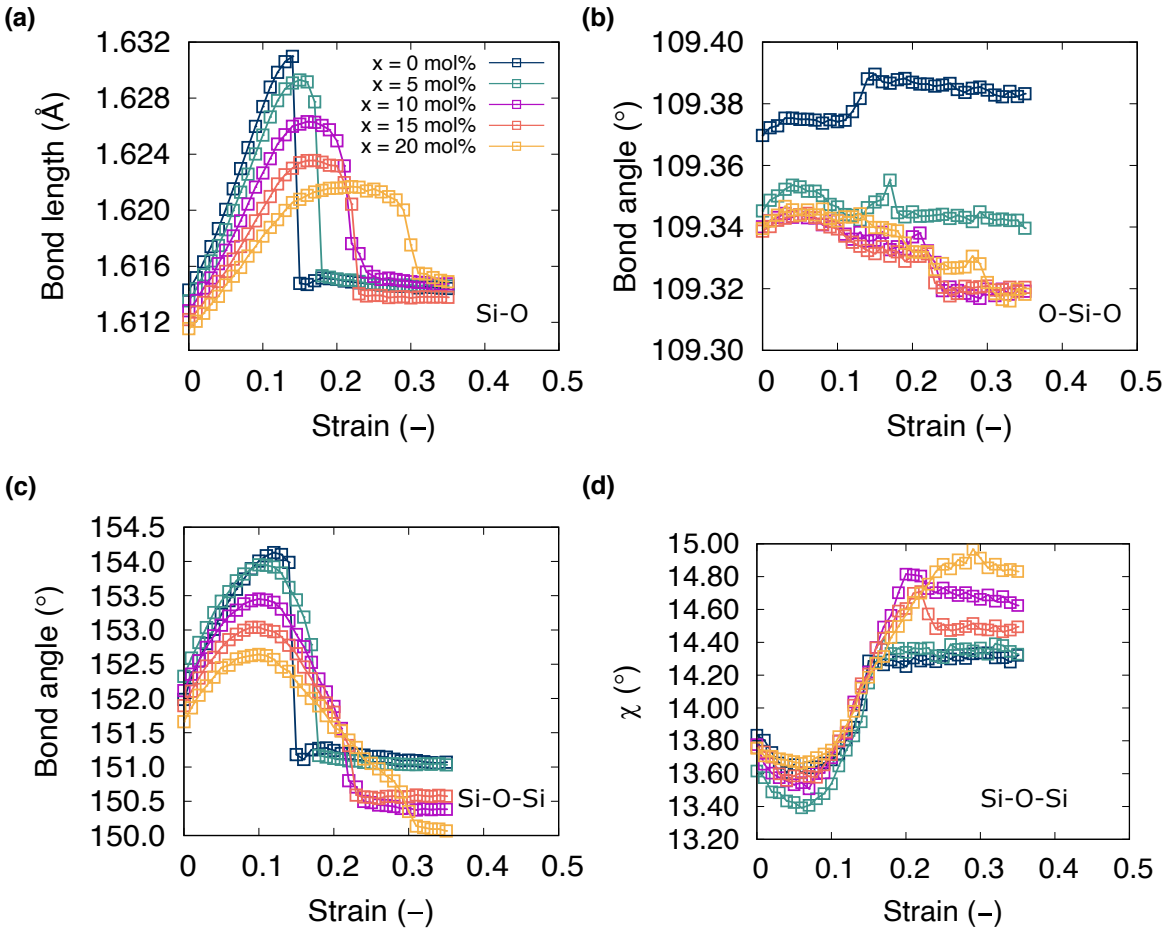

Figure. 8.6: Change of the pristine silicate glass backbone with strain during the tensile test along x-axis at 300 K and using a strain rate of 10^8 s^{-1}. (a) change of the mean Si–O bond length, (b) change of the mean O–Si–O bond angle, (c) change of the mean Si–O–Si bond angle, (d) shows the change in the standard deviation of the Si–O–Si bond angle distribution with strain.

shown in Figure. 8.6, Figure. 8.7, and Figure. 8.8, during tension, compression, and shear, respectively. During tension, one can see that the Si–O (Figure. 8.6a) bond length increases with increasing strain (similar to the stress-strain curve Figure.8.3a) and then decreases again after a fracture. The maximum Si–O bond length change is ≈0.02 Å (1.24%) for silica glass and decreases with increasing Na_2O content. The O–Si–O bond angle (Figure. 8.6b) showed a negligible change with the strain that is ≈0.02°. On the other hand, the change of the Si–O–Si angle (Figure. 8.6c) that represent the bending of tetrahedra showed a significant change compared to Si–O bond length and O–Si–O bond angle, where it increased by ≈2° for silica glass and to ≈0.5° in the glass with 20 mol% of Na_2O. Similar to the Si–O bond length, the Si–O–Si dependence on strain follows the stress-strain curves for all glasses. These structural parameters show no or little change in the unloaded glasses compared to the pristine glasses. The Si–O bond length of the unloaded glasses 1.61 Å for Silica and sodium silicate glass with 5 mol% of Na_2O, and 1.615 Å for all other glasses. The Si–O–SI bond angles of the unloaded glasses did not differ from the pristine glasses. In

Figure. 8.6d, we plotted the standard deviation of the Si–O–Si angles as a function of strain during tensile deformation. The change of the standard deviation gives details about the angle distribution between tetrahedra. Lower values mean that the distribution is narrow and more homogeneous. During tension, the standard deviation values decrease until a strain around 8% and increase again, which is the identical inverse behavior of the tangent modulus with strain.

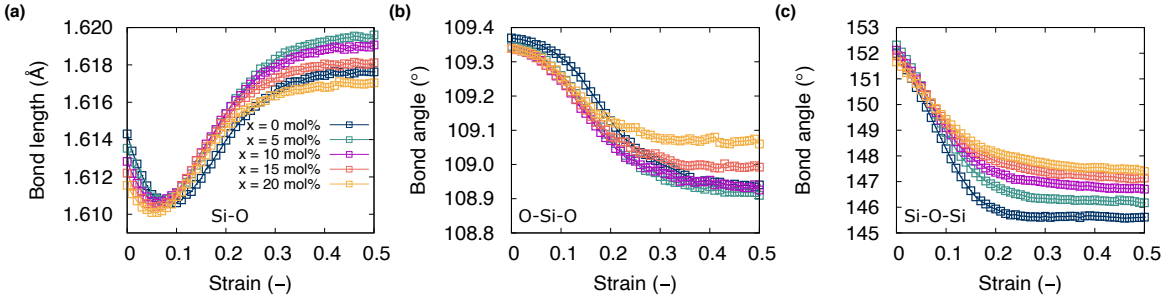

Figure. 8.7: Change of the pristine silicate glass backbone with strain during compression along x-axis at 300 K and using a strain rate of 10^8 s^{-1}. (a) change of the mean Si–O bond length, (b) change of the mean O–Si–O bond angle, and (c) change of the mean Si–O–Si bond angle.

If we look now at the change of these averaged properties during compression shown in Figure. 8.7, the behavior is entirely different. The Si–O bond length strain curve depicted in Figure. 8.7a, shows that during compression, the Si–O bond length decreases by ≈0.04 Å in the case of silica glass, by ≈0.02 Å in the case of the glass with 20 mol% of Na_2O, the decrease for the other glasses is between these boundaries. At a strain $\epsilon = 9\%$, a minimum in the Si–O bond length increases again to reach a steady-state with Si–O bond length values higher than those found in the pristine glasses. The average O–Si–O bond angle (Figure. 8.7b) decreases by ≈0.5° with increasing compressive strain and reaches a plateau starting from strains around 30%. Similar to tension, in compression, the Si–O–Si bond angle showed the most significant change as it decreased by ≈ 7° for the silica glass and ≈5° for the glass with 20 mol% of Na_2O. Moreover, at around 20% strain, the average Si–O–Si angle values reach a steady state. The Si–O bond length of the unloaded glasses 1.61 Å for Silica and sodium silicate glass with 5 mol% of Na_2O, and 1.615 Å for all other glasses. The Si–O–SI bond angles of the unloaded glasses did not differ from the pristine glasses.

During shear loading, the Si–O bond length as depicted in Figure. 8.8 increases by ≈0.011 Å and decreases following the same shape of the stress-strain curves (See Figure. 8.5a). A drop of the Si–O average bond length is also observed for silica glass, which disappears with increasing Na_2O content. The average intra-tetrahedral angle O–Si–O (Figure. 8.8b) slightly decreased with increasing shear strain. The average inter-tetrahedral angle Si–O–Si (Figure. 8.8c) showed a more substantial decrease compared to the O–Si–O bond angle and decreased by a value of ≈1.5° for all glasses.

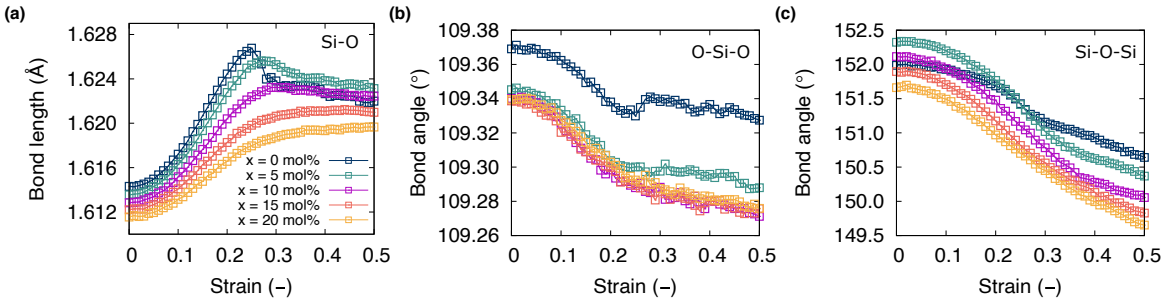

Figure. 8.8: Change of the pristine silicate glass backbone with strain during shear deformation by tilting the y-axis along the x-direction at 300 K and using a strain rate of 10^8 s^{-1}. (a) change of the mean Si–O bond length, (b) change of the mean O–Si–O bond angle, and (c) change of the mean Si–O–Si bond angle.

8.3 Deformation behavior of pre-deformed silicate glasses

In this section the mechanical behavior of sodium silicate glasses pre-deformed in tension, compression, or shear will be presented. The glasses were prepared using the same procedure described in Chapter. 3 with 375000 atoms and a cooling rate of 1 K/ps. Then, the deformations were applied with a strain rate of 10^8 s^{-1} at 300 K. The mechanical response of glasses that were obtained after unloading from different loading modes is investigated by subjecting them to a tensile reloading.

Tensile pre-deformation

The plastic strain of the pre-deformed stress-free glasses is given in Table. 8.6 for all compositions studied here. They were unloaded from relatively lower strains ($\epsilon \langle$ 5%), resulting in no apparent plasticity, and no plastic strain was measured. The deformation of the glasses up to these strains and strains below them is considered purely elastic. This behavior holds even at large sodium content, where more rearrangements are expected due to the mobile Na atoms (See Table. 8.6). However, when the glasses are unloaded from 10% tensile strain and beyond, a limited plasticity sets in as shown in Table. 8.6 with the values of the plastic strains measured. The recorded plastic strains increase with increasing unloading strain and are not more than 2%. The composition also has a minor effect on the values of the plastic strains, which tend to increase slightly with increasing Na_2O content. The positive values of strain indicate elongation, while negative values mean contraction.

In Figure. 8.9 we show the stress-strain curves of silicate glasses pre-deformed in tension along the x-axis at 300 K and using a strain rate of 10^8 s^{-1}. The samples were unloaded to zero stress from different strains before fracture, i.e., 2.5, 10, and 14% for silica glass (fail at a strain around 14.5%); and 2.5, 10, 15% for binary sodium silicate glasses. After unloading to zero stress, the stress-free glasses are independently reloaded back in tension along the three axes, i.e., x-axis, y-axis, or z-axis. The results are shown in Figure. 8.9a - e with increasing Na_2O content. The reloading along each axis is colored as follows x-axis (red), y-axis (yellow), or z-axis (green), with the stress-strain curve of the pristine glass given in black as a reference. The densities of the pristine glasses and the pre-deformed glasses are

given in Table. 8.5 where no differences with the pristine glasses were observed.

The Young's moduli of the pristine and pre-deformed reloaded glass samples along three deformation axes are also given in Table. 8.5. The values of Young's modulus of the pristine glasses along the x-, y-, and z-axis are nearly isotropic and are almost the same. However, Young's modulus does not correlate with the plastic strain in the pre-deformed glasses. The Young's modulus of these pre-deformed glasses reduces slightly for the samples with high sodium content. In Table. 8.5, the values of the Poisson's ratio of the pre-deformed glasses reloaded in tension are higher than the pristine glasses and generally increase with increasing plastic strain. The increase of the Poisson's ratio of the pre-deformed glasses indicates that the glasses tend to show higher contraction in directions perpendicular to the direction of tensile loading. Moreover, it should be noted that the values of the Poisson's ratio are not isotropic for the pre-deformed glasses.

The strength values for the pristine and the reloaded glasses in tension are also given in Table. 8.6. The reloaded glasses were already pre-deformed by applying a uniaxial tensile test along the x-axis and unloaded to zero stress from different strains achieved before fracture. The reloading is performed independently by performing a uniaxial tensile text along with the three box directions. The values clearly show that the strength values are nearly isotropic, meaning that similar values recorded in the three directions are almost identical. The plastic strain present in the network before the reloading simulations has almost no effect on the strength values recorded in the pre-deformed samples compared to the pristine glasses. The effect of the composition is similar to the one observed for the pristine glasses, where with increasing sodium content, the strength decreases.

The deformation behavior of the pre-deformed glasses is depicted by the stress-strain curves shown in Figure. 8.9a - e with increasing sodium content. The failure strains (defined as the strain at which the stress goes to 0 GPa) of the pristine glasses are anisotropic for all glasses, which will be discussed in the next chapter. For the silica glass, the failure strain of the reloaded glasses is almost constant when they are reloaded in the same direction of the pre-loading, i.e., x-axis, with a reduction of 1% for the glass unloaded from 14% tensile strain. When reloaded in the y-axis, the failure strain reduces by around 1% in all reloaded glasses compared to the pristine one. In contrast to the samples reloaded along the x- and y axes, the samples reloaded along the z-axis showed only a negligible change in the failure strains compared to the pristine silica glass. Like the silica glass, the binary sodium silicate glasses showed anisotropic failure strain values for pristine and pre-deformed glasses. The increasing sodium content increased plastic strain for both pristine and reloaded glasses. However, the failure strain values did not show a clear dependence on the plastic strain, and some samples did not fracture even when a 40% tensile strain was reached.

The stress-strain curves can be used to define the failure toughness Π_f [91, 200], which is given by integrating the area under the stress-strain curve up to the failure strain,

$$\Pi_f = \int_0^{\epsilon_f} \sigma d\epsilon. \tag{8.4}$$

The failure toughness is different from fracture toughness, which is defined by the ability of a material to resist the propagation of a pre-existing crack [201].

The failure toughness values of the pristine glasses and the samples pre-deformed in tension and reloaded are shown in Table. 8.5. For the pristine glasses, it is to be noticed that the values of the failure toughness increase with increasing sodium content, which indicates the glass becomes tougher with increasing sodium content. The effect of the pre-deformation did not affect the density of the glass. However, the failure toughness values were almost constant with the plastic strain except for the samples unloaded from 14% tensile strain for silica glass and 15% tensile strain for sodium silicate glasses, where a decrease of Π_f was observed. The values of Π_f of the glass containing 20 mol% of sodium are the highest and show more change with plastic strain.

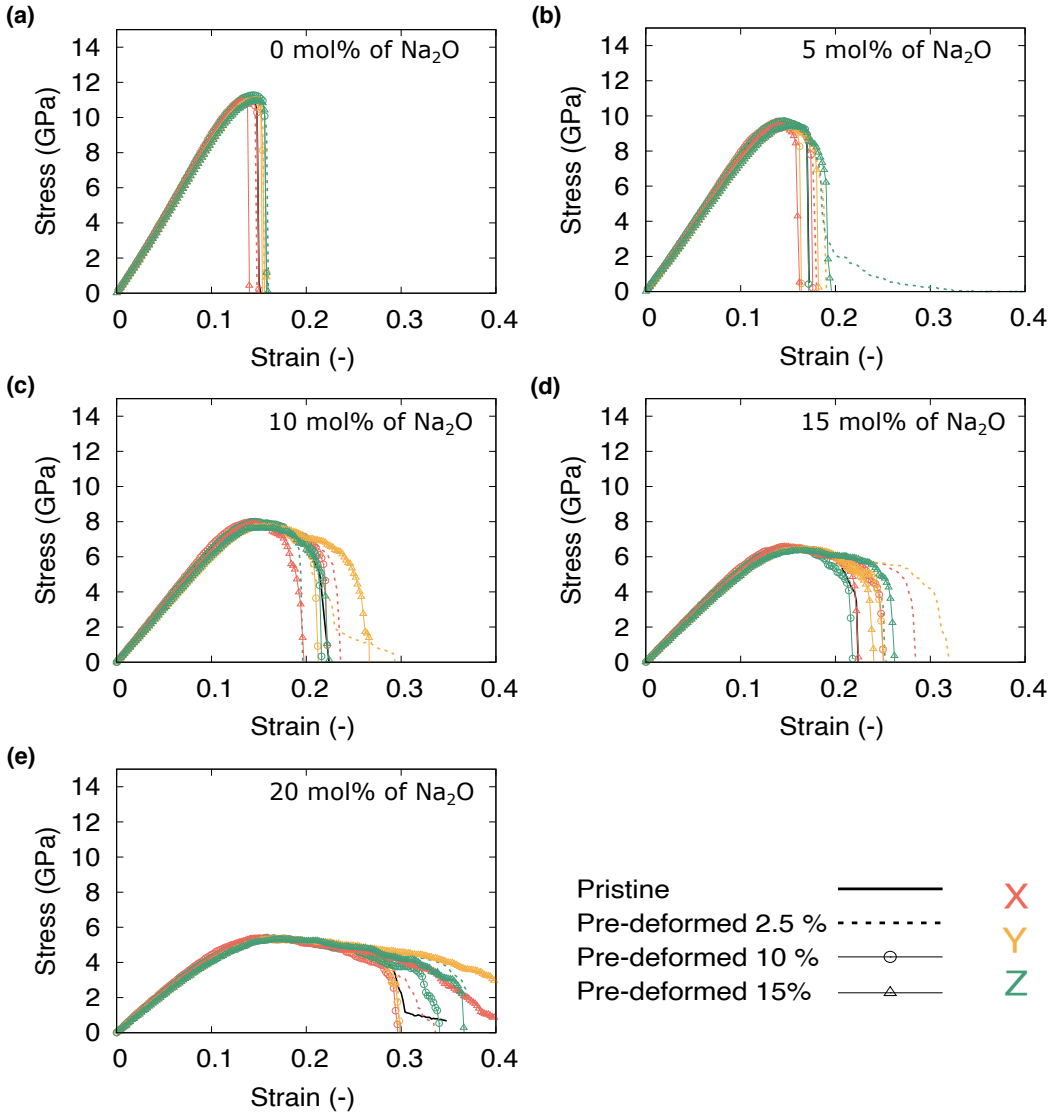

Figure. 8.9: Stress-strain curves of silicate glasses initially pre-deformed using a uniaxial tensile test along the $x-$axis up to different strains, unloaded to zero stress state and reloaded back in tension along the three box axis independently at 300 K using a strain rate of 10^8 s^{-1}.

Table 8.5: Calculated properties of the glasses pre-deformed in tension along the $x-$axis, unloaded to zero stress, and reloaded again in tension along the three box axes independently. Unloading strain, density, Young's modulus along x-axis (E_x), y-axis (E_y), z-axis (E_z), Poisson's ratio ν calculated for the deformations along the x-axis, y-axis, or z-axis; failure toughness along x-axis ($\Pi_{f,x}$) in GPa or 10^9 j/m^3, y-axis ($\Pi_{f,y}$), and z-axis ($\Pi_{f,z}$). The Young's moduli and the failure toughness are given within an error of $\pm$ 0.2 GPa and $\pm$ 0.005 GPa, respectively.

x (mol%)	Unloading strain (%)	Density ρ (g/cm^3)	E_x (GPa)	E_y (GPa)	E_z (GPa)	ν_x	ν_y	ν_z	$\Pi_{f,x}$	$\Pi_{f,y}$	$\Pi_{f,z}$
0	0.0	2.22	79	79	79	0.16	—-	—-	0.95	1.02	1.05
	2.5	2.22	78	78	79	0.18	0.19	0.21	0.93	1.01	1.05
	10.0	2.22	78	78	78	0.21	0.23	0.2	0.95	1.00	1.03
	14.0	2.22	80	78	79	0.23	0.2	0.18	0.83	0.98	1.01
5	0.0	2.30	72.43	72.10	72.00	0.20	—-	—-	1.04	0.96	1.17
	2.5	2.30	72.77	72.21	71.24	0.21	0.23	0.21	1.09	1.17	1.29
	5.0	2.30	71.54	70.55	73.21	0.19	0.22	0.19	1.08	1.07	1.32
	10.0	2.30	70.64	72.00	72.71	0.19	0.22	0.19	1.08	0.96	1.04
	15.0	2.30	69.80	65.85	69.76	0.2	0.28	0.18	0.90	1.06	1.15
10	0.0	2.36	65.94	64.67	64.63	0.21	—-	—-	1.18	1.19	1.27
	2.5	2.36	62.50	64.82	63.30	0.2	0.21	0.21	1.29	1.29	1.03
	5.0	2.36	62.78	62.74	64.74	0.23	0.23	0.22	1.17	1.27	1.23
	10.0	2.36	65.41	63.12	61.15	0.22	0.26	0.2	1.22	1.13	1.17
	15.0	2.36	62.37	58.84	61.48	0.2	0.28	0.17	0.98	1.40	1.15
15	0.0	2.40	57.39	57.96	56.76	0.232	—-	—-	1.00	1.27	1.12
	2.5	2.40	57.33	56.31	58.14	0.22	0.25	0.21	1.37	1.55	1.16
	5.0	2.40	56.95	54.50	57.42	0.2	0.23	0.2	1.29	1.33	1.25
	10.0	2.40	56.03	55.30	55.04	0.22	0.25	0.22	1.18	1.21	0.96
	15.0	2.40	57.92	53.92	52.19	0.22	0.35	0.16	1.01	1.08	1.20
20	0.0	2.44	53.15	53.27	52.08	0.23	—-	—-	1.21	1.33	1.18
	2.5	2.44	49.94	51.00	49.31	0.22	0.24	0.21	1.27	1.20	1.53
	5.0	2.44	50.97	48.16	52.13	0.21	0.23	0.22	1.44	1.36	1.43
	10.0	2.44	52.82	50.50	50.03	0.23	0.31	0.25	1.17	1.18	1.32
	15.0	2.44	50.41	47.14	46.71	0.26	0.36	0.2	1.46	1.60	1.42

Table 8.6: Calculated properties of the glasses pre-deformed in tension along the $x-$axis, unloaded to zero stress, and reloaded again in tension along the three box axes independently. Unloading strain, plastic strains ($\epsilon_{pl,x}$), ($\epsilon_{pl,y}$), ($\epsilon_{pl,z}$), maximum stress measured along the x-axis ($\sigma_{max,x}$), y-axis ($\sigma_{max,y}$), z-axis ($\sigma_{max,z}$), failure strain measured along x-axis ($\epsilon_{f,x}$), y-axis ($\epsilon_{f,y}$), and z-axis ($\epsilon_{f,z}$). The maximum stresses (σ_{max}) are given within an error of $\pm$ 0.1 GPa.

x (mol%)	Unloading strain (%)	$\epsilon_{pl,x}$ (%)	$\epsilon_{pl,y}$ (%)	$\epsilon_{pl,z}$ (%)	$\sigma_{max,x}$ (GPa)	$\sigma_{max,y}$ (GPa)	$\sigma_{max,z}$ (GPa)	$\epsilon_{f,x}$ (%)	$\epsilon_{f,y}$ (%)	$\epsilon_{f,z}$ (%)
0	0.0	—-	—-	—-	11.13	11.21	11.29	14.91	16.26	15.88
	2.5	0.0	0.0	0.0	11.20	11.20	11.20	14.80	15.45	15.86
	10.0	0.1	-0.08	0.0	11.13	11.14	11.27	14.90	15.43	15.80
	14.0	1.0	-0.47	-0.4	10.94	11.01	10.95	13.90	15.37	15.67
5	0.0	—-	—-	—-	9.7	9.57	9.71	17.13	16.38	18.65
	2.5	0.00	0.0	0.0	9.7	9.66	9.74	17.84	18.85	18.63
	5.0	0.0	0.0	0.0	9.65	9.67	9.70	17.58	17.58	20.9
	10.0	0.147	-0.09	-0.035	9.71	9.69	9.72	17.51	16.35	17.18
	15.0	1.399	-0.74	-0.723	9.45	9.39	9.44	16.03	18.10	19.21
10	0.0	—-	—-	—-	8.01	7.92	7.96	21.7	22.27	23.20
	2.5	0.0	0.0	0.02	8.02	8.03	7.92	23.38	22.87	19.48
	5.0	0.04	-0.05	-0.02	7.97	7.99	7.98	21.54	23.75	22.19
	10.0	0.26	-0.12	-0.15	8.00	7.90	8.01	22.16	21.03	21.46
	15.0	1.55	-0.86	-0.76	7.87	7.70	7.67	19.49	26.01	22.09
15	0.0	—-	—-	—-	6.51	6.47	6.53	22.37	26.81	24.53
	2.5	0.0	0.0	0.0	6.52	6.53	6.52	28.28	31.04	25.12
	5.0	0.14	-0.15	-0.03	6.50	6.47	6.46	26.68	27.68	26.57
	10.0	0.39	-0.27	-0.17	6.65	6.52	6.47	24.81	24.77	21.57
	15.0	1.65	-0.89	-0.76	6.55	6.40	6.35	22.23	23.79	26.00
20	0.0	—-	—-	—-	5.40	5.40	5.36	30.23	32.82	29.72
	2.5	0.0	0.0	0.0	5.44	5.35	5.42	31.62	29.73	36.48
	5.0	0.09	-0.06	-0.06	5.42	5.36	5.36	35.16	33.33	35.68
	10.0	0.37	-0.15	-0.22	5.39	5.34	5.42	29.3	29.6	32.45
	15.0	1.8	-0.73	-0.8	5.37	5.33	5.32	> 40	> 40	36.52

Compressive pre-deformation

In Figure. 8.10 we show the stress-strain curves of silicate glasses pre-deformed using uniaxial compression along the x-axis at 300 K and using a strain rate of 10^8 s^{-1}. The samples were unloaded to zero stress from different strains, i.e., 2.5, 5, 16, and 25% for all glass. After unloading to zero stress, the stress-free glasses are then independently reloaded back in tension along the three axes, i.e., x-axis, y-axis, or z-axis. The results are shown in Figure. 8.10a - e with increasing Na_2O content. The densities of the pristine and pre-deformed glasses are given in Table. 8.7 where an increase of the density with increasing plastic strain is observed. The Young's moduli of the pristine and pre-deformed reloaded glass samples along three deformation axes are also given in Table. 8.7. The Young's modulus along measured along the same axis as the pre-loading axis decreases with increasing plastic strain (See Table. 8.8). On the contrary, Young's moduli measure along the orthogonal directions to the pre-loading axis (y-axis or z-axis) increases with increasing plastic strain. This observation is observed for all glasses and is independent of the sodium content.

The plastic strain of the pristine glasses pre-deformed and stress-free is given in Table. 8.8 for all compositions studied here. Unloading from relatively lower strains ($\epsilon \langle$ 5%) resulted in no apparent plasticity, and no plastic strain was measured. The deformation of the glasses up to these strains and strains below them is considered purely elastic. This behavior holds even at large sodium content, where more rearrangements are expected due to the mobile Na atoms (See Table. 8.8). However, when the glasses are unloaded from 10% compressive strain and beyond, a finite plasticity sets in as shown in Table. 8.8 with the values of the plastic strains measured. The recorded plastic strains increase with increasing unloading strain reaching values around 15%. In Table. 8.8, the values of the Poisson's ratio of the pre-deformed glasses reloaded in tension are higher than the pristine glasses and generally increase with increasing plastic strain. The increase of the Poisson's ratio of the pre-deformed glasses indicates that the glasses tend to show higher contraction in directions perpendicular to the direction of tensile loading. Moreover, it should be noted that the values of the Poisson's ratio are not isotropic for the pre-deformed glasses.

The strength values for the pristine and the reloaded glasses in tension are also given in Table. 8.8. The reloaded glasses were already pre-deformed by applying a uniaxial compression along the x-axis and unloaded to zero stress from different strains achieved during the loading. The reloading is performed by performing a uniaxial tensile deformation along with the three-box directions independently. The plastic strain present in the network before the reloading simulations decreases the strength values along all three deformation axes. The effect of the composition is similar to the one observed for the pristine glasses, where with increasing sodium content, the strength decreases.

The deformation behavior of the pre-deformed glasses is depicted by the stress-strain curves shown in Figure. 8.10a - e with increasing sodium content. The failure strain of pristine glasses is anisotropic for all glasses, which will be discussed in the next chapter. For the silica glass, the reloaded glasses' failure strain increases with the plastic strain. When the glass is reloaded in the same direction as the pre-loading, i.e., x-axis, the fracture strain is higher than the one measured for the other directions. Like the silica glass, the binary sodium silicate glasses showed anisotropic failure strain values for pristine and

pre-deformed glasses. The increasing sodium content resulted in increased plastic strain for both pristine and reloaded glasses. However, the failure strain values did not show a clear dependence on the plastic strain, and some samples did not fracture even when a 40% tensile strain was reached.

The failure toughness values of the pristine glasses and the samples pre-deformed in compression and reloaded in tension are shown in Table. 8.7. For the pristine glasses, it is to be noticed that the values of the failure toughness increase with increasing sodium content, which indicates that the glass becomes more resistant to crack nucleation with increasing sodium content. The effect of the pre-deformation increased the glass density, and the values of the failure toughness were also shown to increase with increasing plastic strain. The values of Π_f increases with increasing Na_2O content.

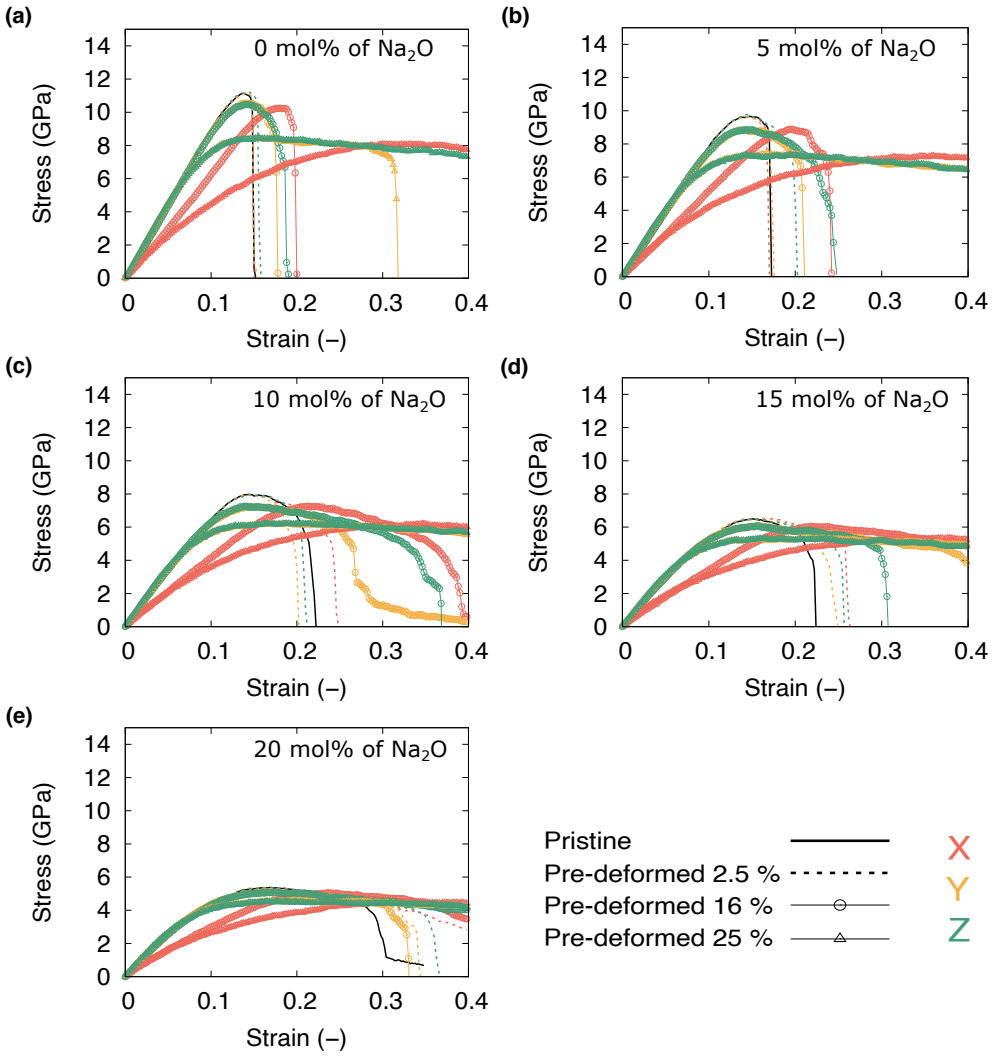

Figure. 8.10: Stress-strain curves of pristine silica and sodium silicate glasses pre-deformed in compression along the x-axis up to different strains, unloaded to zero stress state, and reloaded back in tension along the three box axes independently at 300 K using a strain rate of 10^8 s^{-1}.

Table 8.7: Calculated properties of the glasses pre-deformed in compression along the $x-$axis, unloaded to zero stress, and reloaded again in tension along the three box axes independently. Unloading strain, density, Young's modulus along x-axis (E_x), y-axis (E_y), z-axis (E_z), Poisson's ratio ν calculated for the deformations along the x-axis, y-axis, or z-axis; failure toughness along x-axis ($\Pi_{f,x}$) in GPa or 10^9 j/m^3, y-axis ($\Pi_{f,y}$), and z-axis ($\Pi_{f,z}$). The Young's moduli and the failure toughness are given within an error of $\pm$ 0.2 GPa and $\pm$ 0.005 GPa, respectively

x (mol%)	Unloading strain (%)	Density ρ (g/cm^3)	E_x (GPa)	E_y (GPa)	E_z (GPa)	ν_x	ν_y	ν_z	$\Pi_{f,x}$	$\Pi_{f,y}$	$\Pi_{f,z}$
0	0.0	2.22	79.34	79.01	79.40	0.16	—-	—-	0.95	1.02	1.05
	2.5	2.22	79.47	79.32	81.06	0.19	0.15	0.18	0.95	0.96	1.03
	16.0	2.28	56.87	83.18	82.57	0.19	0.18	0.23	1.18	1.19	1.28
	25.0	2.47	55.64	94.22	93.41	0.19	0.15	0.26	3.11	2.17	3.27
5	0.0	2.30	72.43	72.10	71.00	0.2	—-	—-	1.04	0.96	1.17
	2.5	2.30	71.19	71.00	72.21	0.2	0.21	0.21	1.01	1.05	1.29
	5.0	2.31	70.10	71.31	71.21	0.18	0.23	0.18	1.08	1.10	1.11
	16.0	2.38	51.85	74.81	74.26	0.19	0.18	0.23	1.32	1.29	1.51
	25.0	2.53	61.36	87.35	86.27	0.23	0.21	0.26	2.15	2.47	2.47
10	0.0	2.36	65.94	63.67	63.63	0.21	—-	—-	1.18	1.19	1.27
	2.5	2.36	61.82	63.15	63.17	0.21	0.22	0.22	1.36	1.07	1.16
	5.0	2.36	62.09	64.33	63.71	0.22	0.28	0.2	1.14	1.01	1.07
	16.0	2.44	45.41	70.25	70.20	0.26	0.18	0.29	1.95	1.58	1.98
	25.0	2.55	52.95	78.25	79.06	0.24	0.19	0.31	1.85	2.11	2.13
15	0.0	2.40	57.39	59.96	56.76	0.232	—-	—-	1.00	1.27	1.12
	2.5	2.40	54.85	57.21	57.92	0.21	0.21	0.23	1.25	1.17	1.21
	5.0	2.40	54.82	57.05	56.54	0.28	0.3	0.26	1.52	1.41	1.06
	16.0	2.48	40.98	63.76	63.18	0.22	0.16	0.27	1.78	1.90	1.48
	25.0	2.56	48.22	71.15	70.46	0.22	0.22	0.28	1.59	1.83	1.82
20	0.0	2.44	53.15	50.27	51.08	0.23	—-	—-	1.21	1.33	1.18
	2.5	2.44	49.74	52.37	50.06	0.24	0.23	0.23	1.59	1.39	1.47
	5.0	2.44	48.88	50.68	51.99	0.25	0.24	0.27	1.42	1.62	1.32
	16.0	2.49	39.23	55.64	56.45	0.21	0.21	0.25	1.49	1.33	1.63
	25.0	2.57	41.85	63.33	63.52	0.25	0.17	0.31	1.35	1.57	1.56

Table 8.8: Calculated properties of the glasses pre-deformed in compression along the $x-$axis, unloaded to zero stress, and reloaded again in tension along the three box axes independently. Unloading strain, plastic strains ($\epsilon_{pl,x}$), ($\epsilon_{pl,y}$), ($\epsilon_{pl,z}$), maximum stress measured along the x-axis ($\sigma_{max,x}$), y-axis ($\sigma_{max,y}$), z-axis ($\sigma_{max,z}$), failure strain measured along x-axis ($\epsilon_{f,x}$), y-axis ($\epsilon_{f,y}$), and z-axis ($\epsilon_{f,z}$). The maximum stresses (σ_{max}) are given within an error of $\pm$ 0.1 GPa.

x (mol%)	Unloading strain (%)	$\epsilon_{pl,x}$ (%)	$\epsilon_{pl,y}$ (%)	$\epsilon_{pl,z}$ (%)	$\sigma_{max,x}$ (GPa)	$\sigma_{max,y}$ (GPa)	$\sigma_{max,z}$ (GPa)	$\epsilon_{f,x}$ (%)	$\epsilon_{f,y}$ (%)	$\epsilon_{f,z}$ (%)
0	0.0	—-	—-	—-	11.13	11.21	11.29	14.91	16.26	15.88
	2.5	0.0	0.0	0.0	11.14	11.17	11.23	14.92	14.92	15.62
	16.0	-3.66	0.51	0.59	10.32	10.55	10.54	19.84	17.57	18.75
	25.0	-16.72	3.92	3.89	8.13	8.46	8.47	> 40	31.65	> 40
5	0.0	—-	—-	—-	9.7	9.57	9.71	17.13	16.38	18.65
	2.5	0.0	0.0	0.0	6.65	9.63	9.77	16.85	14.34	20.00
	5.0	0.0	0.0	0.0	9.70	9.65	9.65	17.60	17.87	18.11
	16.0	-5.08	0.91	0.96	8.89	8.88	8.77	24.06	20.96	24.35
	25.0	-17.42	5.09	4.92	7.28	7.30	7.30	> 40	> 40	> 40
10	0.0	—-	—-	—-	8.01	7.92	7.96	21.7	22.27	23.20
	2.5	0.0	0.0	0.0	7.97	7.96	7.99	24.54	20.07	20.84
	5.0	0.0	0.0	0.0	7.91	7.93	7.98	20.73	18.61	19.69
	16.0	-6.01	1.4	1.36	7.22	7.23	7.23	26.7	38.67	34.79
	25.0	-17.73	5.93	5.93	6.21	6.14	6.13	> 40	> 40	> 40
15	0.0	—-	—-	—-	6.51	6.47	6.53	22.37	26.81	24.53
	2.5	0.0	0.0	0.0	6.51	6.51	6.51	25.98	25.49	24.26
	5.0	0.0	0.0	0.0	6.49	6.54	6.51	31.97	28.73	22.34
	16.0	-6.34	1.67	1.8	6.08	6.07	6.07	> 40	> 40	30.45
	25.0	-17.95	6.80	6.8	5.35	5.26	5.26	> 40	> 40	> 40
20	0.0	—-	—-	—-	5.40	5.40	5.36	30.23	32.82	29.72
	2.5	0.0	0.0	0.0	5.29	5.33	5.34	> 40	34.04	36.12
	5.0	0.0	0.0	0.0	5.31	5.39	5.39	> 40	34.33	31.22
	16.0	-5.66	1.94	1.82	5.03	5.07	5.07	> 40	32.92	> 40
	25.0	-18.1	7.67	7.58	4.18	4.18	4.51	> 40	> 40	> 40

Shear pre-deformation

The shear pre-loading was performed by tilting the y-axis along the x-direction at 300 K and using a strain rate of 10^8 s^{-1}. Figure. 8.11 shows the stress-strain curves of silicate glasses pre-deformed using shear. The samples were unloaded to zero stress from different strains, i.e., 2.5, 5, 22, and 33% for all glass. After unloading to zero stress, the stress-free glasses are then independently reloaded back in tension along the three axes, i.e., x-axis, y-axis, or z-axis. The results are shown in Figure. 8.11a - e with increasing Na_2O content. The densities of the pristine glasses and the pre-deformed glasses are given in Table. 8.9. The Young's moduli of the pristine and the pre-sheared glass and reloaded in tension along three deformation axes are also given in Table. 8.9. The Young's modulus along measured along with the x-axis increase with increasing plastic strain (See Table. 8.10). The measured Young's moduli measured along the y-axis and z-axis decrease with increasing plastic strain. This observation is only observed in the silica glass. The measured Young moduli decreased compared to the pristine glasses for the sodium silicate glasses and showed almost no change with plastic strain.

The plastic strain of the pre-deformed stress-free glasses is given in Table. 8.10 for all compositions studied here. Unloading from relatively low strains ($\epsilon < 5\%$) resulted in no apparent plasticity, and no plastic strain was measured. The deformation of the glasses up to these strains is considered purely elastic. This behavior holds even at large sodium content (See Table. 8.10). However, when the glasses are unloaded from larger strains, a finite plasticity sets in, as shown in Table. 8.10 with the values of the plastic strains measured. The recorded plastic strains reach values around 16%. When the glasses are unloaded from the same macroscopic strain, the plastic strain values tend to decrease with increasing sodium content. In Table. 8.10, the values of the Poisson's ratio of the pre-deformed glasses reloaded in tension are higher than the pristine glasses and generally increase with increasing plastic strain. The increase of the Poisson's ratio of the pre-deformed glasses indicates that the glasses tend to show higher contraction in directions perpendicular to the direction of tensile loading. Moreover, it should be noted that the values of the Poisson's ratio are not isotropic for the pre-deformed glasses.

The strength values for the pristine and the reloaded glasses in tension are also given in Table. 8.10. The reloaded glasses were already pre-deformed by applying a shear deformation and unloaded to zero stress state from different strains achieved during the loading. The reloading is performed by performing a uniaxial tensile test along the three box directions independently. The plastic strain present in the network before the reloading simulations decreases the strength values along all three deformation axes. The effect of the composition is similar to the one observed for the pristine glasses, where with increasing sodium content, the strength decreases.

The deformation behavior of the pre-deformed glasses is depicted by the stress-strain curves shown in Figure. 8.11a - e with increasing sodium content. For the silica glass, the failure strain of the reloaded glasses increases with increasing plastic strain. When the glass is reloaded along the x-axis, the fracture strain is lower than measured in the other directions. The binary sodium silicate glasses show a different trend, where the failure strain values generally increase with increasing plastic strain. Moreover, the plastic strain

values of the samples unloaded from 33% shear strain and reloaded along the y-axis are always lower than the values measured for the other directions. This behavior tends to disappear with increasing sodium content. The increasing sodium content increased the plastic strain of the pristine glasses. The failure strain values of the pre-deformed samples did not show a clear dependence on the plastic strain, and some samples did not fracture even when a 40% tensile strain was reached.

The failure toughness values of the pristine glasses and the samples pre-deformed in shear and reloaded are shown in Table. 8.9. For the pristine glasses, it is to be noticed that the values of the failure toughness increase with increasing sodium content, which indicates that the glass becomes tougher with increasing sodium content. However, the effect of the pre-deformation on the failure toughness is unclear. For the silica glass, the values of the failure toughness were almost constant except for the sample unloaded from 33% shear strain. These samples showed highly anisotropic failure toughness values, where the lower values are measured along the y-axis followed by the one measured along the x-axis, then measured along the z-axis. In binary sodium silicate glasses, the behavior of the failure toughness is a bit complex to describe, and we will focus on individual compositions. The failure toughness of the reloaded glasses containing 5 mol% of Na_2O generally increases when the reloading is performed along x- or z-axis, while it increases and decreases again when reloaded along the y-axis. The tensile mechanical behavior of both silica glass and the sodium silicate glass with 5 mol% of Na_2O pre-deformed in shear and unloaded depends on the orientation of the shear band. When reloading orthogonal to the shear band plane the glasses break earlier compared to the pristine glasses and to the glasses reloaded along the shear band plane.

In the sample with 10 mol% of Na_2O, the failure toughness of the reloaded glasses along x- or y-axis increases to reach a maximum around 1.8 and 1.4 GPa, respectively for the reloading along x-axis and y-axis then decreases to reach a value around 1 GPa. The reloading along the z-axis decreased failure toughness with plastic strain, increasing to a value of 1.8 GPa. For the glass containing 15 mol% of Na_2O, the values of the failure toughness measured from the stress-strain curve of the sample reloaded along the x-axis showed, in general, an increase with increasing plastic strain of the unloaded sample. For the y-axis, the values of Π_f initially decrease with increasing plastic strain, then increase to reach a value around 1.4 GPa. When the reloading is performed along the z-axis, the value of Π_f shows no dependence on the plastic strain and initially increases, then decreases, to increase to reach a value of 1.8 GPa. Finally, for the sample with 20 mol% of Na_2O, the values of Π_f when the glass is reloaded along the x-axis or y-axis showed a similar trend where the values of the failure toughness increased with the plastic strain, decreases, and increases again. At low plastic strains, the values of Π_f measured in the samples reloaded along y-axis are higher than those measured from the stress-strain curves of the samples reloaded along the x-axis. However, at larger plastic strain, this behavior is reversed. The failure toughness of the samples reloaded along the z-axis generally increases with increasing plastic strain to reach a value higher than those achieved in the samples reloaded along the x-axis or y-axis.

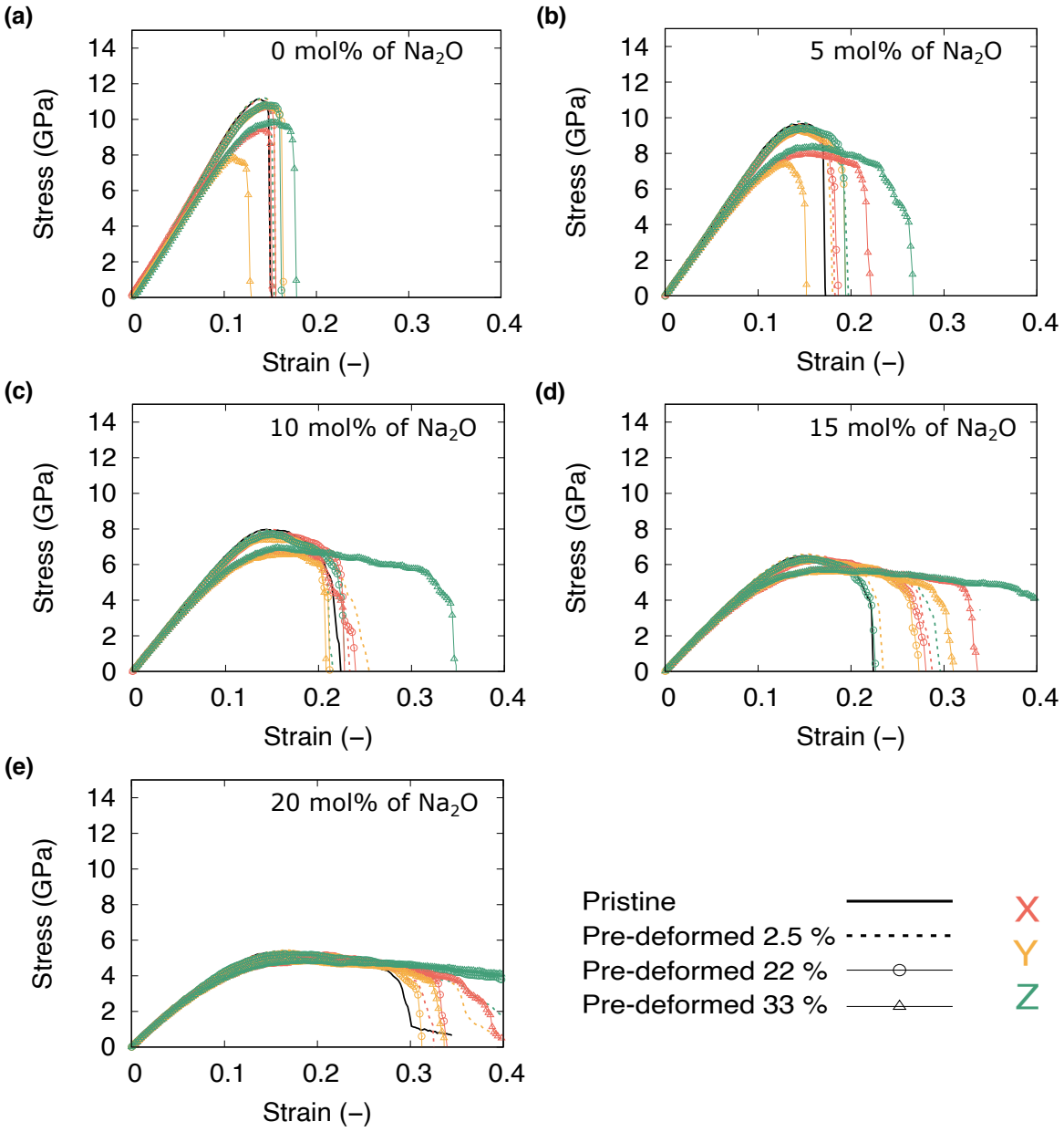

Figure. 8.11: Stress-strain curves of pristine silica and binary sodium silicate glasses pre-deformed in shear by tilting the y-axis along the x-direction up to different strains, unloaded to zero stress state, and reloaded back in tension along the three box axis independently at 300 K using a strain rate of 10^8 s^{-1}.

Table 8.9: Calculated properties of the glasses pre-deformed in shear by tilting the y-axis along the x-direction, unloaded to zero stress, and reloaded again in tension along the three box axes independently. Unloading strain, density, Young's modulus along x-axis (E_x), y-axis (E_y), z-axis (E_z), Poisson's ratio ν calculated for the deformations along the x-axis, y-axis, or z-axis; failure toughness along x-axis ($\Pi_{f,x}$) in GPa or 10^9 j/m^3, y-axis ($\Pi_{f,y}$), and z-axis ($\Pi_{f,z}$). The Young's moduli and the failure toughness are given within an error of $\pm$ 0.2 GPa and $\pm$ 0.005 GPa, respectively

x (mol%)	Unloading strain (%)	Density ρ (g/cm^3)	E_x (GPa)	E_y (GPa)	E_z (GPa)	ν_x	ν_y	ν_z	$\Pi_{f,x}$	$\Pi_{f,y}$	$\Pi_{f,z}$
0	0.0	2.22	79.34	79.01	79.40	0.163	—	—	0.95	1.02	1.05
	2.5	2.22	75.99	77.73	76.75	0.21	0.24	0.19	0.96	1.02	0.99
	22.0	2.23	82.94	72.71	69.08	0.22	0.25	0.2	0.98	1.05	1.04
	33.0	2.25	91.73	72.72	60.49	0.22	0.28	0.2	0.87	0.59	1.10
5	0.0	2.30	72.43	72.10	71.00	0.2	—	—	1.04	0.96	1.17
	2.5	2.30	71.35	71.08	71.33	0.2	0.22	0.2	1.14	1.12	1.31
	5.0	2.30	71.60	70.66	71.00	0.25	0.21	0.25	0.94	1.05	1.11
	22.0	2.31	70.29	70.15	68.86	0.2	0.24	0.19	1.13	1.22	1.22
	33.0	2.35	68.96	68.24	68.37	0.21	0.22	0.23	1.28	0.71	1.61
10	0.0	2.36	65.94	63.67	63.63	0.21	—	—	1.18	1.19	1.27
	2.5	2.36	62.70	63.28	63.46	0.23	0.21	0.24	1.38	1.37	1.19
	5.0	2.36	62.32	63.21	62.60	0.2	0.2	0.22	1.84	1.18	1.11
	22.0	2.37	63.59	62.22	62.05	0.22	0.29	0.2	1.30	1.11	1.21
	33.0	2.40	63.47	62.21	62.00	0.23	0.27	0.23	1.09	1.00	1.81
15	0.0	2.40	57.39	59.96	56.76	0.23	—	—	1.00	1.27	1.12
	2.5	2.40	56.47	57.07	57.31	0.28	0.24	0.28	1.40	1.08	1.39
	5.0	2.40	57.26	56.90	57.64	0.22	0.29	0.19	1.44	1.02	1.05
	22.0	2.41	54.84	56.36	55.85	0.25	0.25	0.26	1.30	1.26	1.00
	33.0	2.43	55.57	55.43	57.06	0.23	0.26	0.26	1.50	1.33	1.82
20	0.0	2.44	53.15	50.27	51.08	0.23	—	—	1.21	1.33	1.18
	2.5	2.44	50.72	51.27	50.01	0.26	0.25	0.24	1.34	1.51	1.54
	5.0	2.44	49.90	50.56	51.05	0.26	0.2	0.26	1.42	1.53	1.37
	22.0	2.45	50.29	51.35	51.07	0.2	0.24	0.23	1.37	1.24	1.63
	33.0	2.47	51.66	50.39	51.41	0.23	0.27	0.23	1.45	1.26	1.58

Table 8.10: Calculated properties of the glasses pre-deformed in shear by tilting the y-axis along the x-direction, unloaded to zero stress, and reloaded again in tension along the three box axes independently. Unloading strain, plastic strain (ϵ_{pl}), strength measured along the x-axis ($\sigma_{max,x}$), y-axis ($\sigma_{max,y}$), z-axis ($\sigma_{max,z}$), failure strain measured along x-axis ($\epsilon_{f,x}$), y-axis ($\epsilon_{f,y}$), and z-axis ($\epsilon_{f,z}$). The maximum stresses (σ_{max}) are given within an error of $\pm$ 0.1 GPa.

x (mol%)	Unloading strain (%)	ϵ_{pl} (%)	$\sigma_{max,x}$ (GPa)	$\sigma_{max,y}$ (GPa)	$\sigma_{max,z}$ (GPa)	$\epsilon_{f,X}$ (%)	$\epsilon_{f,Y}$ (%)	$\epsilon_{f,Z}$ (%)
0	0.0	—	11.13	11.21	11.29	14.91	16.26	15.88
	2.5	0.0	11.14	11.19	11.20	14.96	15.50	15.24
	22.0	2.84	10.75	10.79	10.82	15.50	16.28	16.20
	33.0	19.22	9.45	7.91	9.84	15.13	12.63	17.77
5	0.0	—	9.7	9.57	9.71	17.13	16.38	18.65
	2.5	0.0	9.65	9.60	9.81	18.08	17.81	19.43
	5.0	0.0	9.67	9.66	9.75	15.99	17.14	17.44
	22.0	2.76	9.34	9.34	9.41	18.33	19.28	19.33
	33.0	17.32	7.40	7.95	8.34	21.74	15.07	26.40
10	0.0	—	8.01	7.92	7.96	21.7	22.27	23.20
	2.5	0.0	9.68	9.58	9.79	18.11	17.81	19.43
	5.0	0.0	9.67	9.67	9.75	15.99	17.14	17.44
	22.0	3.7	9.32	9.33	9.41	18.36	19.28	19.33
	33.0	16.78	7.97	7.41	8.35	21.74	15.10	26.45
15	0.0	—	6.51	6.47	6.53	22.37	26.81	24.53
	2.5	0.0	6.55	6.59	6.54	27.92	23.17	29.14
	5.0	0.0	6.51	6.47	6.45	29.30	21.25	22.63
	22.0	4.2	6.26	6.29	6.31	27.54	26.46	22.33
	33.0	16.78	5.71	5.59	5.71	33.13	30.45	> 40
20	0.0	—	5.40	5.40	5.36	30.23	32.82	29.72
	2.5	0.0	5.40	5.52	5.42	31.92	35.86	36.55
	5.0	0.0	5.46	5.39	5.38	32.72	37.25	34.12
	22.0	4.5	5.24	5.26	5.22	33.34	31.01	> 40
	33.0	16.69	4.86	4.87	4.85	38.78	33.09	> 40

9 Discussion

In this chapter, the results presented in the previous chapter on the deformation behavior and fracture of pristine and pre-deformed silica and sodium silicate glasses will be discussed in light of our atomic-scale analysis of the glass structures at different length scales and different stages and modes of the deformations and available related literature.

9.1 Glass structure

In this section, we will discuss the obtained structure of silica and sodium silicate glasses from our MD simulations. The structure of the glasses as depicted by the RDF, BAD, the oxygen species, Q^n and the ring size distributions are consistent with previous simulations using similar and different interatomic potentials [18, 31, 150, 202, 203]. Moreover, the data of the Si–O bond length and the O–Si–O bond angle are in good agreement with experimental measurements [76, 203–206].

The effect of the sodium content on the Si–O bond length is consistent with the experimental findings measured using neutron, and EXAFS experiments [76, 203–206] as well as molecular dynamics simulations [18, 31, 35, 36, 40, 69, 150, 202, 203]. The results of the Si–O bond length from the obtained simulations (See Figure. 8.1) agree well with the experimental results [207], where it was found that the Si–O bond length increases from 1.617 to 1.622 Å for glasses with 22 and 31 mol% of Na_2O. The O–O bond length is 2.61 Å and does not seem to change with the addition of sodium oxide. This value agrees with the neutron diffraction data of 2.629 Å. The Na–O bond lengths range from 2.267 to 2.317 Å, and the pair distribution function shows that the Na–O peak increases and becomes sharper with the addition of Na_2O. These results agree with EXAFS and neutron diffraction data for which the Na–O bond lengths range from 2.30 to 2.36 Å. The coordination number of the sodium ions increases from 5.21 to 5.56 with increasing Na_2O content. Experimental observations from Greaves *et al.* [76] also found that Na atoms are surrounded by five oxygen atoms in the sodium disilicate glass. The calculated Si–Si bond lengths are around 3.1 Å, which are a bit higher than the experimentally measured one, which is 3.129 Å from the data obtained from neutron diffraction to 3.077 Å from the EXAFS measurements [150] indicating the good agreement between the structure of the simulate glasses and the one obtained experimentally. The Si–Si coordination number from our MD simulation was found to be around 4 for silica glass and decreases with increasing Na_2O content to 3.5. This behavior is in good agreement with the data reported in the literature [78, 150]. The mean O–Si–O (109 °) and Si–O–Si angle (152 °) were also found to be in good agreement with the data in the literature [78, 150]. Data from high-energy X-ray studies of silica glass [208] show that the Si–O–Si peak position is 147 °, in agreement with the results of two-dimensional ^{17}O dynamic-angle spinning NMR spectroscopy, which estimated the peak position of the Si–O–Si angle to be 146.7 ° [209]. These similarities between the values obtained using atomistic simulations and the experiments show that the used interatomic potential tends to reproduce the simulated glasses' short-range structure at equilibrium

and at room temperature.

The number of BO and NBO in the glass gives an overview of the connectivity of the glass and how connected the structure is. Also, the distribution of these NBOs per tetrahedron as given by the Q^n species give a picture of the near medium-range structure. In silica glass, the structure is supposed to be fully connected and the only Q^n species expected are the Q^4, which was the case in our simulations. However, minor content of Q^5 was also observed due to the high cooling rate or the potential used in the simulations. With the increase of the Na_2O content, the network becomes less connected (See Table. 8.2), and the content of the Q^4 species decreases while that of the other Q^n units lower than 4 increases gradually (See Table. 8.3). This behavior was observed experimentally [76]. However, the fraction of the Q^n species follow the same experimental trends but with different values [76]. This behavior was shown to be a result of high cooling rates used in MD simulations of glasses [65, 185].

The medium range order can be further characterized using the rings size distribution. Although it was not possible to extract the ring size distribution from our sample dues to the large sample sizes, it is expected to behave similarly to the data available in the literature from other simulations using smaller box sizes. The ring sizes of silicate glasses show a distribution of different ring sizes that changes depending on the composition [18, 210–213]. It was pointed out the ring size distribution of silica glass has a Gaussian shape, ranging from 3- to 11-membered rings [18], and it peaks at around six-membered rings, the same as in quartz [214]. Ebrahem *et al.* [215], using larger simulation boxes (24000 atoms), larger rings were observed up to 20 membered rings.

The addition of Na_2O creates NBOs (See Table. 8.2) and, at the same time, breaks the Si-O network in sodium silicate glasses. Du *et al.* [18] observed an increase in the number of large rings accompanied by a continuous decrease in the number of six-membered rings, which was attributed to the disruption of the Si-O network. The large rings were associated with the alkali-rich regions [202]. The number and size of rings larger than 10 increases with increasing sodium oxide content, indicating the presence of large alkali-rich regions[18].

9.2 Deformation mechanism of pristine silicate glasses

Tensile deformation and fracture

Nonlinear stress-strain curves: Silicate glasses exhibit strong nonlinear stress-strain behavior when the modifier content is low or does not exist at all, as in the case of silica glass [98, 216]. The non-linearity found in the elastic regime is reduced when high modifier content is added to the glass composition, e.g., Na_2O. This is because the silica-rich glasses are known to be anomalous glasses not just in their nonlinear stress-strain behavior (See Figure. 8.3) but also in other properties such as the increase of the isothermal compressibility with increasing pressure or the negative thermal expansion coefficient in some temperature ranges [98, 217].

The glasses that do not show these anomalies are called normal glasses [98, 217]. The nonlinear elastic behavior found in some oxide glasses indicates that the linear Hooke's

law can not be applied to study the elastic response of these materials, and functions with higher terms are required to describe their elastic response at larger strains adequately [62, 62, 98, 101, 102, 218]. As shown in previous sections, we recovered the nonlinear behavior of the stress-strain curves through the tangent modulus. This behavior was in good agreement with the available experimental data [62, 62, 98, 101, 102] and atomistic simulations [63, 91, 219]. Older studies [111] assumed that it is expected for silica glass to remain elastic in tension up to its intrinsic strength ($<$ 15 GPa). This assumption was made by taking the reversibility of silica glass subjected to hydrostatic compression up to 8 GPa, which corresponds to 24 GPa in uniaxial compression. As we showed in Figure. 8.3b, this was not the case in all glasses studied here, even when deformed up to stresses way lower than the intrinsic strength of the glass. With the addition of sodium to the silica network, the tangent modulus changed from anomalous to normal, see Figure. 8.3b. However, an unexpected plateau where observed. The fact that data of the tangent modulus of binary silicate glasses does not exist in the literature makes the current results interesting. Similar observations of the tangent modulus were reported recently in work published at the same time of the writing of this thesis [219].

The structure change then explains silica glass's highly nonlinear stress-strain curves during the deformation. During the deformation in tension, the Si–O bond length increases until fracture with a curve shape similar to the stress-strain curve (See Figure.8.6a). In contrast, the O–Si–O bond angles stayed almost constant. The Si–O–Si bond angles showed the most change indicating that the deformation of the sample and the change in the tangent modulus with strain due to the change of the intertetrahedral linkages [219]. In silica glass and sodium silicate glasses with low sodium content, the tensile strain increases structural homogeneity, as indicated by the decrease of the standard deviation of the Si–O–Si bond angle distribution with strain up to strains around 8% (See Figure. 8.6d). These results indicate that the Si–O–Si bond angle distribution gets narrow with an increase in tensile strain and is anti-correlated with the behavior of the tangent modulus. At a strain of around 8%, the structure starts to be more heterogeneous (See Figure. 8.6d) than the pristine glasses, which is due to the increasing number of bonding change events, and at higher strains, the E_t decrease to reach a value of zero at the fracture point (See Figure. 8.3b).

Figure. 9.1 shows the incremental nonaffine displacement ΔD_{min} for all glasses at different strains. The incremental nonaffine displacement ΔD_{min} is computed using a sliding reference configuration with the strain increment of 2%, i.e., when the current configuration is at strain 4% then, the reference configuration is at 2%. Thus, ΔD_{min} can be seen as the change in D_{min} between two configurations separated by 2% strain. In Figure. 9.1, the strain values are for the current configuration. By comparing the ΔD_{min}, we can see that the non-affine displacement of atoms is limited in silica glass. However, with increasing sodium content, the distribution of ΔD_{min} becomes broader, its intensity decreases monotonically, and shifts toward larger values of ΔD_{min}. This indicates that with increasing sodium content in the glass, the number of atoms that exhibit a non-affine displacement increases compared to the silica glass [219]. This is explained by the fact that Na atoms have a weaker bond with the oxygen atoms, have a higher coordination number than Si atoms, and have weaker bonding to oxygen atoms than Si; thus, they are more prone to move. On the other hand, the movement of Si atoms is constrained by the oxygen tetrahe-

dral network.

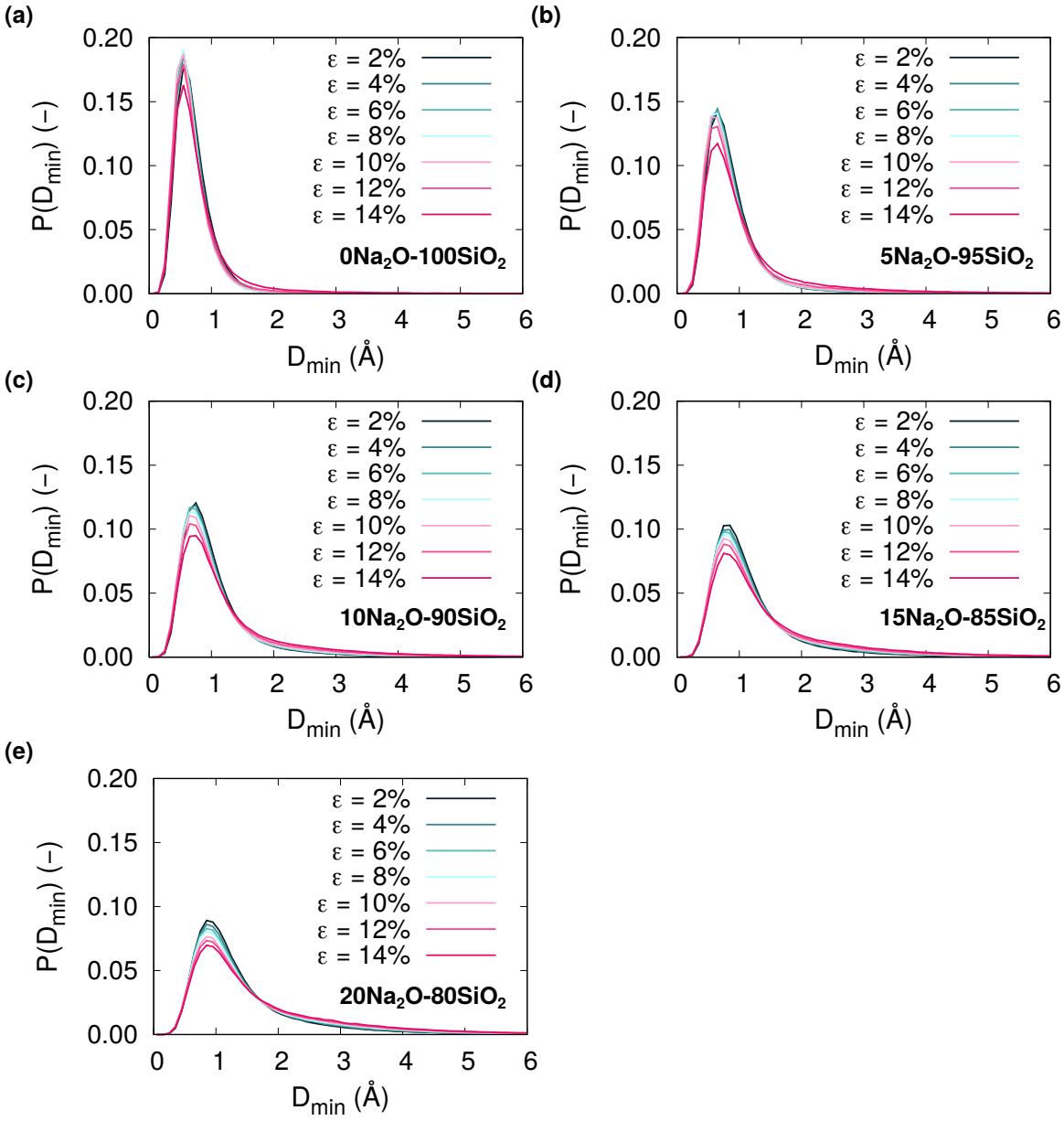

Figure. 9.1: The distribution of the incremental nonaffine displacement D_{min} during tensile test along the $x-$axis at 300 K and using 10^8 s^{-1} as a strain rate. All compositions are shown in the figure.

To better track the evolution of ΔD_{min} as a function of strain, we plotted in Figure. 9.2 the mean incremental non-affine displacement distributions $< \Delta D_{min} >$ as a function of strain for the all glasses and all elements. The mean incremental non-affine displacement was calculated from the distribution of the incremental non-affine displacement. The behavior of $< \Delta D_{min} >$ shows a strong dependence on the composition, which is similar to the stress-strain dependence on the composition. For the silica glass, the values of $< \Delta D_{min} >$

decrease initially with strain until strains around 8% which was found to be the same strain at which the tangent modulus reaches a maximum, then increases with further strain increase. This behavior is observed for both O and Si atoms. The initial decrease of the $< \Delta D_{min} >$ correlates well with the increase of the tangent modulus (hardening of the tangent modulus). On the other hand, the increase of $< \Delta D_{min} >$ highlights the transition of the glass to become less stiff. Similarly, the glass that has 5 and 10 mol% of Na_2O almost a constant $< \Delta D_{min} >$ at the small-strain is observed. With further increase of sodium content, the trend of $< \Delta D_{min} >$ with strain shows no minima, and a continuous increase is seen until fracture strain. The behavior of $< \Delta D_{min} >$ of Si and O atoms follows the same behavior of the total $< \Delta D_{min} >$. The $< \Delta D_{min} >$ of the Na atoms do not show the same trend as Si and O and monotonically increase with increasing strain until fracture. Thus we see that the change of the tangent modulus observed is due to the ability of the atoms to move in a nonaffine manner. Overall, from the found results, we can conclude that the nonaffine part of the atomic displacements influences the stiffness of the glass on the macroscopic scale.

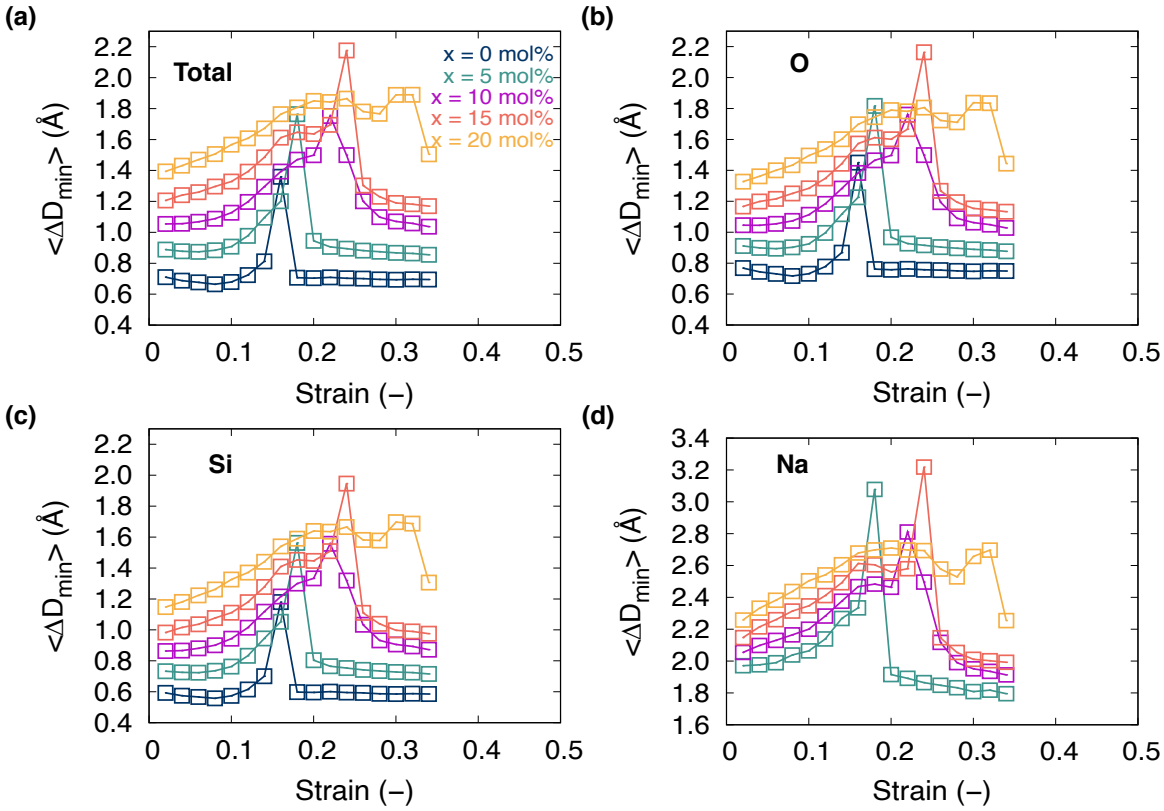

Figure. 9.2: Mean incremental nonaffine displacement $< \Delta D_{min} >$ as a function of strain for pristine silica and sodium silicate glasses during tension along the $x-$axis at 300 K using a strain rate of 10^8 s^{-1}. The subplots are represent the total $< \Delta D_{min} >$ (a), for oxygen atoms (b), for silicon atoms (c), and for sodium atoms (d). The strain increment was chosen as 2%.

The above-discussed behavior is nicely visualized in the snapshots from Figure. 9.3, in which we give visualize the atoms colored base to their values of the non-affine displace-

ment. The figure shows snapshots at three representative strains and for only silica and two sodium silicate glass compositions, i.e., 5 mol% of Na_2O and 20 mol% of Na_2O. As can be seen, at low strains, few atoms are moved nonaffinely, and their distribution is more homogeneous in the glass with low sodium content. While with increasing strain and/or sodium content, more atoms have nonaffine displacement and show a less homogeneous distribution.

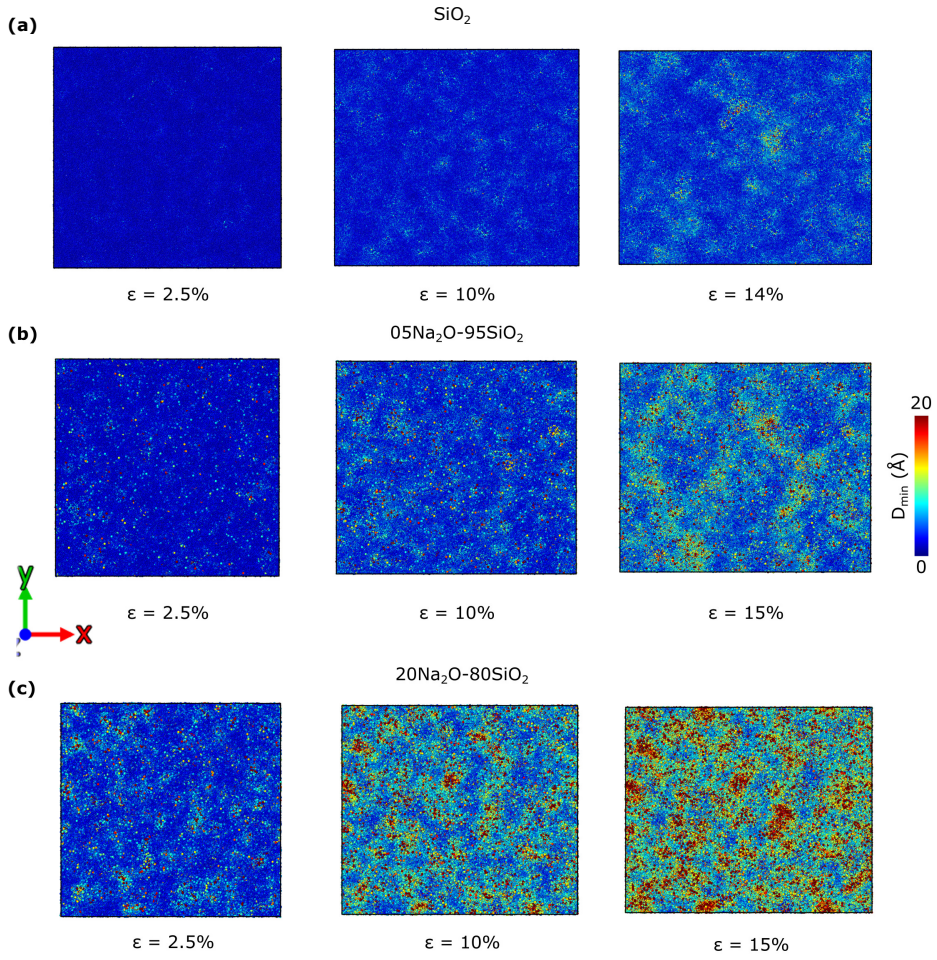

Figure. 9.3: Snapshots at different strains during tensile loading along the $x-$axis at 300 K and using a strain rate of 10^8 s^{-1}, where the atoms are colored based on their value of the nonaffine displacements. (a) for silica glass, (b) for the composition with 5 mol% of Na_2O, and (c) for the composition with 20 mol% of Na_2O. For all samples, the undeformed glass was used as a reference configuration, and a cutoff of 5.5 Å was used for the non-affine displacement calculation to get a smoother gradient and, at the same time, resolve the locality of the changes.

Deformation and fracture: Earlier works using MD simulations of silica glass subjected to uniaxial tensile loading using a fixed volume approach reported brittle fracture behavior for bulk silica glass [220]. In these studies, no Poisson's contraction was taken into account and, therefore, adding more constraints to the glass sample [220]. In other studies, Pedone *et al.* [63], Yuan *et al.* [21], and others [215, 221–225] reported on the difference between

uniaxial tensile deformations of silica glasses performed using the fixed volume method and variable volume method, where the simulation cell was allowed to relax to 0 stress in the direction orthogonal to the loading axis. As a result, a less brittle fracture was reported for the variable volume fracture simulations than the ones performed in the fixed volume tensile test [63].

During tensile deformation of the silicate glasses studied here, the stress-strain curves show that the glasses exhibit more plasticity with increasing sodium content, which is in good agreement with previous studies [79, 219, 226–228]. This behavior is consistent with recent simulations [79, 219, 227, 229]. The silica glass showed the lowest plastic behavior and failed in a brittle manner. With increasing sodium content, the glasses showed a decreasing strength and failure strain, indicating the addition of sodium enhanced the plasticity and toughness of the glass. The obtained strength values of the silica glass compare well with experimental results [98]. Previous simulations showed that the plasticity of oxide glasses is mainly due to the bond switching [61, 230, 231]. The bond topology changes in the glass network were analyzed by comparing the nearest neighbors of an atom at a strain ϵ_x with the state in the undeformed glass following the algorithm described in the method section. The increase of the coordination number indicates that a new bond has formed, a decrease highlight that a bond has been broken, and a similar number of neighbors with different IDs mean that bonds were switched. The results of such analysis are shown in Figure. 9.4. We see that many Si atoms change their neighbors during the deformation. However, the new and broken bonds have a percentage lower than the switched bonds, which increases exponentially with strain until the fracture of the sample. The bond distribution of these bonds is shown for silica glass and sodium silicate glasses with 20 mol% of Na_2O shown in Figure. 9.4. The number of switched bonds is higher in the samples that experienced more plastic behavior, which is in good agreement with previous MD simulations [61, 230, 231]. It can also be concluded from the bond statistics results that Na tends to delay the fracture, which is highlighted by the huge decrease of the broken bonds in the sample with 20 mol% of Na_2O compared to the silica glass.

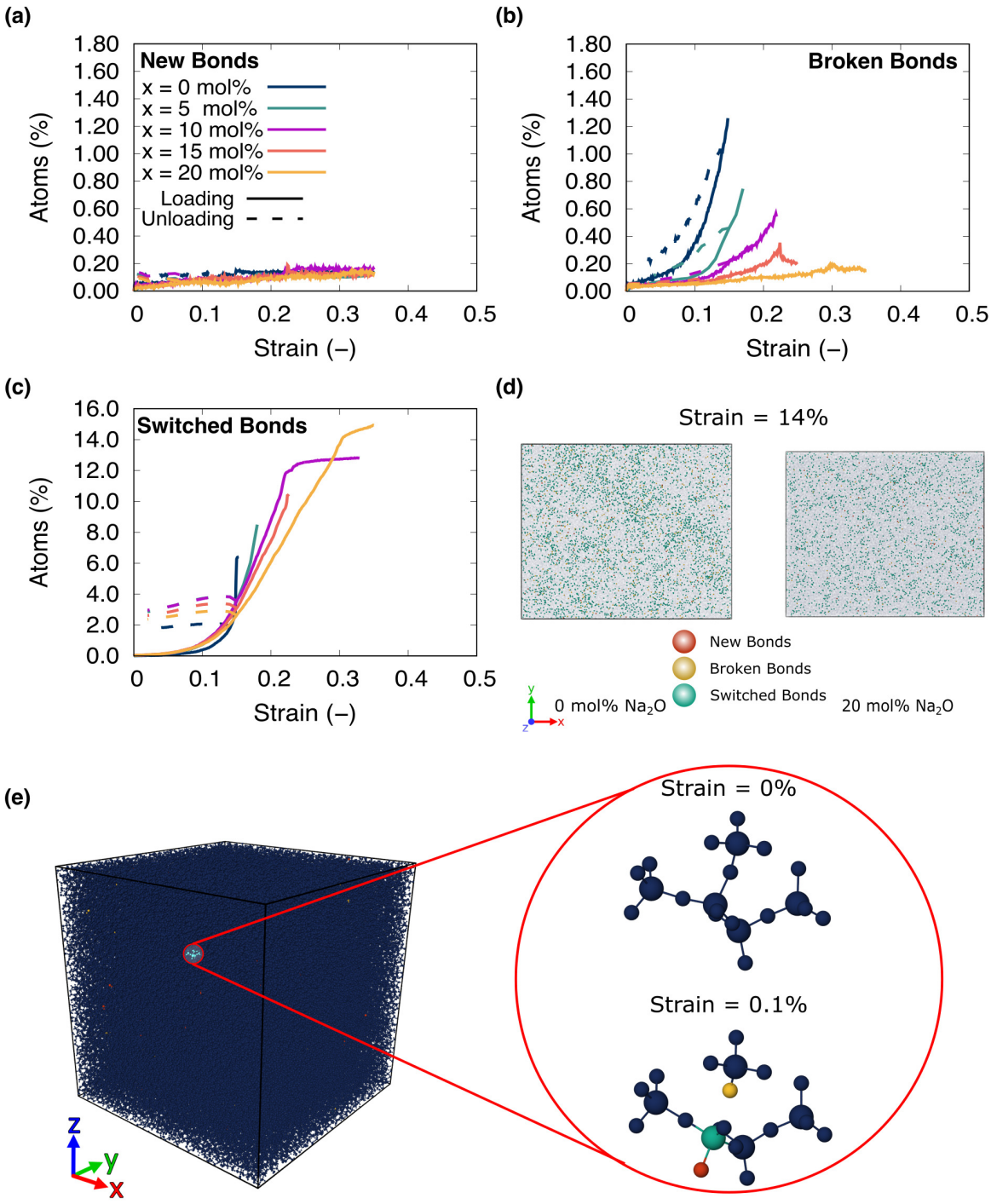

Figure. 9.4: Bond statistics of Si atoms during tension along the $x-$axis at 300 K and using a strain rate of 10^8 s^{-1}. (a) percentage of Si atoms that have a new bond, (b) percentage of atoms that have a broken bond, (c) percentage of atoms that have a switched bond, (d) snapshots are showing only the atoms that have a change in their bonding topology at 14% strain for both a silica glass and the sample with 20 mol% of Na_2O. In (e), snapshots of the bulk silica glass subjected to a tensile deformation at 0.1% strain with atoms that have change in their bonding topology are highlighted. A zoomed-in snapshot showing only the selected atoms are provided on the right side of the figure.

The strain localization parameter calculated as shown in chapter 3 is plotted in Figure. 9.5a. This parameter quantifies the deviation of the strain distribution from a homogeneous behavior, with larger values of the strain localization indicating larger fluctuations in the atomic strain and a more localized deformation mode. The values of the strain localization parameter remained almost unchanged during the tensile test until reaching a strain around 14.6% and started increasing for all samples. At the failure strain, the strain localization parameter increases sharply. This corresponds to the nucleation and growth of the crack in the glass network, shown in Figure. 9.5c - g, where the voids with a radius larger than 3.5 Å are shown for different selected strains during tensile deformation. In silica glass the pristine sample contains voids, which get reduced with increasing Na_2O. With the increase of the tensile strain, voids are merged to form a crack that eventually leads to the fracture of the glass. However, in sodium silicate glasses with higher Na_2O content, there were almost no voids that have a radius larger than 3.5 Å in the pristine glasses, but they are formed during the tensile deformation and merge to form a crack leading the fracture. The increase of the strain localization parameter is less sharp in the glasses with high sodium content due to the higher flexibility of the network due to the mobile Na atoms. The sharp increase of the strain localization parameter is then visualized by the snapshots in Figure. 9.5b, where there is a high localization of shear strain in the region where the crack nucleates in the $20Na_2O$-$80SiO_2$ samples. Similar behavior is observed for all glasses. The origin of the anisotropic failure strains observed in the pristine glasses is related to the initial orientation of the voids and large rings [18, 210–213, 215].

The addition of Na_2O creates NBOs (See Table. 8.2) and, at the same time, breaks the Si-O network, in sodium silicate glasses. Du *et al.* [18] observed an increase in the number of large rings accompanied by a continuous decrease in the number of six-membered rings, which was attributed to the disruption of the Si-O network. The large rings were associated with the alkali-rich regions [202]. The number and size of rings larger than 10 increases with increasing sodium oxide content, indicating the presence of large alkali-rich regions[18].

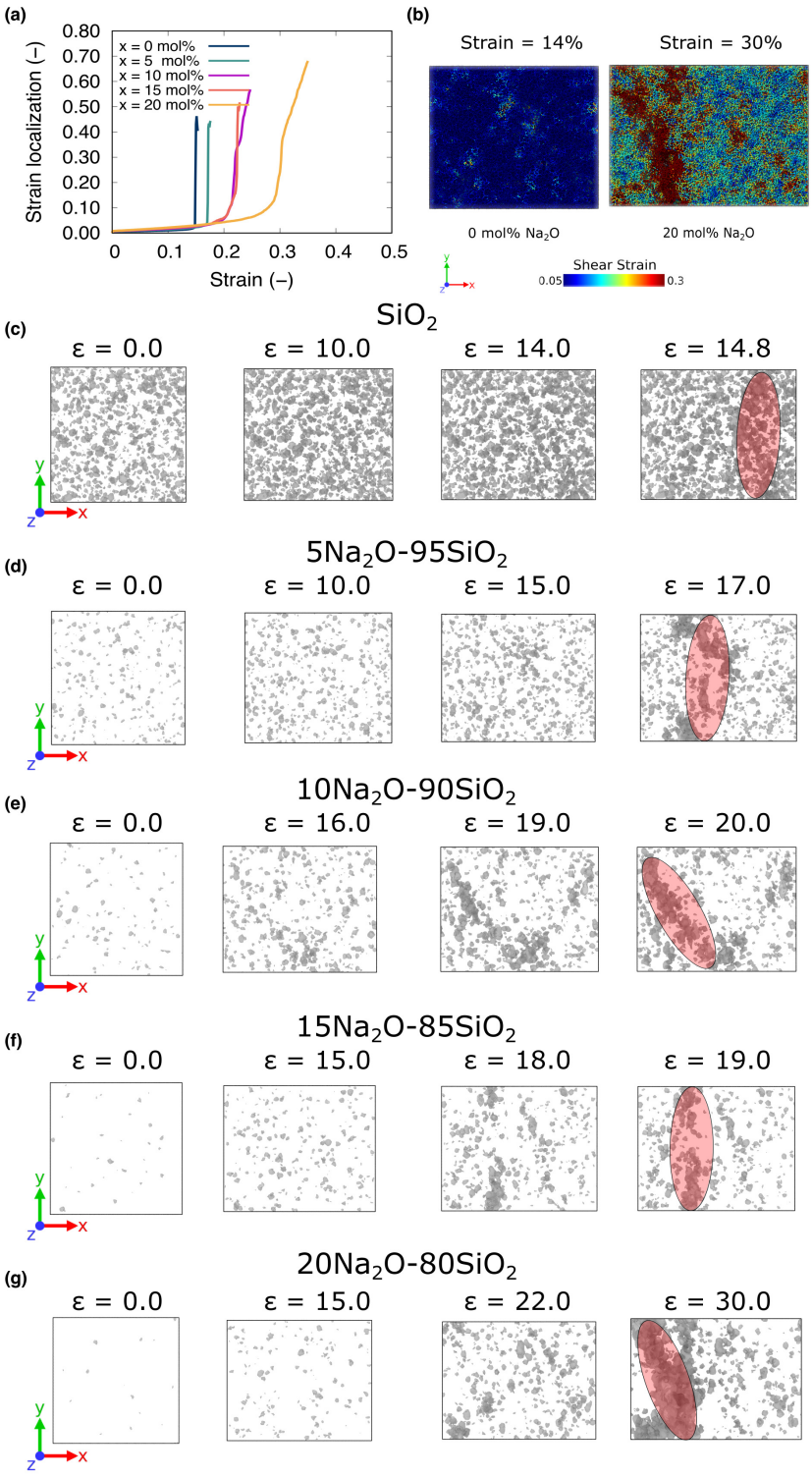

Figure. 9.5: (a) Strain localization parameter as a function of strain during tensile deformation along the $x-$axis at 300 K and using a strain rate of 10^8 s^{-1}. (b) Local atomic shear strain for the silica glass and sodium silicate glass containing 20 mol% of Na_2O at 14% and 30% tensile strain, respectively. (c - g) show snapshots at different selected strains during tensile deformation of the pristine silicate glasses. The snapshots show the evolution of voids constructed using a mesh with a probe radius of 3.5 Å, chosen as the first minimum of Na-O RDF. The strains were selected when a significant change in the void formation or void structure is observed. The red-shaded region highlights the coalescence of voids into a crack.

Plastic flow in compression

A nonlinear stress-strain curve was obtained during compression, as shown in Figure. 8.4. The nonlinearity of the stress-strain curves was better highlighted by the ratio of the stress and strain, which highlight the tangent modulus [91]. The nonlinear stress-strain curves of silica glass under compression were previously observed experimentally [98, 102, 232–236] and MD simulations [19, 63, 117, 227, 229, 237]. Although, compared to tension, the compressive tangent modulus does not show an increase in its values and only decreases nonlinearly. This is because, during compression, there are many bond switching events, and only a few bonds are newly formed or broken. This has also led to a ductile deformation of the compressed samples. The ductility of silica glass has been observed experimentally by Kermouch *et al.*, [120] in silica glass pillars using *in situ* SEM mechanical testing. They highlighted the importance of homogeneous shear flow in the plasticity observed in those silica pillars [120]. The appearance of shear bands mainly characterizes the inhomogeneous deformation [19, 113, 120, 229, 238].

The strain localization parameter during compression shown in Figure. 9.6a increases smoothly with increasing strain during compression, and no sharp increase is observed, indicating a less inhomogeneous flow of the structural units and a less localized distribution of the plastic deformation in all the glass networks. However, the snapshots in Figure. 9.6b visually show the same results as indicated by the strain localization parameter. Although the strain localization parameter values of silica and sodium silicate glasses are similar, the shear strain in the sodium silicate glasses is higher. In the compressed samples from our simulations, shear bands during the compression were observed and are highlighted in the snapshots in Figure. 9.6 and Figure. 9.7.

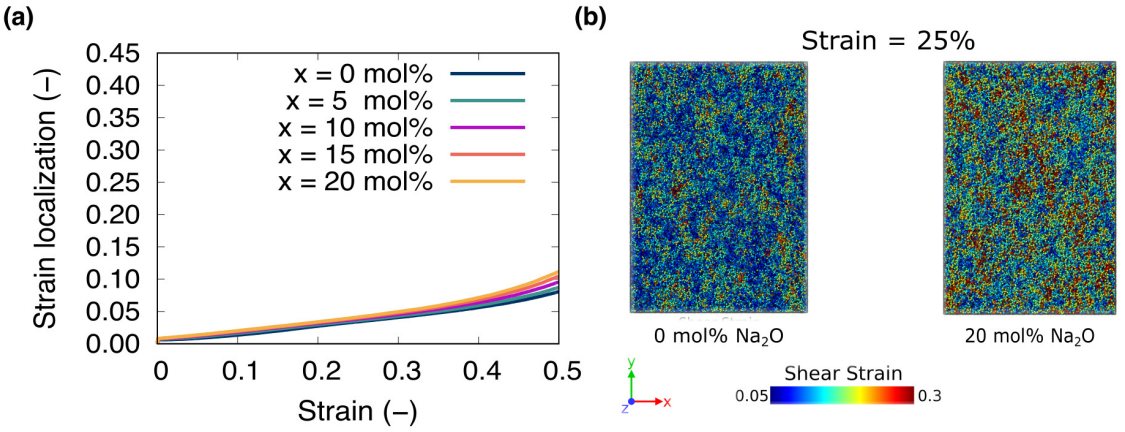

Figure. 9.6: (a) Strain localization parameter *vs.* strain during compressive deformation of pristine glasses along the $x-$axis at 300 K and using a strain rate of 10^8 s^{-1}. (b) Local atomic shear strain for the silica glass and sodium silicate glass containing 20 mol% of Na_2O at 25% and 30% compressive strain, respectively.

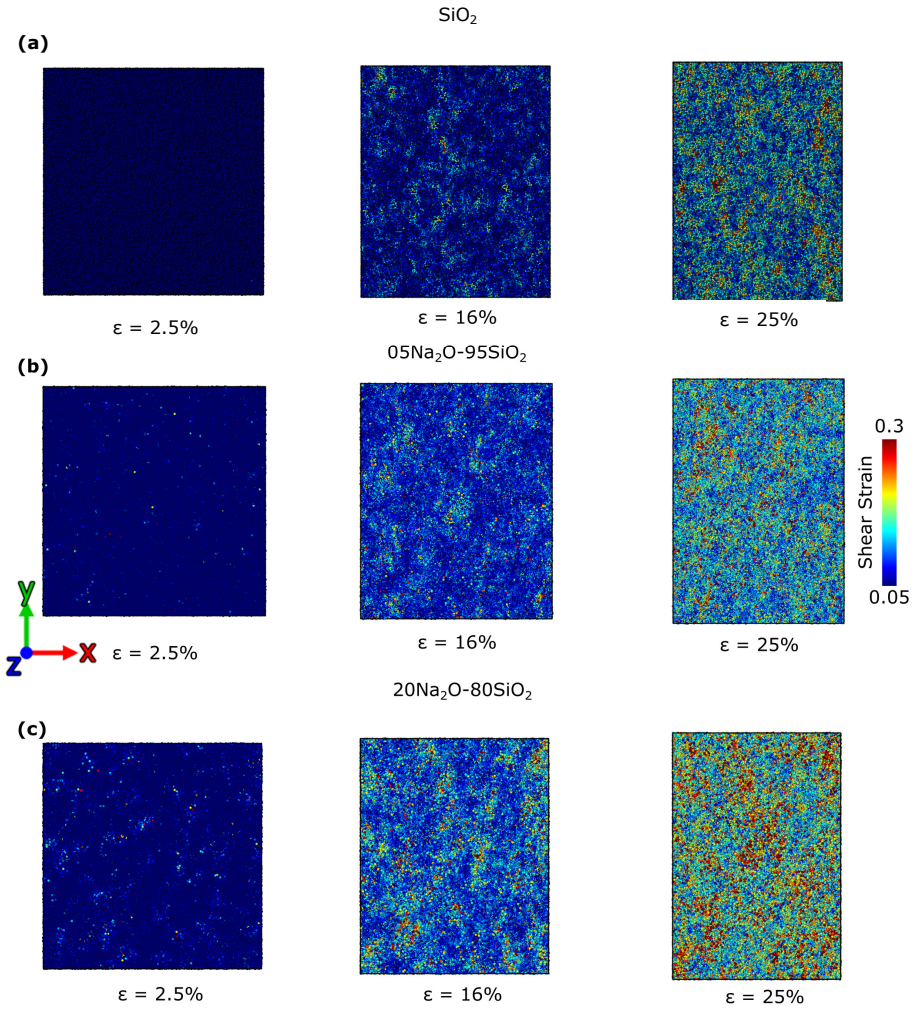

Figure. 9.7: Snapshots at different strains during compression loading of pristine glasses along the $x-$axis at 300 K and using a strain rate of 10^8 s^{-1}, where the atoms are colored based on their value of the local shear strain. (a) for silica glass, (b) for the composition with 5 mol% of Na_2O, and (c) for the composition with 20 mol% of Na_2O. For all samples, the undeformed glass was used as a reference configuration, and a cutoff of 5.5 Å was used for the shear strain calculation to get a smoother gradient and, simultaneously, resolve the locality of the changes.

During compression, we tracked the evolution of the incremental nonaffine displacements ΔD_{min}, which are plotted for all samples in Figure. 9.8. Comparing the ΔD_{min}, we can see that in silica glass, the nonaffine displacement of atoms is small at low strains and increases with increasing compressive strain. With increasing sodium content, we notice that the intensity of the distribution decreases monotonically and shifts toward larger values of ΔD_{min}. This indicates that with increasing deformation and/or sodium content in the glass, the non-affine displacement of the atoms increases. This is explained by the fact that Na atoms have a weaker bond with the oxygen atoms, have a higher coordination number than Si atoms, and have higher atomic volume than Si; thus, they are more space to move. On the other hand, the movement of Si atoms is constrained by the glass network.

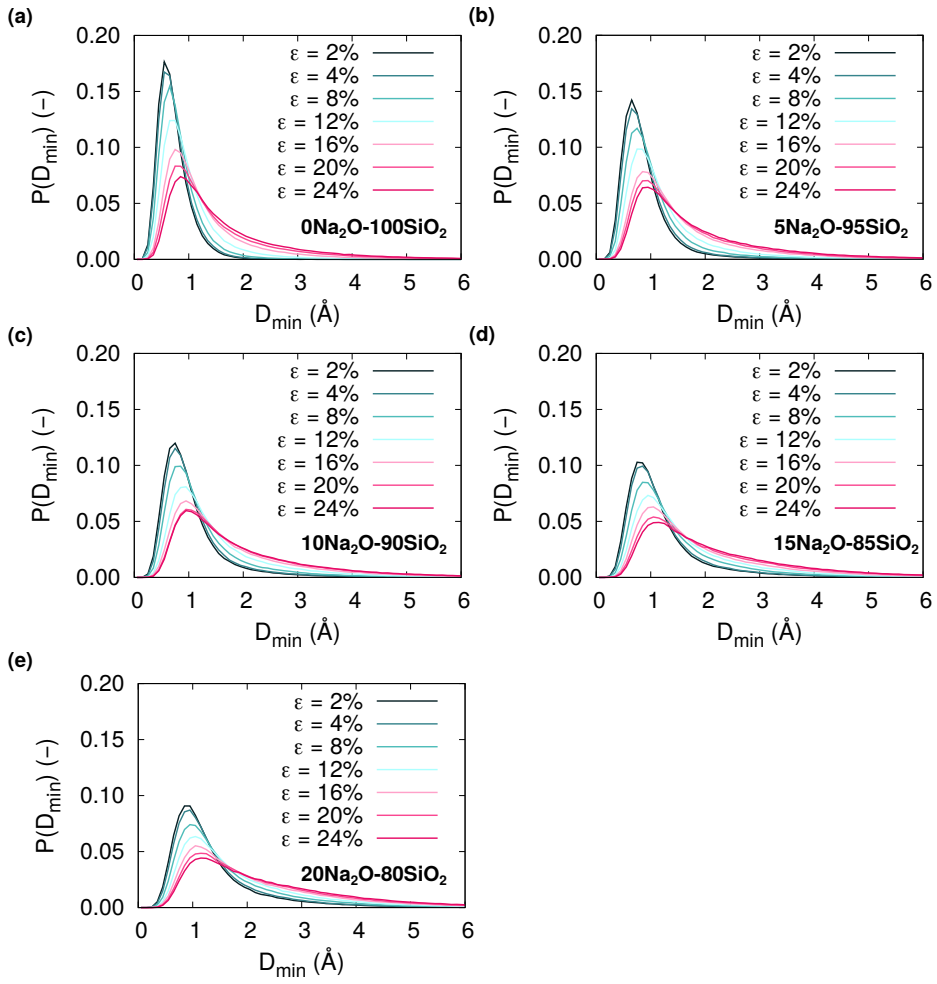

Figure. 9.8: The distribution of the total incremental nonaffine displacement ΔD_{min} during compressive deformation at 300 K and using 10^8 s^{-1} as a strain rate. All compositions are shown in the figure.

In Figure. 9.9 we show the mean incremental non-affine displacement $< \Delta D_{min} >$ as a function of strain for all glasses and all elements. The behavior of $< \Delta D_{min} >$ shows a dependence on the composition. For all glasses, the values of $< \Delta D_{min} >$ increase with strain until strains around 20% (around the maximum stress), then keep increasing but with a slope that is lower. This behavior is observed for all glass elements and is more pronounced for O and Si atoms than for Na atoms. The fact that $< \Delta D_{min} >$ only increases is in good agreement with the data obtained from the tangent modulus, indicating the decrease of the glass stiffness. The decrease of the tangent modulus is strong evidence that there is no hardening with increasing strain during uniaxial compression, which is similar to the experimental conclusions [120]. The behavior of $< \Delta D_{min} >$ of Si and O atoms follows the similar behavior of the total $< \Delta D_{min} >$. The effect of the composition on $< \Delta D_{min} >$ is more visible in the case of Na atoms than O and Si atoms. Thus we see that the change of the tangent modulus observed correlates well with the ability of

the atoms to move in a nonaffine manner. The nonaffine displacement of the atoms during compression is visualized in Figure. 9.10 for silica, and two selected sodium silicate glasses. The snapshots show a homogeneous distribution of the regions that have a high nonaffine displacement which increases with increasing Na_2O content.

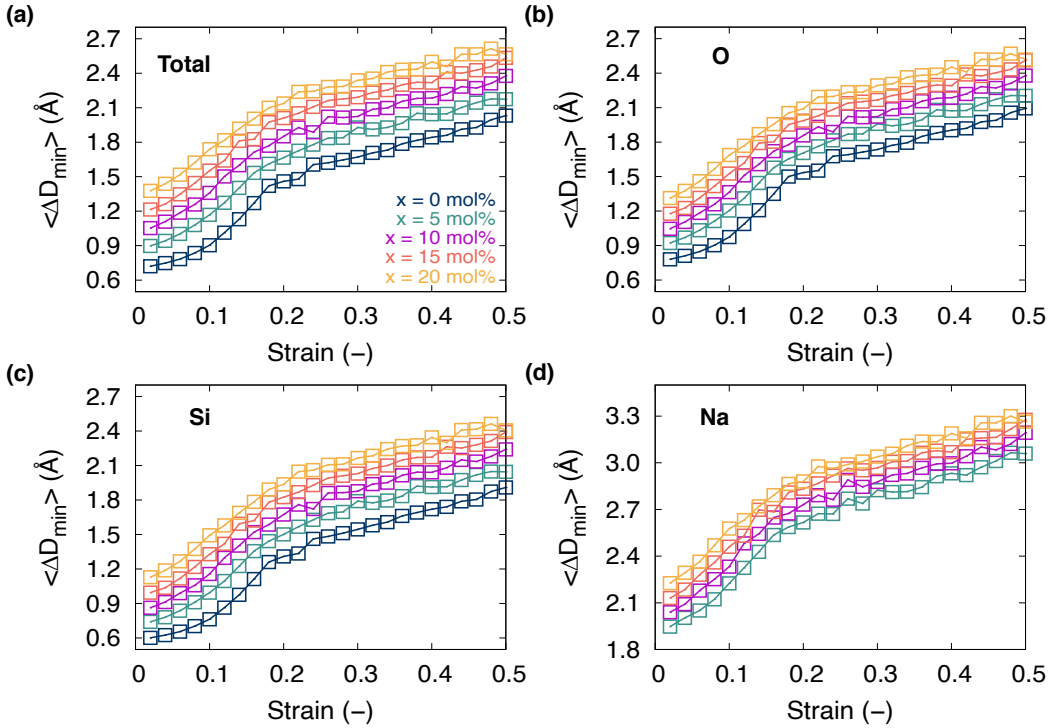

Figure. 9.9: Mean incremental nonaffine displacement $< \Delta D_{min} >$ as a function of strain for all silicate glasses during compression at 300 K using a strain rate of 10^8 s^{-1}. The subplots are represent the total $< \Delta D_{min} >$ (a), for oxygen atoms (b), for silicon atoms (c), and for sodium atoms (d). The strain increment was chosen as 2%.

Previous studies showed that the plasticity of silica glass is due to the bond switching events that occur before fracture [61, 230, 231]. This is observed from our analysis of the bonding events during the deformation. As shown in Figure. 9.11a, the number of bonds that changed their topology compared to the initial pristine state increase with increasing strain, and the percentage of atoms that switched bonds are way higher than those which have lost a bond or gained a bond. The distribution of the bonds that changes topology in the glasses is visualized for silica glass and two sodium silicate glasses in Figure. 9.11b and Figure. 9.12. These figures show that the bond change events occur almost randomly and evenly through the glass network. However, a closer look at the Si atoms that have a change in their neighbors shows that there is a weak localization in the form of a shear band which is highlighted in Figure. 9.12. This observed shear banding is consistent with the experimental observations [19, 113, 120, 229, 238]. More bond switching happens with sodium content increase, and the network has more elements with higher coordination numbers.

Compared to tension, the percentage of new Si–O bonds formed is higher during com-

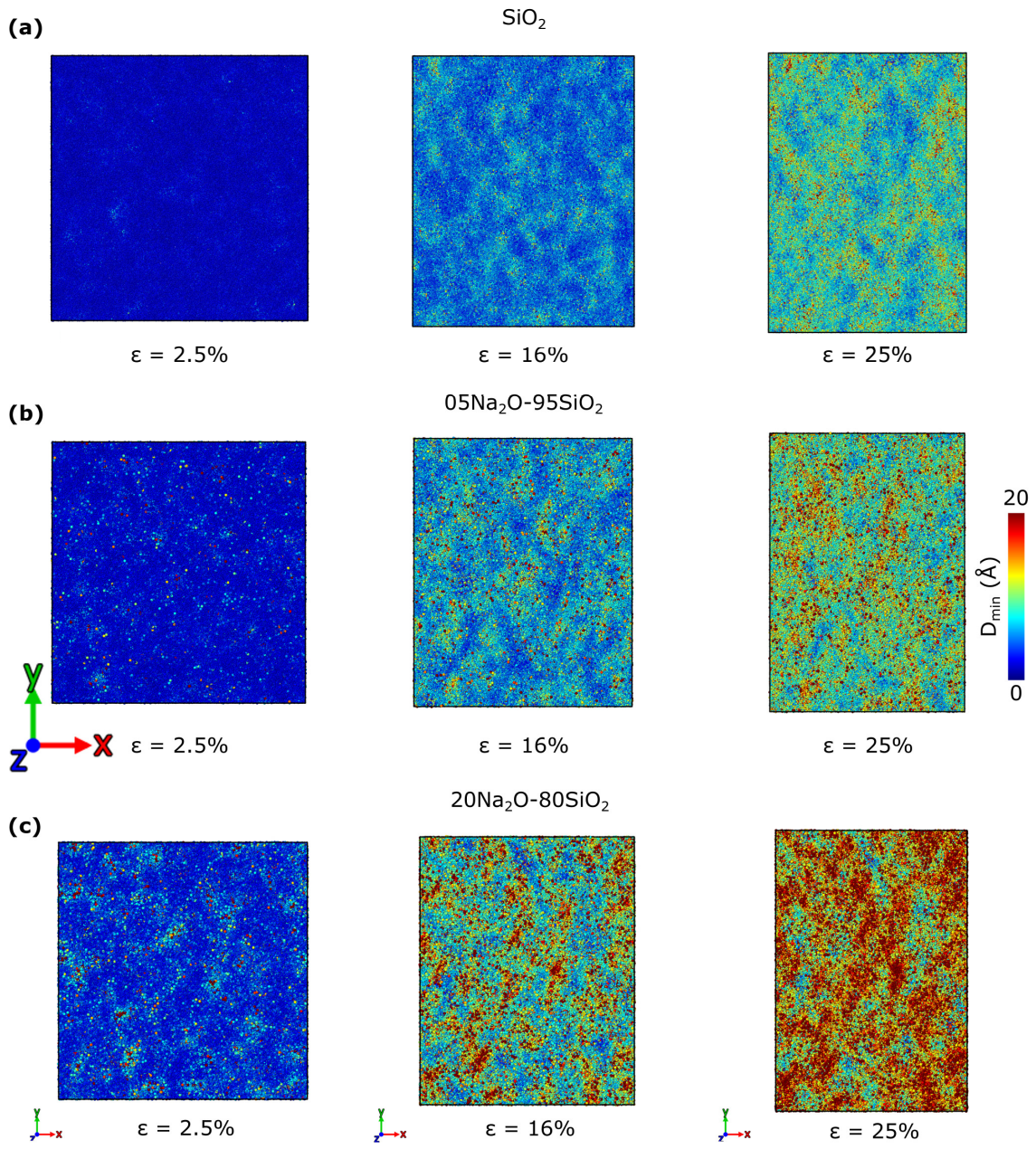

Figure. 9.10: Snapshots at different strains during compression along the $x-$axis at 300 K and using a strain rate of 10^8 s^{-1}. The atoms are colored based on the value of the nonaffine displacements. (a) for silica glass, (b) for the composition with 5 mol% of Na_2O, and (c) for the composition with 20 mol% of Na_2O. For all samples, the undeformed glass was used as a reference configuration, and a cutoff of 5.5 Å was used for the non-affine displacement calculation to get a smoother gradient and, at the same time, resolve the locality of the changes.

pression. The sodium was shown to have almost no effect on forming a new bond during tensile deformation. On the other hand, the number of broken bonds is larger in tension

than in compression, as, during tension, the atoms are separated from each other due to the increase of the strain. It is, however, worth stressing that the effect of Na addition is similar in both deformation modes. The number of Si atoms that switched at least a bond is higher in compression compared to tension, which is also expected from the behavior of the stress-strain curves, as during compression, the glasses deform plastically during compression. As we showed in the previous section, adding Na to the silica glass network tends to limit the Si–O bond breaking and increase the number of Si–O bond switching, which delays the glasses' fracture. During compression, the behavior of Si that switched bonds is similar for all compositions with few changes at strains between 10% and 22% where the number of Si atoms that switched a bond is higher in the sample that contains Na compared to the silica glass. At strains larger than 22% the behavior is reversed. Thus, Na generally reduces Si–O bond breaking and slightly affects bond switching.

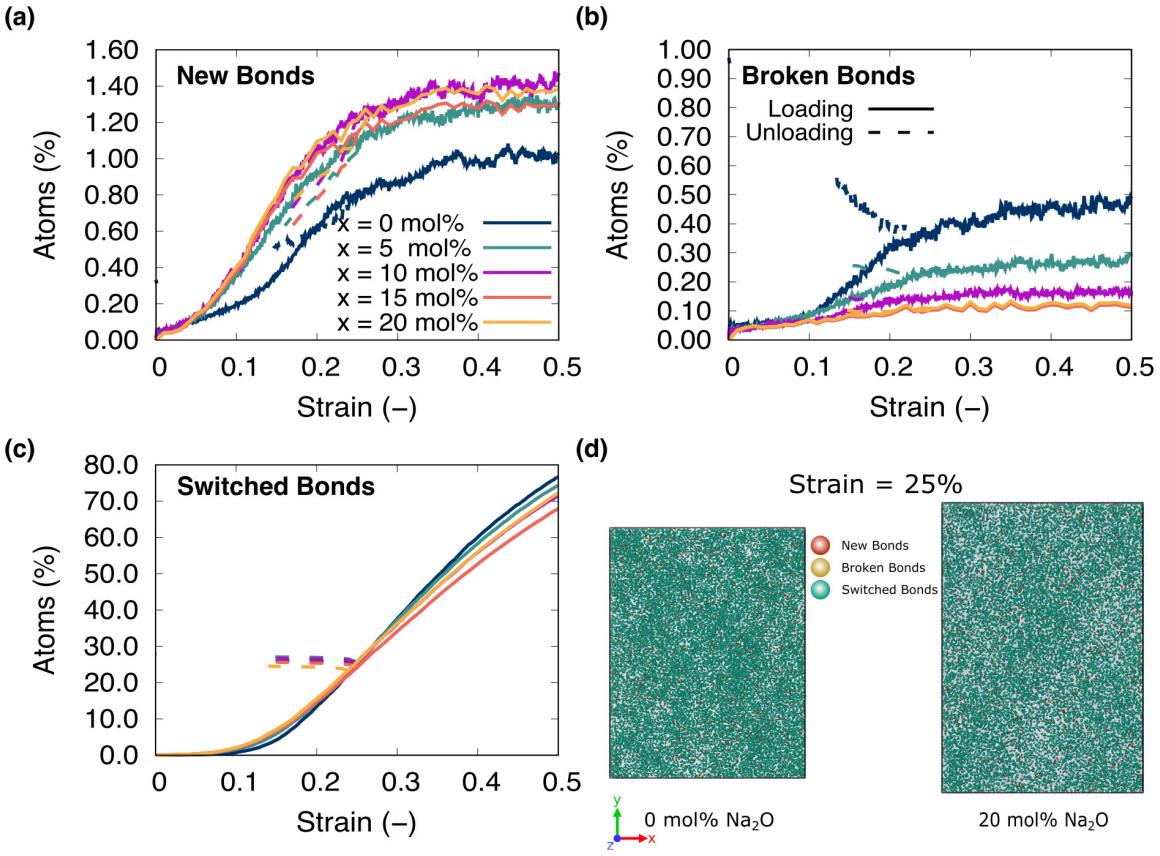

Figure. 9.11: Bond statistics of Si atoms during compression along the $x-$axis at 300 K and using a strain rate of 10^8 s^{-1}. (a) percentage of Si atoms that have a new bond, (b) percentage of atoms that have a broken bond, (c) percentage of atoms that have a switched bond, and (d) snapshots showing only the atoms that have a change in their bonding topology at 25% strain for both a silica glass and the sample with 20 mol% of Na_2O.

During compression, the samples are deformed nearly homogeneously, and the atoms with high shear strain, nonaffine displacement, and that changed bond topology are homo-

geneously distributed in the glass network. The snapshots nicely show this in Figure. 9.7, Figure. 9.10, Figure. 9.11 and is independent of the composition. The sodium content affects the number of Si atoms that had a change in their neighbors; with increasing sodium content, more atoms have a higher shear strain or higher nonaffine displacement. It is, however, worth stressing that some localization of the atoms that had a change in their neighbors was observed, and it is highlighted in Figure. 9.12. The obtained strength of 7.2 GPa for silica glass from our simulations is about 0.2 GPa higher than the reported experiments [120].

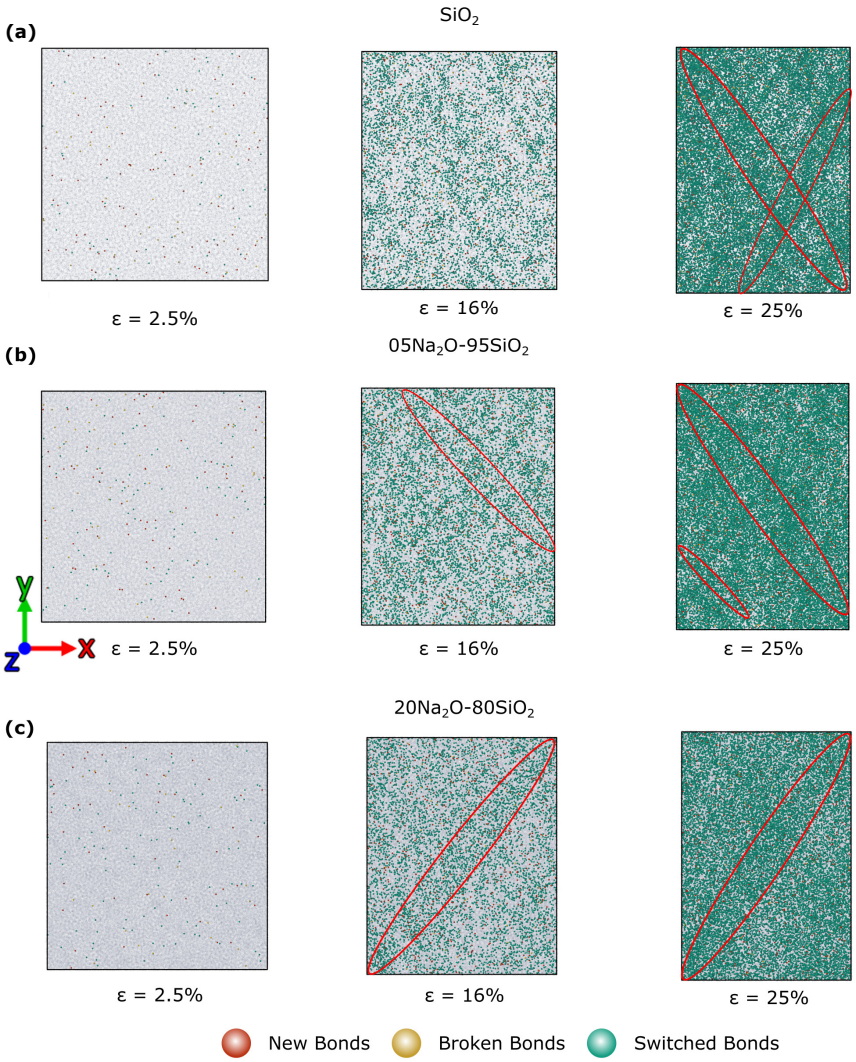

Figure. 9.12: Atomic snapshots at different strains during compression along the $x-$axis at 300 K and using a strain rate of 10^8 s^{-1}, showing only Si atoms that have a change in their bonding topology. (a) for silica glass, (b) for the composition with 5 mol% of Na_2O, and (c) for the composition with 20 mol% of Na_2O.

Deformation under shear

The stress over strain extracted from the stress-strain curves during the shear deformations showed a nonlinear behavior similar to tension and compression. This is expected since this behavior was found in both tension and compression. The current behavior of the tangent modulus obtained from the shear deformation can not be compared to experiments as we are unaware of any work that did a similar study. As in tension and compression, this behavior is more pronounced in the silica glass and reduces with increasing sodium content. This is explained by the higher mobility of sodium and its ability to add more flexibility and heterogeneity to the structure. A clear transition in the stress values over the strain in shear is observed around the strain at which the stress drops for silica and low sodium content sodium silicate glasses. The absence of the transition in the tangent modulus in the glasses with high sodium content is similar to the absence of the stress drop with the increasing sodium content. This is due to the ability of Na atoms to move and release stress.

To compare the elastoplastic response of the samples during shear, we performed several structural analyses. The stress drop in the stress-strain curves (See Figure. 8.5) is due to the appearance of a shear band in the structure. To better quantify this, we calculated the strain localization parameter during the strain deformations as shown in Figure. 9.13. For the silica glass at the same strain at which the stress drop, there is a strong increase in the strain localization parameter, indicating the development of a shear band. The same behavior is valid for glasses with low sodium content. The shear deformation in glasses with higher sodium content is more homogeneous as no increase in the strain localization parameter was observed, and no clear shear band was observed in the structure (See Figure. 9.13b). This shows that the dissipative rearrangements are localized, which is different from the case of compression, where they were evenly distributed in the entire sample.

In Figure. 9.13c - g, we show the local distribution of voids with a radius larger than 3.5 Å for all glasses we studied. The change in the void with strain is also shown in the snapshots for different selected strains during the shear deformation. In the pristine silica glass, a large number of voids is present in the structure, which is normal as silica glass is known to have an open structure compared to other oxide glasses [238]. With the increase of Na_2O content, the number of voids gets reduced until it almost disappears in the sample with 20 mol% of Na_2O. The disappearance of voids with increasing Na_2O content is in line with the fact that Na tends to be located in the empty regions in the glass [76]. With the increase of the shear strain, a coalescence of the voids happens in the silica glass leading to the formation of a large void parallel to the shear band and shear direction. This void is, in fact, within the shear band as highlighted in Figure. 9.13c with the red shape. Similar observations are made for the samples with 5 and 10 mol% of Na_2O, but with a lesser void coalescence (See Figure. 9.13d - e). The sample containing larger sodium content does not show a void coalescence (See Figure. 9.13f - g), which is due to the compact structure of the glass compared with the other compositions with lower Na_2O content.

To further characterize the local structure and better understand the formation of the shear bands, we performed a bond statistics analysis and visualized the location of the atoms that have changed in their bond topology. The results of this analysis are shown in

Figure. 9.14. The number of atoms with a new or broken bond in silica glass is less than 1.5%. However, the percentage of switched bonds is 10 times higher than the new and broken bonds. The percentage of the switched bonds increases rapidly after the stress drop. Since the shear deformation of the samples containing low sodium content is localized, it is expected that the Si atoms that had a change in their neighbors should also be localized. The Figure. 9.14b clearly shows this. Most atoms that change their bonding partner are located within the shear band. With the increase of the sodium content, the distribution of those atoms is more homogeneous.

Another important observation from our simulations and analysis is that adding Na_2O to the silica glass network helps decrease the number of Si atoms than have broken bonds. This behavior is observed in all three deformation modes we studied. The percentage of Si atoms with at least one bond switched is higher in the silica glass than in the sodium silicate glasses.

Analysis using the incremental nonaffine displacement showed an increase in this parameter. However, this increase was low compared to tensile and compressive deformations. The nonaffine displacement is calculated to visualize the atoms involved in the plastic deformation in the glasses. This reflects the displacement of atoms induced by shear deformation. Figure. 9.17 shows the nonaffine displacement distributions at different strains for two glass samples. One can observe that the sample with 5 mol% of Na_2O shows a clear shear band while the sample with 20 mol% of sodium does not show a clear shear band. This is because more atoms are involved in the plastic deformation for the sample with larger sodium content. Therefore, the local plastic events are more localized within confined regions in the sample with 5 mol% of Na_2O content, while they are more homogeneous in the sample with 20 mol% of sodium.

In silica glass, the plasticity is induced by localized rearrangements [239]. Therefore, the localized rearrangements in the glasses are due to the large values of the nonaffine displacement. This is because atoms with large strain cannot be accommodated by the matrix elastically [239, 240]. The nonaffine displacement analysis provided here highlights that the shear localization behavior accompanies the abrupt drop in the stress-strain curve.In addition, the percentage of Si atoms that changed bonding partner decreases with increasing sodium content. The possible explanation for this observed behavior can be ascribed to the higher sodium atom content, which is flexible and can move to accommodate the stress without altering the Si–O network. Thus the structure can adapt to the imposed deformation by not changing the Si–O network too much, and this is not the case in the silica glass or the low sodium content glasses.

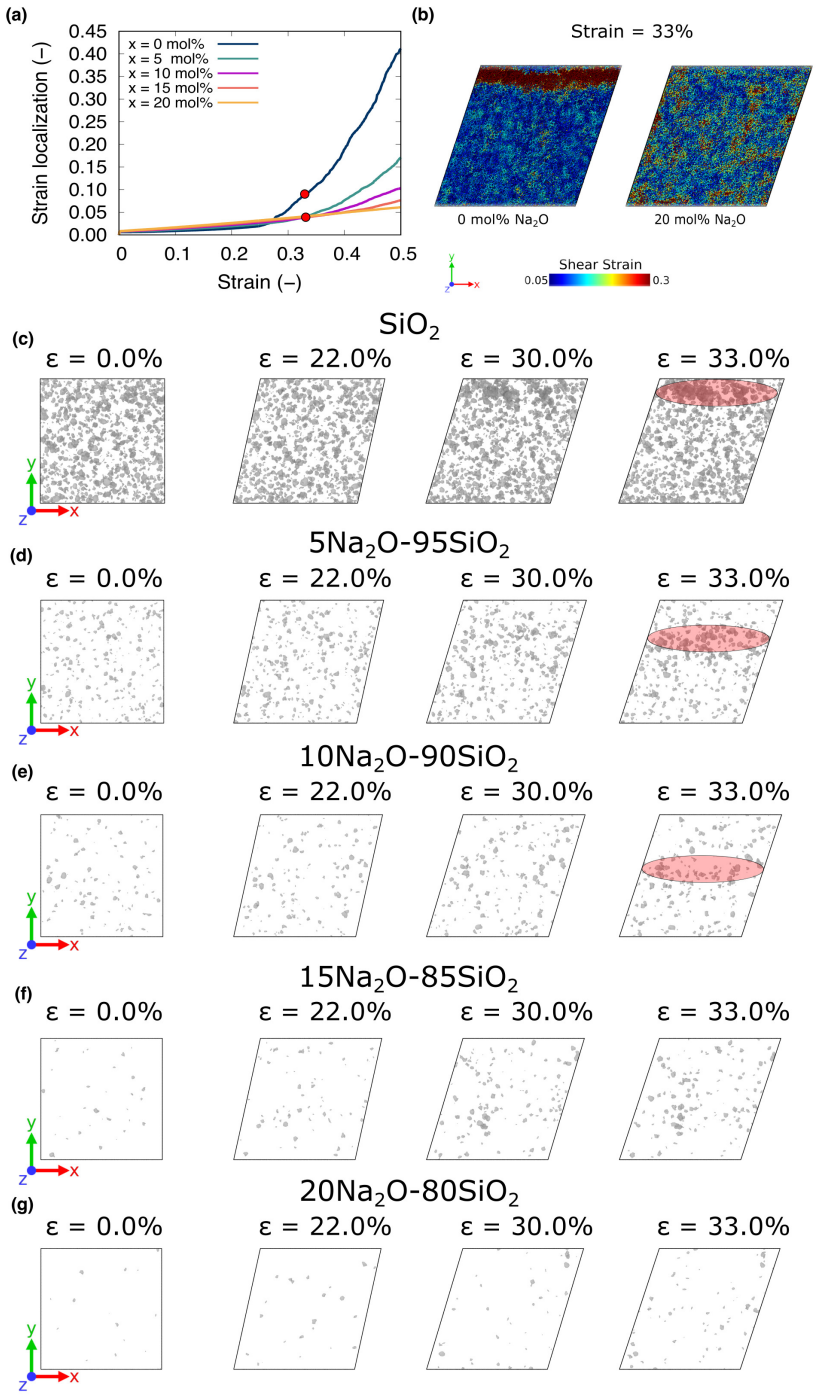

Figure. 9.13: (a) Strain localization parameter *vs.* strain during shear deformation at 300 K and using a strain rate of 10^8 s^{-1}. (b) Local atomic shear strain for the silica glass and sodium silicate glass containing 20 mol% of Na_2O at 33% shear strain. (c - g) show snapshots at different selected strains during shear deformation of the pristine silicate glasses. The snapshots show the evolution of voids constructed using a mesh with a probe radius of 3.5 Å, chosen as the first minimum of Na-O RDF. The strains were selected when a significant change in the void formation or void structure is observed. The red shaded region highlight the location of the shear band.

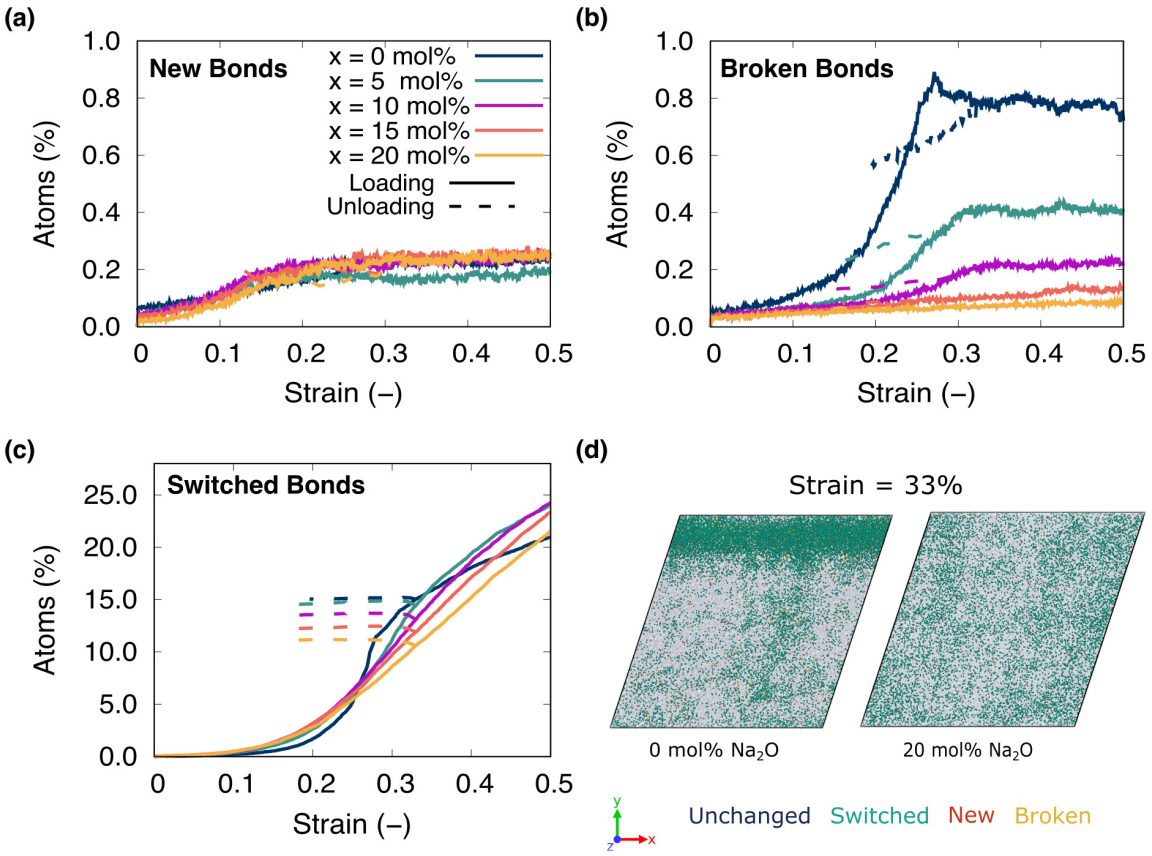

Figure. 9.14: Bond statistics of Si atoms during shear at 300 K and using a strain rate of 10^8 s^{-1}. (a) percentage of Si atoms that have a new bond, (b) percentage of atoms that have a broken bond, (c) percentage of atoms that have a switched bond, and (d) snapshots are showing only the atoms that have a change in their bonding topology at 33% strain for both a silica glass and the sample with 20 mol% of Na_2O.

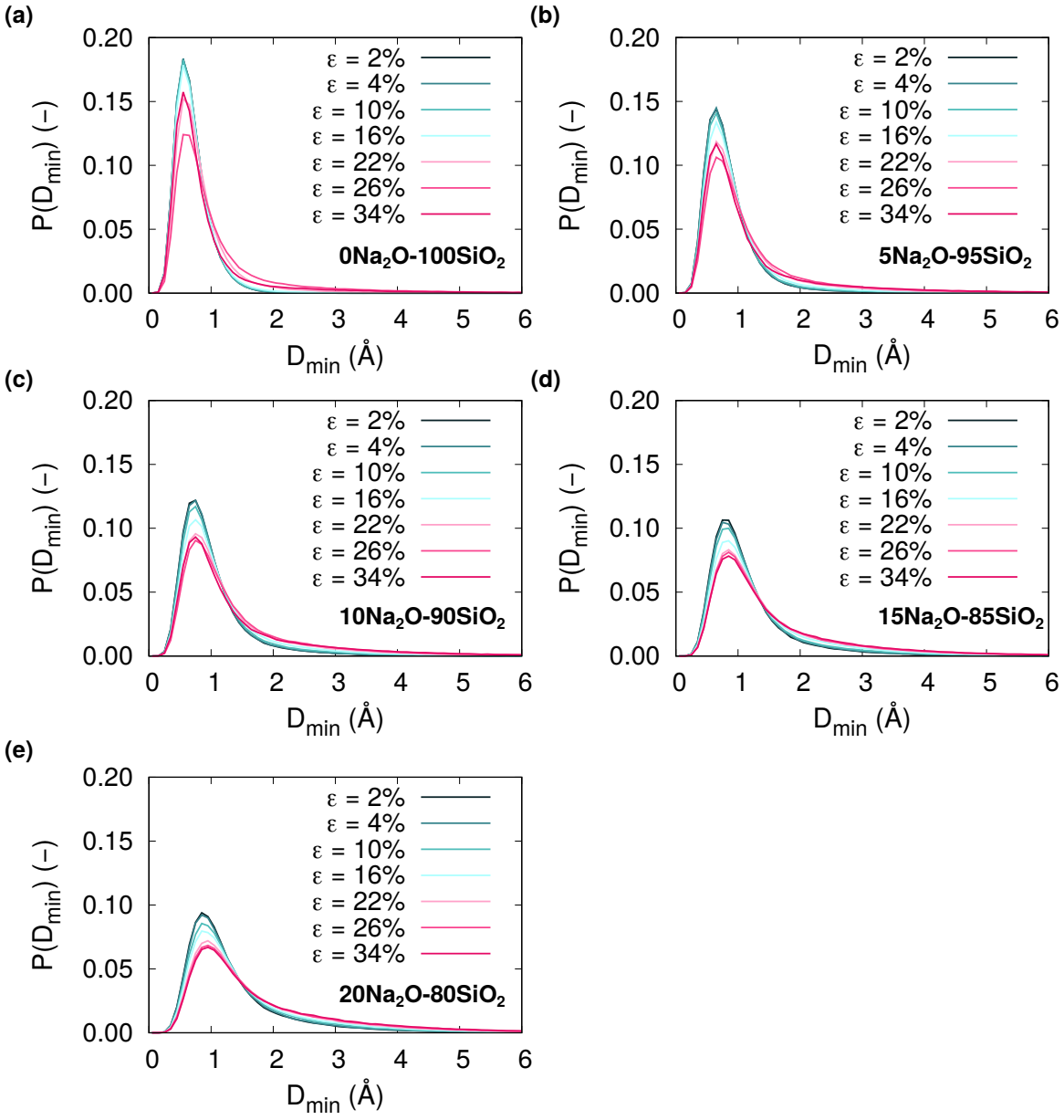

Figure. 9.15: The distribution of the total incremental nonaffine displacement ΔD_{min} during simple shear deformation at 300 K and using a strain rate of 10^8 s^{-1}. All compositions are shown in the figure.

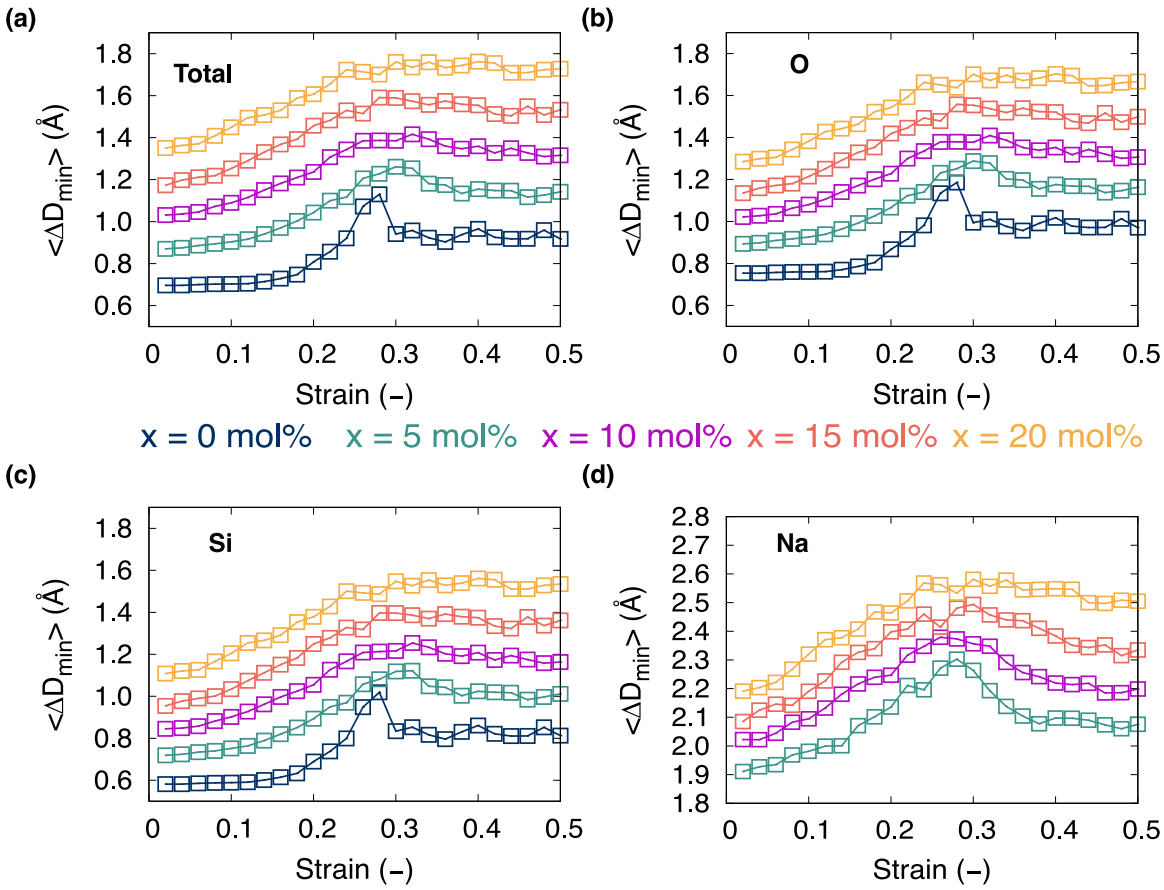

Figure. 9.16: Mean incremental nonaffine displacement $< \Delta D_{min} >$ as a function of strain for all silicate glasses during shear deformation at 300 K and using a strain rate of 10^8 s^{-1}. The subplots are represent the total $< \Delta D_{min} >$ (a), for oxygen atoms (b), for silicon atoms (c), and for sodium atoms (d). The strain increment was choosen as 2%.

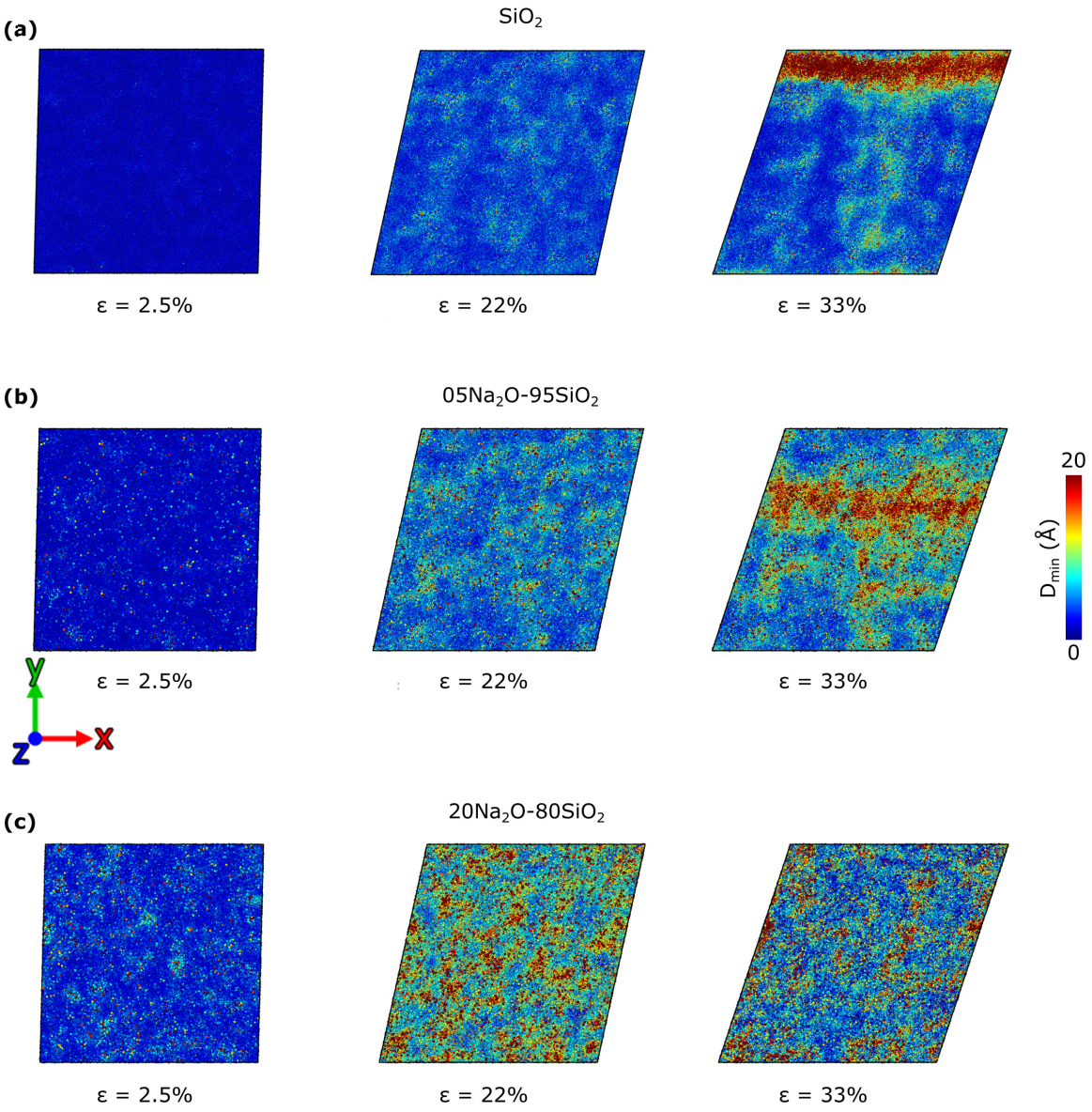

Figure. 9.17: Snapshots at different levels of strain during shearing at 300 K and using a strain rate of 10^8 s^{-1}, the atoms are colored based on their value of the nonaffine displacements. (a) for silica glass, (b) for the composition with 5 mol% of Na_2O, and (c) for the composition with 20 mol% of Na_2O. For all samples, the undeformed glass was used as a reference configuration, and a cutoff of 5.5 Å was used for the non-affine displacement calculation to get a smoother gradient and, at the same time, resolve the locality of the changes.

It is accepted to this point that the flow in disordered materials is due to localized plastic rearrangement [113, 241]. Martens *et al.* [242] observed the spontaneous formation of permanent shear bands using a mesoscopic model of flowing disordered matter. Mantisi *et al.* [19, 117] studied the mechanical response of silica glass under shear and hydrostatic pressure. They revealed that the shear strength decreases with increasing pressure which

was explained by the pressure-induced homogenization of atomic displacement. Similar observations were made by Molnar *et al.* [79, 227, 229], where they studied the effects of composition and pressure on the elastic moduli and shear response of sodium silicate glasses. They observed the same effect of the pressure on the shear stress. However, they showed that the effect of the pressure on the shear stress tends to disappear with increasing sodium content. From our simulations, we observed that the composition has a similar effect on the distribution of the strain localization parameter (See Figure. 9.13), atoms that changed their neighbors (See Figure. 9.14), and distribution of the nonaffine displacement (See Figure. 9.17). With increasing sodium in the glass network, the distribution of these local properties transforms from begin localized in the shear band in the case of silica glass to being homogeneously distributed in the case of silicate glasses with higher sodium content. It is to be noted that performing shear deformation over many glass samples (three in our case) prepared using the same way will lead to a stochastic appearance of either horizontal or vertical shear band(s), which was also reported in the literature [243] and its origin is still being investigated. The effect of the local structural change due to the shear pre-deformation has remained unstudied and will be discussed in the following sections.

9.3 Deformation mechanism of pre-deformed silicate glasses

In this section, we will discuss the deformation behavior of the pre-deformed glasses. The glasses were prepared using the protocol described in Chapter. 3 with 375000 atoms and a cooling rate of 1 K/ps. The as-cooled glasses were loaded in tension, compression, or shear and unloaded to obtain a stress-free sample from different strains achieved in each deformation. The stress-free pre-deformed glasses are then reloaded in tension to evaluate their tensile deformation behavior. All deformations were performed at 300 K and using a strain rate of 10^8 s^{-1}. Since all glasses almost behaved similarly as was shown in the previous chapter, we here will focus only on some selected compositions the samples unloaded from the higher strain level here, i.e., 15%, 25%, and 33% for tension, compression, and shear, respectively. All other glasses behave similarly.

Tensile tests on glasses pre-loaded in tension

In Figure. 8.9, we showed the stress-strain curves of the silicate glasses pre-deformed in tension along the x-axis up to different strains, unloaded to zero-stress state, and reloaded back in tension along the three box axes independently. The deformation behavior of the pre-deformed silica glass showed no significant change. This was expected due to the limited plasticity observed before fracture and the small plastic strain (i.e., 1%) recorded for these unloaded glasses. Moreover, The number of atoms that had a permanent change in their bonding partner after unloading from 14% strain tensile strain to zero stress was less than 2% (See Figure. 9.4).

To discuss the effect of the sodium content, we will focus on the sample with 15 mol% of sodium, and the behavior of other glasses is similar. This exact composition has no rational choice and is mainly based on the authors' preference. The plastic strain values increase with increasing sodium content to reach a value of 2%. This increase in the plastic strain

was found to be due to an increase in the number of atoms that had a permanent change in their bonding topology, as shown in Figure. 9.4. The deformation of the tensile pre-deformed and reloaded glasses showed no change in the behavior of the tangent modulus as indicated by the σ/ϵ-strain curve of silica glass shown in Figure. 9.18a and b, similar behavior is observed for all other glasses. This highlights that the pre-deformation in tension weakly affects the glass structure due to the limited plasticity.

Tensile tests on glasses pre-loaded in compression

In Figure. 8.10, we showed the stress-strain curves of the silicate glasses pre-deformed in compression along the x-axis up to different strains, unloaded to zero stress state, and reloaded back in tension along the three box axes independently. The deformation behavior of the pre-deformed silicate glasses significantly changed with increasing plastic strain. As shown in Table. 8.7, an increase in the density of the unloaded glasses as compared to the pristine ones is observed for all glasses irrespective of the composition, which highlights that uniaxial compression leads to a densification of the glass. This has already been observed experimentally for uniaxial compression of silica glass [244, 245]. As reported in Table. 8.8, the plastic strain increased with increasing unloading strain and also with increasing sodium content. The sample with larger plastic strain showed a significant change in their deformation behavior when reloaded in tension. Focusing on the sample unloaded from 25% compressive strain, we observed a substantial decrease in Young's modulus and strength. In addition to that, the failure toughness and fracture strain increased. This behavior was observed for all glasses irrespective of the composition. The pre-deformed and unloaded glass samples contained around 25% of Si atoms that have a permanent change in their bonding topology (See Figure. 9.11). The distribution of these bonds was homogeneously distributed in the glass network for all glasses. This has led to a significant change in the deformation behavior, and the observed anisotropy in the mechanical properties is due to a change in the orientation of the basic structural units of the silicate glasses [194]. The deformation of the compression pre-deformed and tensile reloaded glasses showed a transition from hardening to a softening of the tangent modulus. The degree of the softening increase with increasing plastic strain and is observed in all directions in the silica glass (See Figure. 9.18c and d). The softening transition observed for silica glass due to the densification and the pre-deformation in compression is qualitatively similar to the one resulting from sodium's addition to the glass network.

The Figure. 9.19 shows the existence and evolution of cavities as a function of the tensile strain and composition from the samples pre-deformed in compression up to 25% strain and unloaded to zero stress. As also was shown in Figure. 9.5c - g and at zero strain (pristine samples), the silica glass has more voids (cavities) with a radius larger than 3.5 Å and with the increase of the sodium content, these voids tend to disappear. This disappearance of cavities with increasing sodium content is consistent with previous MD simulations [246]. Compared to the pristine glasses, the samples pre-deformed up to 25% compressive strain and unloaded to zero stress show a reduced number of cavities with a radius larger than 3.5 Å. When these unloaded glasses are subjected to tension along the same axis as the one used in the pre-deformation (x-axis), the voids start growing, and a coalescence

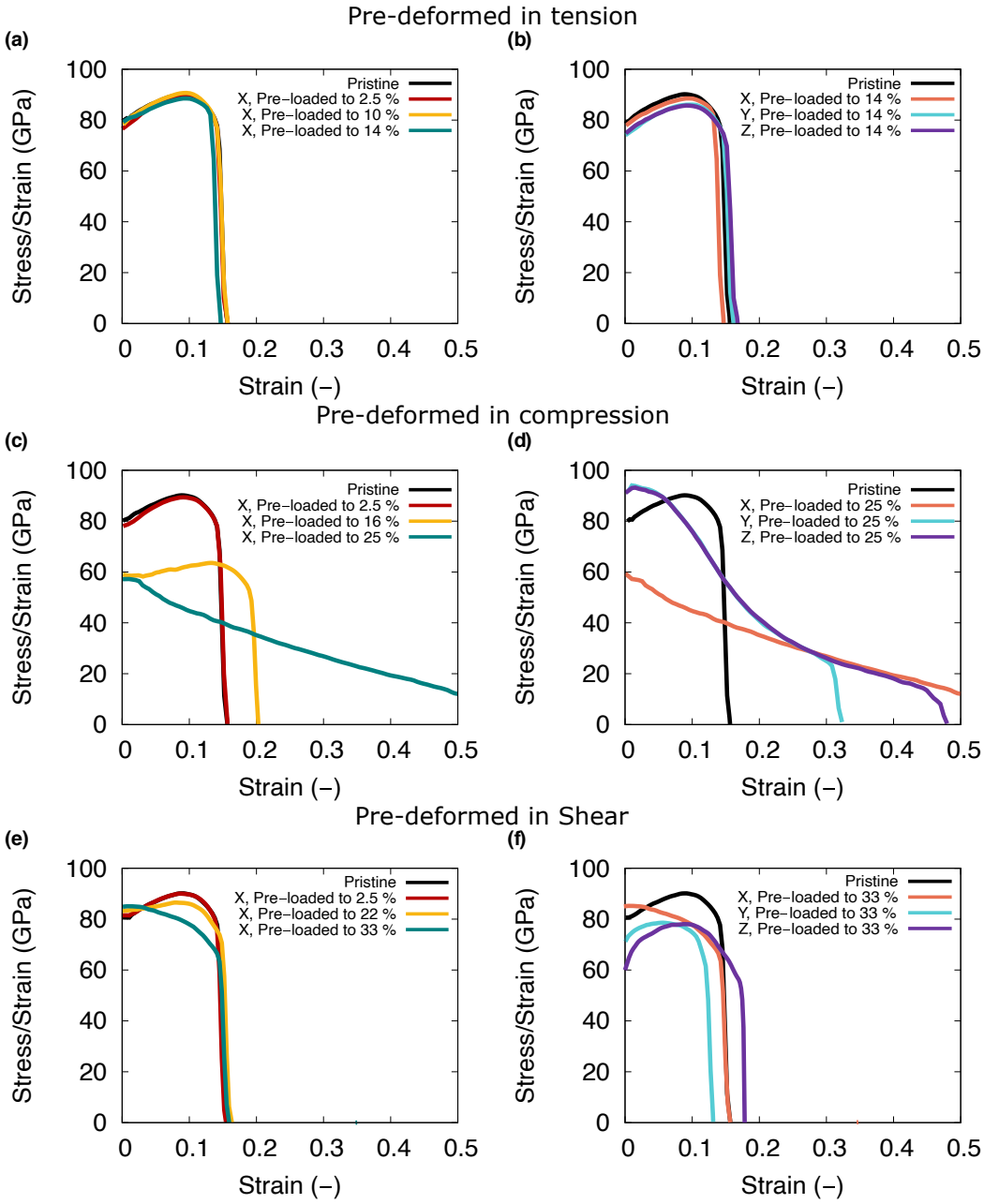

Figure. 9.18: The ratio between stress and strain, σ/ϵ of pristine silica glass and pre-deformed glasses reloaded in tension. (a and b) are for tensile pre-deformation, in (a) we show the effect of the unloading strain, while in (b) we show the effect of reloading along different box axes for only one unloading strain. (c and d) are for compressive pre-deformation, in (c), we show the effect of the unloading strain, while in (d), we show the effect of reloading along different box axes for only one unloading strain. (e and f) are for shear pre-deformation, in (e), we show the effect of the unloading strain, while in (f), we show the effect of reloading along different box axes for only one unloading strain. The initial pre-deformation was performed along the x-axis for tension and compression, while the shear pre-deformation was performed by tilting the y-axis along the x-direction.

of these voids was observed in all samples. It is also worth stressing that the appearance of these cavities and their evolution with strain is strongly dependent on the glass's composition; as shown in Figure. 9.19, the coalescence of the cavities is more to happen in the samples with no or minor sodium content. Moreover, the increase of the fracture strain in the pre-deformed samples is explained by the fact that the pre-compression reduces the number of cavities in the glasses, which in turn will delay the fracture when the glasses are reloaded in tension. This mechanism of fracture through cavities formation agrees with previous simulations and experiments on similar and different types of oxide glasses [246–251].

Here, in our case, we show that the pre-compression can reduce the number of cavities in the glass, eventually leading to a delayed fracture compared to pristine glasses. Also, we show that the voids (cavities) naturally form during fracture or might already exist in the glass (e.g., Silica glass *vs.* sodium silicate glasses), which was studied systematically through the variation of the compositions, which helped in controlling the number of initial cavities in the pristine glasses. This highlights that these cavities also appear without preexisting microscopic flaws during tensile deformation. Sehgal and Ito [252] showed that the composition of the glass plays a very important role in the formation of defects in the glass. They highlighted that slight changes in glass composition strongly affect the formation of surface defects under sharp contact load [4, 252], as a result, new soda-lime-silica glass was developed with 30% lower brittleness than normal soda–lime–silica glass and a crack-initiation load 10 times higher than that of the commercial soda-lime-silica glass [4, 252].

On the other hand Januchta *et al.* and others [253–257] discussed the importance of ν as a parameter that can be used to get an idea on the contribution of the densification to indentation deformation. They showed that, for example, glassy silica exceeds the contribution of the densification to indentation deformation is around 90%, while the addition of modifiers to the silica network reduces the contribution of densification to indentation deformation to 60% taking soda lime silica glass as an example for comparison [256]. These measured contributions of the densification to the indentation deformation were correlated to the values of ν, where the tendency of densification of the glass under indentation decreases with increasing ν [253–256]. Altogether, these results highlight that the deformation mechanisms are not dependent only on the composition but can also be manipulated through the processing of the glass, such as pre-deformation [109, 255, 258].

Tensile tests on glasses pre-loaded in shear

In Figure. 8.11, we showed the stress-strain curves of the silicate glasses pre-deformed in shear by tilting the y-axis along the x-direction up to different strains, unloaded to zero stress state, and reloaded back in tension along the three box axes independently. The deformation behavior of the pre-deformed silicate glasses significantly changed with increasing plastic strain. As shown in Table. 8.9, an increase in the density of the unloaded glasses as compared to the pristine ones is observed for all glasses irrespective of the composition, which highlights that during constant volume shear deformation, the glasses want to densify. This has already been observed for silicate, borosilicate, and other oxide glasses in both

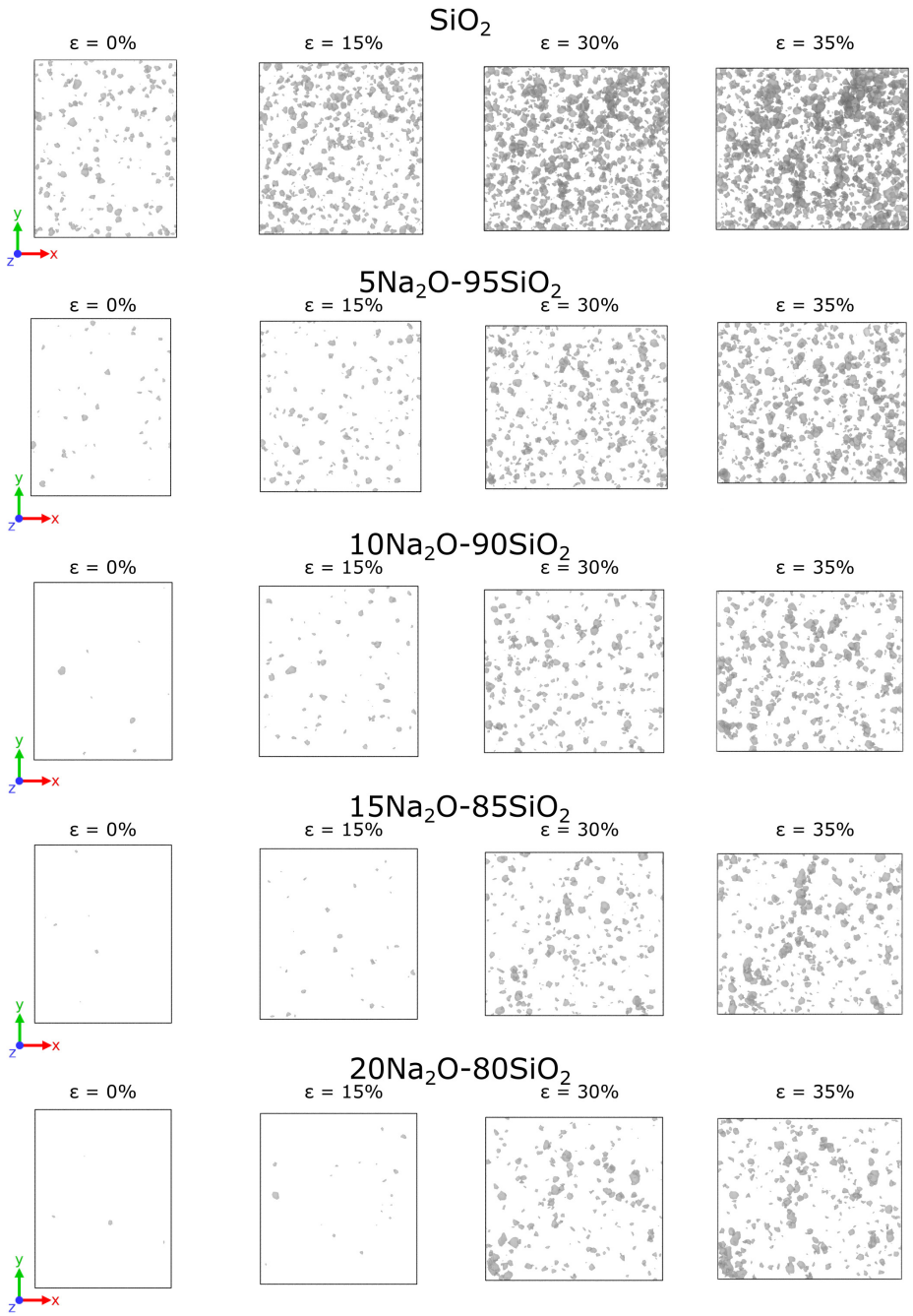

Figure. 9.19: The evolution of voids that have a radius larger 3.5 Å of the glasses pre-deformed up 25% compressive strain along the x-axis and unloaded to zero stress. The samples are reloaded again in tension along the x-axis at 300 K and using a strain rate of 10^8 s^{-1}. (a) Silica glass, (b) sodium silicate glass with 5 mol% of Na_2O, (c) sodium silicate glass with 10 mol% of Na_2O, (d) sodium silicate glass with 15 mol% of Na_2O, (e) sodium silicate glass with 20 mol% of Na_2O.

simulations [79, 239], and experiments [259, 260]. Mackenzie [259] proposed that the shear effect may be induced by the entanglement effect between two parts of the network under

pressure. As reported in Table. 8.10, the plastic strain increased with increasing unloading strain and decreased with increasing sodium content. The sample with larger plastic strain showed a significant change in their deformation behavior when reloaded in tension. Focusing on the sample unloaded from 33% shear strain, no change has been seen for Young's moduli. The strength showed a significant decrease in all reloading directions. However, it should be noted that this decrease is less visible with increasing sodium content and is almost not there in the samples with 20 mol% of Na_2O. This is mainly because with increasing Na_2O content, the structure becomes more flexible, and the decomposition of the structure into two regions leads to enhanced flexibility [261, 262]. Also, it should be noted that the composition that has 20 mol% of Na_2O has the lowest elastic constants C_{11} and C_{44} and is considered as an intermediate phase following the topological constraints theory [261, 262]. The failure toughness and fracture strain increased with increasing unloading strain and sodium content. This behavior was observed for all glasses irrespective of the composition. The pre-deformed and unloaded glass samples contained between 15% and 11% of Si atoms that have a permanent change in their bonding topology (See Figure. 9.14) depending on the composition. The change in the Si atoms that have a permanent change in their bonding topology is due to the ability of Na atoms to move, change partners, and release the stress without altering the Si network too much [219]. The distribution of these bonds was localized within the shear band in the silica glass, and their distribution became more and more random with increasing sodium content. This explains the disappearance of the stress drop from the loading curves as no shear band is formed. Moreover, it should be highlighted that the silica glass unloaded from 33% shear strain contains a large void in its structure which is shown in the snapshots in Figure. 9.20a and b. The snapshots nicely show that in the top-left region of the box, there is a large region with low density, and performing a mesh to extract the region with surfaces using a probe radius of 4 Å showed the existence of this void. Other regions along the shear band have a higher density than the mean value of 2.25 (g/cm^3).

The localization of most atoms that change their bonding topology has significantly changed the deformation behavior. While no change has been observed within the elastic regime, significant changes in the failure strain were recorded. The deformation of the shear pre-deformed and reloaded silica glass showed a considerable change in the strength, failure strain, and failure toughness of the sample reloaded along the three different axes. This is explained by the presence of the large void along the shear band plane (xz-plane), and when performing the reloading tests, this void plays a role of a pre-existing crack. Thus, the mechanical behavior of the glass will depend on the loading direction. When loaded in a direction normal to the shear band plane (y-direction in this case), it is like we are simulating a mode I fracture, and the void quickly extends, and the crack propagates, leading to an early fracture of the sample. This is nicely shown in Figure. 9.20b. However, when reloaded in the other directions orthogonal to the normal shear band plane, the void does not play the role of a crack but weakens the structure, which explains the lower strength compared to the pristine glasses and the similar failure strains. Similar behavior was observed in the sample with 5 mol% of Na_2O but not in the other glass compositions. The increasing Na_2O content explains this, and the structure becomes less open and compact because Na atoms fill the empty space in the silica network. This is confirmed by

increasing the density value with increasing sodium content.

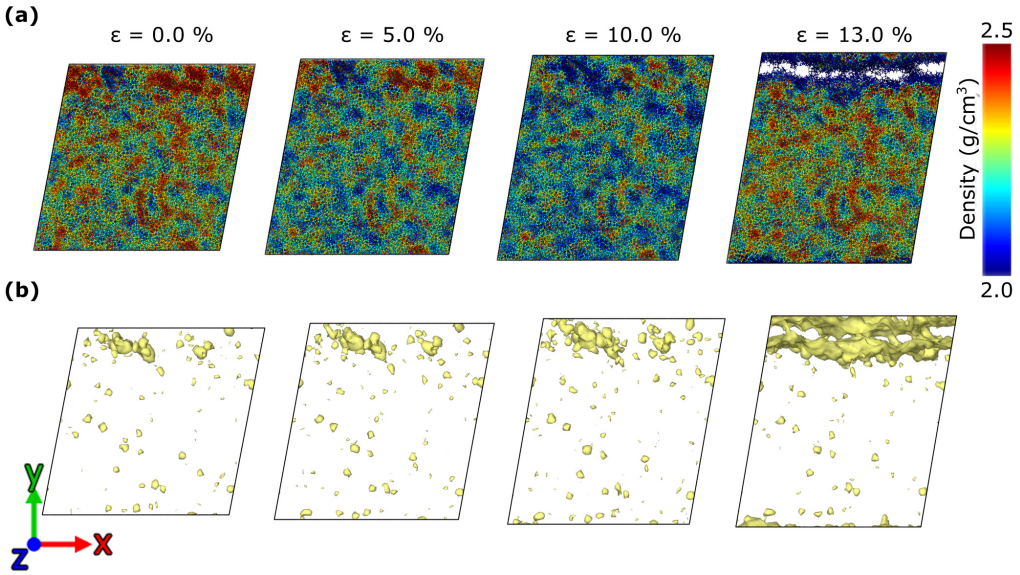

Figure. 9.20: (a) Snapshots are showing the change of the local mass density at different loading states during the uniaxial tensile test along the y-axis of the silica glass pre-deformed in shear by tilting the y-axis along the x-direction at 300 K and using a strain rate of 10^8 s^{-1}. The snapshots shown in (b) are for a mesh indicating the presence of a void. The mesh was constructed by using a probing sphere of 3.5 Å.

The Figure. 9.21, shows the existence and evolution of cavities as a function of the tensile strain and composition from the samples pre-deformed in shear by tilting the y-axis along the x-direction up to 33% strain and unloaded to zero stress. As also shown in Figure. 9.13c - g and at zero strain (pristine samples), the silica glass has more voids (cavities) with a radius larger than 3.5 Å and with the increase of the sodium content, these voids tend to disappear. As we discussed, this disappearance of cavities with increased sodium content is consistent with previous MD simulations [246]. Compared to the pristine glasses, the samples pre-deformed up to 33% shear strain and unloaded to zero stress show that the number of cavities with a radius larger than 3.5 Å generally increases compared to the pristine glasses. They are more localized in the shear band in the samples that showed the presence of shear bands, which is highlighted with the red ellipsoid in Figure. 9.21a - c.

When these unloaded glasses are subjected to tension along x-axis, the voids start growing, and a coalescence of these voids was observed in all samples. It is also worth stressing that the appearance of these cavities and their evolution with strain is strongly dependent on the glass's composition; as shown in Figure. 9.21, the coalescence of the cavities is more to happen in the samples with no or minor sodium content. Moreover, the shear band's location and orientation strongly affect the fracture behavior of these pre-deformed glasses, which was discussed in the above paragraphs for the case of silica, but the same logic applies to all other samples. The effect of sodium content plays a significant role in the appearance of the shear bands. The glasses with more sodium tend not to show the shear bands.

The increase of the fracture strain in these pre-deformed samples is explained by the fact that the pre-compression reduces the number of cavities in the glasses, which will delay the fracture when the glasses are reloaded in tension. This mechanism of fracture through cavities formation agrees with previous simulations and experiments on similar and different types of oxide glasses [246–251].

Here, in our case, we show that the pre-compression can reduce the number of cavities in the glass, eventually leading to a delayed fracture compared to pristine glasses. Also, we show that the voids (cavities) naturally form during fracture or might already exist in the glass (e.g., Silica glass *vs.* sodium silicate glasses), which was studied systematically through the variation of the compositions, which helped in controlling the number of initial cavities in the pristine glasses. This highlights that these cavities also appear without preexisting microscopic flaws during tensile deformation.

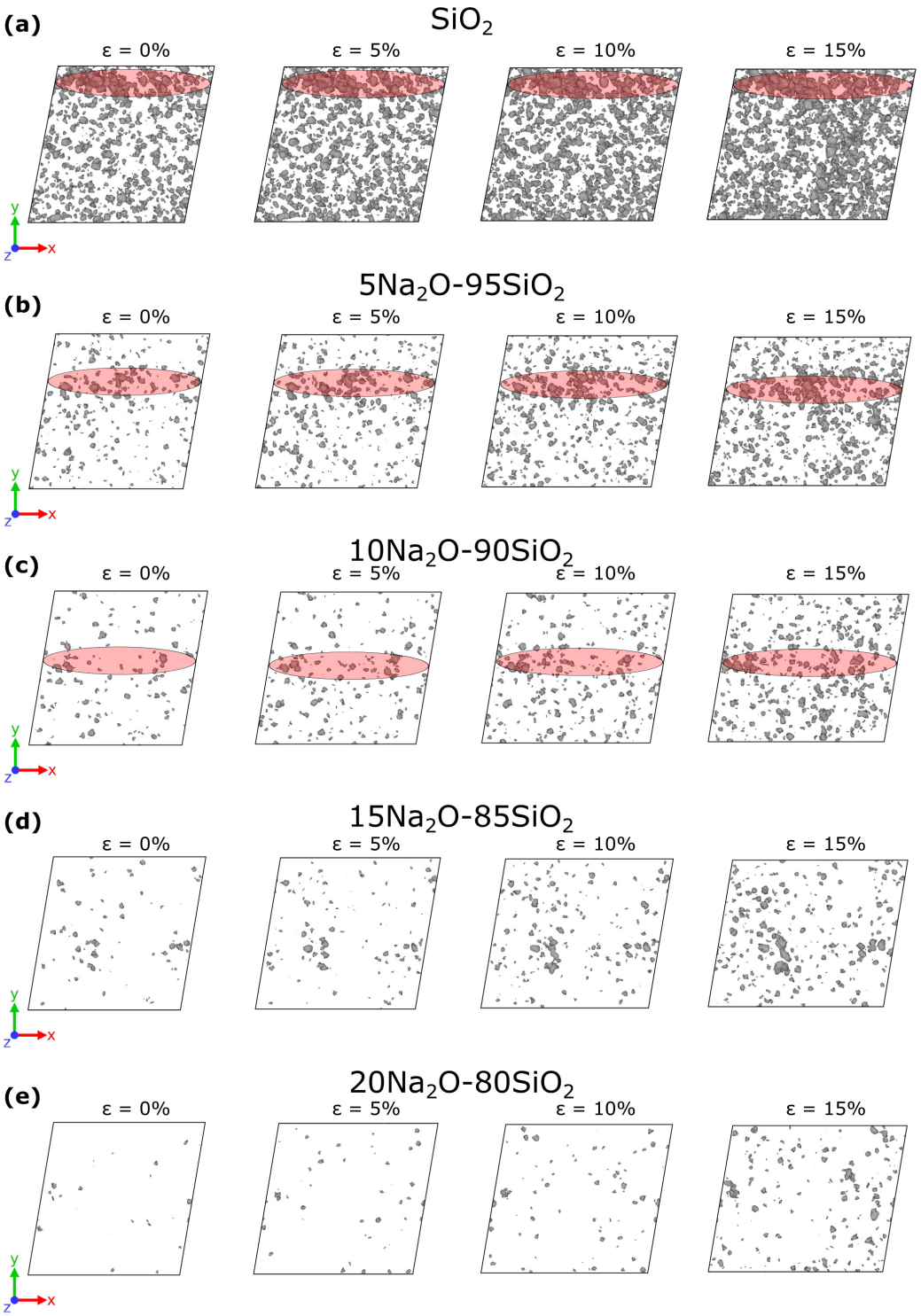

Figure. 9.21: The evolution of voids that have a radius larger 3.5 Å of the glasses pre-deformed up 33% shear strain by tilting the y-axis along the x-direction and unloaded to zero stress at 300 K and using a strain rate of 10^8 s^{-1}. The samples are reloaded again in tension along the x-axis at 300 K and using a strain rate of 10^8 s^{-1}. (a) Silica glass, (b) sodium silicate glass with 5 mol% of Na_2O, (c) sodium silicate glass with 10 mol% of Na_2O, (d) sodium silicate glass with 15 mol% of Na_2O, (e) sodium silicate glass with 20 mol% of Na_2O

9.4 Effect of the simulation parameters

Molecular dynamics simulations enable us to study the properties of the materials at an atomic scale, where mechanistic understanding can be achieved by tracking atomic movement. However, MD simulations are limited by the time and scale that can be adequately simulated. Hence, it is essential to check that the studied properties and the obtained mechanisms are not dependent on the simulation parameters, such as the cooling rate and strain rate. Therefore, the effect of cooling and strain rates was checked for all glasses. The results were compared to experimental data and atomistic simulations available in the literature. In the following section, we will discuss the influence of these parameters on the deformation behavior of silica and sodium silicate glasses.

Cooling rate

The effect of the cooling rate on the deformation behavior of silica and silicate glasses was investigated by deforming several glasses cooling using four different cooling rates (i.e., 10^{12}, 5×10^{12}, 10^{13}, and 5×10^{13} K/s). The number of atoms used for the cooling rate study is 375000 atoms. The cooling procedure is the same as described in Chapter. 3. Due to the limited time scale in MD simulations, it is commonly known that higher cooling rates are used during the cooling simulations [34, 35, 40, 65]. The influence of the cooling rate on the deformation of silica and sodium silicate glasses during tension, compression, and shear is shown in Figure. 9.22. Previous studies showed that the change of the structural properties with cooling rate is described by a logarithmic law [34, 64, 65, 263, 264], which can make us expect that also the mechanical behavior of silicate glasses depends on the cooling rate. In Figure. 9.22a - c, we show the stress-strain curves of the samples that contain 5 mol% of Na_2O cooled using the above-mentioned cooling rates and deformed at room temperature. The other glasses show similar cooling rate dependence. The curves are shown in Figure. 9.22a - c) show that the elastic part of the stress-strain curves does not depend on the cooling rates used. However, the behavior of the stress-strain curves at larger strains depends on the cooling rate, where decreasing the cooling rate leads to a decrease in the failure strain and an increase in the strength (σ_{max}) (See Figure. 9.22d - f). Moreover, it is observed that the effect of the cooling rate is less visible once the rate is below 5×10^{12} K/s. This behavior was observed in other studies [91, 226, 265–267] and is related to glass stability as glasses cooled with a lower cooling rate are more energetically stable compared to glasses cooled using a higher cooling rate [64, 264–267]. The cooling rate used for all production samples was 10^{12} K/s, which was lower than 5×10^{12} K/s.

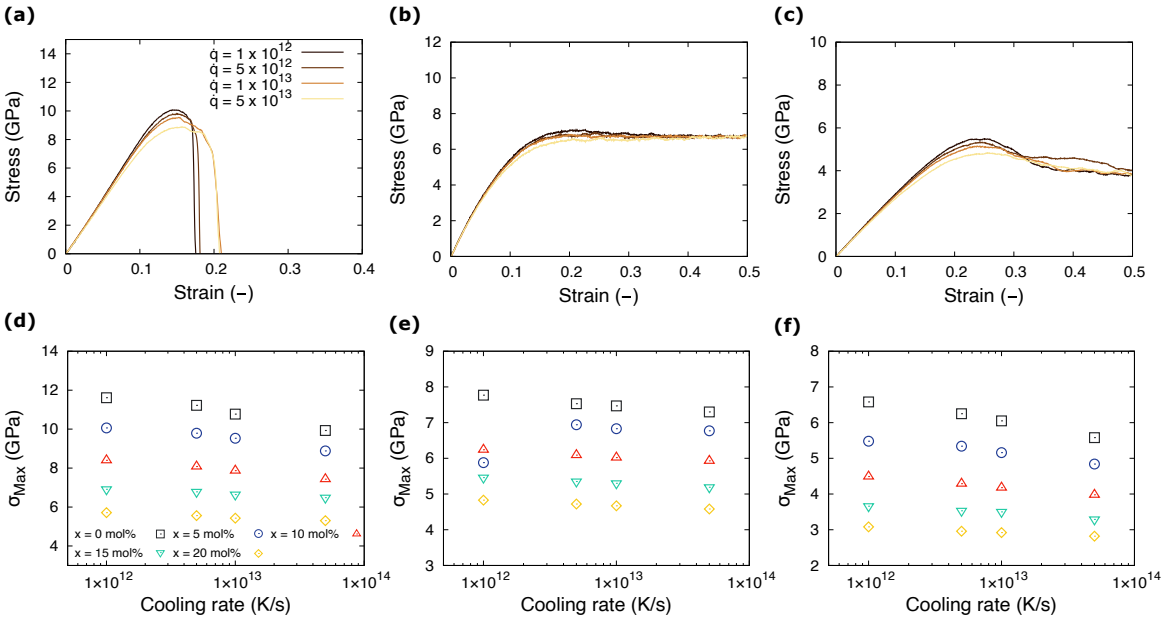

Figure. 9.22: Tensile (a) and compressive (b) stress-strain curves of silica glass deformed at room temperature, using different cooling rates. The sample used for these deformation is the sample containing 375000 atoms and deformed using 5 $\times 10^8$ s^{-1} as a strain rate.

Deformation rate

Another parameter that can affect the mechanical behavior of the materials is the strain rate. In MD simulations of materials deformations, we usually use a strain rate higher than those used experimentally by a few orders of magnitudes due to the limited time and computational power. To investigate the effect of the strain rate of the stress-strain curves and the strength of the glasses, we deformed silica glass and sodium silicate glasses containing 375000 atoms in tension, compression, and shear at 300 K using four strain rates, i.e., 10^8 s^{-1}, 5×10^8 s^{-1}, 1×10^9 s^{-1}, and 5×10^9 s^{-1}. The tension, compression, and shear results using these strain rates are shown in Figure. 9.23a - c for sodium silicate glass with 5 mol% of Na_2O. The elastic regime was unaffected by the strain rate used to perform the deformation in both deformations. However, we observed that the maximum stress achieved was lower for the lower deformation rate. Although the differences are minor, they agree with the previous observations from both MD simulations of oxide glasses [91, 125, 190, 268], and experiments [191, 269, 270]. The observed change in the maximum stress can be explained by the lower time for structural relaxation, as deformation using high strain rates, the structure will not have enough time to adapt to the applied strain, and higher stresses will be achieved as the time for stress relaxation is not enough [190].

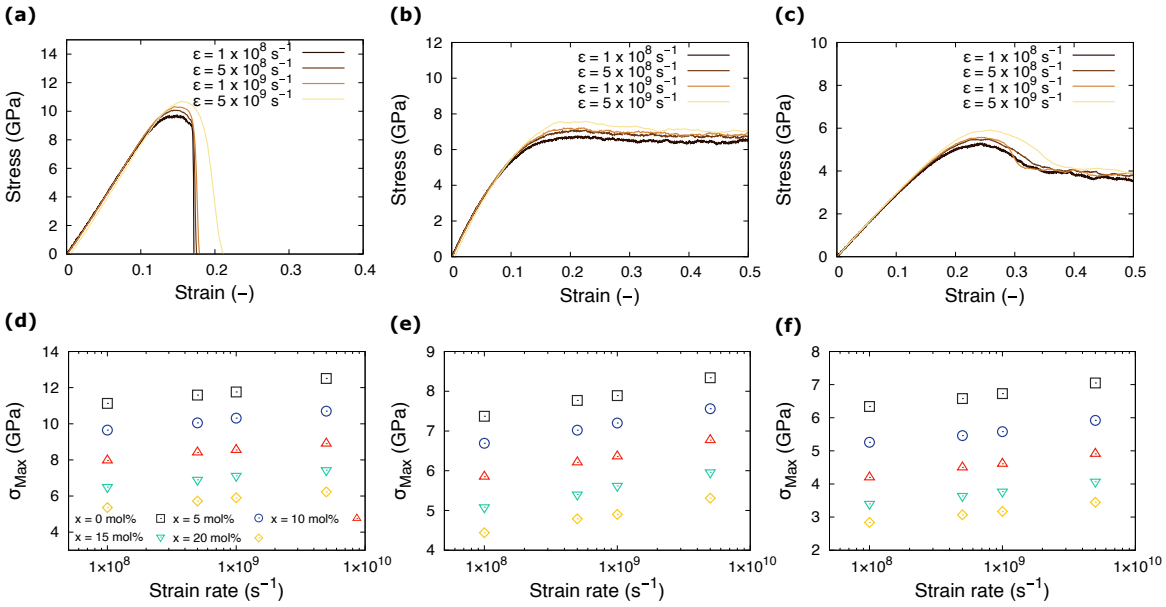

Figure. 9.23: Tensile (a) and compressive (b), and shear (c) stress-strain curves of sodium silicate glasses with 5 mol%of Na_2O deformed at room temperature, using different strain rates. The samples used for these deformation contains 375000 atoms and cooled using 1 K/ps as a cooling rate.

Consistency over many samples

The results have been validated for reproducible of the analysis by preparing three glasses from different starting conditions (change in the initial velocities). The samples were prepared in an identical way, the only change was the initial velocities of the atoms that were drawn from different Maxwell–Boltzmann distributions. Then the glasses were subjected to tension and compression using the same strain rate of 10^8 s^{-1}. Figure. 9.24a and b show the stress strain curves during tension and compression of different silica glass samples. The stress-strain curves show little change from sample to sample highlighting the similarities of the processes involved during the deformation. In Figure. 9.24c - h the bond statistics is shown for both tension and compression. Same trends and small deviations in the values of atoms that had a change in their bonding topology was observed which further confirm the generalizability of our results and conclusions. Performing shear deformation over many glass samples (three in our case) prepared using the same way will lead to a stochastic appearance of either horizontal or vertical shear band(s), which was also reported in the literature [243] and its origin is still being investigated. In the work of Lamp et al.[243] they found that the probability of appearance vertical or horizontal shear band is nearly 50%.

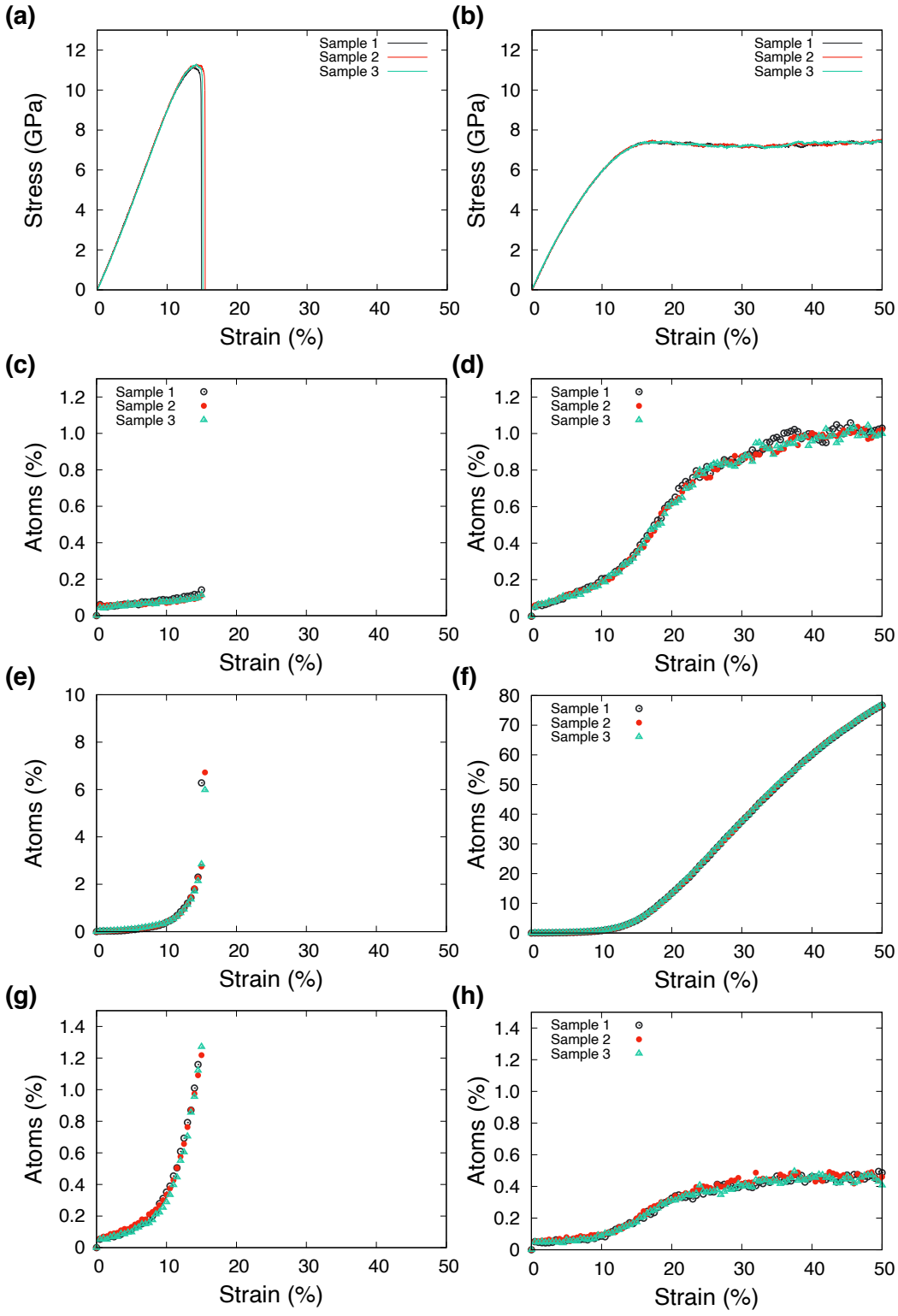

Figure. 9.24: Tensile (a), and compressive (b) stress-strain curves of silica glasses deformed at room temperature, using different samples. The bond statistics for the cooeresponding deformation is shown bellow it, where (c and d) are plots for the new bonds, (e and f) for switched bonds, and (g and h) are for the broken bonds, for both tension (left column) and compression (right column). The samples used for these deformation contains 375000 atoms and cooled using 1 K/ps as a cooling rate with different starting velocity distributions.

10 Conclusions

Within this second part of the work, large-scale atomistic simulations were performed to study and understand the deformation behavior, crack nucleation, and fracture of silica and binary sodium silicate glasses as model systems. In addition, statistical and local analysis tools and methods were used to reveal the mechanisms that lead to fracture and how the pre-deformation and pre-existing defects affected the tensile mechanical behavior of these glasses. From the results and analysis provided in this work we conclude that:

- Tensile pre-deformation and unloading resulted in glasses with very few atoms with a permanent change in their bonding topology and plastic strain.
- Negligible change in the tensile deformation behavior of the glasses pre-deformed in tension. This was explained by the small persistent plastic strain and the number of atoms that changed their neighbors.
- Compression of silicate glasses led to permanent densification of the glass observed for all glasses.
- Large percentage of Si atoms were found to have a permanent change in their bonding topology during compression, most of which are switched bonds homogeneously distributed in the glass network.
- The permanent change in Si bonding topology, their homogeneous distribution in the glass network, and the densification of the glasses during pre-compression resulted in a significant change in the mechanical behavior of silicate glasses, where it transformed from brittle fracture to ductile fracture.
- The changes of the nonaffine atomic displacement during tensile deformation are suggested to be the origin of the changes in the stiffness of the glass dictated by the tangent modulus during tension.
- The silica glass loaded in shear showed a substantial stress drop after reaching maximum stress. The appearance of this stress drop is due to the coalescence of voids already present in the glass that leads to the formation of a shear band. The stress drop reduces with increasing sodium content until it disappears for the glass with 20 mol% of Na_2O, in which no shear bands were observed, which is due to the disappearance of voids with the addition of Na_2O.
- Similar to compression, a large percentage of Si atoms that have a permanent change in their bonding topology were found in the samples pre-deformed in shear and unloaded. The location of these atoms with a permanent change in their bonding topology was found to be within the shear band in the silica glass and the glass with 5 mol% of Na_2O, while their distribution becomes more random in the glasses with higher sodium content.

- The tensile mechanical behavior of the glasses pre-deformed in shear and unloaded to zero-stress can be divided into two cases: (I) with low sodium content, the voids formed in the structure during the pre-shearing play the role of a pre-crack which weakens the glass and affect the failure strain. (II) No crack formation was observed during the pre-shearing samples with higher sodium content due to the lower free volume in those glasses compared to the low sodium glasses. This resulted in similar deformation mechanisms of the reloaded glasses.
- The effect of the pre-deformation on the presence of cavities (defects) in silica and sodium silicate glasses showed that pre-tension does not affect the presence of cavities, pre-compression leads to reducing the number of cavities compared to the pristine glasses, and in the pre-shear, these cavities, if present, tend to align along the shear band.
- The effect of the composition and/or pre-deformation on the cavities strongly influences the tensile deformation behavior of silica and sodium silicate glasses.

11 General discussion

Oxide glasses typically have a three-dimensional network made of glass network forming cations (e.g., Si^{4+}, P^{5+}) surrounded by oxygen anions. For oxide glasses made of only the glass-forming elements, the structure is mainly made by Q^4 and/or Q^3 units. With the addition of modifiers (e.g., Li, Na, K, Ca), the network becomes less connected due to the appearance of NBOs and other tetrahedral units with fewer BOs. On the other hand, the metasilicates and metaphosphate are made of a chain-like structure made of Q^2 units and terminated by Q^1 units. The oxygen tetrahedra in these chain-like structures are connected by their two corners [74, 195]. The metasilicate and metaphosphate glasses chains are made of covalent bonds with an ionic character. These chains are interconnected by ionic bonding through NBO–modifier bonds. Based on these assumptions, the chains in the metasilicate or metaphosphate glasses can be seen as elastically rigid regions in the glass [271, 272], which lay between the stressed-rigid and floppy regions. A feature of these chains is that they can self-organize into oriented structures by when uniaxial or shear stress is applied [3, 90]. Following what we mentioned above, a chain-like structure can be achieved by adding more modifiers to the silicate glass network or the phosphate network. Also, since the second part of this thesis is focused on the deformation behavior of binary sodium silicate glasses, it makes sense to study the sodium metasilicate glasses. However, the choice of metaphosphate glasses to study the structural transient and persistence anisotropy in glasses with a chain-like structure is based on major differences in the chemical and physical bonding nature of the P–O bonds compared to the Si–O bonds. First, metaphosphate glasses tend to form entangled, and longer chains than the metasilicate glasses [1, 74]. The P–O bond strength (6.0 Ncm^{-1}) is stronger than the Si–O bond strength (4.8 Ncm^{-1}) [273, 274]. This indicates that the strongly bonded –P–O–P– chains in metaphosphate glasses can be intact and not switch bonds to release the stress more effectively than in metasilicate glasses. Thus, having more chance of detecting the chain orientation in a metaphosphate glass than in a metasilicate glass. Adding modifiers weakly bonded with oxygen is also effective in reducing interchain interactions and enhancing the chains' flexibility of the chains [1].

The origins of the anisotropy in the metaphosphate glasses were due to orientation and changes at different structural levels. The differences observed when comparing the changes during tension and compression were mainly related to the direction of the orientation of these structural units. Although fewer experimental studies had conjectured that the appearance of the anisotropic glasses is due to the chain orientation [1] the exact mechanisms of how these chains orient and the origins of the anisotropy at different length scales are missing. Our results obtained from MD simulations are indeed confirming the experimental hypotheses and observations where we found that the origins of the structural anisotropy are due to changes in the short-range structure, where the structural anisotropy originates from the alignment of P–O bonds that depend on the loading mode (tension or compression). In the next structural level, called the near medium-range order in which neighboring tetrahedra are involved, is captured by the orientation of the P–P bonds, which are oriented along the tensile axis and orthogonal to the compression

axis. These short-range alignments of the P–O and P–P bonds lead to the changes at the medium-range order as captured by the orientation of the chains to be along the tensile axis and orthogonal to the loading axis. Moreover, the transient and persistent anisotropy observed in all glasses was shown to have the similar origins but with different intensities.

In terms of changes in the mechanical properties, modifiers with high field strength within the glass network lead to higher mechanical properties when compared to the glass with the same content of low field strength modifiers. This is since glasses with modifiers have higher field strength and the average bond strength of the glass increases. The mechanical behavior of the pre-deformed glasses was also evaluated. It showed that Young's modulus in glasses pre-deformed obtained by either tension or compression is lower than the pristine glass due to stretching the structure as indicated by the remaining plastic strain. Furthermore, the glasses pre-deformed by tension showed a higher Young's modulus than those pre-deformed by compression when measured in the same direction as the pre-deformation. This was observed for all glasses studied in this thesis irrespective of their glass structure and is shown in Figure. 4.6, Table.8.5, and Table.8.7

The main difference in the mechanical behavior of the studied glasses in this thesis is that the silica glass showed a brittle fracture with very limited plasticity. While in the metaphosphate glasses, no fracture was observed in the studied strain regime (up to 50%), and ductile fracture is observed to increase with increasing sodium content in the silicate glasses. The silica and silicate glasses with low sodium content showed limited plasticity, and during tensile pre-deformation and unloading, few atoms had a permanent change in their bonding topology, and a low plastic strain was measured. Moreover, negligible change in the deformation behavior of the glasses pre-deformed in tension unloaded and reloaded back in tension was observed. On the other hand, compression of silicate glasses led to permanent densification of the glass observed for all glasses, and its degree depends on the modifier's content, which is in agreement with the experimental observations [275]. This was because a significant fraction of Si atoms had a permanent change in their bonding topology, and most of them are switched bonds that are homogeneously distributed in the glass network. The permanent change in Si bonding topology and the densification of the glasses resulted in a significant change in the mechanical behavior of silicate glasses, where it transformed from brittle fracture to ductile fracture. Similar observations were drawn from other MD simulations of glasses quenched under pressure [116, 276].

The formation of shear bands in oxide glasses strongly depends on the glass composition. After reaching maximum stress, the silica glass loaded in shear showed a substantial stress drop in the stress-strain curves. We found that the appearance of this stress drop is due to the coalescence of pre-existing cavities along a shear band. With the addition of sodium, the stress drop decreases until it disappears for the glass with 20 mol% of Na_2O, in which no shear bands were observed. We attributed this to the effect of sodium, which has weaker bonds with oxygen, enabling structural reorganization that releases stress. Moreover, similar to compression, many Si atoms with a permanent change in their bonding topology were found in the samples pre-deformed in shear and unloaded. The location of these atoms with a permanent change in their neighbors was found to be within the shear band in the silica glass and the glass with 5 mol% of Na_2O, while their distribution becomes more homogeneous in the glasses with higher sodium content. To the author's

knowledge, this is the first time that the appearance of a shear band in silica and silicate glasses was linked to void coalescence and bond statistics. The tensile mechanical behavior of the glasses pre-deformed in shear and unloaded to zero-stress can be divided into two cases: (I) with low sodium content, the voids formed in the structure during the pre-shearing play the role of a pre-crack which weakens the glass and affect the failure strain. (II) No crack formation was observed during the pre-shearing samples with higher sodium content due to the lower free volume in those glasses than in the low sodium glasses. This resulted in similar deformation mechanisms of the reloaded glasses. Moreover, the general fracture mechanism in these glasses was found to be due to voids (cavities) formation and/or coalescence. The effect of composition on the formation of initial cavities and how they were affected by the pre-deformation was discussed, where we showed that uniaxial pre-compression had led to reducing the number of cavities in the glass, while during shear pre-deformation, these cavities tend to merge and aline along the shear band.

Although the microscopic structure and network connectivity of the simulated glasses is different, the mechanical behavior of the glasses pre-deformed in tension or compression is similar irrespective of the simulated composition. This highlights the generalizability of our findings and the role of the composition, topology, and pre-existing defects due to the pre-deformation on the deformation behavior and fracture of oxide glasses, which will guide to further development of oxide glasses with tailored mechanical properties.

References

[1] S. Inaba, H. Hosono, S. Ito, Entropic shrinkage of an oxide glass, Nature Materials 14 (3) (2015) 312–317. (pages 1, 11, 11, 11, 11, 11, 11, 13, 13, 13, 13, 136, 136, and 136).

[2] C. L. Rountree, D. Vandembroucq, M. Talamali, E. Bouchaud, S. Roux, Plasticity-induced structural anisotropy of silica glass, Phys. Rev. Lett. 102 (2009) 195501. (pages 1 and 32).

[3] X. Yang, G. Scannell, C. Jain, B. P. Rodrigues, M. A. Schmidt, L. Wondraczek, Permanent structural anisotropy in a hybrid fiber optical waveguide, Applied Physics Letters 111 (20) (2017) 201901. (pages 1, 11, 11, 13, and 136).

[4] L. Wondraczek, E. Bouchbinder, A. Ehrlicher, J. C. Mauro, R. Sajzew, M. M. Smedskjaer, Advancing the mechanical performance of glasses: Perspectives and challenges, Advanced Materials (2021) 2109029. (pages 1, 15, 15, 15, 124, and 124).

[5] K. D. Sattler (Ed.), 21st Century Nanoscience – A Handbook, CRC Press, 2019. (pages 3 and 14).

[6] I. C. on Glass (ICG), 2022: the un international year of glass (2022).
URL `https://iyog2022.org/` (page 3).

[7] J. C. Mauro, C. S. Philip, D. J. Vaughn, M. S. Pambianchi, Glass science in the united states: Current status and future directions, International Journal of Applied Glass Science 5 (1) (2014) 2–15. (page 3 and 3).

[8] Y. K. Lee, J. S. Lee, J. Heo, W. B. Im, W. J. Chung, Phosphor in glasses with pb-free silicate glass powders as robust color-converting materials for white LED applications, Optics Letters 37 (15) (2012) 3276. (page 3).

[9] V. G. Truong, L. Bigot, A. Lerouge, M. Douay, I. Razdobreev, Study of thermal stability and luminescence quenching properties of bismuth-doped silicate glasses for fiber laser applications, Applied Physics Letters 92 (4) (2008) 041908.

[10] K. Hayashi, S. Nomura, Y. Sakai, Glass substrate for micro display devices, Journal of the Society for Information Display 25 (2) (2017) 71–75. (page 3 and 3).

[11] J. C. Mauro, E. D. Zanotto, Two centuries of glass research: Historical trends, current status, and grand challenges for the future, International Journal of Applied Glass Science 5 (3) (2014) 313–327. (page 3).

[12] L. Wondraczek, J. C. Mauro, J. Eckert, U. Kühn, J. Horbach, J. Deubener, T. Rouxel, Towards ultrastrong glasses, Advanced Materials 23 (39) (2011) 4578–4586. (page 3).

[13] W. P. Eaton, J. H. Smith, Micromachined pressure sensors: review and recent developments, Smart Materials and Structures 6 (5) (1997) 530–539. (page 3).

[14] C. J. Welham, J. Greenwood, M. M. Bertioli, A high accuracy resonant pressure sensor by fusion bonding and trench etching, Sensors and Actuators A: Physical 76 (1-3) (1999) 298–304.

[15] Z. Luo, D. Chen, J. Wang, Y. Li, J. Chen, A high-q resonant pressure microsensor with through-glass electrical interconnections based on wafer-level MEMS vacuum packaging, Sensors 14 (12) (2014) 24244–24257.

[16] M. L. Jepsen, A technology rollercoaster: liquid crystal on silicon, Nature Photonics 1 (5) (2007) 276. (page 3).

[17] K. Binder, Computer simulations of undercooled fluids and the glass transition, Journal of Non-Crystalline Solids 274 (1-3) (2000) 332–341. (page 3).

[18] J. Du, A. Cormack, The medium range structure of sodium silicate glasses: a molecular dynamics simulation, Journal of Non-Crystalline Solids 349 (2004) 66–79. (pages 97, 97, 98, 98, 98, 98, 105, 105, and 105).

[19] B. Mantisi, A. Tanguy, G. Kermouche, E. Barthel, Atomistic response of a model silica glass under shear and pressure, The European Physical Journal B 85 (9) (Sep. 2012). (pages 8, 107, 107, 110, and 120).

[20] Y. Liang, C. R. Miranda, S. Scandolo, Temperature-induced densification of compressed SiO2glass: A molecular dynamics study, High Pressure Research 28 (1) (2008) 35–44.

[21] F. Yuan, L. Huang, Molecular dynamics simulation of amorphous silica under uniaxial tension: From bulk to nanowire, Journal of Non-Crystalline Solids 358 (24) (2012) 3481–3487. (pages 8 and 102).

[22] A. J., E. Bouchbinder, I. Procaccia, Cooling-rate dependence of the shear modulus of amorphous solids, Physical Review E 87 (4) (Apr. 2013).

[23] B. M. Lee, H. K. Baik, B. S. Seong, S. Munetoh, T. Motooka, Generation of glass SiO_2 structures by various cooling rates: A molecular-dynamics study, Computational Materials Science 37 (3) (2006) 203–208.

[24] A. Tilocca, Cooling rate and size effects on the medium-range structure of multicomponent oxide glasses simulated by molecular dynamics, J. Chem. Phys. 139 (11) (2013) 114501. (pages 39 and 60).

[25] H. Lammert, A. Heuer, Contributions to the mixed-alkali effect in molecular dynamics simulations of alkali silicate glasses, Physical Review B 72 (21) (Dec. 2005).

[26] A. Heuer, M. Kunow, M. Vogel, R. D. Banhatti, Characterization of the complex ion dynamics in lithium silicate glasses via computer simulations, Physical Chemistry Chemical Physics 4 (14) (2002) 3185–3192.

[27] E. Sunyer, P. Jund, R. Jullien, Characterization of channel diffusion in a sodium tetrasilicate glass via molecular-dynamics simulations, Physical Review B 65 (21) (May 2002).

[28] P. Jund, W. Kob, R. Jullien, Channel diffusion of sodium in a silicate glass, Physical Review B 64 (13) (Sep. 2001).

[29] J. Horbach, W. Kob, K. Binder, Dynamics of sodium in sodium disilicate: Channel relaxation and sodium diffusion, Physical Review Letters 88 (12) (Mar. 2002).

[30] J. Du, L. R. Corrales, Compositional dependence of the first sharp diffraction peaks in alkali silicate glasses: A molecular dynamics study, Journal of Non-Crystalline Solids 352 (30-31) (2006) 3255–3269.

[31] X. Yuan, A. Cormack, Local structures of MD-modeled vitreous silica and sodium silicate glasses, Journal of Non-Crystalline Solids 283 (1-3) (2001) 69–87. (page 97 and 97).

[32] W. Smith, G. N. Greaves, M. J. Gillan, Computer simulation of sodium disilicate glass, The Journal of Chemical Physics 103 (8) (1995) 3091–3097.

[33] U. Voigt, H. Lammert, H. Eckert, A. Heuer, Cation clustering in lithium silicate glasses: Quantitative description by solid-state NMR and molecular dynamics simulations, Physical Review B 72 (6) (Aug. 2005).

[34] K. Vollmayr, W. Kob, K. Binder, Cooling-rate effects in amorphous silica: A computer-simulation study, Physical Review B 54 (22) (1996) 15808–15827. (page 130 and 130).

[35] A. Atila, E. M. Ghardi, A. Hasnaoui, S. Ouaskit, Alumina effect on the structure and properties of calcium aluminosilicate in the percalcic region: A molecular dynamics investigation, Journal of Non-Crystalline Solids 525 (2019) 119470. (pages 10, 21, 67, 97, and 130).

[36] A. Atila, E. M. Ghardi, S. Ouaskit, A. Hasnaoui, Atomistic insights into the impact of charge balancing cations on the structure and properties of aluminosilicate glasses, Physical Review B 100 (14) (2019). (pages 10, 21, 29, 30, 60, 65, 65, 66, 77, and 97).

[37] E. M. Ghardi, A. Atila, M. Badawi, A. Hasnaoui, S. Ouaskit, Computational insights into the structure of barium titanosilicate glasses, Journal of the American Ceramic Society 102 (11) (2019) 6626–6639. (page 3).

[38] E. D. Zanotto, J. C. Mauro, The glassy state of matter: Its definition and ultimate fate, Journal of Non-Crystalline Solids 471 (2017) 490–495. (pages 4, 4, 4, 4, 4, 4, 5, and 5).

[39] J. A. McEwan, A. J. Clulow, A. Nelson, N. R. Yepuri, P. L. Burn, I. R. Gentle, Dependence of organic interlayer diffusion on glass-transition temperature in OLEDs, ACS Applied Materials & Interfaces 9 (16) (2017) 14153–14161. (page 4).

[40] A. Atila, S. Ouaskit, A. Hasnaoui, Ionic self-diffusion and the glass transition anomaly in aluminosilicates, Physical Chemistry Chemical Physics (2020). (pages 67, 97, and 130).

[41] A. Atila, M. Kbirou, S. Ouaskit, A. Hasnaoui, On the presence of nanoscale heterogeneity in al70ni15co15 metallic glass under pressure, Journal of Non-Crystalline Solids 550 (2020) 120381.

[42] R. Xie, A. R. Weisen, Y. Lee, M. A. Aplan, A. M. Fenton, A. E. Masucci, F. Kempe, M. Sommer, C. W. Pester, R. H. Colby, E. D. Gomez, Glass transition temperature from the chemical structure of conjugated polymers, Nature Communications 11 (1) (Feb. 2020).

[43] Z. Zheng, R. Ni, Y. Wang, Y. Han, Translational and rotational critical-like behaviors in the glass transition of colloidal ellipsoid monolayers, Science Advances 7 (3) (2021) eabd1958.

[44] M. Batens, T. A. Shmool, J. Massant, J. A. Zeitler, G. V. den Mooter, Advancing predictions of protein stability in the solid state, Physical Chemistry Chemical Physics 22 (30) (2020) 17247–17254. (page 4).

[45] M. Tomozawa, Fundamentals of inorganic glasses, Journal of Non-Crystalline Solids 170 (1) (1994) 112. (page 5).

[46] P. K. Gupta, Non-crystalline solids: glasses and amorphous solids, Journal of Non-Crystalline Solids 195 (1-2) (1996) 158–164. (page 5).

[47] G. Tammann, Kristallisieren und schmelzen-ja barth (1903). (page 5).

[48] J. T. Randall, H. P. Rooksby, B. S. Cooper, 13. x-ray diffraction and the structure of vitreous solids — i, Zeitschrift für Kristallographie - Crystalline Materials 75 (1) (1930) 196–214. (page 5).

[49] W. Vogel, Glass chemistry, Springer-Verlag, 1994. (pages 5, 7, 7, 7, 7, 8, 8, and 8).

[50] V. M. Goldschmidt, Geochemische verteilungsgesetze der elemente, no. 1, In Kommission bei J. Dybwad, 1927. (pages 5 and 7).

[51] W. H. Zachariasen, The atomic arrangement in glass, Journal of the American Chemical Society 54 (10) (1932) 3841–3851. (pages 6 and 10).

[52] A. Dietzel, Die kationenfeldstärken und ihre beziehungen zu entglasungsvorgängen, zur verbindungsbildung und zu den schmelzpunkten von silicaten, Zeitschrift für Elektrochemie und angewandte physikalische Chemie 48 (1) (1942) 9–23. (pages 7, 10, and 65).

[53] L. Pauling, The Nature of the Chemical Bond An Introduction to Modern Structural Chemistry, Cornell University Press, 1940. (page 7).

[54] J. Stevels, The glass considered as a polymer, Glass Ind 35 (2) (1954) 69–72. (pages 7 and 8).

[55] R. Pettifer, R. Dupree, I. Farnan, U. Sternberg, NMR determinations of Si-O-Si bond angle distributions in silica, Journal of Non-Crystalline Solids 106 (1-3) (1988) 408–412. (page 8).

[56] R. Dupree, D. Holland, P. McMillan, R. Pettifer, The structure of soda-silica glasses: A mas NMR study, Journal of Non-Crystalline Solids 68 (2-3) (1984) 399–410.

[57] L. Lichtenstein, C. Büchner, B. Yang, S. Shaikhutdinov, M. Heyde, M. Sierka, R. Włodarczyk, J. Sauer, H.-J. Freund, The atomic structure of a metal-supported vitreous thin silica film, Angewandte Chemie International Edition 51 (2) (2011) 404–407. (page 8).

[58] P. Y. Huang, S. Kurasch, J. S. Alden, A. Shekhawat, A. A. Alemi, P. L. McEuen, J. P. Sethna, U. Kaiser, D. A. Muller, Imaging atomic rearrangements in two-dimensional silica glass: Watching silica's dance, Science 342 (6155) (2013) 224–227.

[59] S. Sansotta, Molecular simulations study of silver precipitation from aqueous solution and on silica substrate : Control of shape and charge via redox condition, Doctoral thesis, Friedrich-Alexander-Universität Erlangen-Nürnberg (FAU) (2021). (page 26).

[60] T. Sato, N. Funamori, T. Yagi, Differential strain and residual anisotropy in silica glass, Journal of Applied Physics 114 (10) (2013) 103509. (pages 11, 12, 12, and 12).

[61] J. Luo, J. Wang, E. Bitzek, J. Y. Huang, H. Zheng, L. Tong, Q. Yang, J. Li, S. X. Mao, Size-Dependent Brittle-to-Ductile Transition in Silica Glass Nanofibers, Nano Letters 16 (1) (2016) 105–113. (pages 8, 9, 17, 17, 17, 33, 103, 103, and 110).

[62] M. Guerette, C. R. Kurkjian, S. Semjonov, L. Huang, Nonlinear elasticity of silica glass, Journal of the American Ceramic Society 99 (3) (2015) 841–848. (pages 8, 8, 15, 99, 99, 99, and 99).

[63] A. Pedone, G. Malavasi, M. Cristina Menziani, U. Segre, A. N. Cormack, Molecular dynamics studies of stress-strain behavior of silica glass under a tensile load, Chem. Mater. 20 (13) (2008) 4356–4366. (pages 8, 15, 25, 80, 82, 99, 102, 103, and 107).

[64] J. M. D. Lane, Cooling rate and stress relaxation in silica melts and glasses via microsecond molecular dynamics, Physical Review E - Statistical, Nonlinear, and Soft Matter Physics 92 (1) (2015) 12320. (pages 8, 9, 130, and 130).

[65] X. Li, W. Song, K. Yang, N. M. A. Krishnan, B. Wang, M. M. Smedskjaer, J. C. Mauro, G. Sant, M. Balonis, M. Bauchy, Cooling rate effects in sodium silicate glasses: Bridging the gap between molecular dynamics simulations and experiments, The Journal of Chemical Physics 147 (7) (2017) 074501. (pages 8, 60, 75, 78, 78, 78, 98, 130, and 130).

[66] L. L. Velli, C. P. Varsamis, E. I. Kamitsos, D. Möncke, D. Ehrt, Structural investigation of metaphosphate glasses, Physics and Chemistry of Glasses 46 (2) (2005) 178–181. (page 9).

[67] W. Jia, H. Hu, A. Li, H. Deng, C. L. Hogue, J. C. Mauro, C. Zhang, Q. Fu, Glass-activated regeneration of volumetric muscle loss, Acta Biomaterialia 103 (2020) 306–317. (page 9).

[68] J. C. Knowles, Phosphate based glasses for biomedical applications, Journal of Materials Chemistry 13 (10) (2003) 2395–2401.

[69] A. Atila, Y. Ouldhnini, S. Ouaskit, A. Hasnaoui, Atomistic insights into the mixed-alkali effect in phosphosilicate glasses, Physical Review B 105 (13) (Apr. 2022). (pages 9 and 97).

[70] T. K. Pietrzak, P. E. Kruk-Fura, P. J. Mikołajczuk, J. E. Garbarczyk, Syntheses and nanocrystallization of NaF–M_2O_3–P_2O_5 NASICON-like phosphate glasses (M = V, Ti, Fe), International Journal of Applied Glass Science 11 (1) (2020) 87–96. (page 9).

[71] Z. Zhang, J. Ren, L. Hu, Fast Ionic Conducting Glasses in the System 20LiCl-40Li_2O-(80- x)PO_5/2- xMoO_3: The Structural Dependence of Ion Conductivity Studied by Solid-State Nuclear Magnetic Resonance Spectroscopy, Journal of Physical Chemistry C 124 (12) (2020) 6528–6535. (page 21).

[72] J. Fu, Fast Li+ ion conduction in Li2O-(Al2O3 Ga2O3)-TiO2-P2O5 glass-ceramics, Journal of Materials Science 33 (6) (1998) 1549–1553. (page 9).

[73] N. N. Greenwood, A. Earnshaw, Chemistry of the Elements, Elsevier, 2012. (pages 9, 10, and 10).

[74] R. K. Brow, Review: the structure of simple phosphate glasses, Journal of Non-Crystalline Solids 263 (2000) 1–28. (pages 10, 10, 10, 10, 11, 63, 136, and 136).

[75] E. Thilo, Die kondensierten Phosphate, Die Naturwissenschaften 46 (11) (1959) 367–373. (page 10).

[76] G. N. Greaves, A. Fontaine, P. Lagarde, D. Raoux, S. J. Gurman, Local structure of silicate glasses, Nature 293 (5834) (1981) 611–616. (pages 10, 97, 97, 97, 98, 98, and 114).

[77] Y. Y. Huang, J. L. Hunt, J. R. Stevens, Determination of elastic constants in isotropic silicate glasses by brillouin scattering, Journal of Applied Physics 44 (8) (1973) 3589–3592. (page 11, 11, and 11).

[78] A. Pedone, G. Malavasi, A. N. Cormack, U. Segre, M. C. Menziani, Insight into elastic properties of binary alkali silicate glasses; prediction and interpretation through atomistic simulation techniques, Chemistry of Materials 19 (13) (2007) 3144–3154. (pages 76, 80, 97, and 97).

[79] G. Molnár, P. Ganster, J. Török, A. Tanguy, Sodium effect on static mechanical behavior of MD-modeled sodium silicate glasses, Journal of Non-Crystalline Solids 440 (2016) 12–25. (pages 11, 11, 11, 103, 103, 121, and 125).

[80] J. Endo, S. Inaba, S. Ito, Mechanical properties of anisotropic metaphosphate glass, Journal of the American Ceramic Society 98 (9) (2015) 2767–2771. (pages 11, 11, 13, 13, 13, 65, 65, and 66).

[81] Y. Suzuki, J. Haimovich, T. Egami, Bond-orientational anisotropy in metallic glasses observed by x-ray diffraction, Physical Review B 35 (5) (1987) 2162–2168. (pages 11 and 12).

[82] M. D. Lund, Y. Yue, Impact of drawing stress on the tensile strength of oxide glass fibers, Journal of the American Ceramic Society 93 (10) (2010) 3236–3243. (pages 11 and 12).

[83] M. Ya, J. Deubener, Y. Yue, Enthalpy and anisotropy relaxation of glass fibers, Journal of the American Ceramic Society 91 (3) (2008) 745–752. (page 11).

[84] M. Ballauff, J. M. Brader, S. U. Egelhaaf, M. Fuchs, J. Horbach, N. Koumakis, M. Krüger, M. Laurati, K. J. Mutch, G. Petekidis, M. Siebenbürger, T. Voigtmann, J. Zausch, Residual tresses in glasses, Physical Review Letters 110 (21) (2013) 215701. (page 11).

[85] J. Wu, J. Deubener, J. F. Stebbins, L. Grygarova, H. Behrens, L. Wondraczek, Y. Yue, Structural response of a highly viscous aluminoborosilicate melt to isotropic and anisotropic compressions, The Journal of Chemical Physics 131 (10) (2009) 104504. (pages 11, 11, 12, and 12).

[86] R. Brueckner, Anisotropic glasses and glass melts : a survey, Glass science and technology 69 (1996) 396–411. (page 12).

[87] L. N. G. Filon, F. Harris, On the di-phasic nature of glass, as shown by photo-elastic observations, Proceedings of the Royal Society of London. Series A, Containing Papers of a Mathematical and Physical Character 103 (723) (1923) 561–571. (page 12).

[88] T. TAKAMORI, M. TOMOZAWA, Anomalous birefringence in oxide glasses, in: Glass I: Interaction with Electromagnetic Radiation - Treatise on Materials Science and Technology, Elsevier, 1977, pp. 123–155. (page 12).

[89] B. Champagnon, S. Degioanni, C. Martinet, Anisotropic elastic deformation of silica glass under uniaxial stress, Journal of Applied Physics 116 (12) (2014) 123509. (page 12 and 12).

[90] S. Inaba, Y. Benino, S. Kohara, H. Hosono, S. Ito, Anisotropic structure of alkali metaphosphate glasses, Journal of the American Ceramic Society 103 (6) (2020) 3631–3641. (pages 13, 63, 65, and 136).

[91] Z. Zhang, Fracture, Surface, and Structure of Silicate Glasses: Insights from Atomistic Computer Simulations, Theses, Universite de Montpellier ; Laboratoire Charles Coulomb (May 2020). (pages 14, 14, 15, 67, 68, 69, 78, 86, 99, 107, 130, and 131).

[92] J. C. Mauro, Topological constraint theory of glass, American ceramic society bulletin 90 (4) (2011) 31. (page 14, 14, 14, 14, and 14).

[93] C. Hermansen, B. P. Rodrigues, L. Wondraczek, Y. Yue, An extended topological model for binary phosphate glasses, The Journal of Chemical Physics 141 (24) (2014) 244502. (page 14).

[94] M. Wang, M. M. Smedskjaer, J. C. Mauro, G. Sant, M. Bauchy, Topological origin of the network dilation anomaly in ion-exchanged glasses, Physical Review Applied 8 (5) (Nov. 2017). (pages 14, 14, and 21).

[95] M. M. Smedskjaer, J. C. Mauro, Y. Yue, Prediction of glass hardness using temperature-dependent constraint theory, Physical Review Letters 105 (11) (Sep. 2010). (page 14).

[96] P. K. Gupta, J. C. Mauro, Composition dependence of glass transition temperature and fragility. i. a topological model incorporating temperature-dependent constraints, The Journal of Chemical Physics 130 (9) (2009) 094503. (page 14).

[97] K. Yang, B. Yang, X. Xu, C. Hoover, M. M. Smedskjaer, M. Bauchy, Prediction of the young's modulus of silicate glasses by topological constraint theory, Journal of Non-Crystalline Solids 514 (2019) 15–19. (pages 14 and 21).

[98] P. K. Gupta, C. R. Kurkjian, Intrinsic failure and non-linear elastic behavior of glasses, Journal of Non-Crystalline Solids 351 (27-29) (2005) 2324–2328. (pages 15, 15, 15, 15, 79, 80, 80, 80, 98, 98, 98, 99, 99, 103, and 107).

[99] W. Griffioen, Effect of nonlinear elasticity on measured fatigue data and lifetime estimations of optical fibers, Journal of the American Ceramic Society 75 (10) (1992) 2692–2696.

[100] E. Suhir, Elastic stability, free vibrations, and bending of optical glass fibers: effect of the nonlinear stress–strain relationship, Applied Optics 31 (24) (1992) 5080.

[101] M. J. Matthewson, Optical fiber mechanical testing techniques, in: D. K. Paul (Ed.), Fiber Optics Reliability and Testing: A Critical Review, Vol. 10272, International Society for Optics and Photonics, SPIE, 1993, pp. 34 – 61. (page 99 and 99).

[102] E. Suhir, The effect of the nonlinear stress-strain relationship on the mechanical behavior of optical glass fibers, International Journal of Solids and Structures 30 (7) (1993) 947–961. (pages 99, 99, and 107).

[103] M. Muraoka, The maximum stress in optical glass fibers under two-point bending, Journal of Electronic Packaging 123 (1) (2000) 70–73. (page 15).

[104] E. Bitzek, J. R. Kermode, P. Gumbsch, Atomistic aspects of fracture, International Journal of Fracture 191 (1-2) (2015) 13–30. (pages 15 and 21).

[105] E. Le Bourhis, Glass: mechanics and technology, John Wiley & Sons, 2014. (pages 15, 16, 16, 16, 16, 16, and 16).

[106] J. Luo, K. D. Vargheese, A. Tandia, G. Hu, J. C. Mauro, Crack nucleation criterion and its application to impact indentation in glasses, Sci. Rep. 6 (1) (2016) 23720. (page 15).

[107] J. Luo, B. Deng, K. D. Vargheese, A. Tandia, S. E. DeMartino, J. C. Mauro, Atomic-scale modeling of crack branching in oxide glass 216 (2021) 117098. (page 16 and 16).

[108] S. Yoshida, Indentation deformation and cracking in oxide glass –toward understanding of crack nucleation, Journal of Non-Crystalline Solids: X 1 (2019) 100009. (page 16, 16, and 16).

[109] K. Januchta, Structural perspective on fracture in oxide glasses (2019). (pages 16 and 124).

[110] K. Niihara, A fracture mechanics analysis of indentation-induced palmqvist crack in ceramics, Journal of Materials Science Letters 2 (5) (1983) 221–223. (page 16).

[111] J. D. Musgraves, J. Hu, L. Calvez, Springer Handbook of Glass, Springer, 2019. (pages 17, 17, 17, 17, 17, 17, 17, and 99).

[112] Y. Zhang, L. Huang, Y. Shi, Towards damage resistant al2o3–SiO2 glasses with structural and chemical heterogeneities through consolidation of glassy nanoparticles, Acta Materialia 215 (2021) 117016. (page 17).

[113] A. Greer, Y. Cheng, E. Ma, Shear bands in metallic glasses, Materials Science and Engineering: R: Reports 74 (4) (2013) 71–132. (pages 17, 17, 107, 110, and 120).

[114] H. Ni, X. Li, H. Gao, Elastic modulus of amorphous SiO_2 nanowires, Applied Physics Letters 88 (4) (2006) 043108. (page 17).

[115] G. Brambilla, F. Xu, P. Horak, Y. Jung, F. Koizumi, N. P. Sessions, E. Koukharenko, X. Feng, G. S. Murugan, J. S. Wilkinson, D. J. Richardson, Optical fiber nanowires and microwires: fabrication and applications, Advances in Optics and Photonics 1 (1) (2009) 107. (page 17).

[116] F. Yuan, L. Huang, Brittle to ductile transition in densified silica glass, Scientific Reports 4 (1) (May 2014). (pages 17, 17, and 137).

[117] B. Mantisi, G. Kermouche, E. Barthel, A. Tanguy, Impact of pressure on plastic yield in amorphous solids with open structure, Physical Review E 93 (3) (Mar. 2016). (pages 17, 107, and 120).

[118] G. Kumar, P. Neibecker, Y. H. Liu, J. Schroers, Critical fictive temperature for plasticity in metallic glasses, Nature Communications 4 (1) (Feb. 2013). (page 17).

[119] Y. Wu, D. Cao, Y. Yao, G. Zhang, J. Wang, L. Liu, F. Li, H. Fan, X. Liu, H. Wang, X. Wang, H. Zhu, S. Jiang, P. Kontis, D. Raabe, B. Gault, Z. Lu, Substantially enhanced plasticity of bulk metallic glasses by densifying local atomic packing, Nature Communications 12 (1) (Nov. 2021). (page 17).

[120] G. Kermouche, G. Guillonneau, J. Michler, J. Teisseire, E. Barthel, Perfectly plastic flow in silica glass, Acta Materialia 114 (2016) 146–153. (pages 18, 18, 81, 107, 107, 107, 109, 110, and 113).

[121] E. Barthel, V. Keryvin, G. Rosales-Sosa, G. Kermouche, Indentation cracking in silicate glasses is directed by shear flow, not by densification, Acta Materialia 194 (2020) 473–481. (page 18).

[122] B. J. Alder, T. E. Wainwright, Phase transition for a hard sphere system, The Journal of Chemical Physics 27 (5) (1957) 1208–1209. (page 21 and 21).

[123] A. Atila, E. Bitzek, Atomistic origins of deformation-induced structural anisotropy in metaphosphate glasses and its influence on mechanical properties. (page 21).

[124] N. J. Schrenker, Z. Xie, P. Schweizer, M. Moninger, F. Werner, N. Karpstein, M. Mačković, G. D. Spyropoulos, M. Göbelt, S. Christiansen, C. J. Brabec, E. Bitzek, E. Spiecker, Microscopic deformation modes and impact of network anisotropy on the mechanical and electrical performance of five-fold twinned silver nanowire electrodes, ACS Nano 15 (1) (2020) 362–376.

[125] E. J. Frankberg, J. Kalikka, F. G. Ferré, L. Joly-Pottuz, T. Salminen, J. Hintikka, M. Hokka, S. Koneti, T. Douillard, B. L. Saint, P. Kreiml, M. J. Cordill, T. Epicier, D. Stauffer, M. Vanazzi, L. Roiban, J. Akola, F. D. Fonzo, E. Levänen, K. Masenelli-Varlot, Highly ductile amorphous oxide at room temperature and high strain rate, Science 366 (6467) (2019) 864–869. (pages 21, 21, and 131).

[126] S. S. Sørensen, C. A. N. Biscio, M. Bauchy, L. Fajstrup, M. M. Smedskjaer, Revealing hidden medium-range order in amorphous materials using topological data analysis, Science Advances 6 (37) (2020) eabc2320.

[127] Z. Zhang, S. Ispas, W. Kob, Structure and vibrational properties of sodium silicate glass surfaces, The Journal of Chemical Physics 153 (12) (2020) 124503. (page 21, 21, and 21).

[128] Z. Yu, Q. Liu, I. Szlufarska, B. Wang, Structural signatures for thermodynamic stability in vitreous silica: Insight from machine learning and molecular dynamics simulations, Physical Review Materials 5 (1) (Jan. 2021). (page 21).

[129] S. S. Sørensen, H. Johra, J. C. Mauro, M. Bauchy, M. M. Smedskjaer, Boron anomaly in the thermal conductivity of lithium borate glasses, Physical Review Materials 3 (7) (Jul. 2019). (page 21).

[130] Z. Zhang, S. Ispas, W. Kob, Roughness and scaling properties of oxide glass surfaces at the nanoscale (2020). arXiv:2007.07474. (page 21).

[131] A. R. Hinkle, W. G. Nöhring, R. Leute, T. Junge, L. Pastewka, The emergence of small-scale self-affine surface roughness from deformation, Science Advances 6 (7) (2020) eaax0847. (page 21).

[132] D. Richard, K. González-López, G. Kapteijns, R. Pater, T. Vaknin, E. Bouchbinder, E. Lerner, Universality of the nonphononic vibrational spectrum across different classes of computer glasses, Physical Review Letters 125 (8) (Aug. 2020). (page 21).

[133] L. Wang, A. Ninarello, P. Guan, L. Berthier, G. Szamel, E. Flenner, Low-frequency vibrational modes of stable glasses, Nature Communications 10 (1) (Jan. 2019).

[134] M. Shimada, H. Mizuno, A. Ikeda, Anomalous vibrational properties in the continuum limit of glasses, Physical Review E 97 (2) (Feb. 2018). (page 21).

[135] I. Deshpande, J. Liang, D. Hedeen, K. J. Roberts, Y. Zhang, B. Ha, N. R. Latorraca, B. Faust, R. O. Dror, P. A. Beachy, B. R. Myers, A. Manglik, Smoothened stimulation

by membrane sterols drives hedgehog pathway activity, Nature 571 (7764) (2019) 284–288. (page 21).

[136] M. P. Allen, D. J. Tildesley, Computer simulation of liquids, Oxford university press, 2017. (pages 21, 22, 25, 25, 26, 26, 26, and 29).

[137] D. C. Rapaport, D. C. R. Rapaport, The art of molecular dynamics simulation, Cambridge university press, 2004. (pages 21 and 29).

[138] W. Andreoni, S. Yip, Handbook of Materials Modeling: Methods: Theory and Modeling, Springer, 2018. (page 21).

[139] D. Frenkel, B. Smit, Understanding Molecular Simulation: From Algorithms to Applications, second edition Edition, Academic Press, San Diego, 2002. (page 21).

[140] W. C. Swope, H. C. Andersen, P. H. Berens, K. R. Wilson, A computer simulation method for the calculation of equilibrium constants for the formation of physical clusters of molecules: Application to small water clusters, The Journal of Chemical Physics 76 (1) (1982) 637–649. (page 22).

[141] L. Verlet, Computer "experiments" on classical fluids. i. thermodynamical properties of lennard-jones molecules, Physical Review 159 (1) (1967) 98–103. (page 22).

[142] J. W. Gibbs, Elementary principles in statistical mechanics: developed with especial reference to the rational foundation of thermodynamics, C. Scribner's sons, 1902. (page 23).

[143] J. W. Gibbs, On the equilibrium of heterogeneous substances, American Journal of Science (96) (1878) 441–458. (page 23).

[144] D. McQuarrie, Statistical mechanics, Harper & Row, New York, 1975. (page 24).

[145] S. J. Blundell, K. M. Blundell, Concepts in thermal physics, OUP Oxford, 2009. (page 24).

[146] F. Reif, Fundamentals of statistical and thermal physics, Waveland Press, 2009. (page 24).

[147] A. Berlinsky, A. Harris, Statistical Mechanics An Introductory Graduate Course, Springer, 2019. (page 24).

[148] J. H. Luscombe, Statistical Mechanics: From Thermodynamics to the Renormalization Group, CRC Press, 2021. (page 24).

[149] M. P. Tosi, Cohesion of ionic solids in the born model, in: Solid state physics, Vol. 16, Elsevier, 1964, pp. 1–120. (page 24).

[150] A. Pedone, G. Malavasi, M. C. Menziani, A. N. Cormack, U. Segre, A new self-consistent empirical interatomic potential model for oxides, silicates, and silicas-based glasses, J. Phys. Chem. B 110 (24) (2006) 11780–11795. (pages 25, 25, 25, 25, 25, 76, 82, 97, 97, 97, 97, and 97).

[151] B. Deng, J. Luo, J. T. Harris, C. M. Smith, M. E. McKenzie, Toughening of Li_2O-$2SiO_2$ glass-ceramics induced by intriguing deformation behavior of lithium disilicate nanocrystal, Journal of the American Ceramic Society 103 (2) (2019) 965–972.

[152] Y. Yu, M. Wang, N. M. Anoop Krishnan, M. M. Smedskjaer, K. Deenamma Vargheese, J. C. Mauro, M. Balonis, M. Bauchy, Hardness of silicate glasses: Atomic-scale origin of the mixed modifier effect, J. Non. Cryst. Solids 489 (2018) 16–21.

[153] A. Pedone, G. Malavasi, A. N. Cormack, U. Segre, M. C. Menziani, Elastic and dynamical properties of alkali-silicate glasses from computer simulations techniques, Theoretical Chemistry Accounts 120 (4-6) (2008) 557–564.

[154] J. Luo, K. D. Vargheese, A. Tandia, J. T. Harris, J. C. Mauro, Structural origin of intrinsic ductility in binary aluminosilicate glasses, Journal of Non-Crystalline Solids 452 (2016) 297–306.

[155] V. V. Le, H. T. Dinh, Structural and mechanical properties of densified $(Li_2O)_{0.2}(SiO_2)_{0.8}$ glasses: A molecular dynamics simulations study, Journal of Non-Crystalline Solids 530 (2020) 119815. (page 25).

[156] D. Wolf, P. Keblinski, S. R. Phillpot, J. Eggebrecht, Exact method for the simulation of coulombic systems by spherically truncated, pairwise r^{-1} summation, The Journal of Chemical Physics 110 (17) (1999) 8254–8282. (page 26, 26, and 26).

[157] C. J. Fennell, J. D. Gezelter, Is the ewald summation still necessary? pairwise alternatives to the accepted standard for long-range electrostatics, The Journal of Chemical Physics 124 (23) (2006) 234104. (page 26 and 26).

[158] W. G. Hoover, Canonical dynamics: Equilibrium phase-space distributions, Physical Review A 31 (3) (1985) 1695–1697. (page 27).

[159] M. Parrinello, A. Rahman, Polymorphic transitions in single crystals: A new molecular dynamics method, Journal of Applied Physics 52 (12) (1981) 7182–7190. (page 27).

[160] F. Vasconcelos, S. Cristol, J.-F. Paul, L. Delevoye, F. Mauri, T. Charpentier, G. L. Caër, Extended czjzek model applied to NMR parameter distributions in sodium metaphosphate glass, Journal of Physics: Condensed Matter 25 (25) (2013) 255402. (page 27).

[161] K. Griebenow, E. I. Kamitsos, L. Wondraczek, Mixed-modifier effect in (Ca, Mg) metaphosphate glasses, Journal of Non-Crystalline Solids 468 (2017) 74–81. (pages 27, 27, 40, 40, 60, and 65).

[162] Y. Vaills, Y. Luspin, G. Hauret, Two opposite effects of sodium on elastic constants of silicate binary glasses, Materials Science and Engineering: B 40 (2-3) (1996) 199–202. (page 27, 27, 27, 27, and 27).

[163] J. Zausch, J. Horbach, The build-up and relaxation of stresses in a glass-forming soft-sphere mixture under shear: A computer simulation study, EPL (Europhysics Letters) 88 (6) (2009) 60001. (page 30).

[164] J. Ruiz-Franco, N. Gnan, E. Zaccarelli, Rheological investigation of gels formed by competing interactions: A numerical study, The Journal of chemical physics 150 (2) (2019) 024905.

[165] C. P. Amann, D. Denisov, M. T. Dang, B. Struth, P. Schall, M. Fuchs, Shear-induced breaking of cages in colloidal glasses: Scattering experiments and mode coupling theory, The Journal of Chemical Physics 143 (3) (2015) 034505.

[166] T. Tomida, T. Egami, Molecular-dynamics simulation of structural anisotropy in glassy metals and its relationship to magnetic anisotropy, Journal of applied physics 69 (8) (1991) 5451–5453.

[167] T. Tomida, T. Egami, Molecular dynamics simulation of structural anisotropy in glassy metals, Materials Science and Engineering: A 134 (1991) 931–934. (page 30).

[168] J. Ding, G. Pan, L. Du, J. Lu, W. Wang, X. Wei, J. Li, Molecular dynamics simulations of the local structures and transport properties of Na_2CO_3 and K_2CO_3, Applied Energy 227 (2018) 555–563. (page 30).

[169] S. L. Roux, P. 6d, Ring statistics analysis of topological networks: New approach and application to amorphous GeS_2 and SiO_2 systems, Computational Materials Science 49 (1) (2010) 70–83. (page 31).

[170] H. Hinrichsen, D. E. Wolf, The physics of granular media, John Wiley & Sons, 2006. (page 32 and 32).

[171] F. Shimizu, S. Ogata, J. Li, Theory of shear banding in metallic glasses and molecular dynamics calculations, Materials Transactions 48 (11) (2007) 2923–2927. (page 33, 33, and 33).

[172] A. Stukowski, Visualization and analysis of atomistic simulation data with OVITO–the open visualization tool, Modelling and Simulation in Materials Science and Engineering 18 (1) (2009) 015012. (page 33).

[173] M. L. Falk, J. S. Langer, Dynamics of viscoplastic deformation in amorphous solids, Physical Review E 57 (6) (1998) 7192–7205. (page 34).

[174] Y. Cheng, A. Cao, E. Ma, Correlation between the elastic modulus and the intrinsic plastic behavior of metallic glasses: The roles of atomic configuration and alloy composition, Acta Materialia 57 (11) (2009) 3253–3267. (page 34 and 34).

[175] U. Hoppe, G. Walter, A. Barz, D. Stachel, A. C. Hannon, The P-O bond lengths in vitreous probed by neutron diffraction with high real-space resolution, Journal of Physics: Condensed Matter 10 (2) (1998) 261–270. (pages 36, 36, 59, 59, and 59).

[176] B. Al-Hasni, G. Mountjoy, Structural investigation of iron phosphate glasses using molecular dynamics simulation, Journal of Non-Crystalline Solids 357 (15) (2011) 2775–2779. (pages 36, 36, and 59).

[177] C. R. Kurkjian, Mechanical properties of phosphate glasses, J. Non. Cryst. Solids 263 (2000) 207–212. (pages 40 and 65).

[178] U. Hoppe, A structural model for phosphate glasses, Journal of Non-Crystalline Solids 195 (1-2) (1996) 138–147. (page 59).

[179] U. Hoppe, G. Walter, R. Kranold, D. Stachel, Structural specifics of phosphate glasses probed by diffraction methods: a review, Journal of Non-Crystalline Solids 263-264 (2000) 29–47. (page 59, 59, 59, 59, and 59).

[180] U. Hoppe, G. Walter, R. Kranold, D. Stachel, An X-ray Diffraction Study of the Structure of Vitreous P_2O_5, Zeitschrift für Naturforschung A 53 (3-4) (1998) 93–104. (page 59).

[181] U. Hoppe, D. Stachel, D. Beyer, The oxygen coordination of metal ions in phosphate and silicate glasses studied by a combination of X-ray and neutron diffraction, Physica Scripta T57 (1995) 122–126. (page 59 and 59).

[182] G. Herms, J. Sakowski, W. Gerike, U. Hoppe, D. Stachel, Short-range and medium-range order in solid and molten metaphosphate glasses, Journal of Non-Crystalline Solids 232-234 (1998) 427–433. (page 59).

[183] U. Hoppe, R. Kranold, D. Stachel, J. Neuefeind, Oxygen Coordination of Modifier Cations in Metaphosphate Glasses Probed by High-Energy X-Ray Diffraction, Phosphorus Research Bulletin 10 (0) (1999) 546–551. (page 59).

[184] U. Hoppe, G. Walter, R. Kranold, D. Stachel, A. Barz, X-ray diffraction study on the mixed alkali and alkaline earth effect in ba, na metaphosphate glasses, Journal of Non-Crystalline Solids 224 (2) (1998) 153–162. (page 59).

[185] P. Bhaskar, R. Kumar, Y. Maurya, R. Ravinder, A. R. Allu, S. Das, N. N. Gosvami, R. E. Youngman, M. S. Bødker, N. Mascaraque, M. M. Smedskjaer, M. Bauchy, N. A. Krishnan, Cooling rate effects on the structure of 45s5 bioglass: Insights from experiments and simulations, Journal of Non-Crystalline Solids 534 (2020) 119952. (pages 60 and 98).

[186] K. Januchta, M. Bauchy, R. E. Youngman, S. J. Rzoska, M. Bockowski, M. M. Smedskjaer, Modifier field strength effects on densification behavior and mechanical properties of alkali aluminoborate glasses, Phys. Rev. Materials 1 (2017) 063603. (page 65).

[187] M. Bauchy, M. Micoulaut, Atomic scale foundation of temperature-dependent bonding constraints in network glasses and liquids, Journal of Non-Crystalline Solids 357 (14) (2011) 2530–2537. (page 66).

[188] U. Hoppe, Short-range order of phosphate glasses studied by a difference approach using x-ray diffraction results, Journal of Non-Crystalline Solids 183 (1-2) (1995) 85–91. (page 66).

[189] A. I. Fu, J. C. Mauro, Topology of alkali phosphate glass networks, Journal of Non-Crystalline Solids 361 (2013) 57–62. (page 66 and 66).

[190] S. C. Chowdhury, B. Z. G. Haque, J. W. Gillespie, Molecular dynamics simulations of the structure and mechanical properties of silica glass using ReaxFF, Journal of Materials Science 51 (22) (2016) 10139–10159. (pages 70, 70, 131, and 131).

[191] R. Limbach, B. P. Rodrigues, L. Wondraczek, Strain-rate sensitivity of glasses, Journal of Non-Crystalline Solids 404 (2014) 124–134. (pages 70 and 131).

[192] I. Avramov, T. Vassilev, I. Penkov, The glass transition temperature of silicate and borate glasses, Journal of Non-Crystalline Solids 351 (6-7) (2005) 472–476. (page 75 and 75).

[193] M. Bouhadja, N. Jakse, A. Pasturel, Striking role of non-bridging oxygen on glass transition temperature of calcium aluminosilicate glass-formers, The Journal of Chemical Physics 140 (23) (2014) 234507. (page 75).

[194] S. Ganisetti, Atomistic simulations of silica glass: Topological anisotropy and mechanical properties, Ph.D. thesis, unpublished, unpublished. (pages 75 and 122).

[195] H. Nesbitt, G. Bancroft, G. Henderson, R. Ho, K. Dalby, Y. Huang, Z. Yan, Bridging, non-bridging and free (O2–) oxygen in Na_2O-SiO_2 glasses: An X-ray Photoelectron Spectroscopic (XPS) and Nuclear Magnetic Resonance (NMR) study, Journal of Non-Crystalline Solids 357 (1) (2011) 170–180. (pages 77 and 136).

[196] H. Maekawa, T. Maekawa, K. Kawamura, T. Yokokawa, The structural groups of alkali silicate glasses determined from 29si MAS-NMR, Journal of Non-Crystalline Solids 127 (1) (1991) 53–64. (page 78).

[197] W. Griffioen, Optical fiber mechanical reliability, Eindhoven University of Technology, 1995. (page 79 and 79).

[198] N. P. Lower, R. K. Brow, C. R. Kurkjian, Inert failure strain studies of sodium silicate glass fibers, Journal of Non-Crystalline Solids 349 (2004) 168–172. (page 80, 80, 80, 80, and 80).

[199] Handbook of Glass Properties, Elsevier, 1986. (page 80, 80, 80, and 80).

[200] T. Hao, Z. M. Hossain, Atomistic mechanisms of crack nucleation and propagation in amorphous silica, Physical Review B 100 (1) (Jul. 2019). (page 86).

[201] A. A. Griffith, Vi. the phenomena of rupture and flow in solids, Philosophical transactions of the royal society of london. Series A, containing papers of a mathematical or physical character 221 (582-593) (1921) 163–198. (page 86).

[202] X. Yuan, A. Cormack, Efficient algorithm for primitive ring statistics in topological networks, Computational Materials Science 24 (3) (2002) 343–360. (pages 97, 97, 98, and 105).

[203] N. M. Vedishcheva, B. A. Shakhmatkin, M. M. Shultz, B. Vessal, A. C. Wright, B. Bachra, A. G. Clare, A. C. Hannon, R. N. Sinclair, A thermodynamic, molecular dynamics and neutron diffraction investigation of the distribution of tetrahedral si(n) species and the network modifying cation environment in alkali silicate glasses, Journal of Non-Crystalline Solids 192-193 (1995) 292–297. (page 97, 97, 97, and 97).

[204] D. I. Grimley, A. C. Wright, R. N. Sinclair, Neutron scattering from vitreous silica iv. time-of-flight diffraction, Journal of Non-Crystalline Solids 119 (1) (1990) 49–64.

[205] G. Henderson, A Si K-edge EXAFS/XANES study of sodium silicate glasses, Journal of Non-Crystalline Solids 183 (1-2) (1995) 43–50.

[206] C. Mazzara, J. Jupille, A.-M. Flank, P. Lagarde, Stereochemical order around sodium in amorphous silica, The Journal of Physical Chemistry B 104 (15) (2000) 3438–3445. (page 97 and 97).

[207] A. C. Wright, Neutron scattering from vitreous silica. v. the structure of vitreous silica: What have we learned from 60 years of diffraction studies?, Journal of Non-Crystalline Solids 179 (1994) 84–115. (page 97).

[208] M. Misawa, D. Price, K. Suzuki, The short-range structure of alkali disilicate glasses by pulsed neutron total scattering, Journal of Non-Crystalline Solids 37 (1) (1980) 85–97. (page 97).

[209] T. M. Clark, P. J. Grandinetti, P. Florian, J. F. Stebbins, Correlated structural distributions in silica glass, Physical Review B 70 (6) (aug 2004). (page 97).

[210] Q. Zhou, T. Du, L. Guo, M. M. Smedskjaer, M. Bauchy, New insights into the structure of sodium silicate glasses by force-enhanced atomic refinement, Journal of Non-Crystalline Solids 536 (2020) 120006. (pages 98 and 105).

[211] L. Deng, S. Urata, Y. Takimoto, T. Miyajima, S. H. Hahn, A. C. T. Duin, J. Du, Structural features of sodium silicate glasses from reactive force field-based molecular dynamics simulations, Journal of the American Ceramic Society 103 (3) (2019) 1600–1614.

[212] Y. Shi, J. Neuefeind, D. Ma, K. Page, L. A. Lamberson, N. J. Smith, A. Tandia, A. P. Song, Ring size distribution in silicate glasses revealed by neutron scattering first sharp diffraction peak analysis, Journal of Non-Crystalline Solids 516 (2019) 71–81.

[213] H. Liu, S. H. Hahn, M. Ren, M. Thiruvillamalai, T. M. Gross, J. Du, A. C. T. Duin, S. H. Kim, Searching for correlations between vibrational spectral features and structural parameters of silicate glass network, Journal of the American Ceramic Society 103 (6) (2020) 3575–3589. (pages 98 and 105).

[214] C. S. Marians, L. W. Hobbs, Network properties of crystalline polymorphs of silica, Journal of Non-Crystalline Solids 124 (2-3) (1990) 242–253. (page 98).

[215] F. Ebrahem, F. Bamer, B. Markert, The influence of the network topology on the deformation and fracture behaviour of silica glass: A molecular dynamics study, Computational Materials Science 149 (2018) 162–169. (pages 98, 102, and 105).

[216] C. Kurkjian, P. Gupta, R. Brow, N. Lower, The intrinsic strength and fatigue of oxide glasses, Journal of Non-Crystalline Solids 316 (1) (2003) 114–124. (page 98).

[217] M. Vukcevich, A new interpretation of the anomalous properties of vitreous silica, Journal of Non-Crystalline Solids 11 (1) (1972) 25–63. (page 98 and 98).

[218] A. Godet, T. Sylvestre, V. Pêcheur, J. Chrétien, J.-C. Beugnot, K. P. Huy, Nonlinear elasticity of silica nanofiber, APL Photonics 4 (8) (2019) 080804. (page 99).

[219] Z. Zhang, S. Ispas, W. Kob, Origin of the non-linear elastic behavior of silicate glasses, Acta Materialia 231 (2022) 117855. (pages 99, 99, 99, 99, 103, 103, and 126).

[220] K. Muralidharan, J. Simmons, P. Deymier, K. Runge, Molecular dynamics studies of brittle fracture in vitreous silica: Review and recent progress, Journal of Non-Crystalline Solids 351 (18) (2005) 1532–1542. (page 102 and 102).

[221] T. P. Swiler, J. H. Simmons, A. C. Wright, Molecular dynamics study of brittle fracture in silica glass and cristobalite, Journal of Non-Crystalline Solids 182 (1-2) (1995) 68–77. (page 102).

[222] H. Mei, Y. Yang, A. C. van Duin, S. B. Sinnott, J. C. Mauro, L. Liu, Z. Fu, Effects of water on the mechanical properties of silica glass using molecular dynamics, Acta Materialia 178 (2019) 36–44.

[223] S. C. Chowdhury, E. A. Wise, R. Ganesh, J. W. Gillespie, Effects of surface crack on the mechanical properties of silica: A molecular dynamics simulation study, Engineering Fracture Mechanics 207 (2019) 99–108.

[224] J. M. Rimsza, R. E. Jones, L. J. Criscenti, Crack propagation in silica from reactive classical molecular dynamics simulations, Journal of the American Ceramic Society 101 (4) (2017) 1488–1499.

[225] T. Vo, B. Reeder, A. Damone, P. Newell, Effect of domain size, boundary, and loading conditions on mechanical properties of amorphous silica: A reactive molecular dynamics study, Nanomaterials 10 (1) (2019) 54. (page 102).

[226] Z. Zhang, S. Ispas, W. Kob, The critical role of the interaction potential and simulation protocol for the structural and mechanical properties of sodosilicate glasses, Journal of Non-Crystalline Solids 532 (2020) 119895. (pages 103 and 130).

[227] G. Molnár, P. Ganster, A. Tanguy, E. Barthel, G. Kermouche, Densification dependent yield criteria for sodium silicate glasses – an atomistic simulation approach, Acta Materialia 111 (2016) 129–137. (pages 103, 107, and 121).

[228] T. F. Soules, R. F. Busbey, The rheological properties and fracture of a molecular dynamic simulation of sodium silicate glass, The Journal of Chemical Physics 78 (10) (1983) 6307–6316. (page 103).

[229] G. Molnár, P. Ganster, A. Tanguy, Effect of composition and pressure on the shear strength of sodium silicate glasses: An atomic scale simulation study, Physical Review E 95 (4) (Apr. 2017). (pages 103, 107, 107, 110, and 121).

[230] S. Bonfanti, E. E. Ferrero, A. L. Sellerio, R. Guerra, S. Zapperi, Damage accumulation in silica glass nanofibers, Nano Letters 18 (7) (2018) 4100–4106. (pages 103, 103, and 110).

[231] T. To, S. S. Sørensen, J. F. S. Christensen, R. Christensen, L. R. Jensen, M. Bockowski, M. Bauchy, M. M. Smedskjaer, Bond switching in densified oxide glass enables record-high fracture toughness, ACS Applied Materials & Interfaces 13 (15) (2021) 17753–17765. (pages 103, 103, and 110).

[232] E. H. Bogardus, Third-order elastic constants of Ge, MgO, and fused SiO_2, Journal of Applied Physics 36 (8) (1965) 2504–2513. (page 107).

[233] K. ichi Kondo, S. Iio, A. Sawaoka, Nonlinear pressure dependence of the elastic moduli of fused quartz up to 3 GPa, Journal of Applied Physics 52 (4) (1981) 2826–2831.

[234] H. J. McSkimin, Measurement of elastic constants at low temperatures by means of ultrasonic waves–data for silicon and germanium single crystals, and for fused silica, Journal of Applied Physics 24 (8) (1953) 988–997.

[235] C. Payan, V. Garnier, J. Moysan, P. A. Johnson, Determination of third order elastic constants in a complex solid applying coda wave interferometry, Applied Physics Letters 94 (1) (2009) 011904.

[236] T. Du, S. S. Sørensen, T. To, M. M. Smedskjaer, Oxide glasses under pressure: Recent insights from experiments and simulations, Journal of Applied Physics 131 (17) (2022) 170901. (page 107).

[237] F. Yuan, L. Huang, Size-dependent elasticity of amorphous silica nanowire: A molecular dynamics study, Applied Physics Letters 103 (20) (2013) 201905. (page 107).

[238] H. Bhaumik, G. Foffi, S. Sastry, Avalanches, clusters, and structural change in cyclically sheared silica glass, Physical Review Letters 128 (9) (Feb. 2022). (pages 107, 110, and 114).

[239] K.-H. Lee, Y. Yang, L. Ding, B. Ziebarth, M. J. Davis, J. C. Mauro, Pressure effects on shear deformation of borosilicate glasses, Journal of the American Ceramic Society 104 (7) (2021) 3073–3086. (pages 115, 115, and 125).

[240] P. Cao, M. P. Short, S. Yip, Potential energy landscape activations governing plastic flows in glass rheology, Proceedings of the National Academy of Sciences 116 (38) (2019) 18790–18797. (page 115).

[241] J. J. Lewandowski, A. L. Greer, Temperature rise at shear bands in metallic glasses, Nature Materials 5 (1) (2005) 15–18. (page 120).

[242] K. Martens, L. Bocquet, J.-L. Barrat, Spontaneous formation of permanent shear bands in a mesoscopic model of flowing disordered matter, Soft Matter 8 (15) (2012) 4197. (page 120).

[243] K. Lamp, N. Küchler, J. Horbach, Brittle yielding in supercooled liquids below the critical temperature of mode coupling theory, The Journal of Chemical Physics 157 (3) (2022) 034501. (pages 121, 132, and 132).

[244] S. Romeis, J. Paul, P. Herre, D. de Ligny, J. Schmidt, W. Peukert, Local densification of a single micron sized silica sphere by uniaxial compression, Scripta Materialia 108 (2015) 84–87. (page 122).

[245] D. Wakabayashi, N. Funamori, T. Sato, Enhanced plasticity of silica glass at high pressure, Physical Review B 91 (1) (Jan. 2015). (page 122).

[246] B. Wang, Y. Yu, M. Wang, J. C. Mauro, M. Bauchy, Nanoductility in silicate glasses is driven by topological heterogeneity, Physical Review B 93 (6) (Feb. 2016). (pages 122, 124, 127, and 128).

[247] Y.-C. Chen, Z. Lu, K. ichi Nomura, W. Wang, R. K. Kalia, A. Nakano, P. Vashishta, Interaction of voids and nanoductility in silica glass, Physical Review Letters 99 (15) (Oct. 2007).

[248] D. Bonamy, S. Prades, L. Ponson, D. Dalmas, C. Rountree, E. Bouchaud, C. Guillot, Experimental investigation of damage and fracture in glassy materials at the nanometre scale, International Journal of Materials and Product Technology 26 (3/4) (2006) 339.

[249] Z. Lu, K. ichi Nomura, A. Sharma, W. Wang, C. Zhang, A. Nakano, R. Kalia, P. Vashishta, E. Bouchaud, C. Rountree, Dynamics of wing cracks and nanoscale damage in glass, Physical Review Letters 95 (13) (Sep. 2005).

[250] S. Prades, D. Bonamy, D. Dalmas, E. Bouchaud, C. Guillot, Nano-ductile crack propagation in glasses under stress corrosion: spatiotemporal evolution of damage in the vicinity of the crack tip, International Journal of Solids and Structures 42 (2) (2005) 637–645.

[251] L.-H. Kieu, J.-M. Delaye, C. Stolz, Modeling the effect of composition and thermal quenching on the fracture behavior of borosilicate glass, Journal of Non-Crystalline Solids 358 (23) (2012) 3268–3279. (pages 124 and 128).

[252] J. Sehgal, S. Ito, A new low-brittleness glass in the soda-lime-silica glass family, Journal of the American Ceramic Society 81 (9) (2005) 2485–2488. (page 124, 124, and 124).

[253] K. Januchta, M. M. Smedskjaer, Indentation deformation in oxide glasses: Quantification, structural changes, and relation to cracking, Journal of Non-Crystalline Solids: X 1 (2019) 100007. (page 124 and 124).

[254] V. Keryvin, L. Charleux, R. Hin, J.-P. Guin, J.-C. Sangleboeuf, Mechanical behaviour of fully densified silica glass under vickers indentation, Acta Materialia 129 (2017) 492–499.

[255] T. Rouxel, H. Ji, J. P. Guin, F. Augereau, B. Rufflé, Indentation deformation mechanism in glass: Densification versus shear flow, Journal of Applied Physics 107 (9) (2010) 094903. (page 124).

[256] S. Yoshida, J.-C. Sanglebœuf, T. Rouxel, Quantitative evaluation of indentation-induced densification in glass, Journal of Materials Research 20 (12) (2005) 3404–3412. (page 124 and 124).

[257] T. Rouxel, Elastic properties and short-to medium-range order in glasses, Journal of the American Ceramic Society 90 (10) (2007) 3019–3039. (page 124).

[258] K. Januchta, M. Stepniewska, L. R. Jensen, Y. Zhang, M. A. J. Somers, M. Bauchy, Y. Yue, M. M. Smedskjaer, Breaking the limit of micro-ductility in oxide glasses, Advanced Science 6 (18) (2019) 1901281. (page 124).

[259] J. D. MACKENZIE, High-pressure effects on oxide glasses: I, densification in rigid state, Journal of the American Ceramic Society 46 (10) (1963) 461–470. (page 125 and 125).

[260] J. D. MACKENZIE, High-pressure effects on oxide glasses: II, subsequent heat treatment, Journal of the American Ceramic Society 46 (10) (1963) 470–476. (page 125).

[261] M. Micoulaut, M. Bauchy, H. Flores-Ruiz, Topological Constraints, Rigidity Transitions, and Anomalies in Molecular Networks, Springer International Publishing, Cham, 2015, pp. 275–311. (page 126 and 126).

[262] Y. Vaills, T. Qu, M. Micoulaut, F. Chaimbault, P. Boolchand, Direct evidence of rigidity loss and self-organization in silicate glasses, Journal of Physics: Condensed Matter 17 (32) (2005) 4889–4896. (page 126 and 126).

[263] S. Ganisetti, A. Atila, J. Guénolé, A. Prakash, J. Horbach, L. Wondraczek, E. Bitzek, The origin of deformation induced topological anisotropy in silica glass (2022). (page 130).

[264] W. Song, X. Li, B. Wang, N. M. A. Krishnan, S. Goyal, M. M. Smedskjaer, J. C. Mauro, C. G. Hoover, M. Bauchy, Atomic picture of structural relaxation in silicate glasses, Applied Physics Letters 114 (23) (2019) 233703. (page 130 and 130).

[265] X. Yue, C. Liu, S. Pan, A. Inoue, P. Liaw, C. Fan, Effect of cooling rate on structures and mechanical behavior of Cu50Zr50 metallic glass: A molecular-dynamics study, Physica B: Condensed Matter 547 (2018) 48–54. (page 130).

[266] F. Wang, D. Yin, J. Lv, S. Zhang, M. Ma, X. Zhang, R. Liu, Effect on microstructure and plastic deformation behavior of a Zr-based amorphous alloy by cooling rate control, Journal of Materials Science & Technology 82 (2021) 1–9.

[267] S. D. Feng, K. C. Chan, S. H. Chen, L. Zhao, R. P. Liu, The role of configurational disorder on plastic and dynamic deformation in Cu64Zr36 metallic glasses: A molecular dynamics analysis, Scientific Reports 7 (1) (Jan. 2017). (page 130 and 130).

[268] J. Yeon, S. C. Chowdhury, J. W. Gillespie, Mechanical properties and damage analysis of s-glass: A reactive molecular dynamics study, Composites Part B: Engineering 234 (2022) 109706. (page 131).

[269] C. Zehnder, S. Bruns, J.-N. Peltzer, K. Durst, S. Korte-Kerzel, D. Möncke, Influence of cooling rate on cracking and plastic deformation during impact and indentation of borosilicate glasses, Frontiers in Materials 4 (Mar. 2017). (page 131).

[270] T. Nieh, C. Schuh, J. Wadsworth, Y. Li, Strain rate-dependent deformation in bulk metallic glasses, Intermetallics 10 (11-12) (2002) 1177–1182. (page 131).

[271] M. Micoulaut, J. Phillips, Onset of rigidity in glasses: From random to self-organized networks, Journal of Non-Crystalline Solids 353 (18-21) (2007) 1732–1740. (page 136).

[272] D. I. Novita, P. Boolchand, M. Malki, M. Micoulaut, Fast-ion conduction and flexibility of glassy networks, Physical Review Letters 98 (19) (May 2007). (page 136).

[273] K. Meyer, Characterization of the structure of binary zinc ultraphosphate glasses by infrared and raman spectroscopy, Journal of Non-Crystalline Solids 209 (3) (1997) 227–239. (page 136).

[274] J. Wong, C. A. Angell, Application of spectroscopy in the study of glassy solids, part II. infrared, raman, EPR, and NMR spectral studies, Applied Spectroscopy Reviews 4 (2) (1971) 155–232. (page 136).

[275] C. Sonneville, A. Mermet, B. Champagnon, C. Martinet, J. Margueritat, D. de Ligny, T. Deschamps, F. Balima, Progressive transformations of silica glass upon densification, The Journal of Chemical Physics 137 (12) (2012) 124505. (page 137).

[276] T. Deschamps, J. Margueritat, C. Martinet, A. Mermet, B. Champagnon, Elastic moduli of permanently densified silica glasses, Scientific Reports 4 (1) (Nov. 2014). (page 137).

Acknowledgments

This thesis is the culmination of work of four years, which would not have been possible without the help and support of several people. I am filled with gratitude as I reflect upon the completion of my PhD journey, a path that has been difficult yet immensely rewarding and valuable. I would like to express my deepest appreciation to all those who have supported and guided me along the way.

First and foremost, I extend my heartfelt thanks to my supervisor, Prof. Dr.-Ing Erik Bitzek. Your mentorship, support, and insights have been instrumental in shaping my research and myself as a scientist. Your dedication to academic excellence has inspired me to strive for greatness. I am truly grateful for guiding me through the challenges and providing constructive feedback that has significantly enhanced the quality of this dissertation.

I would also like to express my sincere gratitude to Prof. Dr. Dominique de Ligny for reviewing the thesis. Your expertise and careful attention to detail have been a great support during the PhD defense. I would like to express my sincere gratitude to Prof. Dr. Erdmann Spiecker for being the chairman of my defense. I would like to thank Prof. Dr. Michael Engel for being the external examiner.

I wish to express my gratitude for Dr.-Ing. Duancheng Ma for his support and encouragement. Dr. Julien Guénolé was a good source of motivation, and he still is, to which I am really grateful. I wish to express my gratitude for Zhuocheng (Ray) Xie for being such a great colleague, collaborator, and friend. Hao Lyu for being an amazing colleague and friend. To all my dear colleagues in the SimGroup, Shivraj Karewar, Tarakeshwar Lakshmipathy, Frédéric Houllé, Aviral Vaid, Polina Baranova, Saba Khadivianazar, and Benedikt Eggle-Sievers, thank you for your unwavering support and companionship throughout this challenging journey. Your intellectual exchanges, and shared experiences have made the PhD experience more enjoyable and enriching.

I would also like to extend my appreciation to all the colleagues in WW1, the chair Prof. Dr. Mathias Göken, PD. Dr. Heinz Werner Höppel, the secretaries and other technicians for the friendly and supportive working atmosphere.

Finally, I would like to express my deepest gratitude to my family. Your unconditional love, and encouragement have been the source of my motivation and my thrive for success. I am truly lucky and blessed to have you.

I acknowledge the funding from DFG (SPP1594 and SFB1394), and European Union through (ERC, MicroKIC), without their funding this work would not be possible. I would like to acknowledge Regionales Rechenzentrum Erlangen (RRZE) for providing compute resources and support.

To all those mentioned above and to the countless others who have contributed to my journey in ways both big and small, I offer my sincere thanks. This dissertation would not have been possible without your support, and belief in my abilities. May our paths continue to intertwine, and may we all strive for academic excellence and personal growth.

Saarbrücken
26.05.2023

Achraf Atila